NANOPLASMONIC EFFICACY OF GOLD TRIANGULAR NANOPRISMS IN MEASUREMENT SCIENCE: APPLICATIONS RANGING FROM BIOMEDICAL TO FORENSIC SCIENCES

by

Thakshila Liyanage

A Dissertation

Submitted to the Faculty of Purdue University

In Partial Fulfillment of the Requirements for the degree of

Doctor of Philosophy

Department of Chemistry and Chemical Biology

Indianapolis, Indiana

December 2019

THE PURDUE UNIVERSITY GRADUATE SCHOOL
STATEMENT OF COMMITTEE APPROVAL

Dr. Rajesh Sardar, Chair

Department of Chemistry and Chemical Biology

Dr. John Goodpaster

Department of Chemistry and Chemical Biology

Dr. Christoph Naumann

Department of Chemistry and Chemical Biology

Dr. Mangilal Agarwal

Department of Mechanical and Energy Engineering

Approved by:

Dr. Eric Long

This Dissertation is dedicated to my loving parents

Mr. Habarakada Liyanage Ananda

&

Mrs. Indrani Suriyaarachchi

ACKNOWLEDGMENTS

First of all, I would like to express my heartfelt gratitude to my thesis advisor Dr. Rajesh Sardar for sharing his knowledge, and the support he provided me during my PhD. Without his guidance and relentless help, this dissertation would not have been possible. His support enabled me to develop into a competent scientist who is involved in cutting-edge research to improve the quality of human life. I am also grateful that he helped me to flourish into a good mentor, team worker and for all the great tips he gave me that enabled me to expand my horizons. Thank you for standing with me during hard times and all your help to ease my stay in the USA. Dr. Sardar always encouraged my areas of strength but never ignored my weaknesses and I am thankful for this. I am very appreciative of the opportunities he provided me to participate in prestigious conferences that also helped improve my presentation skills and networking. Again, thank you so much for all of your input for my future success as a scientist and individual.

Also, I wish to express my sincere gratitude to my dissertation committee— Dr. John Goodpaster, Dr. Christoph Naumann, and Dr. Mangilal Agarwal for their time, guidance and comment into my thesis work. I am extremely grateful for the collaboration you provided with some of my research work and all of your assistance. Thank you for everything.

I wish to also convey my thanks to Dr. Partha Basu, the head of the chemistry department and all the faculty especially Dr. Frédérique Deiss for giving her input for presentations and other special events as a mole council advisor and the staff, Beverly Foley, Lynn Gerrard, Wai Ping Kam and Donna Roskowski for supporting my research and laboratory functions. Especially, thank you, Kitty O'Doherty, for following up with me to ensure I meet the various deadlines and for making things smooth for me until my graduation. Finally, thank you for the all shared resources that the department has provided to facilitate my research work at IUPUI.

Also, my gratitude extends to Dr. Gayatri K. Joshi, Dr. Katie Lawrence and Dr. Meghan Tunis, former graduate students for their enormous support at the early stages of my PhD, especially Dr. Gayatri K. Joshi, my first immediate mentor who trained me in the all fundamentals of my research. A special thanks goes to current graduate students Adriana Masterson, Jacob Lee, and post-doc. Dr. Gyanaranjan Prusty for all their support and encouragement. Thanks for making working in the lab a lot of fun! Finally, to my fellow graduate students in the department and all

mole council members for their support especially listen to my presentations and offer encouragement.

Last, but not least, I wish to express my sincere thanks to my loving parents, wonderful two sisters and three brothers. Without them, it would have been impossible to achieve this level of success in my life. Thank you for steadfastly supporting me during all the challenges I encountered these past five years, for encouraging me to see the good in all situations, regardless of the challenges and reminding me not to give up. A special thanks also goes out to my friends Rex Miller and Cinthia Miller for their support as a family that eased my life as I resided thousands of miles away from home. Thank you.

A final thanks to all those who helped me and even those who tried to discourage me during the past five years—your influences improved my personality and strengthened my character. Thank you.

TABLE OF CONTENTS

LIST OF TABLES

LIST OF FIGURES

ABBREVIATION

LSPR	Localized Surface Plasmon Resonance
SPR	Surface Plasmon Resonance
SPP	Surface Plasmon Polarization
NPs	Nanoparticles
Au TNPs	Gold Triangular Nanoprisms
BRI	Bulk Refractive Index
LDI MS	Laser Desorption/Ionization Mass Spectrometry
NMR	Nuclear Magnetic Resonance
DNP	Dynamic Nuclear Polarization
cTnT	Cardiac Troponin T
RDX	Cyclotrimethylene Trinitro Amine
TNT	Trinitrotoluene
PETN	Pentaerythritol Tetranitrate
SERS	Surface Enhanced Raman Spectroscopy
EM	Electro Magnetic
CT	Charge Transfer
FOM	Figure of Merit
PEFS	Plasmon Enhanced Fluorescence Spectroscopy
RI	Refractive Index
RIU	Refractive Index Unit
UPS	Ultraviolet Photoelectron Spectroscopy
PEG	polyethylene Glycol
2D/3D	2-Dimentional, 3-Dimentional
NH_2	Amine
OCH_3	Trimethoxy
CH_3	Methyl
Cl	Chloro
Br	Bromo
NO_2	Nitro

CF_3	Trifluoro Methyl
EWG	Electro Withdrawing Group
EDG	Electro Donating Group
CID	Chemical Interface Damping
Au BPs	Gold Bipyramids
ppq	Parts-Per-Quadrillion
EF	Enhancement Factor
GC-MS	Gas Chromatography-Mass Spectrometry
TOA	Trioctylamine
PMHS	Poly(methylhydrosiloxane)
APTES	(3-Aminopropyl)-Triethoxysilane
CH_3CN	Acetonitrile
Et3PAuCl	Chloro(triethylphosphine) gold (I)
SEM	Scanning electron
TEM	Transmission Electron Microscopy
DNT	4-Dinitrotoluene
TNB	Trinitrobenzene
LOD	Limit of Detection
PTES	Phenyl-Triethoxysilane
OTES	n-Octyl-Triethoxysilane
TEA	Triethylamine
NHS	N-hydroxysulfosuccinimide Solution
EDC	1-Ethyl-3-(3-Dimethylamino)propyl Carbodiimide
BC	Bladder Cancer
MT	Metathesis
NMT	Non-Metathesis
NC	Normal Control
DNA	Deoxyribonucleic Acid
ssDNA	Single Stranded Deoxyribonucleic Acid
RNA	Ribonucleic Acid

ABSTRACT

Noble metal nanostructures display collective oscillation of the surface conduction electrons upon light irradiation as a form of localized surface plasmon resonance (LSPR) properties. Size, shape and the refractive index of surrounding environment are the key features that controls the LSPR properties. Surface passivating ligands have the ability to modify the charge density of nanostructures to allow resonant wavelength to match that of the incident light, a phenomenon called "plasmoelectric effect,". According to the drude model Red and blue shifts of LSPR peak of nanostructures are observed in the event of reducing and increasing charge density, respectively. However, herein we report unusual LSPR properties of gold triangular nanoprisms (Au TNPs) upon functionalization with para-substituted thiophenols (X-Ph-SH, X = $-NH_2$, $-OCH_3$, $-CH_3$, -H, -Cl, $-CF_3$, and $-NO_2$). Accordingly, we hypothesized that an appropriate energy level alignment between the Au Fermi energy and the HOMO or LUMO of ligands allows delocalization of surface plasmon excitation at the hybrid inorganic-organic interface, and thus provides a thermodynamically driven plasmoelectric effect. We further validated our hypothesis by calculating the HOMO and LUMO levels and also work function changes of Au TNPs upon functionalization with para substituted thiol. We further utilized our unique finding to design ultrasensitive plasmonic substrate for biosensing of cancer microRNA in bladder cancer and owe to unpresidential sensitivity of the developed Au TNPs based LSPR sensor, for the first time we have been utilized to analysis the tumor suppressor microRNA for more accurate diagnosis of BC. Additionally, we have been advancing our sensing platform to mitigate the false positive and negative responses of the sensing platform using surface enhanced fluorescence technique. This noninvasive, highly sensitive, highly specific, also does not have false positives technique provide strong key to detect cancer at very early stage, hence increase the cancer survival rate. Moreover, the electromagnetic field enhancement of Surface-Enhanced Raman Scattering (SERS) and other related surface-enhanced spectroscopic processes resulted from the LSPR property. This dissertation describes the design and development of entirely new SERS nanosensors using flexible SERS substrate based on unique LSPR property of Au TNPs and developed sensors shows excellent SERS activity (enhancement factor = ~6.0 x 106) and limit of detection (as low as 56 parts-per-quadrillions) with high selectivity by chemometric analyses among three commonly used explosives (TNT, RDX, and PETN). Further we achieved the programable self-assembly of Au

TNPs using molecular tailoring to form a 3D supper lattice array based on the substrate effect. Here we achieved the highest reported sensitivity for potent drug analysis, including opioids and synthetic cannabinoids from human plasma obtained from the emergency room. This exquisite sensitivity is mainly due to the two reasons, including molecular resonance of the adsorbate molecules and the plasmonic coupling among the nanoparticles. Altogether we are highly optimistic that our research will not only increase the patient survival rate through early detection of cancer but also help to battle the “war against drugs” that together is expected to enhance the quality of human life.

CHAPTER 1. NANOPLASMONIC EFFICACY OF GOLD TRIANGULAR NANOPRISMS IN MEASUREMENT SCIENCE: APPLICATIONS RANGING FROM BIOMEDICAL TO FORENSIC SCIENCES

1.1 Motivation

The field of nanotechnology has rapidly advanced over the past decade[1-5], achieving novel synthetic procedures for a wide range of nanoscale materials owing to their unique optical, electronic, magnetic, chemical, mechanical, and catalytic properties[6-10]. These properties can be easily tuned by size, shape, and composition of the nanostructure[11, 12]. Nanomaterials can be defined as any material with at least one dimension in the 1−100 nm range[14]. When the matter is reduced to nanoscale, the above-mentioned unique physical properties occur in comparison with bulk materials[15]. Nanomaterials can be metals, polymers, semiconductors, and carbon-based materials; however, this work is mainly focused on metallic nanostructures[11, 12]. Due to the nanoscale, intense and confined electromagnetic fields generated by surface plasmons in metal, in addition to the high surface to volume ratio, have led metallic nanostructures becoming attractive for analytical applications[16]. Scientists in different fields, including physicists, chemists, material scientists, and biologists have widely explored this plasmonic-based phenomenon and its potential applications in practice. Metallic nanoparticles have been utilized in various applications within analytical chemistry, including spectroscopy[17-19], electronic detection separations,[20-22] and sensors[23-28].

When a nanoscale metal structure interacts with light waves at the metal-dielectric interface, it results in the generation of charge density waves which have been identified as surface plasmons (SP) due to the collective oscillation of surface electrons. Collective oscillation occurring in localized mode has been identified as localized surface plasmon resonance (LSPR), and that taking place in propagation mode is known as surface plasmon resonance (SPR). Comparison of the bulk plasmon, SPR, and LSPR is shown in **Figure 1.1**[11, 12, 15, 29].

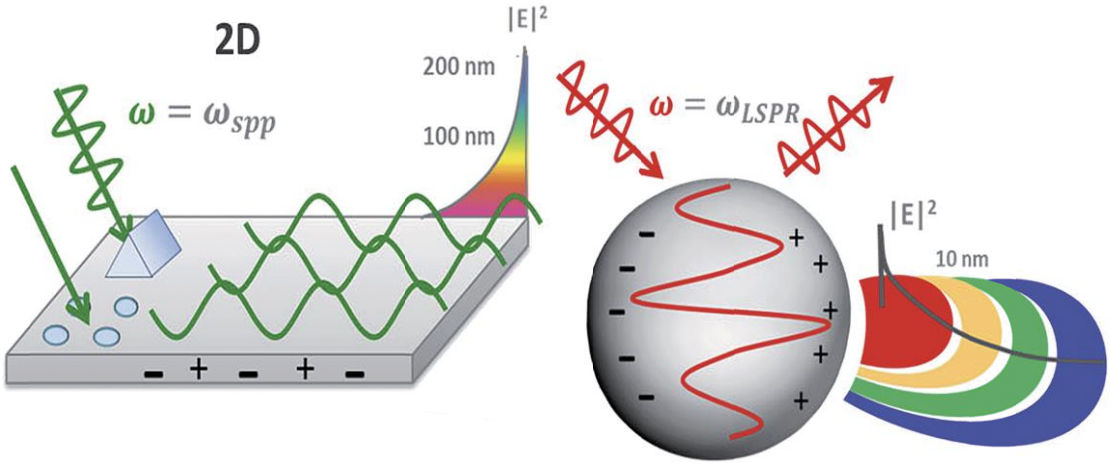

Figure 1.1. Comparison between SPR vs LSPR. A) Surface plasmon resonance (SPR) on a 2D surface. The oscillating electrons propagate along the surface like ripples across the surface of water, coupling to an electromagnetic field that propagates along the interface, and the resulting amplitude oscillation decreases exponentially as the distance from the interface increases. **B)** When the metallic nanoparticle is smaller than the incident wavelength, Due to the collective oscillation of electrons, the localized surface plasmon resonance (LSPR) occurs. As a result, scattering, absorption, and an amplified electromagnetic (EM) field occurs. The EM field associated with LSPR generally extends to the surrounding medium (10–30 nm) and displays exponential decay of the dipole as the distance increases[15].

The resulting plasmon resonance has been utilized in various applications. For instance, scientists working in the optic field have attempted to use plasmons to concentrate, channel, and change the phase of light, with a view to miniaturizing plasmonic circuits as compared with those currently used[30-33]. SPR can more efficiently transfer information in microprocessors as compared with current electronic transistors. The surface plasmons resulted from SPR has the same frequency as the electromagnetic waves. However, wavelength several times shorter at engineered metal dielectric interfaces[33]. Further, metallic nanostructures can provide higher information density due to plasmonic properties, which have been utilized in surface-enhanced Raman spectroscopy/scattering (SERS) to amplify the signal, providing a powerful method to detect single molecules[32, 33].

Fluorescence is a common technique used in sensing applications. The biggest challenge associated with a short lifetime, photobleaching, is the limited brightness associated with conventional fluorophores; however, owing to their special properties at nanoscale, fluorescent nanoparticles are more stable and resistant to photobleaching, possessing a higher luminescent intensity and a longer lifetime. Moreover, fluorescent nanoparticles have more symmetrical and narrower emissions and can be easily tuned by size, shape, and composition as compared with organic dyes[34, 35].

Interestingly, plasmonic nanomaterials are further involved in plasmon-enhanced laser desorption/ionization mass spectrometry (LDI MS) via two mechanisms[36]: (1) amplified cross-sectional absorption; and (2) increased generation of hot carriers at the resonance wavelength. The plasmonic properties of metallic nanostructures create larger absorption cross-sections, which further induce a greater photothermal effect. As a result, the energy transfer transferred to the analytes. and due to this extra energy, analytes undergo a phase transition from condensed to gaseous ions, which can be detected by a mass detector. To avoid the photodecomposition of complexes of metal ions due to the large generation of hot carriers, mass spectroscopy can be used in the UV-NIR range, for which Au36 and Cu38 metallic nanoparticles (e.g., nanospheres, nanoshells, and nanorods) are ideal. Recently, it has been demonstrated that the anti-bonding modes of Au nanoshells can generate hot carriers in the UV range, resulting in higher sensitivity over organic matrices for enhanced LDI MS-based detection[36, 37].

Conventional nuclear magnetic resonance (NMR) is challenged by its sensitivity, due to weak equilibrium nuclear spin polarization even with the strongest magnets[37]. Hyperpolarization is the newest concept, which has been shown to be capable of transiently uplifting the nuclear spin polarization far above its thermal equilibrium value, increasing NMR sensitivity[38, 39]. Here, the hyperpolarization technique has been achieved in different ways, including semiconductor dynamic nuclear polarization (DNP), by either chemically or photochemically induced DNP, and optical nuclear polarization[40]. Highly polarizable nanoparticles have been used to achieve hyperpolarization to give the highest NMR sensitivity[41].

The most common electronic-based detection methods used with metal nanoparticles are electrochemical detection[42] and chemiresistive sensing[43]. The distinctive properties of metallic nanoparticles, includes large surface area, easy functionalization, and ability to catalyze reactions, makes them highly applicable. This process involves the synthesis of various monolayers or ion-

protected nanoparticles and assembly on the electrode of interest. The resulting sensors are usually low-cost and portable.

There are several conventional techniques involved in separation, such as Which includes ultracentrifugation, chromatographic separation, electrophoresis techniques and precipitation based on size. Even though these techniques have a high efficiency and reproducibility, multi-step preparation, performance in batch mode, and minimum sample volume are the greatest challenges. Recently, continuous particle separation using nanofluidic technologies has become popular for highly efficient separation as it is less expensive, required less sample volume, and no extensive sample handling involved. Therefore the separation techniques that involve nanofluidic technologies has been advantaged in various types of field including medical diagnostic field for separation of biomolecules[44].

1.2 The Importance of Nanoplasmonics in Measurement Science

The interaction of metal surfaces with light has been utilized in a wide range of sensing applications[29, 44]. SPR has largely contributed to the optical phenomena based on the geometry of sensor surface-related factors. SPR is a technique that uses the SP phenomena in biosensing applications. Accordingly, the propagating SP, electromagnetic waves that appear at the metal surface-dielectric interface resulting from excitation of thin metal films, are used in SPR measurement[29]. This electromagnetic field is highly sensitive to the refractive index of the surrounding medium, and therefore the SPR technique can detect analytes with high sensitivity. Further, SPR measurement has been improved, owing to the efficient nanosurface fabrication methods; however, SPR still has some disadvantages as listed in below[29]:

1) Challenges in using this technique in miniaturized portable applications due to the requirement of sophisticated laboratory instrumentation for light-coupling mechanisms.
2) Since the SPR technique is based on bulk refractive index changes, it is very sensitive to the environment, and therefore the experiment must be carried out in a well-controlled area.
3) The decay length of the EM field in SPR is approximately 100–400 nm, which is much larger than the length of biological macromolecules. Therefore, this technique is less responsive to the arrangement and conformation of absorbed macro- or nanoscale

biological particulates. However, sometimes SPR is conducted using two wavelengths simultaneously, which helps to evaluate the size of the adsorbed particles.

However, upon light irradiation to the metallic nanostructure a special type of locally confined collective plasmon oscillation occurs, LSPR. Here the dimension of metallic nanostructure is smaller than the wavelength of the incident light. In comparison with SPR, LSPR is very sensitive, with a decay length of approximately 10–30 nm. Additionally, LSPR is less responsive to the background changes, rendering this technique much more stable. Additionally, LSPR does not require complex instrumentation, and excitation of nanostructures can be achieved using simple laboratory spectrophotometers. LSPR nanoplasmonic techniques have drawn growing attention in measurement science due to their simple instrumental requirements, measurement stability, and unique high surface sensitivity for bio-interfacial science[29].

1.3 The Scientific Scope of The Thesis

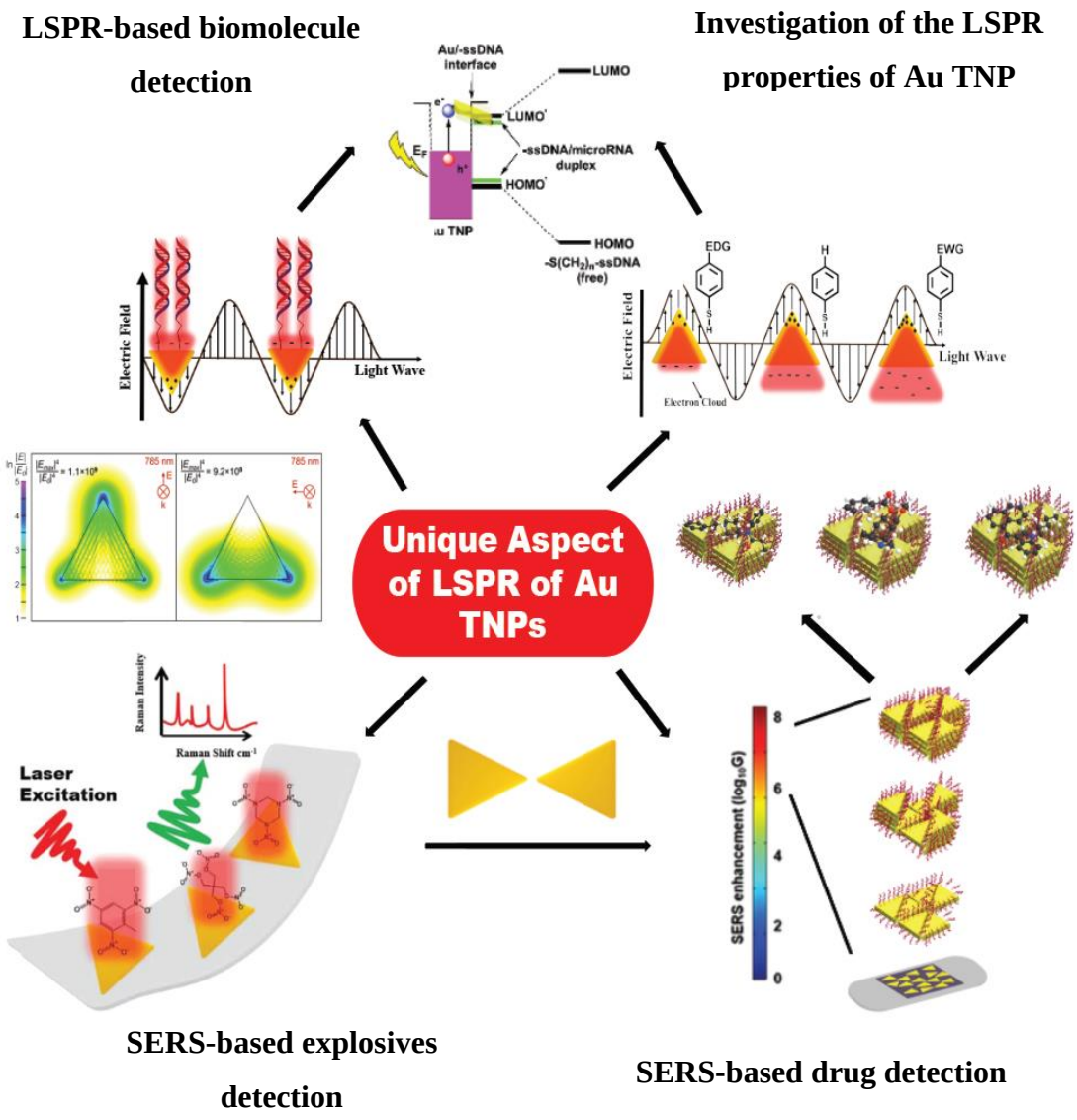

Figure 1.2. Summary of the scientific scope of the dissertation. LSPR investigation of Au TNP properties has been utilized as the focus. The unique LSPR properties of Au TNP with para-substituted thiophenol were investigated, showing delocalization of the conduction electron wave function from the nanostructure to the ligand monolayer. Further, based on these unique findings, we designed an ultrasensitive LSPR-based biomolecule detection of microRNA 10b and cTnT. Additionally, a flexible, highly sensitive, selective SERS substrate was developed via plasmonic coupling of Au TNPs via an evaporative self-assembly process for the efficient analysis of illicit drugs.

The scientific scope of this study was to explore the unique LSPR properties of chemically synthesized gold triangular nanoprisms (Au TNPs), and to utilize these finding in various types of optoelectronic applications. Accordingly, a unique LSPR-based sensor was employed to develop highly selective and sensitive cardiac troponin T and bladder cancer microRNA detection methods. Here, we investigated the mechanism that caused the unprecedented sensitivity of the newly developed microRNA sensors. Further, we advanced the sensing platform to mitigate the false-positive and -negative responses of the developed microRNA using the plasmon-enhanced fluorescence (PEF) properties of Au TNPs. Additionally, the unique LSPR properties of Au TNPs were used to develop an efficient SERS substrate for real-life SERS-based explosives and drug detection, including an assay for the evaluation of emergency room patient plasma samples. The main scope of this thesis is summarized in **Figure 1.2** and each step is explained in detail below:

1.3.1 Investigation of the Surface Chemistry Effects of the LSPR Properties of Au TNPs

Metalic nanoparticles exhibiting LSPR are valuable tools in various types of applications, including sensing, imaging, bio-diagnostics, and medical therapy. The tunability of the LSPR properties of noble metalic nanostructures via simple ligand exchange provides unique fundamental information for the advancement of applications related with optoelectronic, for instance sensing, photocatalysis and photovoltaics. In the present study, we demonstrate that the carrier electron density of Au TNPs can be tuned up to 12% via surface functionalization with para-substituted thiophanate ligands. An intensive analysis was performed with a view to understanding the unique LSPR properties of Au TNPs following functionalization of electron-donating or -withdrawing groups. We believe that this newly discovered plasmoelectronic effect will help the development of advanced organic ligand-noble metal nanoconjugates.

1.3.2 LSPR-based Biomolecule Detection

Firstly, the effects of the structural parameters of Au TNPs on the detection of cardiac troponin T (cTnT) were investigated. Accordingly, through the selective control of the spacing between the receptor and the nanoprism, and the number of receptors per nanoprism, quantitation of cTnT in human serum and plasma at concentrations as low as 0.5 pg/L was achieved.

Further, the unique sensing mechanism of the microRNA assay, which we developed using the unique LSPR properties of Au TNPs, was investigated, and advancement of the substrate was performed to mitigate the false-positive and -negative responses in the microRNA assay. Hence, we report an ultrasensitive LSPR assay for microRNA detection in bladder cancer patient samples; this assay can detect zeptomolar concentrations (10^{-21}) of microRNAs in patient plasma without any further purification.

Moreover, changes in the functional parameters yielding the unprecedented high sensitivity were investigated based on delocalization of SP excitation through the DNA-RNA duplex. Further, advancement of our sensor was performed with a view to avoiding false-positive and -negative results using UV-Vis and fluorescence techniques for the simultaneous quantitation of microRNA and sensor design based on the DNA/RNA hybridization kinetics.

Taken together, our intensive characterization of the unique LSPR properties of Au TNPs has directed to the design and development of highly sensitive SERS- and LSPR-based nanosensors that have potential applications in fields from biomedical to forensic sciences.

1.3.3 A Flexible SERS-Based Nanosensor for The Detection of Explosives in Fingerprints

Here, highly LSPR-active Au TNPs were employed to develop a highly sensitive, flexible, self-assembly sensor based on SERS, for explosives detection utilizing the strong EM field enhancement of gold Au TNPs. The developed sensor can detect explosives (cyclotrimethylene trinitro amine - RDX, trinitrotoluene -TNT, and pentaerythritol tetranitrate - PETN) at parts-per-quadrillion (ppq) levels and has proven it's a stability over a long time period and hence the long shelf-life.

1.3.4 Evaporative Self-Assembly of Au TNPs for Highly Sensitive SERS-Based Drug Detection

Here, a simple and efficient solvent-evaporation method was used to obtain 2D or 3D self-assembly of Au TNPs. Accordingly, polyethylene glycol (PEG)-functionalized Au TNPs were added to hydrophobic and hydrophilic substrates. Finally, the developed substrate was utilized for efficient, and highly selective and sensitive drug (Cocaine, JWH-018, Fentanyl) detection in emergency room patient plasma.

1.4 Localized Surface Plasmon Resonance (LSPR)

This section is focused on describing classical electromagnetic theory with a view to understanding the fundamentals of light interaction with small discrete particles, which will further help to realize the mechanism and plasmonic properties of metallic nanoparticles.

In space, an EM is generated due to the movement of electrically charged objects. When a charged objective moves, both the electric and magnetic fields change simultaneously[45]; therefore, it is important to consider the two vectors E- (electric vector) and M- (magnetic induction). In addition, during the movement of charged objects, an electric current can form. Therefore, the magnetic vector (H) electric current density (J) and the electric displacement is D, can be obtained. Moreover, the magnetic and electric and charges (ρ) and field fluxes (Φ) through the loops. Therefore, Maxwell's equations in a vacuum with SI units can be represented as shown in **Table 1.1**[45, 46].

Table 1.1. Maxwell's equations in a vacuum expressed in SI units

Differential Form	Integrated Form
$\nabla . e = \frac{\rho E}{\epsilon_0}$	$\int E . dA = \frac{Q_E}{\epsilon_0}$
$\nabla . B = \rho B$	$\int E . dA = Q_B$
$\nabla \text{ x E} = \frac{\partial B}{\partial t} + J_B$	$\int E . dI = \frac{d \oint_B}{d_t} + I_B$
$\nabla \text{ x E} = \frac{\partial E}{\partial t} + \mu_0 J_E$	$\int E . dI = \mu_0 \epsilon_0 \frac{d \oint_B}{d_t} + \mu_0 I_E$

In practical applications, it is impossible to find the magnetic charge (a magnetic monopole), therefore it is considered that ρ_B, J_B, and I_B are zero. Moreover, since the system is in a vacuum, electrical quantities are equal to zero, thus a symmetrical Maxwell's equation can be obtained with no magnetic charge or current, as shown in **Table 1.2**[45, 46].

Table 1.2. Maxwell's equations obtained without magnetic charges or currents.

Differential Form	Integrated Form	Known as
$\nabla . E = \frac{\rho E}{\epsilon_0}$	$\int E . dA = \frac{Q_E}{\epsilon_0}$	Gauss's Law
$\nabla . B = 0$	$\int B . dA = 0$	No magnetic monopoles
$\nabla \text{ x E} = -\frac{\partial B}{\partial t}$	$\int E . dI = -\frac{d\oint_B}{d_t}$	Faraday's Law
$\nabla \text{ x B} = \mu_0 \epsilon_0 \frac{\partial E}{\partial t} + \mu_0 J_E$	$\int B . dI = \mu_0 \epsilon_0 \frac{d\oint_B}{d_t} + \mu_0 I_E$	Ampere's Law/Displacement current

To interpret the relationship between the field vectors and the differential equations, to better obtain the wave equation ρ_B, J_B should be considered zero, and the above equations can be further simplified as follows (**Equations 1.1−1.4**)[45, 46]:

$$\nabla . E = O \tag{1.1}$$

$$\nabla . B = 0 \tag{1.2}$$

$$\nabla \text{ x E} = -\frac{\partial B}{\partial t} \tag{1.3}$$

$$\nabla \text{ x B} = \mu_0 \epsilon_0 \frac{\partial E}{\partial t} \tag{1.4}$$

The wave equation with respect to E (**Equation 1.5**) can be obtained by taking the curl of Equation 1.3 and using Equation 1.4 to remove B.

$$\frac{\partial^2 E}{\partial t^2} = \frac{1}{\mu_0 \epsilon_0} \boldsymbol{\nabla^2 E} \tag{1.5}$$

Similarly, the wave equation for B can be obtained as **Equation 1.6**.

$$\frac{\partial^2 B}{\partial t^2} = \frac{1}{\mu_0 \epsilon_0} \boldsymbol{\nabla^2 B} \tag{1.6}$$

In a dielectric medium, the above-mentioned vacuum quantities, μ_0 and ϵ_0, are replaced by μ and ϵ, and the velocity (U) in the medium can be obtained as **Equation 1.7[47].**

$$\upsilon = \frac{1}{\sqrt{\mu\epsilon}} \tag{1.7}$$

Comparison of **Equation 1.7** with the refractive index η is given by **Equation 1.8.**

$$\eta = \frac{c}{\upsilon} \tag{1.8}$$

Further, **Equation 1.8** can be rewritten as $\eta = \sqrt{\epsilon\mu}$.

1.4.1 Scattering from Homogeneous Media

In 1871, Lord Rayleigh introduced the electric dipole concept to understand the light scattering of small particles[48]. When the wavelength of the incident light is greater than the size of particles, the electromagnetic phase remains constant. Due to the induced polarization of the homogenous field of the incident light, light scattering occurs. The dielectric function of the material is the main reason for the polarization of materials which occurs as a response to an electromagnetic field; however, at this level, we only consider the dipole scattering mode, omitting the higher-level scattering modes (quadrupole and octupole)[47, 48].

This dielectric function of the material is mainly determined by the electronic structure. The dielectric function of a non-conducting material can be expressed as **Equation 1.9,** using classical harmonic oscillator formalism which has derived by Lorentz. Accordingly, the oscillator strength is given by f and frequency related to the bound electrons is given as ω_0, , and damping constant is given by γ[48] .

$$\varepsilon = 1 + \frac{f}{\omega_0^2 - \omega^2 - i\gamma\omega} \tag{1.9}$$

For metals, the Lorentz-Drude model needs to consider contributions of free electrons in the dielectric function calculations. Accordingly, **Equation 1.20** summarizes the Lorentz-Drude model, and j is obtained from the sum of different oscillators. Here, in this equation the free electron component is generated due to the electron plasma cloud of the metal, and ω_p^2 is the resonant frequency and γ_e is the damping constant of bulk plasma[48].

$$\varepsilon = 1 - \frac{\omega_p^2}{\omega^2 - i\gamma_e\omega} + \sum \frac{f_j}{j\omega_j^2 - \omega^2 - i\gamma_j\omega} \quad (1.20)$$

However, LSPR frequency of a spherical particle is different from surface polaritons, which can exist at the boundary of dielectric and metal and within the structures. As shown in **Equations 1.21** and **1.22,** the Laplace equation can be used to understand the space distribution of metal particles in a vacuum[49].

$$\Phi_1(r,\theta,\varphi) = \sum_{l-0}^{\infty}\sum_{m=-1}^{\infty} a_{lm} r^1 Y_{lm}\ (\theta,\varphi) \quad 0 < r \leq R \quad (1.21)$$

$$\Phi_1(r,\theta,\varphi) = \sum_{l-0}^{\infty}\sum_{m=-1}^{\infty} b_{lm} \frac{1}{r^{l+1}} Y_{lm}\ (\theta,\varphi) \quad r > R \quad (1.22)$$

The quasi-static approximation suggests that the wavelength of the incident light much higher than the particle size, hence the dipole excitation is most important, and due to the azimuthal symmetry, **Equation 1.22** can be rewritten as **Equation 1.23**. Accordingly, Legendre polynomials of order l is given from, $P_1\ (cos\ \theta)$ and as shown in **Figure 1.3,** θ is the angle between the line P and z-axis. Here, the position vector r represents the P line[47].

$$\phi(r,\theta) = \sum_{l-0}^{\infty}\left[A_l r^1 + B_l r^{-(l+1)}\right] P_1\ (cos\ \theta) \quad (1.23)$$

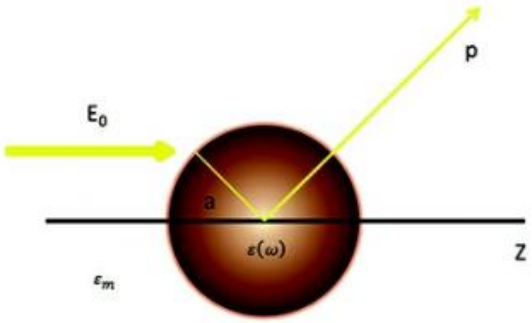

Figure 1.3. Homogeneous metal particle in an electrostatic field.

To better understand the scattering potentials, we consider the function within the sphere (ϕ_{in}) and out of the sphere (ϕ_{out}), and the obtained results are represented as **Equation 1.24 and 1.25,** respectively[50].

$$\phi_{in}(r,\theta) = \sum_{l-0}^{\infty} A_l r^1 P_1\ (cos\ \theta) \tag{1.23}$$

$$\phi_{out}(r,\theta) = \sum_{l-0}^{\infty} \left[B_l r^{-(l+1)} \right] P_1\ (cos\ \theta) \tag{1.24}$$

The dipole moment p induced by the applied electromagnetic field in the sphere, which is proportional to the strength of the applied electric field |E0|. Therefore The polarizability α of a single metallic nanosphere in vacuum, can be derived by applying continuous boundary conditions as $\propto = 4\pi\varepsilon_0\varepsilon_m a^3 \frac{\varepsilon-\varepsilon_m}{\varepsilon+2\varepsilon_m}$ followed by an effective dipole moment (P); ($P = \propto E_0$), which can be expressed as **Equation 1.26[48].**

$$P = 4\pi\varepsilon_0\varepsilon_m a^3 \frac{\varepsilon-\varepsilon_m}{\varepsilon+2\varepsilon_m} E_0 \tag{1.26}$$

As shown in **Equation 1.27**, the cross-section of the extinction spectrum can be calculated by adding the absorption and scattering cross-sections[48].

$$C_{ext} = C_{abs} + C_{sca} \tag{1.27}$$

scattering field radiated by the dipole is given the C_{abs} and C_{sca}. The obtained expressions are given as **Equations 1.28−1.29[48].**

$$C_{sca} = \sigma_{geom}\ Q_{SC}\ ;\ Q_{SC} = \frac{8}{3} q^4 \left[\frac{\varepsilon_d - 1}{\varepsilon_d + 2}\right]^2 \tag{1.28}$$

$$C_{abs} = \sigma_{geom}\ Q_{abs}\ ;\ Q_{abs} = 4qIm\left[\frac{\varepsilon_d - 1}{\varepsilon_d + 2}\right] \tag{1.29}$$

In this formula, the geometrical cross-section is represented by σ_{geom} and $\sigma_{geom} = \pi a^2$, and the dimensionless cross-sections of scattering and absorption are given as Q_{SC} and Q_{abs}, respectively. q is the dimensionless size, given by $q = Ka$. Here, K is the wave vector and a is the

radius of the particle. The relative dielectric function of the medium (ε_d) is equal to $\frac{\varepsilon_p}{\varepsilon_m}$, where the dielectric function of particle (ε_p) and dielectric function of the medium (ε_m). Therefore, the final equation can be shown by **Equations 1.30−1.31**, substituting the $\sigma_{geom}\ Q_{abs}$ values[48].

$$C_{sca} = \frac{8\pi}{3} K^4 a^6 \left[\frac{\varepsilon_d - 1}{\varepsilon_d + 2}\right]^2 \quad (1.30)$$

$$C_{abs} = 4\pi K a^3 lm\left[\frac{\varepsilon_d - 1}{\varepsilon_d + 2}\right] \quad (1.31)$$

According to the above equations, when the particle size decreases ($a \ll \lambda$), the absorption cross-section ($C_{abs} \propto a^3$) governs the scattering efficiency ($C_{abs} \propto a^6$), which is the main reason that particles of a small size are difficult to detect by light scattering, since the background scattering is too large to visualize small objects. However, above-mentioned theory cannot be utilized to explain the effect of size, or changes in position and width of plasmon peaks. Therefore, the general Mie solution provides a formula with a Raleigh approximation, and accordingly, the scattering and absorption cross-sections are given as Q_{SC} and Q_{abs} , respectively, as represented by **Equations 1.32−1.34[48].**

$$Q_{ext}^{Mie} = \frac{2}{q^2}\sum_{l=1}^{\infty}(2l+1)Re(a_l + b_l) \quad (1.32)$$

$$Q_{sca}^{Mie} = \frac{2}{q^2}\sum_{l=1}^{\infty}(2l+1)\{|a_l|^2 + |b_l|^2\} \quad (1.33)$$

$$Q_{abs}^{Mie} = Q_{ext} - Q_{sca} \quad (1.34)$$

In these equations, a non-magnetic spherical particle with a a radius is immersed in a transparent medium, which has a real positive refractive index (η_m). q represents the size parameter, and for a small particle, $q \ll 1$. Further, $= \frac{\eta_m m\omega}{C}$, where speed of the light (C) in a vacuum and ω is the frequency of the incident light. The dipole, quadrupole, and higher multipoles of the scattering is symbolized by the integer l. The s amplitude of scattering, a_l and b_l, are defined as shown in **Equation 1.35[51].**

$$a_l = \frac{F_a^e\ (l)}{F_a^e\ (l) + \ iG_a^e\ (l)} \quad and \ \ b_l = \frac{F_a^m\ (l)}{F_b^m\ (l) + \ iG_b^m\ (l)} \tag{1.35}$$

Here, $F_a^e(l), G_a^e(l), F_b^m\ (l), G_b^m\ (l)$ are represented the Bessel and Neumann functions. Where the formulas of these functions can be obtained by expanding the Bessel and Neumann functions in a power series for small q, the resulted equation is given in **Equation 1.36**[51].

$$F_a^e(l) \approx q^{2l+1}\ \frac{(l+1)}{[(2l+1)!!]^2}\tilde{n}^1\ (\tilde{n}^2 - 1) \tag{1.36}$$

$$G_a^e(l) \approx \tilde{n}^1\ \frac{l}{2l+1}\left[\tilde{n}^2 + \ \frac{l+1}{l} - \frac{q^2}{2}\ (\tilde{n}^2 - 1)(\frac{\tilde{n}^2}{2l+3} + \frac{l+1}{l(2l-1)})\right]$$

$$F_b^m(l) \approx \frac{\tilde{n}^1\, q^2}{2l+1} F_a^e\ (l)$$

$$G_b^e(l) \approx \tilde{n}^1\ \left[1 + \ \frac{1-\tilde{n}^2}{2(2l+1)} q^2\right]$$

Here, the relative complex refractive index is represented by $\tilde{n}$ and can be shown as a function of the relative absorption index (k_d) and the relative refractive index n_d. Accordingly, $\tilde{n} \ = \sqrt{\varepsilon_d} = \ n_d + ik_d$. For the dipole scattering $l = 1$ and for the smaller particles magnetic scattering amplitudes, b_l is negligible and therefore can be ignored. Accordingly, the scattering cross-section can be expressed as $Q_{sca}^{Mie} \approx \frac{6\,|a_1|^2}{q}$, and here, $a_1 = a_1(l = 1)$, which was determined based on **Equation 1.36**[51]**.**

The dielectric permittivity of a metallic nanostructure can be expressed as **Equation 1.37,** according to the drude formula.

$$\varepsilon = \ \tilde{n}^2 = 1 - \frac{\omega_p^2}{\omega^2 + \ \gamma^2} + i\frac{\gamma}{\omega}\frac{\omega_p^2}{\omega^2 + \ \gamma^2} \tag{1.37}$$

As explained earlier, plasma frequency is given by the ω_p and γ denotes the frequency of electron collisions, thus the dipole resonance occurs due to the scattering cross-section is expressed as shown in the Lorentzian profile in **Equation 1.38**.

$$Q_{sca}^{dip-Mie} = \frac{8}{3}\frac{\omega_{sp}^4}{(\omega^2 - \omega_{sp}^2)^2 \ + \ \frac{4}{9}\ q^6\, \omega_{sp}^4} q^4 \tag{1.38}$$

Unlike the Lorentz profile of Rayleigh scattering $Q_{sca}^{Ra} = \frac{8}{3}\frac{\omega_{sp}^4}{(\omega^2-\omega_{sp}^2)^2 + \omega^2\gamma^2}q^4$, the above equation was derived by ignoring γ, which corresponds to the dissipative losses occurs as a result of electron collisions. However, comparing the two equations, **Equation 1.38** has an effective parameter γ_{eff} damping, which is caused by the radiative losses of plasmons and can be expressed as $\gamma_{eff} = \frac{2}{3}\,\omega_{sp}\,q^3$. Further, γ_{eff} represents a parameter like the dissipation parameter occurs in the Rayleigh spectrum.

The LSPR peak position is hypersensitive to the shape, size, and dielectric constant of the metallic nanostructure. Accordingly, as the size increases, the LSPR peak red shifts, mainly due to the weakening of the restoring faces. This can further explain why, when the size of the particle increases, the distance from the opposite site of the nanoparticles increases, leading to a decrease in their interaction. Mie theory can be directly utilized to explain the red shift of the resonance peak upon size increases. If one could plot a scattering cross-section with respect to the dipole term by neglecting the dissipation parameter, a clear red shift of the resonance particle would be seen, as shown in **Figure 1.4a,** but the scatter cross-section would be similar even at different sizes. However, if one considers the dissipation parameter, as the particle size reduces, the scattering cross-section also decreases, as shown in **Figure 1.4b**[48].

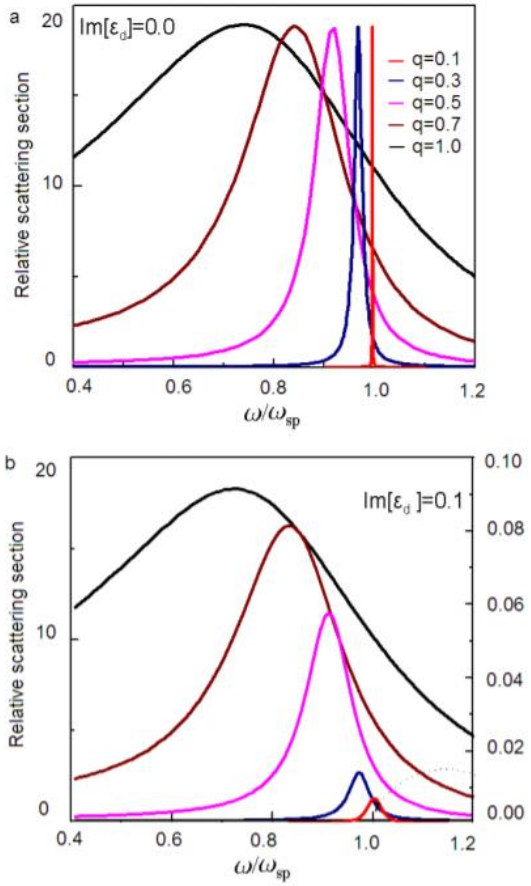

Figure 1.4. The obtained relative cross-section of scattering as a function of frequency. The red shift of the dipole resonance peak of different size parameters is summarized. q. **A)** considering no dissipation parameter, where Im[ε] = 0 and **B)** considering the dissipation parameter, where Im[ε] = 0.1.

We have discussed the Mie theory, which is the exact analytical solution for the sphere. It is surprising that even after 100 years, the Mie's general theory of light scattering remains valid today for small spherical particles. However, years later, the Mie theory was further corrected to examine the light scattering of other structures. Several modifications of the Mie theory have been reported: the Gans modification, which is used for spheroid particles such as plasmonic nanoparticles with elongated shapes. Maxwell-Garnett equations, which provides an effective medium approach to explain the light scattering of other structures. However, here I would like to bring your attention to the numerical implementation that was developed by Voshchinnikov and Farafonov to understand the extinction and scattering cross-section of non-spherical nanoparticles.[52]

Thus far, we have utilized the quasi-static approximation to solve the electrostatics which occurs due to the light interacting upon particle, and in the results, we utilized the wavelength-dependent dielectric constant. However, to develop an accurate theory for non-spherical nanostructures, it is important to utilize the finite wavelength effect, and such conditions can be identified as a modified long-wavelength approximation.

Accordingly, as explained earlier, $p = \propto E$ and the polarizability $\propto'$ is the spheroid polarizability, which can be given as **Equation 1.39.**

$$\propto = \frac{\varepsilon_i - \varepsilon_0}{\varepsilon_i - \chi\varepsilon_0} \frac{b^3(1+\chi)\xi_0^2 + 2}{3\xi_0^2} \tag{1.39}$$

Here, ξ_0^2 and χ are parameters that depend on spheroid geometry, and a and b are the minor and major axes, respectively, as expanded in **Equation 1.40**.

$$\chi = -1 - 2\left[\xi_0^2 - \frac{\xi_0(\xi_0^2+1)}{2} cos^{-1}\left(\frac{\xi_0^2-1}{\xi_0^2+1}\right)\right]^{-1} \; and \; \xi_0 = \left(\frac{b^2}{a^2-1}\right)^{-1/2} \tag{1.40}$$

Further, if we compare p of the sphere with that of the spheroid, it is clear that only the denominator has replaced the number 2 with χ, which further explains why, when the b/a ratio increases, the resonance peak gets red shifted, as the spheroid turn into more oblate. Additionally, corrected electrodynamic forces related with the MLWA can be given as $P = \alpha[E + E_{rad}]$, where E_{rad} is the radiative correction field, which can be expressed as a combination of two forms as shown in Equation **1.41**.

$$E_{rad} = \frac{2}{3} ik^3 P + \frac{K^2}{b} P \tag{1.41}$$

Here in the first term, it explains the effect of radiative damping, and this form is closely related to the line width of the resonance peak. Accordingly, when radiative damping arises with the particle size, and the particle size reduces, a dipole is induced, which leads to an increase in the plasmon width. The second term of the given **Equation 1.41** is related to the depolarization of the radiation across the particle surface. This mainly occurs as a result of finite ratio of particle size to wavelength. As the particle size increases, the dynamic depolarization causes the resonance peaks to be red shifted[52].

In addition to the effect of all the other factors on the excitation of the LSPR, the surrounding medium also plays an important role. The wavelength of light in the vicinity of the nanoparticles is determined by the dielectric function of the surrounding medium, which leads to an alteration in the geometry of the electric field at the surface of the nanoparticles. Upon light irradiation of the nanoparticle surface, the charge accumulation creates an electric field that further induces the polarization of the dielectric medium. As a result, the charge accumulates between the dielectric environment and the metallic nanoparticles. The dielectric function of the media controls the reduction of charge. For instance, the larger the ε_m, the larger the polarization charge, leading to a greater effect on LSPR. As discussed earlier, the larger the charge accumulation, the larger the reduction in net charge of the nanoparticle surface, reducing the restoring forces and leading to a smaller resonance frequency. As a result, the LSPR peak shifts toward a higher wavelength, as shown in **Figure 1.5**[12, 53].

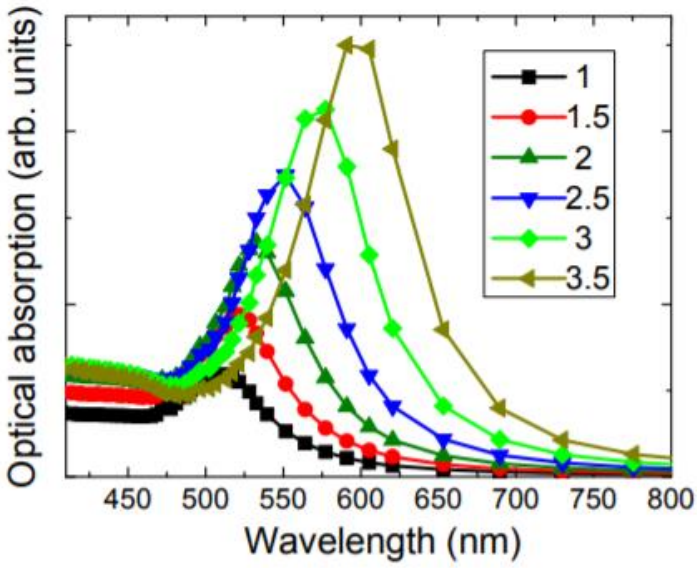

Figure 1.5. Changes in the wavelength of 10-nm Au Nps with changes in the dielectric medium. Different dielectric functions were calculated using Mie theory[53].

The wavelength of the LSPR peak based on the dielectric function of the medium can be derived using the Drude model of metalic nanoparticle as shown in the Equation 1.41). Here the Drude model explains the collisions between electrons which are freely moving around and the ionic lattice core. This can be considered as a classical model for electronic transport in conductors.

$$\varepsilon_1 = 1 - \frac{\omega_p^2}{\omega^2 + \gamma^2} \quad (1.41)$$

However, Equation 1.42 can be further simplified for the visible and near-infrared LSPR frequencies as $\gamma << \omega_p$ under these conditions[12, 53, 54].

$$\varepsilon_1 = 1 - \frac{\omega_p^2}{\omega^2} \quad (1.42)$$

Equation 1.43 can be obtained using the expression for ε_1 as $\varepsilon_1 = -2\ \varepsilon_m$ based on the resonance conditions.

$$\omega_{max} = \frac{\omega_p^2}{\sqrt{2\ \varepsilon_m + 1}} \quad (1.43)$$

Here, ω_{max} is the LSPR peak frequency, and when rearranged, the frequency in the form of wavelength $\boldsymbol{\lambda}$p, and the dielectric constant to index of refraction using $\varepsilon_m = \eta^2$, can be expressed as **Equation 1.44**.

$$\lambda_{max} = \lambda_p\sqrt{2n_m^2 + 1} \quad (14)$$

Here, λ_p is the wavelength of the bulk metal plasma frequency and the λ_{max} is the LSPR peak wavelength. **Equation 1.44** explains the dependence of LSPR on the refractive index[12, 53, 54].

1.5 Sensing Using LSPR Structures

Sensing platforms are created using LSPR-based nanoparticles or either a simple colorimetric sensor or a typical plasmonic sensor based on refractive index changes[12, 29, 53, 54].

1.5.1 Colorimetric Sensing

This is the easiest method used in nanoparticle-based sensing applications. The first colorimetric-based assay was reported by Mirkin et al., who utilized oligonucleotide-functionalized Au NPs. A distinguished red shift of the LSPR peak was observed, followed by a color change of the nanoparticles upon aggregation when the complimentary nucleotide was

present. The basic theory behind this application is as the distance between the nanoparticles reduces, enhanced the localized electric field occurs due to the nearfield coupling. This is the reason for the LSPR red shift, which is always followed by a visible color change that can be utilized as a simple sensor readout. Two main criteria required attention when designing the colorimetric-based assay:

1. Binding of the target analyte should result in aggregation of the nanoparticles. Accordingly, the capability of simultaneous binding of more than one nanoparticle at a time is preferred.
2. It is important to have small inter-particle separation for efficient plasmonic coupling; therefore, it is preferred that the analyte of choice be smaller.

The colorimetric-based sensing mechanism has evolved over last decade and has been reported to act as an efficient assay with a fM sensitivity; however, the work reported here is mainly focused on an LSPR sensor based on changes in the refractive index.

1.5.2 Refractive Index Sensing

The sensing mechanism based on variations in the dielectric environment of the metallic nanostructure is the most widely used LSPR-based sensing concept, and this type of nanoplasmonic sensor has provided the opportunity to use a LSPR-based assay to compete with other advanced techniques such as microfluidics and inflow assays, in addition to the miniaturization and regeneration of sensors[12, 13, 29, 53, 54].

1.5.3 Bulk Refractive Index Changes

LSPR-active metallic nanoparticles have been utilized for sensing applications by detecting variations in the bulk refractive index (BRI) of their surroundings via recording the shift changes in the LSPR peak wavelength. Typically, the LSPR peak is recorded as an extinction spectrum for a metallic film or as a scattering measurement for a single nanoparticle. The effect of the size and shape of the materials in the LSPR sensing mechanism will be discussed separately. **Figure 1.5** shows the schematic representation of bulk refractive index-based LSPR sensing and changes in the LSPR peak of an Au NPs array following a change in the solvent environment[12, 13, 29, 53, 54]

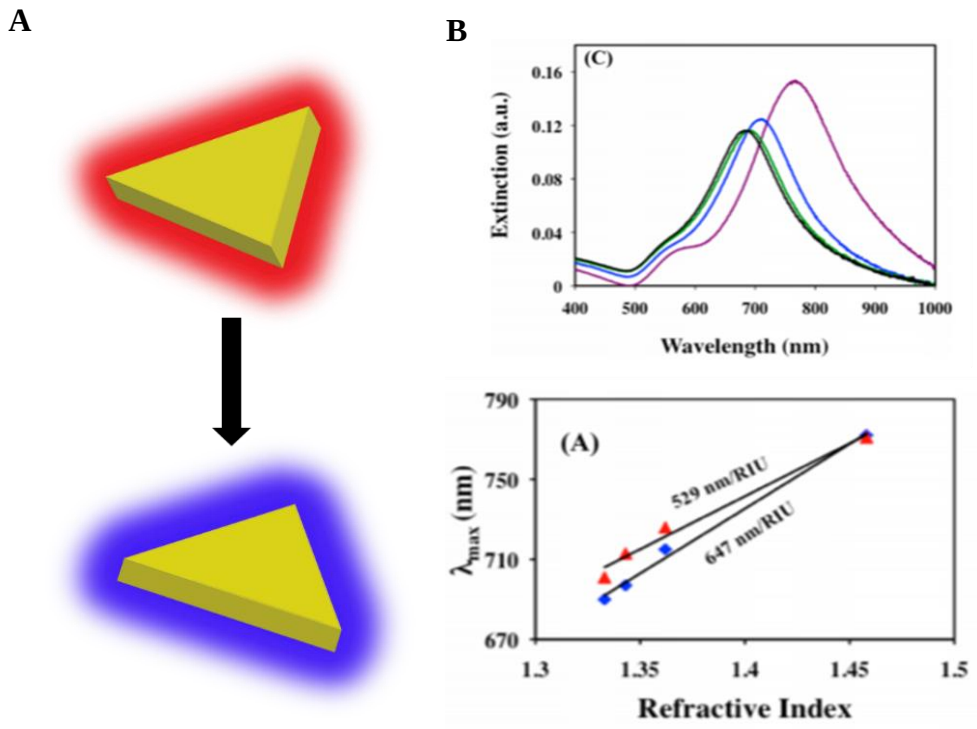

Figure 1.6. A) Schematic representation of the changes in bulk refractive index sensing by LPSR. B) The effect of bulk refractive index changes in 28-nM edge length Au TNPs were studied by measuring the LSPR peak in different medium. Accordingly, extinction spectra were obtained using different solvent systems: H_2O (black), acetonitrile (green), ethanol (blue), and carbon tetrachloride (purple). **C)** The LSPR dipole peak position of 28-nm edge length nanoprisms vs. the refractive index of the bulk solutions before (red triangles) and after (blue diamonds) removing non prismatic structure by performing tape cleaning technique of 28-nM edge length Au TNPs, and BRI sensitivity, are shown in the diagram[13].

The relationship between changes in the LSPR spectral shift (Δλ) and changes in the BRI is shown in **Equation 1.45**.

$$\Delta\lambda = m(n_{dilectric} - n_{reference})\left[1 - exp\left(-\frac{2d_{dielectric}}{I_d}\right)\right] \quad (1.45)$$

Here, m is the BRI sensitivity of the nanoparticle interface, and the difference in the refractive index of the local dielectric environment before and after binding with the analyte is defined as $n_{dilectric}$ and $n_{reference}$, respectively. $d_{dielectric}$ and I_d are the thickness of the dielectric layer and decay length of the electromagnetic field of the sensor, respectively. However, the above equation can be further simplified for the thickness of the adlayer, since it is higher than the decay length of the sensor. The simplified version is shown in **Equation 1.46**[11, 12, 29, 53, 54].

$$\Delta\lambda = m\Delta n \quad (1.46)$$

FOM is the most general form that can be used to account for variations in the refractive index depending on the bulk refractive index sensitivity and the peak line width. This is important to consider, especially for large nanoparticles that show a higher sensitivity, as explained earlier, but are subject to peak broadening due to radiative damping and multipolar excitations. Therefore, **Equation 1.47** can be used to receive the highly precise generalized application of bulk RI sensitivity[12, 29, 53-56].

$$FOM = \frac{m(nm/RIU)}{FWHM(nm)} \quad (1.47)$$

Here, m is the bulk RI sensitivity, and full width at half maximum is denoted as a FWHM The higher the FOM value, the higher LSPR sensitivity of the sensor. However, in order to further generalize the FOM for applications where it is difficult to elucidate the exact line width, Becker et al., proposed a different figure of merit (FOM*), as shown in **Equation 1.48**. Here, FOM is calculated using the relative intensity change is represented as dI/I, which occurs at a wavelength $\boldsymbol{\lambda}$[12, 29, 53-56].

$$FOM = \frac{\frac{dI}{dn}}{I} = \frac{S\frac{dI}{d\lambda}}{I} \quad (1.48)$$

1.5.4 Molecular or Local Refractive Index Sensitivity

The highly localized sensing volume of a metallic nanostructure, which is very close to the nanostructure surface, strongly influences changes in the local refractive index. **Figure 1.7** shows the schematic representation of the local refractive index based LSPR sensing mechanism. In comparison with SPR, the decay length of the LSPR system is limited to 10–20 nm, and as a result, LSPR acts as an efficient biological recognition interface. Accordingly, **Equation 1.48** can be rearranged to **Equation 1.49** when the analyte of thickness d_A binds to the LSPR sensor, which has the d_L thickness of the receptor/molecular recognition element. Here, we assume that both layers have the same refractive index.

$$\Delta\lambda = m(n_{dilectric} - n_{reference})exp\left(-\frac{2d_L}{I_d}\right)\left[1 - exp\left(-\frac{2d_A}{I_d}\right)\right] \quad (2.49)$$

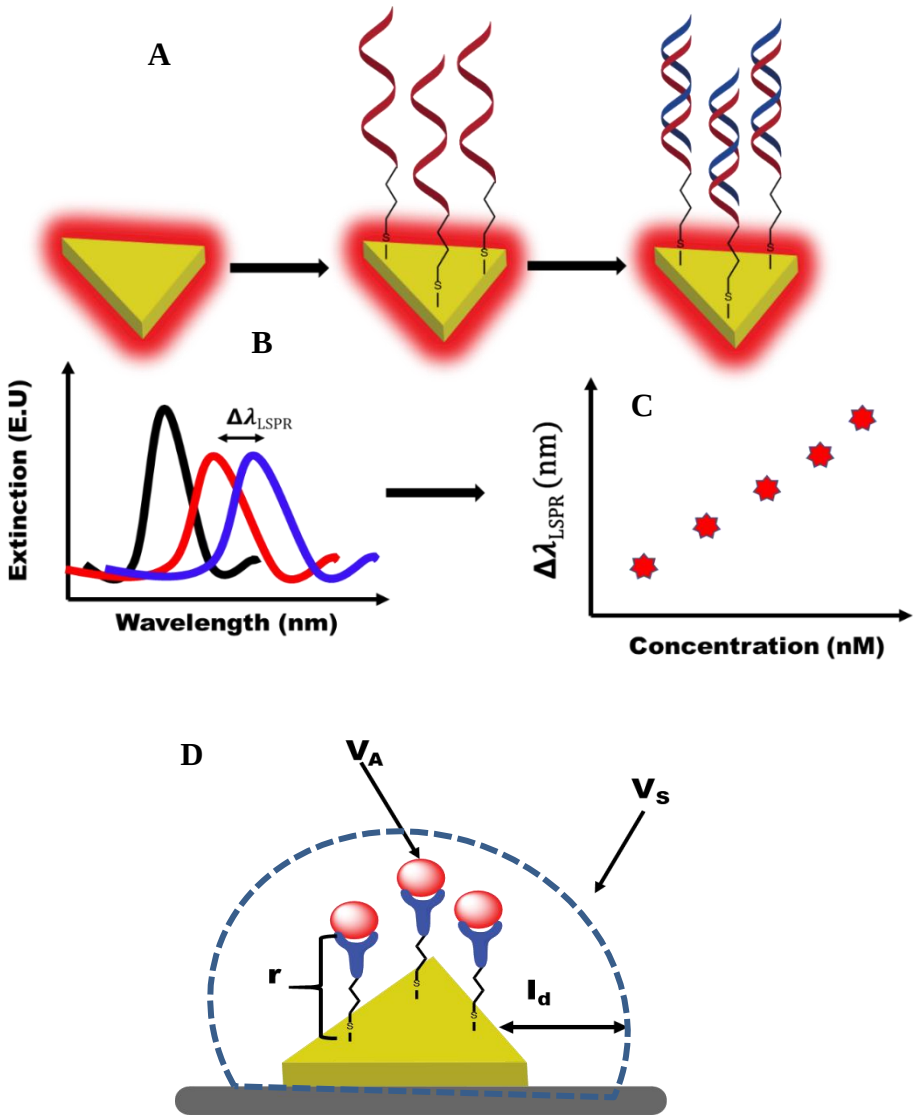

Figure 1.7. A) Schematic representation of the local refractive index based LSPR sensing mechanism. B) Changes in the LSPR peak position based on each functionalization step. Red spectrum shows DNA (receptor) attached to the Au TNPs and the blue spectrum is following binding to microRNA (analyte). **C)** The obtained $\boldsymbol{\Delta\lambda}_{LSPR}$ peak vs. concentration for calculation of the molecular detection limit (MDL) value. D) The main geometric parameters that controls the MDL as shown in **Equation 1.50**[12].

The sensitivity and selectivity of the LSPR-based sensor is controlled by the receptor molecule attached to the LSPR surface. Therefore, the sensing volume (V_s), decay length (I_d), distance from the surface of the nanoparticle to the receptor, and analyte volume (V_a) are important parameters

that control the molecular detection limit (MDL) of the LSPR sensing platform and is shown in **Equation 1.50**[12, 29, 53-56].

$$MDL = \frac{V_S\sqrt{U_{system}^2 + U_{fit}^2}}{V_A \Delta RI e^{-2r/l_d} 3S_0} \quad (1.50)$$

LSPR sensing is mainly carried out by monitoring LSPR peak position following chemical or physical changes to the surface of the metallic nanostructure. This has been achieved by forming a self-assembled monolayer (SAM) on the nanostructure surface; well-known metal thiol chemistry has been utilized to form a SAM of the receptor onto the nanostructure. The literature indicates that intensive research has been conducted to study the effect of the SAM length; it has been shown that LSPR sensitivity reduces as the SAM length increases. Linear dependence of the LSPR band is obtained when the SAM thickness is up to 3 nm from the nanostructure surface, and when the SAM thickness is above 20 nm, non-linear dependency is obtained. It is important to keep the thickness of the SAM of the receptor and analyte below 20 nm to obtain an efficient LSPR-based sensing platform[12, 29, 53-56].

1.5.5 LSPR Applications and Future Challenges

LPSR is one of the leading techniques in measurement science and is known as a label-free and cost-effective (less expensive instruments required) technique with the ability to be miniaturized to portable and multiplexed devices[11]. Therefore, LSPR has been widely applied in molecular and biosensing applications. Among the plasmonic nanoparticles, Au NPs have attracted wide interest in biomedical applications (diagnostic, imaging, and therapeutics) due to their stability, easy preparation, inertness, and biocompatibility[57]. Moreover, surface modification of Au NPs is easy, by forming either mercapto or amino covalent interactions. Au-based LSPR sensors have been utilized to quantitate DNA, microRNA, proteins, and many other biomolecules[29].

Although the LSPR technique has had a significant impact on biological sensing applications, several limitations exist. Increasing the sensitivity by improving the detection limit is one of the greatest challenges[58-60]. In the work reported in this thesis, we have focused on increasing the sensitivity and the detection limit of LSPR sensors by thoroughly investigating the structural parameters, properties of the ligand and metal interface, and the sensing mechanism of the

developed sensors. Another challenge is the selectivity and reproducibility of the developed sensors[58-60]. Advancements in specific self-assembled monolayers for the highly specific binding of target analytes and in the prevention of binding with unwanted species is the key to ensuring specificity. In this work we have achieved the highest selectivity and reproducibility of the developed sensors.

Additionally, the stability of biological materials has been a huge challenge in the development of a platform for commercialized portable LSPR-based sensors. To overcome this issue, the literature has reported that replacing DNA binding proteins with a DNA-binding hairpin pyrrole-imidazole (Py-Im) polyamide, to increase the stability of DNA for the DNA detection, and peptide nucleic acid (PNA), is a good replacement for DNA/RNA/aptamers[12, 53, 54, 57, 58, 60].
Consequently, the recent increase in the sensitivity, selectivity, stability, reproducibility, and multiplexing ability of LSPR-based sensors will enhance the chemical, biological, and medical fields within measurement science[11].

1.6 Surface-Enhanced Raman Spectroscopy

1.6.1 Background

The Raman phenomenon was first observed by Raman and Krishnan, who found that molecules can scatter the light as a result of the interaction with a small portion of incident light, and the resulting beam has a different energy (either gains or loses energy due to molecular vibration or rotation modes) that the incident beam[61-65]. This is known as Raman scattering, and the resulting scattering intensity vs. wavelength graph is known as the Raman spectrum. However, application of the Raman technique is limited due to the weak strength of the Raman signal (approximately 1 in 10^6–10^{10} photons are scattered inelastically)[66, 67].

The surface-enhanced Raman scattering phenomenon was first discovered in 1973, when pyridine absorbed onto a silver electrode; however, it was not correctly interpreted until 1977. Two decades after the discovery of SERS, the observation of single-molecule SERS was reported in 1997[68]. Today, SERS has attracted attention in a wide selection of fields including chemistry disciplines, material sciences, physical sciences and life sciences, and the growing knowledge regarding SERS has had a large impact on improving the quality of human life[69-72].

Unlike normal Raman, SERS requires the presence of a metallic nanostructure, and therefore two important interactions exist: light/target analyte and light/metallic nanostructure.

1.6.2 SERS Enhancement Mechanism

The SERS enhancement mechanism has two main contributors: electromagnetic field enhancement (EM) and chemical enhancement (CE). EM dominates the total enhancement in SERS and LSPR and is the major contributor to EM field enhancement. As shown in **Figure 1.8,** Au NPs are subjected to charge separation upon resonance excitation. Here, conduction electrons in Au oscillate due to the oscillating electric field of the incoming laser. Here the angular frequency is given from $\boldsymbol{\omega}_{inc}$ and amplitude is shown as the E_0[67, 68, 73].

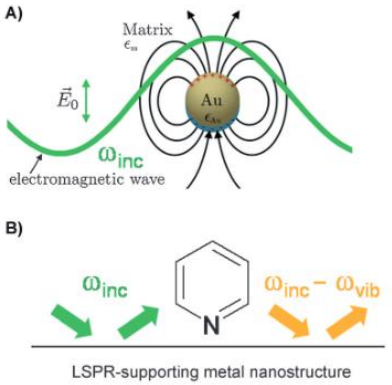

Figure 1.8. Schematic representation of EM field enhancement of SERS. A) Contribution of the LSPR of Au NPs to EM field enhancement. B) The effect of the incoming field (green) and the outgoing field (orange) on elastic light scattering enhancement[73].

Earlier, we discussed the P polarizability of the metal sphere. Further, the magnitude of the induced dipole ($P_{\text{ind(metal}}$) is determined by (α_{metal}) and the strength of the incident electric field E ($\boldsymbol{\omega}_{inc}$), as shown in **Equation 1.51.**

$$P_{\text{ind(metal}} = \alpha_{metal} E_0(\omega_{inc}) \qquad 1.51)$$

Accordingly, the $\boldsymbol{\omega}$inc of the electromagnetic wave changes the sign of the localized induced dipole (P_{ind}) as an external driving force. As a result, Hertzian dipole, which can radiate at the same incident frequency ($\boldsymbol{\omega}_{inc}$), is generated as shown in **Figure 1.8** (green).

In addition to the plasmon-based SERS enhancement, the interaction of the local electric field with molecules near the metal surface is important and induces dipoles in molecules, as shown in **Equation 1.52**[73]**.**

$$P = \alpha_{molecule} E_{IOC}(\omega_{inc}) \quad (1.52)$$

Here, three dipole components occur, named Rayleigh $P_{ind}(\omega_{inc})$, Stokes Raman $P(\omega_{inc} - \omega_{vib})$, and anti-Stokes Raman ($P_{ind}(\omega_{inc} + \omega_{vib})$. Therefore, the overall SERS intensity is fully dependent on both incoming and outgoing electric fields and can be summarized as **Equation 1.53**[66, 68, 73].

$$I_{SERS} = I_{inc}(\omega_{inc}) I(\omega_{inc} - \omega_{vib}) = \ |E_{inc}(\omega_{inc})|^2 \ |E(\omega_{inc} - \omega_{vib})|^2 \quad (1.53)$$

To obtain the optimal SERS enhancement, the plasmon peak of the metal needs to be in resonance with both the incident radiation at ω_{inc} and the Stokes Raman shifted radiation at $\omega_{inc} - \omega_{vib}$.

When the incident laser light ω_{inc} and the Stokes Raman scattering for a specific vibration/Raman band $\omega_{inc} - \omega_{vib}$ are close to each other, $I_{SERS} = |E(\omega_{inc})|^4$. This is known as the $|E_4|$ approximation and is mostly applicable to ω_{inc} in the blue region. As stated earlier, EM field enhancement is the most dominant contributor to SERS enhancement and lies in the range of 10^3–10^{10}.

To obtain an extremely strong localized electric field enhancement, it is important to have a minimum gap between the NPs. As shown in **Figure 7**, very high electric fields are reported in between two nanoparticles, where hot spots (highly localized regions) of plasmons occur. Moreover, as shown in the first and second column of **Figure 7,** as the gap size increases, the SERS enhancement factor decreases between two particles[66, 68, 73].

When considering the effect of nanomaterial on SERS EM field enhancement, silver is gaining greater attention due to its high plasmonic activity, but at the same time, gold is competing, since it is highly chemical stability due to its inert nature[74]. The EM field enhancement of gold and silver is similar in region of infrared.

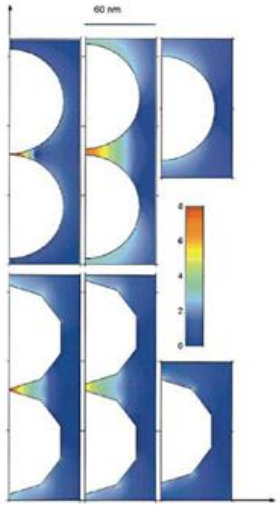

Figure 1.9. The gap-dependent EM field enhancement of Ag NPs. The colored log scale is explained as the EM field enhancement factor. The first and second column from the right represent the Ag dimers and changes in the EM field enhancement based on the gap in comparison with that of single Ag Nps, which is shown in the third column[73].

1.6.3 Chemical Enhancement to Increase SERS Intensity

Chemical enhancement (CE) is mainly dependent on the electronic properties of the adsorbate. Due to the CE the electronic polarizability ($\alpha_{molecule@metal}$) of the adsorbed molecule is increased. However, the overall contribution of CE to the EM field enhancement is extremely low and may lie between 10^1–10^3.

Changing the polarizability of the molecule is the main step in the CE process and is mainly controlled via charge transfer among the molecule (which is in the electronic ground state) and the metallic nanoparticles. Different models have been suggested in the literature to explain the CE process. Among them, Otto et al., explains the CE process as including four consecutive steps: 1) the creation of SP excitation; 2) the formation of the negative ionic molecule of adsorbate; 3) the return of the excited electron to the metal; and 4) the radiation of photons via emission. Additionally, the literature has reported other concepts with slight variations to explain CE depending on the SERS intensity[75-78].

1.6.4 SERS Applications and Challenges Faced in Real-life Applications

This extremely sensitive SERS technique is used for the detection of molecules in the biological, chemical, and biomedical fields, since it has the capability of detecting trace concentrations and provides the all structural information[73]. Despite being a versatile analytical technique, there are certain challenges that need to be addressed during real-time applications[67]; poor reproducibility and poor stability are the two main obstacles that limit its application in measurement science[67]. Achieving the controlled assembly of nanoparticles on the SERS substrate is key to responding to the reproducibility challenges. The literature has reported successful programable self-assembly of nanoparticles using organic molecules, polymers, proteins, and DNA/DNA hybridization[79-81]. In some cases, the liquid/liquid interfacial assembly technique is used to achieve efficient SERS activity[79-81]. In this thesis, we report a very sensitive, reproducible SERS-based drug detection sensor using programable self-assembly of Au TNPs by controlling particle-particle and particle-substrate interactions.

Another major problem associated with the SERS technique is the lower sampling efficiency of the SERS substrates[82-84]. The rigid/fragile SERS substrates are less convenient to use and are associated with high fabrication costs. Nevertheless, flexible SERS substrates have provided highly efficient, cost-effective direct sampling, and other non-invasive or minimally invasive sampling capabilities provide the advantage of easy transposition and stable storage[85-87]. The literature has reported the generation of many flexible substrates using the dip-coating method, printing on to the substrate, and self-assembly techniques of the interface. In this thesis, we have used a simple technique of Au TNPs to create a highly sensitive, flexible SERS substrate for the detection of explosives.

Furthermore, portable Raman devices should be considered with a view to making SERS more suitable to real-life applications. The literature has reported the use of smartphone-based point-of-care testing for genetic applications for user-friendly and cost-effective SERS analysis; therefore, it is important to advance the portable Raman spectrometers associated with SERS-active substrates to provide a reliable user-friendly application in measurement science in a cost-effective manner[88-91].

1.7 Plasmon-Enhanced Fluorescence Spectroscopy

When a fluorophore is subjected to irradiation by white light or monochromatic electromagnetic radiation, molecular fluorescence is generated[92]. In contrast, metal nanoparticles show extremely weak fluorescence following monochromatic electromagnetic irradiation. However, as discussed earlier, the extinction cross-section of plasmonic nanostructures is distinctly higher for metallic nanostructures as compared with molecular fluorophores[93]. The LSPR properties of metallic nanostructures cause local field enhancement, since they increase the absorption and emission cross-sections[93]. When the LSPR of a metallic nanostructure is coupled to the frequencies emitted by a fluorophore, it causes metal nanoparticles to radiate light with higher intensity; this light will be the same frequency as the fluorescence emitted by the fluorophore. This has identified as the metal-enhanced fluorescence (MEF), and since the technique is coupled to surface plasmons, it has been identified as surface plasmon-enhanced fluorescence spectroscopy (PEFS)[93].

1.7.1 Mechanism of Plasmon-Enhanced Fluorescence

The electromagnetic field intensity is due to the coupling of light to LSPs or SP polarizations (SPP), which can interact with the absorption ($\boldsymbol{\lambda}_{abs}$) and emission ($\boldsymbol{\lambda}_{ems}$) wavelengths of the fluorophores, further causing modifying corresponding transitions between the ground state and higher excited states, which is depicted in Figure **2.0.** Here, the excitation rate of the fluorophore at the absorption wavelength $\boldsymbol{\lambda}_{ab}$,due to the incident wave that has an electric field E, can be expressed in **Equation 1.54** as a function of the absorption dipole (P_{abs}) of the fluorophore[93].

$$\gamma_e = |E.P_{abs}|^2 \tag{1.54}$$

There are two possible ways for the excited fluorophore to be returned to the ground state: either by emitting a photon at a higher wavelength, which is referred to as the radiative decay (γ_r), or without emitting a photon, which is identified as non-radiative decay (γ_{nr}). Therefore, the quantum yield (η_0) of a fluorophore in a homogenous aqueous environment can be expressed as **Equation 1.55**[93]**.**

$$\eta_0 = \frac{\gamma_r^0}{(\gamma_r^0 + \gamma_{nr}^0)} \tag{1.55}$$

However, when the fluorophore is close to the metallic structure due to the local density of optical states which has the plasmon-enhanced field intensity $|E|^2$ at λ_{em}, the γ_{nr} and γ_r are changed to $\gamma_{nr} = \gamma_{nr}^0 + \gamma_{abs}$ and $\gamma_r = \gamma_r^0 + \gamma_{abs}$, respectively. As a result, the modified quantum yield is shown in **Equation 1.56**[93]**.**

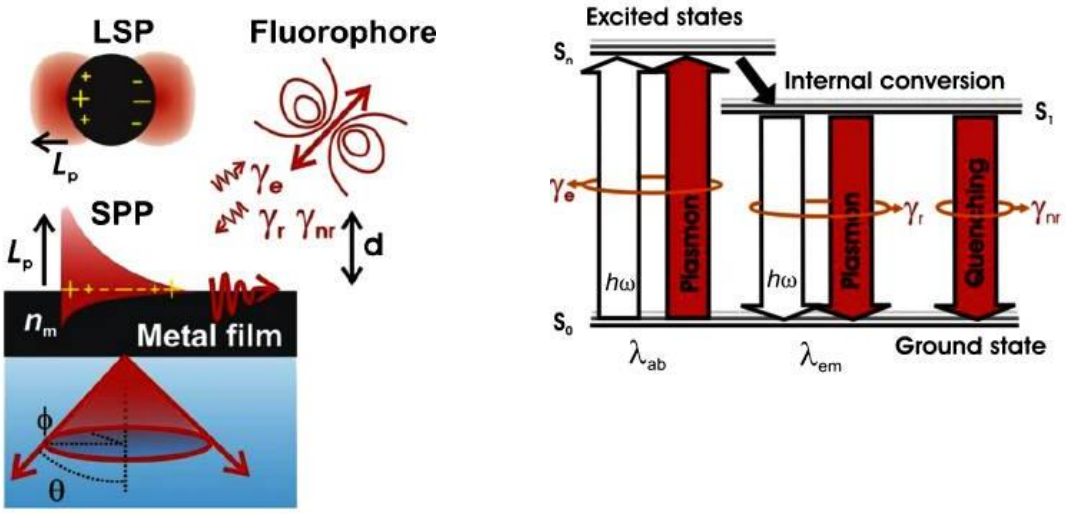

Figure 1.10. A) Schematic representation of the fluorophore coupled to the SPP and LSP modes. B) Jablonski diagram showing the plasmon-mediated transition of the ground state to higher excited state of the fluorophore[93].

$$\eta = \frac{\gamma_r/\gamma_r^0}{\gamma_r/\gamma_r^0 + \gamma_{abs}/\gamma_r^0 + (1-\eta^0)/\eta^0} \tag{1.56}$$

The main challenges associated with the detection limit of fluorescence-based sensing applications are the challenges with the fluorophore quantum yield, the less photostability of the fluorophores and the resulted autofluorescence of the samples. However, as explained earlier, the use of metallic nanostructures is further modified, since the fluorophores improve some of their photophysical limitations[93].

Forster energy transfer from the metallic nanostructure to the fluorophore takes place over short distances (<15 nm). The resulting quenching is due to the prominent non-radiative decay, which further cause to reduce the lifetime of the fluorophore. On the other hand, when the distance from the fluorophore to the metallic surface increases, radiative decay is enhanced and therefore increases the quantum yield[93, 94].

The enhancement factor (E_f) of the PES can be calculated using **Equation 1.57.** Here, we measured the fluorescence intensity of the fluorophore in the presence of the metallic structure as compared with in its absence. The fluorophore orientation plays an crucial role in the E_f due to the polarization sensitivity of SPR[93].

$$EF\alpha \frac{\gamma_e}{\gamma_e^0} X \frac{\eta}{\eta^0} Xf \tag{1.57}$$

In recent years, the use of PES has increased and involved the detection of important analytes including biomarkers (DNA, microRNA, and proteins), pathogens, and toxins, and the reported sensitivity has been in the fM range[95-98]. For instance, microwave-accelerated metal-enhanced fluorescence (MAME) is a clinically validated technique that was utilized to detect less than 10 copies of a genome within 1 minute[99, 100]. However, to date, PEF has shown an average $E_f < 10^2$, and current advancements in the field are expected to increase this value to $>10^3$. It is important to use a developed, advanced, cost-effective method to fabricate metallic nanoparticles onto the substrate in order to achieve an enhanced E_f. In this thesis, we address these challenges and use this rapidly developing field, in combination with LSPR, to develop more accurate biosensing application by mitigating the false-positive and -negative responses that result from the LSPR technique.

1.8 Organization of The Thesis

The introduction above provides a background of the use of nanoplasmonics in analytical chemistry and measurement science. This was the main foundation and motivation for the research work presented herein, and a summary of the scientific scope of this thesis is given in **Figure 1.10**. Herein, chemically synthesized gold triangular nanoprisms (Au TNPs) were utilized for the rational development of LSPR-, SERS-, and confocal-based nanosensors. Au TNPs have attracted attention in measurement science due to their high stability under conventional laboratory conditions as compared with other metals such as Ag, easy surface modification, and simple measurement instrumentation. Importantly, the high localized EM-field enhancement at the sharp tips and edges ensure a large sensing volume, and hence, high sensitivity to decay length and atomically flat surfaces, which facilitates the perfect SAM formation, easy functionalization, and

high reproducibly of the measurement. The size of the Au TNPs can be easily tuned by monitoring the LSPR peak position in the range of 650–900 nm, which helps to control the sensitivity of applications.

Chapter 2 considers the investigation of reversible tuning of LSPR properties of noble metal nanostructures via manipulation of organic ligand energy levels with a fermi level of a metallic nanostructure. For the first time, we report the spectroscopic investigation of reversible charge delocalization at the inorganic nanostructure and organic ligand interface. These studies were carried out using LSPR, SERS, and UPS and show self-assembled monolayers of para-substituted conjugated thiols on the nanostructure, inducing the delocalization of conduction electron wave function from the nanostructure to the ligand monolayer. Additionally, density functional theory calculations were utilized to validate the energy level orientation. Based on the calculation and spectroscopic data, we determined that in order to have an efficient charge delocalization, it is important to have appropriate alignment between the Fermi energy of the nanostructure and the highest occupied (HOMO) and lowest unoccupied (LUMO) molecular orbital energies of ligands. This understanding resulted in previously unknown plasmonic properties of hybrid inorganic-organic nanomaterials. We believe that this investigation will open new fields of scientific research and promote the design of advanced biosensors, plasmon-enhanced photocatalysts, and metamaterials.

In **Chapter 3,** we report our findings regarding the fabrication of self-assembled and flexible SERS nanosensors for the detection of explosives in fingerprints at parts-per-quadrillion levels**.** Here, we developed an ultra-sensitive, SERS-based, self-assembled, flexible sensor for explosives detection utilizing the strong electromagnetic enhancement of gold triangular nanoprisms. Our sensor is capable of detecting explosives (cyclotrimethylene trinitro amine - RDX, trinitrotoluene – TNT, and pentaerythritol tetranitrate - PETN) at parts-per-quadrillion (ppq) levels and has a long-term stability and shelf life. We believe that this highly sensitive and selective SERS-based sensor can be used to detect trace levels of explosives for the investigation of national security concerns.

Chapter 4 reports the “programable assembly of plasmonic gold triangular nanoprisms based on the substrate properties which resulted an ultra-sensitive SERS-based emergency room patient plasma assay. We employed a simple and efficient evaporative self-assembly method using polyethylene glycol (PEG)-functionalized Au TNPs. Here we controlled the substrate properties,

mainly the hydrophobic and hydrophilic nature, to obtain 2D, 2D/3D, or 3D assembly. The developed substrate has been utilized for efficient, highly selective, and sensitive drug detection in emergency room patient plasma samples.

Chapter 5 considers the achievement of biosensing of cardiac Troponin T in human biofluids at attomolar concentrations. Here, we investigated the effects of the structural parameters of receptor molecules for the detection of cardiac Troponin T (cTnT). Further, via the selective control of the spacing between the receptor and the nanoprism, and the number of receptors per nanoprism, we were able to quantitate cTnT in human serum and plasma samples at levels as low as 0.5 pg/L. We believe that our ultrasensitive detection of cTnT could be an affective early diagnostic test for myocardial infarction.

Finally, in **Chapter 6,** we report a ultrasensitive assay which is based on plasmoelectronic properties for the detection of tumor suppressor microRNAs in patient plasma as a liquid biopsy for the highly specific early diagnosis of bladder cancer. We developed a novel ultrasensitive optical-based assay using the unique aspects of the LSPR properties of chemically synthesized gold triangular nanoprisms. The reported technique can detect zeptomolar concentrations of microRNAs in patient plasma without any further purification. Additionally, we describe the investigation of changes in the functional parameters that yield the unprecedented high sensitivity based on delocalization of surface plasmon excitation through the DNA chain. The demonstrated sensitivity and feasibility of our novel methodology has the potential to effectively quantitate microRNA. Further, we successfully detected three different types of microRNAs in bladder cancer patients using only a few microliters of the plasma samples, without requiring further extraction or purification. Importantly, with our highest sensitivity for the first time, we were able to effectively detect the tumor suppressor microRNA in patient plasma.

1.9 References

1. Abalde-Cela, S.; Taladriz-Blanco, P.; de Oliveira, M. G.; Abell, C., Droplet microfluidics for the highly controlled synthesis of branched gold nanoparticles. *Scientific Reports* **2018,** *8* (1), 1-6.
2. Alabastri, A.; Yang, X.; Manjavacas, A.; Everitt, H. O.; Nordlander, P., Extraordinary Light-Induced Local Angular Momentum near Metallic Nanoparticles. *ACS Nano* **2016,** *10* (4), 4835-4846.

3. Alabastri, A.; Yang, X.; Nordlander, P.; Manjavacas, A.; Everitt Henry, O.; Everitt Henry, O., Extraordinary Light-Induced Local Angular Momentum near Metallic Nanoparticles. *ACS Nano* **2016,** *10* (4), 4835-46.
4. Bahrami, A.; Hejazi, P., Electrostatic immobilization of pectinase on negatively charged AOT-Fe3O4 nanoparticles. *Journal of Molecular Catalysis B: Enzymatic* **2013,** *93*, 1-7.
5. Zhang, X.; Wang, Y.; Cheng, F.; Zheng, Z.; Du, Y., Ultrathin lanthanide oxides nanomaterials: synthesis, properties and applications. *Science Bulletin* **2016,** *61* (18), 1422-1434.
6. Ameen, S.; Akhtar, M. S.; Seo, H.-K.; Shin, H. S., Metal oxide semiconductors and their nanocomposites application towards photovoltaic and photocatalytic. *Advanced Energy Materials* **2014**, 105-166.
7. Bally, M.; Voeroes, J., Nanoscale labels: nanoparticles and liposomes in the development of high-performance biosensors. *Nanomedicine (London, United Kingdom)* **2009,** *4* (4), 447-467.
8. Lee, Y. T.; Lee, J.; Ju, H.; Lim, J. A.; Yi, Y.; Choi, W. K.; Hwang, D. K.; Im, S., Nonvolatile Charge Injection Memory Based on Black Phosphorous 2D Nanosheets for Charge Trapping and Active Channel Layers. *Advanced Functional Materials* **2016,** *26* (31), 5701-5707.
9. Rabouw, F. T.; de Mello Donega, C., Excited-state dynamics in colloidal semiconductor nanocrystals. *Photoactive Semiconductor Nanocrystal Quantum Dots* **2017**, 1-30.
10. Trache, D.; Hussin, M. H.; Haafiz, M. K. M.; Thakur, V. K., Recent progress in cellulose nanocrystals: sources and production. *Nanoscale* **2017,** *9* (5), 1763-1786.
11. Zamborini, F. P.; Bao, L.; Dasari, R., Nanoparticles in Measurement Science. *Analytical Chemistry (Washington, DC, United States)* **2012,** *84* (2), 541-576.
12. Mayer, K. M.; Hafner, J. H., Localized surface plasmon resonance sensors. *Chemical Reviews (Washington, DC, United States)* **2011,** *111* (6), 3828-3857.
13. Joshi, G. K.; McClory, P. J.; Muhoberac, B. B.; Kumbhar, A.; Smith, K. A.; Sardar, R., Designing Efficient Localized Surface Plasmon Resonance-Based Sensing Platforms: Optimization of Sensor Response by Controlling the Edge Length of Gold Nanoprisms. *Journal of Physical Chemistry C* **2012,** *116* (39), 20990-21000.

14. Emam, A. N.; Girgis, E.; Khalil, W. K. B.; Mohamed, M. B., Toxicity of plasmonic nanomaterials and their hybrid nanocomposites. *Advances in Molecular Toxicology* **2014,** *8*, 173-202.
15. Li, M.; Cushing, S. K.; Wu, N., Plasmon-enhanced optical sensors: a review. *Analyst (Cambridge, United Kingdom)* **2015,** *140* (2), 386-406.
16. Chung, T.; Lee, S.-Y.; Song, E. Y.; Chun, H.; Lee, B., Plasmonic nanostructures for nano-scale bio-sensing. *Sensors* **2011,** *11*, 10907-10929.
17. Frolov, L.; Dix, A.; Tor, Y.; Tesler Alexander, B.; Chaikin, Y.; Vaskevich, A.; Rubinstein, I., Direct observation of aminoglycoside-RNA binding by localized surface plasmon resonance spectroscopy. *Analytical chemistry* **2013,** *85* (4), 2200-7.
18. Lei, G.; Gao, P. F.; Yang, T.; Zhou, J.; Zhang, H. Z.; Sun, S. S.; Gao, M. X.; Huang, C. Z., Photoinduced Electron Transfer Process Visualized on Single Silver Nanoparticles. *ACS Nano* **2017,** *11* (2), 2085-2093.
19. Sherry Leif, J.; Chang, S.-H.; Schatz George, C.; Van Duyne Richard, P.; Wiley Benjamin, J.; Xia, Y., Localized surface plasmon resonance spectroscopy of single silver nanocubes. *Nano letters* **2005,** *5* (10), 2034-8.
20. Austin Suthanthiraraj, P. P.; Sen, A. K., Localized surface plasmon resonance (LSPR) biosensor based on thermally annealed silver nanostructures with on-chip blood-plasma separation for the detection of dengue non-structural protein NS1 antigen. *Biosensors & Bioelectronics* **2019,** *132*, 38-46.
21. Li, J.; Li, H.; Wang, W.; Gao, L.; Li, W. Method for constructing photoelectrochemical sensor with ultra-sensitivity and high specificity for detecting mercury ion. 2013-10328748

103344685, 20130731., 2013.

22. Park, J. Y., Hot electron-mediated surface chemistry on solid-gas and solid-liquid interfaces. *Abstracts of Papers, 253rd ACS National Meeting & Exposition, San Francisco, CA, United States, April 2-6, 2017* **2017**, COLL-476.
23. Ferhan Abdul, R.; Jackman Joshua, A.; Cho, N.-J.; Cho, N.-J., Integration of Quartz Crystal Microbalance-Dissipation and Reflection-Mode Localized Surface Plasmon Resonance Sensors for Biomacromolecular Interaction Analysis. *Analytical chemistry* **2016,** *88* (24), 12524-12531.

24. Ferhan, A. R.; Jackman, J. A.; Cho, N.-J., Integration of Quartz Crystal Microbalance-Dissipation and Reflection-Mode Localized Surface Plasmon Resonance Sensors for Biomacromolecular Interaction Analysis. *Analytical Chemistry (Washington, DC, United States)* **2016,** *88* (24), 12524-12531.
25. Odom Teri, W.; Nehl Colleen, L., How gold nanoparticles have stayed in the light: the 3M's principle. *ACS Nano* **2008,** *2* (4), 612-6.
26. Odom, T. W.; Nehl, C. L., How Gold Nanoparticles Have Stayed in the Light: The 3M's Principle. *ACS Nano* **2008,** *2* (4), 612-616.
27. Tseng, Y.-T.; Lu, H.-Y.; Li, J.-R.; Tung, W.-J.; Chen, W.-H.; Chau, L.-K., Facile Functionalization of Polymer Surfaces in Aqueous and Polar Organic Solvents via 3-Mercaptopropylsilatrane. *ACS Applied Materials & Interfaces* **2016,** *8* (49), 34159-34169.
28. Tseng, Y.-T.; Tung, W.-J.; Chen, W.-H.; Chau, L.-K.; Lu, H.-Y.; Li, J.-R., Facile Functionalization of Polymer Surfaces in Aqueous and Polar Organic Solvents via 3-Mercaptopropylsilatrane. *ACS applied materials & interfaces* **2016,** *8* (49), 34159-34169.
29. Jackman, J. A.; Abdul Rahim, F.; Cho, N.-J., Nanoplasmonic sensors for biointerfacial science. *Chemical Society Reviews* **2017,** *46* (12), 3615-3660.
30. Pendry, J., Playing tricks with light. *Science (Washington, D. C.)* **1999,** *285* (5434), 1687-1688.
31. Hecht, B.; Bielefeldt, H.; Novotny, L.; Inouye, Y.; Pohl, D. W., Local excitation, scattering, and interference of surface plasmons. *Physical Review Letters* **1996,** *77* (9), 1889-1892.
32. Heeres, R. W.; Kouwenhoven, L. P.; Zwiller, V., Quantum interference in plasmonic circuits. *arXiv.org, e-Print Archive, Condensed Matter* **2013**, 1-26, arXiv:1309 6942v1 [cond-mat mes-hall].
33. Barbillon, G., Nanoplasmonics fundamentals and applications. **2017**.
34. Vercruysse, D.; Zheng, X.; Sonnefraud, Y.; Verellen, N.; Di Martino, G.; Lagae, L.; Vandenbosch, G. A. E.; Moshchalkov, V. V.; Maier, S. A.; Van Dorpe, P., Directional fluorescence emission by individual V-antennas explained by mode expansion. *ACS Nano* **2014,** *8* (8), 8232-8241.

35. Yao, H.; Fukui, C., Size and morphology effects on the fluorescence properties of π-conjugated poly(p-phenylene) polyelectrolyte nanoparticles synthesized via polyion association. *Journal of Materials Chemistry C: Materials for Optical and Electronic Devices* **2016,** *4* (14), 2945-2953.
36. Picca, R. A.; Calvano, C. D.; Cioffi, N.; Palmisano, F., Mechanisms of nanophase-induced desorption in LDI-MS. A short review. *Nanomaterials* **2017,** *7* (4), 75/1-75/19.
37. Chu, H.-W.; Unnikrishnan, B.; Anand, A.; Mao, J.-Y.; Huang, C.-C., Nanoparticle-based laser desorption/ionization mass spectrometric analysis of drugs and metabolites. *Journal of Food and Drug Analysis* **2018,** *26* (4), 1215-1228.
38. Richardson, P. M.; Parrott, A. J.; Semenova, O.; Nordon, A.; Duckett, S. B.; Halse, M. E., SABRE hyperpolarization enables high-sensitivity 1H and 13C benchtop NMR spectroscopy. *Analyst (Cambridge, United Kingdom)* **2018,** *143* (14), 3442-3450.
39. Equbal, A.; Leavesley, A.; Jain, S. K.; Han, S., Cross-Effect Dynamic Nuclear Polarization Explained: Polarization, Depolarization, and Oversaturation. *Journal of Physical Chemistry Letters* **2019**, Ahead of Print.
40. Griesinger, C.; Bennati, M.; Vieth, H. M.; Luchinat, C.; Parigi, G.; Hoefer, P.; Engelke, F.; Glaser, S. J.; Denysenkov, V.; Prisner, T. F., Dynamic nuclear polarization at high magnetic fields in liquids. *Progress in Nuclear Magnetic Resonance Spectroscopy* **2012,** *64*, 4-28.
41. Chen, Y.-Z.; Jiang, H.-L.; Chen, Y.-Z.; Gu, B.; Liu, J.; Ye, B.-J.; Uchida, T.; Xu, Q.; Liu, X., Location determination of metal nanoparticles relative to a metal-organic framework. *Nature communications* **2019,** *10* (1), 3462.
42. Govindhan, M.; Adhikari, B.-R.; Chen, A., Nanomaterials-based electrochemical detection of chemical contaminants. *RSC Advances* **2014,** *4* (109), 63741-63760.
43. Konvalina, G.; Haick, H., Effect of Humidity on Nanoparticle-Based Chemiresistors: A Comparison between Synthetic and Real-World Samples. *ACS Applied Materials & Interfaces* **2012,** *4* (1), 317-325.
44. Salafi, T.; Zeming, K. K.; Zhang, Y., Advancements in microfluidics for nanoparticle separation. *Lab on a Chip* **2017,** *17* (1), 11-33.

45. Longair, M., '...a paper ...I hold to be great guns': a commentary on Maxwell (1865) 'A dynamical theory of the electromagnetic field'. *Philosophical transactions. Series A, Mathematical, physical, and engineering sciences* **2015,** *373* (2039).
46. Morin, D., Electromagnetic waves. *Harvard University Physics Course, affiliated with MIT Education. Ch.8*.
47. Yi-Tao Long, Chao J., Localized Surface Plasmon Resonance Based Nanobiosensors. **2014**.
48. Fan, X.; Zheng, W.; Singh, D. J., Light scattering and surface plasmons on small spherical particles. *Light: Science & Applications* **2014,** *3* (6), e179.
49. Hohenester, U.; Krenn, J., Surface plasmon resonances of single and coupled metallic nanoparticles: A boundary integral method approach. *Physical Review B: Condensed Matter and Materials Physics* **2005,** *72* (19), 195429/1-195429/9.
50. SA, M., Plasmonics: fundamentals and applications. **2007**.
51. Luk'yanchuk, B. S.; Tribelsky, M. I.; Ternovsky, V.; Wang, Z. B.; Hong, M. H.; Shi, L. P.; Chong, T. C., Peculiarities of light scattering by nanoparticles and nanowires near plasmon resonance frequencies in weakly dissipating materials. *Journal of Optics A: Pure and Applied Optics* **2007,** *9* (9), S294-S300.
52. Kelly, K. L.; Coronado, E.; Zhao, L. L.; Schatz, G. C., The Optical Properties of Metal Nanoparticles: The Influence of Size, Shape, and Dielectric Environment. *Journal of Physical Chemistry B* **2003,** *107* (3), 668-677.
53. Garcia, M. A., Surface plasmons in metallic nanoparticles: fundamentals and applications [Erratum to document cited in CA156:297211]. *Journal of Physics D: Applied Physics* **2012,** *45* (38), 389501/1.
54. Unser, S.; Bruzas, I.; He, J.; Sagle, L., Localized Surface Plasmon Resonance Biosensing: Current Challenges and Approaches. *Sensors (Basel, Switzerland)* **2015,** *15* (7), 15684-716.
55. Albanese, A.; Tang, P. S.; Chan, W. C. W., The effect of nanoparticle size, shape, and surface chemistry on biological systems. *Annual Review of Biomedical Engineering* **2012,** *14*, 1-16.
56. Duque, J. S.; Blandon, J. S.; Riascos, H., Localized plasmon resonance in metal nanoparticles using Mie theory. *Journal of Physics: Conference Series* **2017,** *850* (5th Colombian Conference of Engineering Physics, 2016), 012017/1-012017/7.

57. Khan, I.; Saeed, K.; Khan, I., Nanoparticles: Properties, applications and toxicities. *Arabian Journal of Chemistry* **2017**, Ahead of Print.
58. Hong, Y.; Huh, Y.-M.; Yoon, D. S.; Yang, J., Nanobiosensors based on localized surface plasmon resonance for biomarker detection. *Journal of Nanomaterials* **2012**, 759830, 13 pp.
59. Hsieh, M.-L.; Chau, L.-K., Noble metal nanoparticles in optical biosensing based on localized surface plasmon resonance. *Huaxue* **2010,** *68* (1), 21-32.
60. Sepulveda, B.; Angelome, P. C.; Lechuga, L. M.; Liz-Marzan, L. M., LSPR-based nanobiosensors. *Nano Today* **2009,** *4* (3), 244-251.
61. Ilyushin, A. S.; Miller, F. A., The discovery of the Raman effect. *Philatelia Chimica et Physica* **2009,** *31* (4), 136-143.
62. Klisinska-Kopacz, A., An investigation of a unique group of painted silk banners from a Polish collection. *Journal of Raman Spectroscopy* **2017,** *48* (12), 1725-1731.
63. Masters, B. R., C.V. Raman and the Raman effect. *Optics & Photonics News* **2009,** *20* (3), 40-45.
64. Mutter, S. T.; Zielinski, F.; Popelier, P. L. A.; Blanch, E. W., Calculation of Raman optical activity spectra for vibrational analysis. *Analyst (Cambridge, United Kingdom)* **2015,** *140* (9), 2944-2956.
65. Surovtsev, N. V.; Kupriyanov, I. N., Temperature dependence of the Raman line width in diamond: Revisited. *Journal of Raman Spectroscopy* **2015,** *46* (1), 171-176.
66. Sharma, B.; Frontiera, R. R.; Henry, A.-I.; Ringe, E.; Van Duyne, R. P., SERS: Materials, applications, and the future. *Materials Today (Oxford, United Kingdom)* **2012,** *15* (1-2), 16-25.
67. Shi, R.; Liu, X.; Ying, Y., Facing Challenges in Real-Life Application of Surface-Enhanced Raman Scattering: Design and Nanofabrication of Surface-Enhanced Raman Scattering Substrates for Rapid Field Test of Food Contaminants. *Journal of Agricultural and Food Chemistry* **2018,** *66* (26), 6525-6543.
68. Sur, U. K., Surface-enhanced Raman scattering. *Raman Spectroscopy and Applications* **2017**, 293-312.
69. Bora, T., Recent developments on metal nanoparticles for SERS applications. *Noble and Precious Metals* **2018**, 117-135.

70. Hwang, J. S.; Yang, M., Sensitive and reproducible gold SERS sensor based on interference lithography and electrophoretic deposition. *Sensors* **2018,** *18* (11), 4076/1-4076/15.
71. Ma, L.; Wang, J.; Huang, H.; Zhang, Z.; Li, X.; Fan, Y., Simultaneous thermal stability and ultrahigh sensitivity of heterojunction SERS substrates. *Nanomaterials* **2019,** *9* (6), 830.
72. Nehra, K.; Pandian, S. K.; Byram, C.; Moram, S. S. B.; Soma, V. R., Quantitative Analysis of Catalysis and SERS Performance in Hollow and Star-Shaped Au Nanostructures. *Journal of Physical Chemistry C* **2019,** *123* (26), 16210-16222.
73. Schluecker, S., Surface-Enhanced Raman Spectroscopy: Concepts and Chemical Applications. *Angewandte Chemie, International Edition* **2014,** *53* (19), 4756-4795.
74. Lee, K.-S.; El-Sayed, M. A., Gold and Silver Nanoparticles in Sensing and Imaging: Sensitivity of Plasmon Response to Size, Shape, and Metal Composition. *Journal of Physical Chemistry B* **2006,** *110* (39), 19220-19225.
75. Anon, Chemical enhancement in SERS. *Anal. Chem.* **1996,** *68* (3), 81A.
76. Liang, X.; Liang, B. L.; Pan, Z.; Lang, X.; Zhang, Y.; Wang, G.; Yin, P.; Guo, L., Tuning plasmonic and chemical enhancement for SERS detection on graphene-based Au hybrids. *Nanoscale* **2015,** *7* (47), 20188-20196.
77. Liu, L.; Chen, D.; Ma, H.; Liang, W., Spectral Characteristics of Chemical Enhancement on SERS of Benzene-like Derivatives: Franck-Condon and Herzberg-Teller Contributions. *Journal of Physical Chemistry C* **2015,** *119* (49), 27609-27619.
78. Yu, X.; Cai, H.; Zhang, W.; Li, X.; Pan, N.; Luo, Y.; Wang, X.; Hou, J. G., Tuning Chemical Enhancement of SERS by Controlling the Chemical Reduction of Graphene Oxide Nanosheets. *ACS Nano* **2011,** *5* (2), 952-958.
79. Kundu, S.; Jayachandran, M., The self-assembling of DNA-templated Au nanoparticles into nanowires and their enhanced SERS and catalytic applications. *RSC Advances* **2013,** *3* (37), 16486-16498.
80. Lan, C.; Zhao, J.; Zhang, L.; Wen, C.; Huang, Y.; Zhao, S., Self-assembled nanoporous graphene quantum dot-Mn3O4 nanocomposites for surface-enhanced Raman scattering based identification of cancer cells. *RSC Advances* **2017,** *7* (30), 18658-18667.
81. Wang, X.; Xu, S.; Li, H.; Tao, J.; Zhao, B.; Xu, W., A three-dimensional surface-enhanced Raman scattering substrate: Au nanoparticle supramolecular self-assembly in anodic aluminum oxide template. *Journal of Raman Spectroscopy* **2012,** *43* (3), 459-463.

82. Eryilmaz, M.; Acar Soykut, E.; Cetin, D.; Boyaci, I. H.; Suludere, Z.; Tamer, U., SERS-based rapid assay for sensitive detection of Group A Streptococcus by evaluation of the swab sampling technique. *Analyst (Cambridge, United Kingdom)* **2019,** *144* (11), 3573-3580.
83. K, J.; S, B.; Ganiga, M.; R, D.; S, A.; Cyriac, J.; George, B. K., Effective SERS detection using a flexible wiping substrate based on electrospun polystyrene nanofibers. *Analytical Methods* **2017,** *9* (26), 3998-4003.
84. Wen, H.; Wang, H.; Hai, J.; He, S.; Chen, F.; Wang, B., Photochemical Synthesis of Porous CuFeSe2/Au Heterostructured Nanospheres as SERS Sensor for Ultrasensitive Detection of Lung Cancer Cells and Their Biomarkers. *ACS Sustainable Chemistry & Engineering* **2019,** *7* (5), 5200-5208.
85. Ding, Q.; Kang, Z.; He, X.; Wang, M.; Lin, M.; Lin, H.; Yang, D.-P., Eggshell membrane-templated gold nanoparticles as a flexible SERS substrate for detection of thiabendazole. *Microchimica Acta* **2019,** *186* (7), 1-9.
86. Fu, H.; Chen, J.; Chen, L.; Zhu, X.; Chen, Z.; Qiu, B.; Lin, Z.; Guo, L.; Chen, G., A calcium alginate sponge with embedded gold nanoparticles as a flexible SERS substrate for direct analysis of pollutant dyes. *Microchimica Acta* **2019,** *186* (2), 1-7.
87. Xiu, X.; Guo, Y.; Li, C.; Li, Z.; Li, D.; Zang, C.; Jiang, S.; Liu, A.; Man, B.; Zhang, C., High-performance 3D flexible SERS substrate based on graphene oxide/silver nanoparticles/pyramid PMMA. *Optical Materials Express* **2018,** *8* (4), 844-857.
88. Fang, W.; Zhang, X.; Chen, Y.; Wan, L.; Huang, W.; Shen, A.; Hu, J., Portable SERS-enabled micropipettes for microarea sampling and reliably quantitative detection of surface organic residues. *Analytical Chemistry (Washington, DC, United States)* **2015,** *87* (18), 9217-9224.
89. Gao, M.; Fang, W.; Ren, J.; Shen, A.; Hu, J., Reliable SERS detection of nitrite based on pH and laser irradiance-dependent diazotization through a convenient sampling micro-chamber. *Analyst (Cambridge, United Kingdom)* **2016,** *141* (17), 5195-5201.
90. Gu, H.-X.; Li, D.-W.; Xue, L.; Zhang, Y.-F.; Long, Y.-T., A portable microcolumn based on silver nanoparticle functionalized glass fibers and its SERS application. *Analyst (Cambridge, United Kingdom)* **2015,** *140* (23), 7934-7938.

91. Tan, C.; Zhang, Z.; Qu, Y.; He, L., Ag2O/TiO2 Nanocomposite Heterostructure as a Dual Functional Semiconducting Substrate for SERS/SEIRAS Application. *Langmuir* **2017,** *33* (22), 5345-5352.
92. Taraska, J. W.; Zagotta, W. N., Fluorescence applications in molecular neurobiology. *Neuron* **2010,** *66* (2), 170-189.
93. Bauch, M.; Toma, K.; Toma, M.; Zhang, Q.; Dostalek, J., Plasmon-Enhanced Fluorescence Biosensors: a Review. *Plasmonics* **2014,** *9* (4), 781-799.
94. Bohlen, J.; Cuartero-Gonzalez, A.; Pibiri, E.; Ruhlandt, D.; Fernandez-Dominguez, A. I.; Tinnefeld, P.; Acuna, G. P., Plasmon-assisted Förster resonance energy transfer at the single-molecule level in the moderate quenching regime. *Nanoscale* **2019,** *11* (16), 7674-7681.
95. Santos, G. M.; Zhao, F.; Zeng, J.; Li, M.; Shih, W.-C., Label-free, zeptomole cancer biomarker detection by surface-enhanced fluorescence on nanoporous gold disk plasmonic nanoparticles. *Journal of Biophotonics* **2015,** *8* (10), 855-863.
96. Santos Greggy, M.; Zhao, F.; Zeng, J.; Li, M.; Shih, W.-C., Label-free, zeptomole cancer biomarker detection by surface-enhanced fluorescence on nanoporous gold disk plasmonic nanoparticles. *Journal of biophotonics* **2015,** *8* (10), 855-63.
97. Yuan, C.; Deng, Y.; Li, X.; Li, C.; Xiao, Z.; Liu, Z., Synthesis of Monodisperse Plasmonic Magnetic Microbeads and Their Application in Ultrasensitive Detection of Biomolecules. *Analytical Chemistry (Washington, DC, United States)* **2018,** *90* (13), 8178-8187.
98. Yuan, C.; Li, X.; Li, C.; Xiao, Z.; Deng, Y.; Liu, Z., Synthesis of Monodisperse Plasmonic Magnetic Microbeads and Their Application in Ultrasensitive Detection of Biomolecules. *Analytical chemistry* **2018,** *90* (13), 8178-8187.
99. Melendez, J. H.; Huppert, J. S.; Jett-Goheen, M.; Hesse, E. A.; Quinn, N.; Gaydos, C. A.; Geddes, C. D., Blind evaluation of the microwave-accelerated metal-enhanced fluorescence ultrarapid and sensitive Chlamydia trachomatis test by use of clinical samples. *Journal of Clinical Microbiology* **2013,** *51* (9), 2913-2920.
100. Joshi, L. T.; Mali, B. L.; Geddes, C. D.; Baillie, L., Extraction and sensitive detection of toxins A and B from the human pathogen Clostridium difficile in 40 seconds using microwave-accelerated metal-enhanced fluorescence. *PLoS One* **2014,** *9* (8), e104334/1-e104334/9, 9 pp.

CHAPTER 2. REVERSIBLE TUNING OF THE PLASMOELECTRIC EFFECT IN NOBLE METAL NANOSTRUCTURES THROUGH MANIPULATION OF ORGANIC LIGAND ENERGY LEVELS

This article has been reprinted with permission, Liyanage, T.; Nagaraju, M.; Johnson, M.; Muhoberac, B. B.; Sardar, R., Reversible Tuning of the Plasmoelectric Effect in Noble Metal Nanostructures Through Manipulation of Organic Ligand Energy Levels. Nano Letters 2019, Ahead of Print. DOI/10.1021/acs.nanolett.9b03588

2.1 Synopsis

. Interestingly, in this chapter, we report the complete opposite spectral observation to the well-known Drude model with gold triangular nanoprisms (Au TNPs) functionalized with para-substituted thiophenols (X-Ph-SH; X =-NH_2, -OCH_3, -CH_3, -H, -Cl, -Br, -NO_2, and –CF_3) in the solid-state. Accordingly, with respect to thiophenol-functionalized Au TNPs, electron-withdrawing groups substituted with thiophenol showed a red shift of the $\boldsymbol{\lambda}_{\mathrm{LSPR}}$ position, and the electron-donating groups substituted with thiophenol showed a blue shift of the $\boldsymbol{\lambda}_{\mathrm{LSPR}}$ position. We were able to tune the electron density of Au TNPs up to 12% by functionalization with para-substituted thiophenolate (X-Ph-S-) ligands. Importantly, all the observed spectroscopic properties are fully reversible either way by exchanging thiophenolates containing electron-withdrawing groups with those containing electron-donating groups, or vice versa. Further, we developed Frontier molecular orbital (MO) diagrams of Au-thiophenolate interactions utilizing density functional theory calculations to explain the observed spectral changes. Hence, for the first time, we propose that delocalization of excitation wave functions of Au TNPs control the LSPR properties following functionalization. Further, we conducted UPS calculations to validate the molecular orbital theory based on the changes in working function of Au TNPs following functionalization. Taken together, these unique findings have fundamental importance in various optoelectronic applications such as photocatalysis, photovoltaics, and sensing.

2.2 Introduction

When the electric field of incident light interacts with the surface conduction electrons of a noble metal, collective oscillation occurs via surface plasmon excitation, and the resulting resonance is identified as localized surface plasmon resonance (LSPR)[1, 2]. As discussed in Chapter

1, the LSPR properties of metallic nanostructures are mainly controlled by the size, shape, and local dielectric environment[3-5]. The Drude model (Equations 2.1 and 2.2) has been executed to explain how the wavelength position of the LSPR peak varies by increases or decreases in the electron density. Accordingly, when the carrier electron density (N_e) of a metallic nanostructure is increased, the bulk plasma frequency (ω_p) is also increased, and as a result, the LSPR peak position ($\boldsymbol{\lambda}_{LSPR}$) is decreased[6]. Similarly, when N_e is decreased, $\boldsymbol{\lambda}_{LSPR}$ is increased. Here, m is the effective mass of the electron and ε_0 is the dielectric function.

$$\omega_p^2 = \frac{Ne^2}{m\varepsilon_0} \tag{2.1}$$

$$\omega_p \; \alpha \; \frac{1}{\lambda} \tag{2.2}$$

Therefore, noble metallic nanostructures can be identified as "plasmoelectric materials" that allow easy tuning of the $\boldsymbol{\lambda}_{LSPR}$ position by an external electric field upon light irradiation of the conductive surface of the nanostructure[7]. The literature has reported in-depth study of tuning the position by changing the Ne of the metallic nanostructure. As an example, Sheldon et al., changed the $\boldsymbol{\lambda}_{LSPR}$ position using an external electric field to increase the N_e of the nanostructure[8]. Further, Hoener et al., and Moskovits reported modifying the LSPR response of an Au nanostructure by changing the Ne using a capacitive charge or a thin layer of conducting metal-oxide[9, 10].

Intuitively, $\boldsymbol{\lambda}_{LSPR}$ of the metallic nanostructure can be tuned via modification of the electron density, which can be achieved by functionalization with electron-donating group (EDG) or electron-withdrawing group (EWG)-substituted organic ligands, controlling the plasmoelectric effect via inductive or resonance effects. However, such tuning of the LSPR position is expected to be fully reversible in either direction by replacing the EWG ligands with EDG ligands or vice versa. To the best of our knowledge, there is no literature evidence for the ligand-controlled, fully reversible tuning of plasmoelectric effects in metal nanostructures, and such application will be highly advantageous in a wide range of chemical and biological sensors, molecular microelectronics, and other applications with highly controllable photocatalytic and photovoltaic properties.

Therefore, the data reported in this chapter show for the first time how the plasmoelectric properties of Au TNPs are changed following solid-state functionalization with para-substituted

thiophenol (X-Ph-S-; X = -NH_2, -OCH_3, -CH_3, -H, -Cl, -Br, -NO_2, and –CF_3). Our unique findings reveal that the N_e of Au TNPs can be controlled up to 12% based on the energy level alignment between the TNPs and the molecular orbitals (MOs) of the organic X-Ph-S- ligands. Most importantly, this is the first time that the fully reversible tuning of the $\boldsymbol{\lambda}_{LSPR}$ position of Au TNPs has been reported for at least five cycles following functionalization with X-Ph-S- ligands. Surprisingly, our experimental results are the exact opposite of those observed with the Drude model (Equations 2.1 and 2.2), and we propose MO theory of the TNP-S-Ph-X system to explain this unique observation. Accordingly, we hypothesize the delocalization of excitation electron wave functions, either from or to hybrid orbitals that are formed between the electronic states of Au TNPs and MOs of thiophenol due to the appropriate alignment of their MO energy levels, which was further confirmed with the calculated changes in overall charge density of the TNPs and the corresponding LSPR properties. Most importantly, we successfully achieved a ~1.9 eV change in the working function (ϕ) of Au TNPs, between EDG- and EWG-substituted thiophenol-functionalized Au TNPs. This finding further supports the proposed excitation electron wave delocalization mechanism.

Taken together, this remarkable solid-state large range of ligand-controlled spectral tunability of noble metal nanostructures in the visible region of the solar spectrum[11-13] has great potential for solar cell and photocatalytic applications[14, 15], since it offers the opportunity to bypass the complication of off-resonance LSPR activation of noble metal-doped semiconductor nanocrystals[8, 16]. Further, this unique finding will be highly advantaged in design and development of nanoelectronic devices using metallic nanoparticles cross-linked to organic molecules possessing based on functional properties of the substitution[17]. Nanoparticle-assisted photothermal therapy is a unique drug-free approach that induces cell death by utilizing the localized heat generated upon excitation of LSPR and has already been successfully demonstrated as cancer therapy where excitation of laser at different wavelength used to destroy the tumor cells. In this case, the EM energy density on the nanostructure is very important, since it is converted into thermal energy that locally heats the metal nanoparticles. Controlling the electron density on the nanostructure without changing the shape or size of the nanostructure based on the ligand chemistry will be highly advantageous in this unique drug-free approach in destroying cancerous cells[17].

2.3 Materials and Methods

2.3.1 Material

Chloro(triethylphosphine) gold (I) (Et3PAuCl, 97%) was purchased from Gelest, poly(methylhydrosiloxane) (PMHS, Mn = 1700-3300), trioctylamine (TOA, 98%), ACS grade acetonitrile (CH3CN, 99.9%), methanol (99.8%)), Para substituted aminothiophenol (97%), methoxythiophenol (97%), methylthiophenol (98%), thiophenol (97%), bromothiophenol (95%), chlorothiophenol (97%), nitrothiphenol (80%), trifluromethylthiophenol (96%) and 1-hexanethiol (95%) were purchased from Sigma Aldrich and were used as recieved. (3-mercaptopropyl)-triethoxysilane (MPTES, 94%) was purchased from Alfa Aesar. 98% sadium borohydride powder was obtained from Acros organics and ethanol (alcohol 200 proof) was purchased from Decon labs. The glass coverslips were purchased from Fisher Scientific. RBS 35 Detergent was obtained from Thermo Scientific and used as received. All water was purified using a Thermo Scientific Barnstead Nanopure system.

2.3.2 Absorbance, Extinction, SERS, NMR, and Ultraviolet Photoelectron (UPS) Spectroscopy, and Atomic Force Microscopy Measurements

Absorption and extinction spectra in the range of 300-1100 nm were collected with a Varian Cary 50 Scan UV-visible spectrophotometer using 1 cm glass cuvette. All the absorbance spectra were collected using 0.3 mL of reaction solution diluted in 2.0 mL of acetonitrile. Acetonitrile was used as a background for these measurements, and the background was run before collecting the absorbance spectra. All extinction spectra were measured in air at room temperature. Here, a blank MPTES-functionalized glass coverslip was placed in a clean cuvette and used as a background. The chemically synthesized gold triangular nanoprisms (Au TNPs) attached onto the silanized glass coverslips were characterized by atomic force microscopy (AFM) using a Bioscope AFM instrument. Surface-enhanced Raman scattering (SERS) analyses were performed using a Foster & Freman Foram 785 HP Raman system with a 785 nm diode laser excitation source with 20 mW of power and 5-μm spot size. The SERS data were acquired for nanosensors with 10 scans from 400-2000 cm-1 with a 16 sec acquisition time. Automatic baseline correction was performed in OMNIC software before acquired spectra were plotted. 1H NMR spectra were collected on a Bruker AVANCE III 500 instrument at 500 MHz frequency using CD2Cl2 as solvent at room temperature. A minimum of 1000 scans were collected for quantification. A 15 sec relaxation delay

time was used for accurate integration of the phenyl peak region. Photoelectron spectroscopy (UPS) was performed in a Kratos Axis Ultra UPS/XPS spectrometer. UPS spectra were acquired with a 21.2 eV He(I) source at a pass energy of 5.0 eV. In the UPS experiments, a -10 V bias was applied to the sample to increase the kinetic energy of all photoelectrons, improving the instrument response and resolution of the low KE electrons. UPS data were also collected for a piece of Au foil cleaned in the UPS chamber with an Ar+ sputter gun, which allowed the measurement if the Fermi level and.

2.3.3 Silanization of Glass Coverslips and Attachment of Au TNPs

MPTES-functionalized glass coverslips were prepared using our previously published methods.1-3 Briefly, glass coverslips were immersed and sonicated in a 10% (v/v) aqueous RBS 35 detergent solution for 10 min at 90 ℃. Then coverslips were thoroughly rinsed with nanopure water, and incubated in a solution of conc. hydrochloric acid and methanol (1:1 v/v) for 30 min. The coverslips were then washed several times with nanopure water and dried in a vacuum oven at 60 ℃ overnight. Following day, the dried coverslips were incubated for 30 min in a solution of 15% MPTES in purged ethanol. The coverslips were then sonicated in N2 purged ethanol. After 10 min ethanol was decanted and repeated the four other washing cycles and each time ethanol solution has been changed. After the last washing step, coverslips were placed in a vacuum oven at 120 ℃ for minimum 3 hr. The prepared MPTES-functionalized coverslips were then stored at 4 ℃ for further use.

2.3.4 Synthesis of Au TNPs

Our previously reported methods were followed for the colloidal synthesis of Au TNPs.4-6 Briefly, 12.0 mg $Et_3PAu(I)Cl$ was dissolved in 10 mL of CH3CN and allowed to stir for 5 min at room temperature in a covered Erlenmeyer flask, which was kept on a hot-plate stirrer. Then 0.085 mL of TOA and 0.3 mL of PMHS were mixed in a 1.0 mL of CH_3CN in a separated vial and injected into the above gold salt solution. Within 2 min of addition of PMHS and TOA mixture heat was applied to the reaction mixture and the inside temperature was maintained at 42-44 ℃ throughout the entire synthesis. The solution color started to change from colorless to pink, purple, and then light blue and at this stage 7.0 mL of additional CH_3CN was added to the reaction, and

the reaction was allowed to run until it resulted in a dark blue solution with a stable absorbance dipole peak at 800 nm in CH_3CN. The solution was then removed from heat, centrifuged at 5000 rpm for 20 sec. Finally, previously prepared MPTES-functionalized coverslips were incubated in the freshly synthesized Au TNPs solution for ~1.0 hr. After incubation, the glass coverslip-bound Au TNPs were rinsed with acetonitrile, dried under nitrogen flow, and stored under nitrogen at 4 ℃.

2.3.5 Functionalization of Au TNPs with Para-Substituted Thiophenols (X-Ph-SH), and Extinction and SERS Measurements

Tape-cleaning procedure was performed to remove non-prismatic nanostructures from glass coverslip-bound Au TNPs. During the process, an adhesive (scotch) tape was placed onto the glass substrate and gently pressed with the thumb, and then the tape was slowly removed at a 90^O angle. The glass coverslip-bound Au TNPs were incubated in 1.0 mM ethanolic solution of p-substituted thiophenol for overnight. After that, coverslips were rinsed with plenty of ethanol to remove loosely bound p-substituted thiophenols, and then functionalized Au TNPs were dried using N2 flow. Finally, the LSPR dipole peak position of Au TNPs was determined by using UV-vis spectroscopy. During the measurement we used we kept the bulk refractive index constant by collecting all spectra in N2-filled cuvette. After collecting the λ_{LSPR} of the X-Ph-S-functionalized Au TNPs, the same on to the sensor glass coverslips were analyzed by SERS spectroscopy. SERS intensity of C=C and C-S stretching was utilized to quantify the relative number of X-Ph-S-attached on to Au TNPs.

2.3.6 Quantification of Au TNP-Bound X-Ph-SH by 1H NMR

After obtaining the $\boldsymbol{\Delta\lambda}_{\mathrm{LSPR}}$ of the p-substituted thiophenol on to the sensor same sensor was utilized obtain the SERS spectroscopy using 785 nm diode laser excitation source with 20 mW of power and 5-μm spot size. For the SERS data we used h 10 scans (1 x 20 mW, 9 x 80 mW) from 400-2000 cm^{-1}, and 16 sec acquisition time and with a 5-μM laser spot diameter. Automatic baseline correction was performed using OMNIC software before acquired spectra were plotted. Raman intensity of C=C and C-S stretching was utilized to quantify the number of p-substituted thiophenol on to the Au TNPs.

2.3.7 Quantification of Au TNP-Bound X-Ph-SH by 1H NMR

We determined the number of X-Ph-S-/nm^2 through a 1H NMR analysis using ferrocene as an internal standard. We used chemical displacement reactions for the analysis as follows. Firstly, X-Ph-S-functionalized Au TNPs were incubated in 10.0 mM of 1-hexanethiol solution in ethanol for overnight to replace X-Ph-S- from the surface of Au TNPs. The exchange solution then carefully collected in a vial, and ethanol was completely evaporated using rotatory evaporator. Then the vial was dried under medium vacuum for overnight to bring it to complete dryness. Secondly, 0.7 mL, 0.25 mM ferrocene solution in CD2Cl2 was added into the vial and sonicated for 2 min to prepare a homogeneous solution. Finally, NMR spectroscopy data were obtained and using integration of the peak of interest (A) (e.g.- aromatic peaks of X-Ph-S-) and integration of the peak of the internal standard (B), the moles of X-Ph-S-were calculated as explained in Equation 2.3. Here N represent the number of nuclei represented by the peaks of interest.

$$r_{A/B} = \frac{(integral_A/N_A)}{(integral_B/N_B)} \quad \textbf{(2.3)}$$

2.3.8 Density Functional Theory (DFT) Calculations

The molecular geometry optimization-based DFT calculations was conducted using LANL2DZ for Au with 6-311+G** basis set and B3LPY functional.

2.4 Results and Discussion

To investigate ligand-controlled reversible tunability of plasmoelectric effects of noble metal nanostructures, we selected Au TNPs because their atomically flat surface should allow the formation of a well-controlled self-assembled monolayer of X-Ph-S- ligands. Moreover, several important nanoscale structural properties such as (1) strong electromagnetic (EM) field enhancement at their sharp tips and edges should induce a large LSPR response,[18-20] (2) sharp structural features of TNPs are expected to facilitate strong Au-S-Ph-X interactions at the metal-ligand interface,[21] and (3) high stability of the Au-S bond due to soft-soft covalent interactions. These properties allow spectroscopic characterization in the solid-state that is critical for device applications.[20, 22, 23] As shown in **Figure 2.1A**, we investigated the LSPR response of Au TNPs by

attaching them onto a silanized glass substrate followed by ligand exchange reactions with X-Ph-S-; X= -NH_2, -OCH_3, -CH_3, -H, -Cl, -Br, -NO_2, and –CF_3 in the solid-state. **Figure 2.1B** represent atomic force (AFM) and scanning electron (SEM) microscopy images of trioctylamine (TOA)-passivated, Au TNPs with an average 42 nm edge-length and 8.5 nm height that display an LSPR dipole peak (also defined as $\boldsymbol{\lambda}_{LSPR}$) at 775 nm in air.

Ligand exchange by thiophenol produces fully X-Ph-S- ligand-passivated TNPs as confirmed by surface-enhanced Raman scattering (SERS) measurements in which disappearance of the C-N Raman stretch at 1035 cm^{-1} and appearance of the C-S and aromatic C=C stretches at 1083 and 1573 cm^{-1}, respectively, are observed. As illustrated in **Figure 2.1C and D**, an ~24 nm red shift in the $\boldsymbol{\lambda}_{LSPR}$ of TNPs is observed that could be due to the change in the local dielectric environment around the TNPs. Passivation of Au TNPs with X-Ph-S- ligands containing strong electron withdrawing (X = -CF_3) and strong electron donating (X = –NH_2) groups produces ~20 and ~25 nm blue and red shifts of the $\boldsymbol{\lambda}_{LSPR}$ position, respectively, with respect to H-Ph-S- (see **Figure 2.1C and D**). Interestingly, the magnitude of the LSPR red and blue shifts follows the increasing order of electron donation (-CH_3> -OCH_3> -NH_2) and electron withdrawal (-Cl> -Br> -NO_2> -CF_3) abilities of the para-substitutions, respectively. The change in the $\boldsymbol{\lambda}_{LSPR}$ position ($\Delta\boldsymbol{\lambda}_{LSPR}$ in nm) from fully TOA-passivated TNPs and upon ligand exchange with X-Ph-S- ligands does not follow the refractive index trend (see **Figure 2.1E**) because one would expect nearly identical $\Delta\boldsymbol{\lambda}_{LSPR}$ values for -Br and -NH_2 substitutions, whereas -CH_3 and -OCH_3 substituted X-Ph-S- ligands should provide lesser shifts than either Cl or Br substituted X-Ph-S- ligands. Furthermore, the trend in $\Delta\boldsymbol{\lambda}_{LSPR}$ values with respect to the electronic character of para-substitutions is somewhat surprising because ω_p is expected to increase (decrease) [$\boldsymbol{\lambda}_{LSPR}$ blue shift (red) shift] for X-Ph-S- ligands containing an electron-donating (-withdrawing) group [i.e., X = -NH_2(-CF_3], as described by Eq. 1 and 2 (i.e. Drude model). Two other factors, refractive index of different X-Ph-S- ligands and variation in the number of X-Ph-S- ligands attached per TNP, also would influence the LSPR properties including the $\boldsymbol{\lambda}_{LSPR}$ position of metal nanostructures. We hypothesize that the attachment of X-Ph-S- ligands onto Au TNPs produces hybrid HOMOs and LUMOs that together allow delocalization of photo-excited electron or hole wave functions, thus resulting in the changes in the N_e of TNPs and the $\boldsymbol{\lambda}_{LSPR}$ response, see **Figure 2.2**.

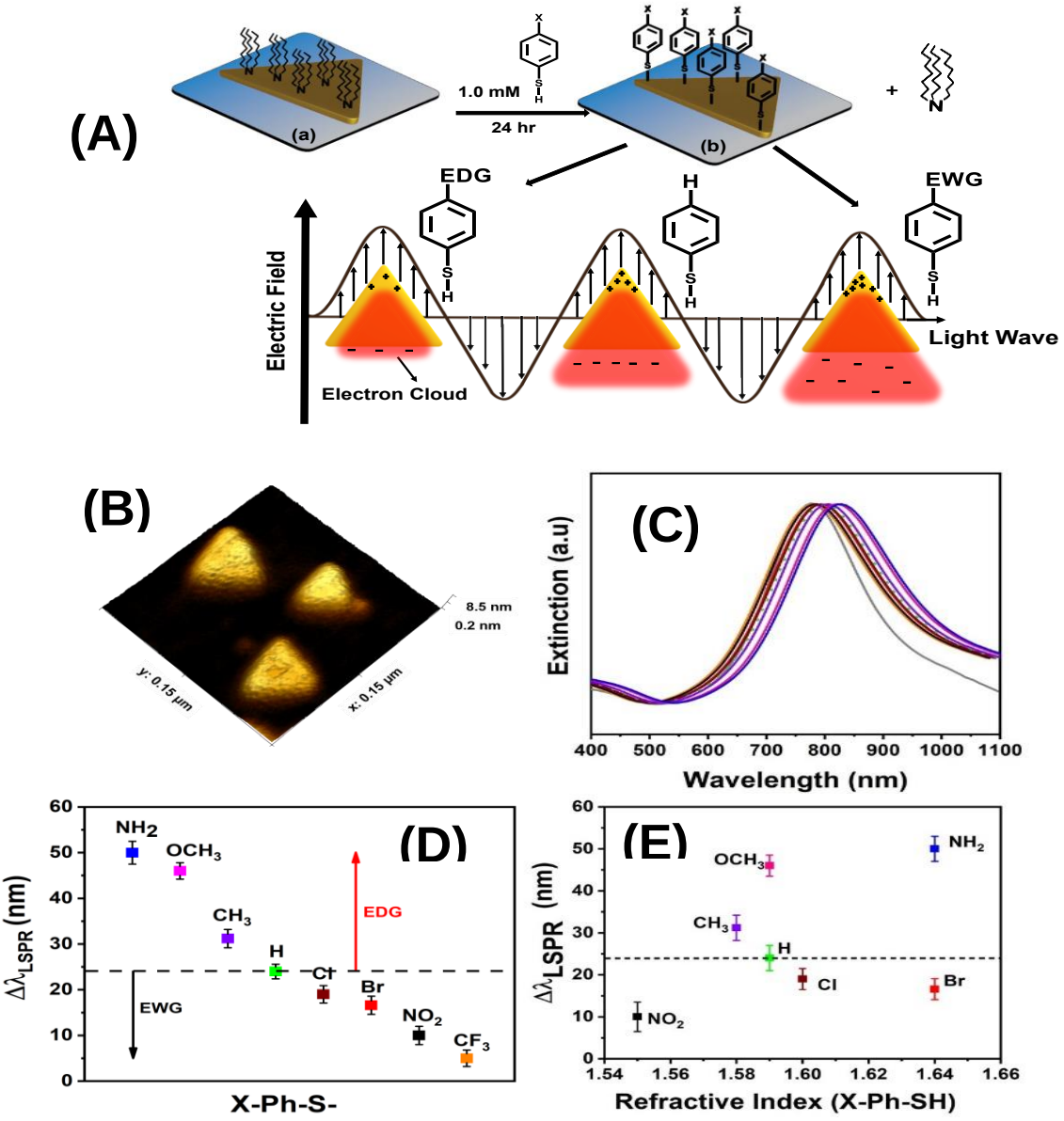

Figure 2.1. Structural and optical characterizations of different X-Ph-S-passivated Au TNPs in the solid-state. (A) Schematic diagram showing reversible delocalization exciton (electron or hole) wave functions along Au-S interface. The image is not to scale. (B) AFM image of the TOA-passivated Au TNPs. (C) Experimentally determined LSPR spectra of para-substituted thiophenolate (X-Ph-S-)-passivated Au TNPs: TOA- (black-774 nm), and X-Ph-S-)- passivated: X = CF_3 (Dark Blue-779 nm), X = NO_2 (Pink-784 nm), X = Br (Brown-791 nm), X = Cl (Green-793 nm), X = H (Red dotted line-798 nm), X = CH_3 (Purple-805 nm), X = OCH_3 (orange-820 nm), X = NH_2 (Blue-824 nm). (D) Figure summarizes the observed $\Delta\lambda_{LSPR}$ (X-Ph-S-passivated –TOA-passivated Au TNPs) upon passivation of Au TNPs with X-Ph-S-. Red arrow indicates the $\Delta\lambda_{LSPR}$ shifts after passivation with electron donating groups (EDGs) and black arrow indicates the $\Delta\lambda_{LSPR}$ shifts after passivation with electron withdrawing groups (EWGs), comparatively when Au TNPs functionalized with H-Ph-S-. (E) Figure summarize the $\Delta\lambda_{LSPR}$ changes upon passivation of Au TNPs with X-Ph-S- vs. refractive index of X-Ph-S- ligands.

As reported in the literature for Au nanostructures[24] and according to MO theory,[25] chemical attachment or adsorption of organic molecules creates new hybrid orbitals. We predict that in the case of X-Ph-S- ligands containing electron-donating groups (e.g., -NH_2, -CH_3, etc.) hybrid bonding (HOMO') and anti-bonding (LUMO') orbitals are formed when two empty orbitals interact considering Au has continuum of energetic states (**Figure 2.2A**)[25]. When illuminated with visible light during the UV-visible spectroscopic characterization, the LSPR active hot electrons are generated. There are two possibilities involving these electrons: (1) Wave functions of hot electrons could delocalize into empty HOMO', which reside below the Au Fermi level (E_F, -5.5 eV)[26]; (2) Hot electrons are being transferred to empty HOMO'. In our system, we believe that the electron wave functions are delocalizing because if the electrons are transferred from Au-to-HOMO' then excess positive charge (residual holes) will build up that can slowly destroy the TNPs and permanently change the LSPR properties because all the measurements were conducted in N_2 filled cuvette where no potential hole scavengers were available. Delocalization of electron wave functions decreases the overall N_e of Au TNPs that support the red shifting of the $\boldsymbol{\lambda}_{LSPR}$ position. In contrast, as shown in **Figure 2.2B**, an interaction between X-Ph-S- ligands (containing electron-withdrawing groups e.g., -NO_2, -CF_3, etc.) and Au is a four-electron and two-orbital system in which LUMO' rises above the Au Fermi energy. Extension of LUMO' electron functions up to the Au Fermi level stabilizes the system and increases the N_e of TNPs. This electronic process leads to blue shifting of the $\boldsymbol{\lambda}_{LSPR}$ position. We performed density functional theory (DFT) calculations of NH_2-Ph-S-Au. We used Au-thiolate *"staple"* structures [Au(X-Ph-S-)$_2$][27-29] in the DFT to calculate the MO energy levels to determine energies of HOMO' and LUMO' and found to be -5.850 and -3.158 eV, respectively. Similarly, DFT calculation provided HOMO' and LUMO' of NO_2-Ph-S-Au at -6.911 and -4.005 eV, respectively. Considering an 8 nm thick Au TNP is a plasmonic slab, then the distribution of plasmonic electron would be -5.5 (E_f) ± 2.22 eV; excited hole and electron energy levels are ~ -7.72 and -3.28 eV, respectively[26]. Under this calculation delocalization of photoexcited electrons (plasmonic electrons) wave function into the HOMO' orbital is thermodynamically favorable for NH_2-Ph-S- passivation (**Figure 2.2A**). Also, in order to stabilize the excited holes, delocalization of electrons wave function from LUMO' to Au would be energetically favorable for NO_2-Ph-S-Au system (**Figure2.2B**). Together, the slab theory and DFT calculations support the proposed MO diagram. Newly formed hybrid MOs contain the property of both metal and ligands. Supporting Information file contains further

information concerning DFT calculations. It is also important to mention that the formation of hybrid orbitals (HOMOs' and LUMOs') due to mixing of individual energy levels of Au and X-Ph-S-, one must consider that the metal-ligand interactions follow perturbation theory in which different ligand will interact differently with the metal. This interaction depends on the appropriate energy level alignment between the MOs of metal and ligand and their coupling constants. Therefore, better is the energy level alignment and higher is the coupling constant, the probability of the formation of larger number of hybrid MOs is also higher that allows facile delocalization of excitons wave functions. Together, this electronic process strongly modulates the LSPR properties of ligand-passivated Au TNPs.

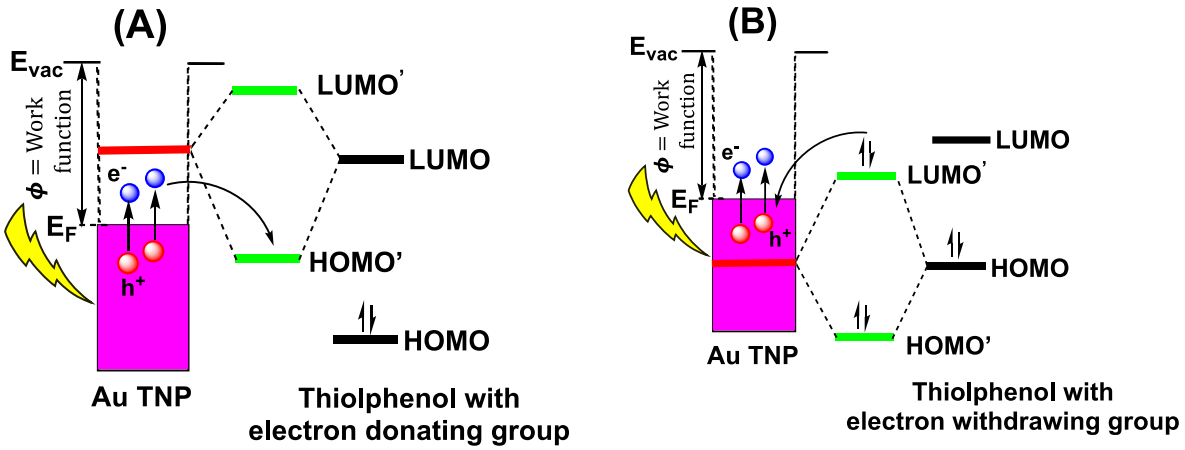

Figure 2.2. Proposed mechanism of exciton wave functions delocalization in the solid at the Au TNP and para-substituted, thiophenolate interface. (A) An electron wave function moves from Au to hybrid HOMO' reducing the overall electron density in the nanostructure. (B) An electron wave function moves from hybrid LUMO' to Au Fermi level. This process is similar to hole wave function delocalization.[30]

In order to support the proposed excitons wave function delocalization-controlled modulation of the LSPR properties of Au TNPs, we carefully examined UV-visible extinction spectra of all the X-Ph-S-passivated TNPs. **Figure 2.3A** illustrates the relationship between full-width at half maxima (FWHM) and various para-substitutions in which NH_2-Ph-S- and CF_3-Ph-S-passivated Au TNPs show an ~8 decrease and 23% increase of the FWHM of the extinction spectra, respectively, in comparison to the FWHM of extinction spectrum of H-Ph-S-passivated Au TNPs. Our experimental spectral linewidth data are in agreement with literature suggesting that an increase in N_e of a nanostructure leads to increase damping in the oscillation of the

conduction electrons[9, 31] This electronic phenomenon is responsible for the broadening of the LSPR spectrum[31]. As shown in **Figure 2.3B**, we calculated N_e of Au TNPs upon functionalization with X-Ph-S- utilizing **Equation 2.3 and 2.4**. Clearly NH_2-Ph-S- and CF_3-Ph-S-passivated Au TNPs show an ~6.2 decrease and 5.2% increase in N_e, respectively, as compared to the N_e of H-Ph-S-passivated Au TNPs. Importantly, an 8 nm thick Au TNP as a plasmonic slab is capable of generating ~10^5 hot electrons under illumination of incident light perpendicular to the TNP height[26]. Therefore, the change in electron density upon surface ligand passivation is in good agreement. We do not fully understand the reason underlying the relatively larger change in FWHM of the extinction spectrum of CF_3-Ph-S-passivated Au TNPs, which provides a smaller change in N_e compared to NH_2-Ph-S-passivated Au TNPs. Because one would expect that the higher the N_e change larger higher is the FWHM value.

$$\omega_{sp} = \sqrt{\frac{\omega_p^2}{1+2\varepsilon_m} - \gamma^2} \tag{2.3}$$

Here ω_{sp} is the plasmon frequency, ε_m is the dielectric constant of plasmonic materials. And the electrons of the metal oscillated due to the electromagnetic field and the motion of collision damped with a bulk collision frequency γ. As metals have free electrons in their conduction band, therefore for large frequencies in the visible and near visible region lead to a negligible damping frequency, and this approximation leads to the modification of Drude model where damping oscillator **Equation 2.3** and **Equation 2.4** can be rewritten as **Equation 2.4**. We obtained the ω_{sp} value for different X-Ph-S-passivated Au TNPs from the UV-visible extinction spectra (**Figure 2.1C**).

$$\omega_{sp} = \sqrt{\frac{\omega_p^2}{1+2\varepsilon_m}} \tag{2.4}$$

It is also important to note that in the N_e calculations, we considered $\Delta\boldsymbol{\lambda}_{LSPR}$ is induced only by nanostructures charging effects and not due to the changes in their local refractive index for individual X-Ph-S- ligands. Delineating individual components to fully quantify N_e, and refractive index effects on overall $\Delta\boldsymbol{\lambda}_{LSPR}$ value of Au TNPs upon surface modification with various X-Ph-

S- ligands require sophisticated theoretical calculations, which are beyond our expertise. We should also mention that the change in FWHM of metallic nanostructures due to charging and discharging is somewhat controversial. During the preparation of our manuscript, Lee et al.,[21] reported the chemical interface damping (CID) phenomenon – direct energetic electrons transfer from plasmonic metals to their surface-bound, strongly interacting passivating ligands that causes damping in a homogenous LSPR linewidth - in thiolate ligand-passivated gold bipyramids where the authors observed weak FWHM of ~20 and ~15 meV for NO_2-Ph-S- (electron withdrawing) and NH_2-Ph-S- (electron donating), respectively, that also opposite to the Drude model. The reported work, however, lacks proper ligand reference (e.g., H-Ph-S-) to fully rationalize the CID effect along with a very limited selection of X-Ph-S- ligands. Moreover, CID should induce excess positive charge ("hot-hole) accumulation within the occupied state of a noble metal and without the use of hole capturing species (i.e., solid-state optical measurements), accumulation of positive charges would eventually destroy metal-sulfur bond during prolong light exposure and long timescale of experimental measurements. Below we show that the $\boldsymbol{\lambda}_{LSPR}$ is fully reversible by exchanging NO_2-Ph-S- with NH_2-Ph-S- and vice versa, thus CID phenomenon is very unlikely occurred under our experimental conditions. Nevertheless, the experimental data presented herein is a simplified approximation of the Drude model, which suggests broadening of the spectral linewidth in metal nanostructures is expected to occur with an increasing N_e.

Finally, we experimentally measured the work function (ϕ) of X-Ph-S- ligand-passivated Au TNPs using the ultra-violet photoelectron spectroscopy (UPS) technique to further examine and support our excitons wave function delocalization mechanism. **Figure 2.3C** demonstrate the UPS spectra of Au when TNPs were functionalized with various X-Ph-S- ligands. Additional UV-photoelectron spectra are provided in Supporting Information. The secondary electron cutoff shifts gradually to lower binding energy with electron donating X-Ph-S- ligands with respect to H-Ph-S-, while an opposite trend is observed for X-Ph-S- ligands bearing electron withdrawing functional groups. We observe an increase in ϕ (Fermi level of Au moves towards more negative energy with respect to vacuum) value for NH_2-Ph-S-passivated Au TNPs that suggests decreasing N_e in TNPs, see **Figure 2.3D**. Parallelly, NO_2-Ph-S- provides a decreasing ϕ value of Au indicating an increase in N_e value. Ligand-induced changes in ϕ are reported in the literature for semiconductor PbS nanocrystals and planar metallic (Au and Ag) substrates by utilizing the UPS

technique,[32-34] but to our knowledge, first time we shown a large change in ϕ (1.9 eV) for plasmonic nanostructures because of the variation in their surface passivating ligands. Nevertheless, our UPS data are in agreement with the literature demonstrating changes in redox potential[35] of ultrasmall Au nanocrystals upon functionalization with X-Ph-S- ligands. Taken together, under our experimental conditions the changes in N_e support our proposed model (**Figure 2.2**) that X-Ph-S- with the capability of donating electrons to metal nanostructures can reduce the N_e and increase the ϕ of a plasmonic nanostructures under special circumstances.

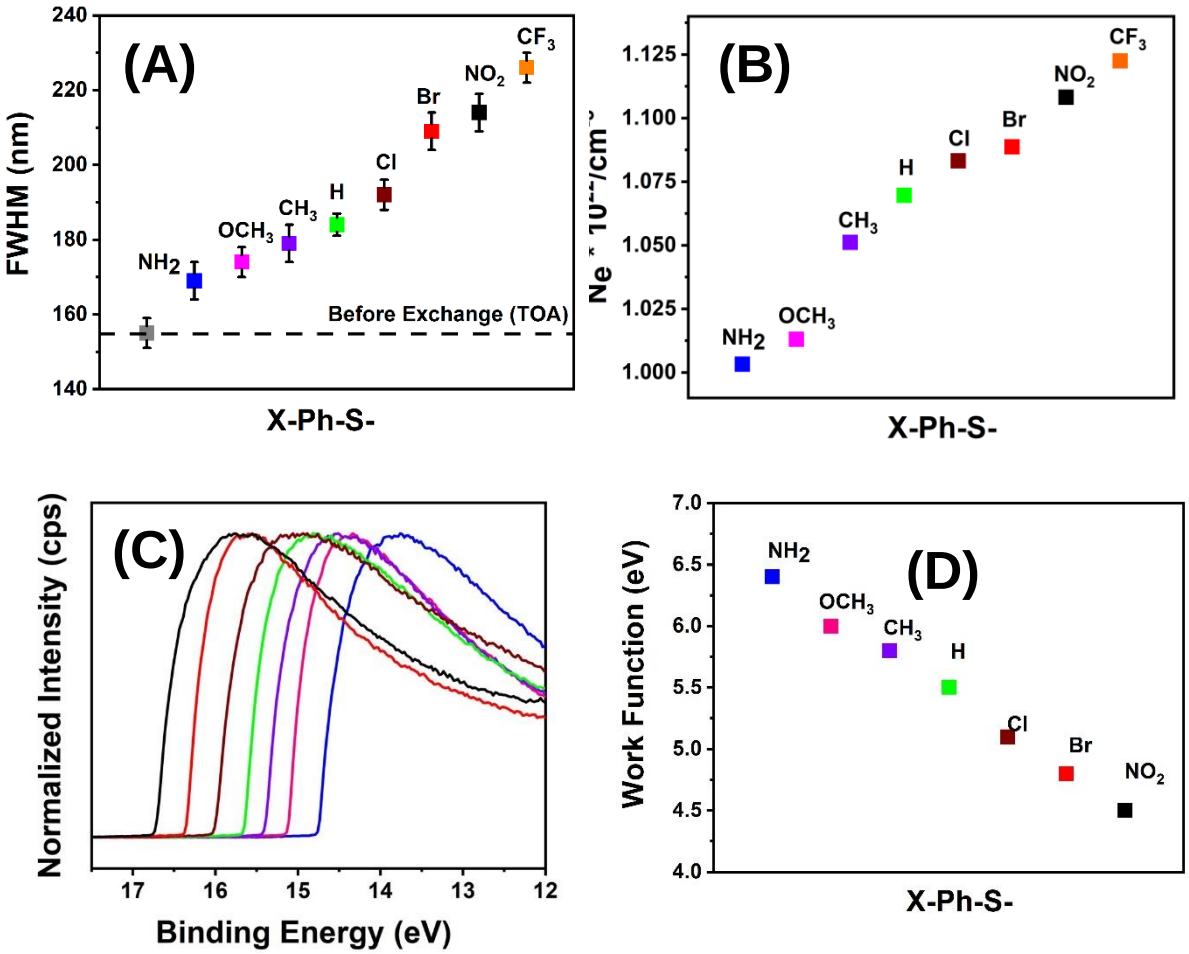

Figure 2.3. Quantification of ligand-controlled electronic parameters of Au TNPs. (A) Figure summarizes the full width half maxima of the LSPR peak upon passivation of Au TNPs with X-Ph-S- ligands vs. the refractive index of the X-Ph-SH ligands. (B) Figure summarizes the calculated N_e changes upon passivation of TNPs with X-Ph-S- ligands. As figure shows upon passivation with CF_3-Ph-S-, N_e increases to 5.2% and NH_2-Ph-S- passivation leads to decrease in N_e to 6.2% in comparison to the N_e of H-Ph-S-passivated Au TNPs. (C) Secondary electron cut-off region of UPS spectra used to determine the work function of X-Ph-S-passivated Au TNPs: -NH_2 (blue curve), -CH_3 (pink curve), OCH_3 (wine curve), -H (black curve), -Cl (purple curve), -Br (green curve), and -NO_2 (red curve). (D) Calculated ϕ of Au TNPs as a function of electronic properties of surface passivating ligands.

Figure 2.4A-C show the reversible tuning of the $\boldsymbol{\lambda}_{LSPR}$ and FWHM of Au TNPs upon passivation with different X-Ph-S- ligands. Exchanging H-Ph-S- by NH_2-Ph-S- provides a $\Delta\boldsymbol{\lambda}_{LSPR}$ of +26 nm (red-shift), and then a $\Delta\boldsymbol{\lambda}_{LSPR}$ of -40 nm (blue-shift) is observed when NH_2-Ph-S- was replaced by NO_2-Ph-S- from the surface of Au TNPs. Finally, a $\Delta\boldsymbol{\lambda}_{LSPR}$ of +14 nm (red-shift) is detected upon exchanging NO_2-Ph-S- by H-Ph-S-. The exchange reactions have been performed up to five cycles without detecting any noticeable differences in the overall $\Delta\boldsymbol{\lambda}_{LSPR}$ values. Fully reversible $\Delta\boldsymbol{\lambda}_{LSPR}$ shifts are also achieved by exchanging H-Ph-S- with NO_2-Ph-S- followed by NH_2-Ph-S-. Simultaneously, ligand exchange reactions produce reversible changes in the FWHM values, as shown in **Figure 2.4C**. the Drude model does not follow the trends in $\Delta\boldsymbol{\lambda}_{LSPR}$ and FWHM during reversible ligand exchange in our system. It is important to mention that we conducted SERS measurements during the exchange reaction to confirm the complete removal of bound ligands by exchange ligands by utilizing the strong EM-field enhancement property of our chemically synthesized Au TNPs. [36-39] As illustrated in **Figure 2.5A**, the SERS intensity of the C-S stretch at 1083 cm^{-1} is present in all the samples during the exchange reactions. Importantly, the intensity of C-S and aromatic C=C (1573 cm^{-1}) stretches are constant throughout the exchange (see **Figure 2.5B**). This is an expected result because exchanging H-Ph-S- by NH_2-Ph-S-, and then again attaching NO_2-Ph-S- by replacing NH_2-Ph-S- should not change the overall density of surface passivating ligands, and thus the number of C-S and aromatic C=C bonds, and thus the SERS intensities. Furthermore, we observe continuous disappearance of N-H stretch at 1390 cm^{-1} and appearance of N-O stretch at 1340 cm^{-1} when was NH_2-Ph-S- replaced from the surface of TNPs by NO_2-Ph-S-.We should mention that a 24h exchange reaction was sufficient to replace TNPs surface bound ligands with incoming ligands in order to achieve a stable $\boldsymbol{\lambda}_{LSPR}$ position and SERS intensity (see **Figure 2.5B**), however, we did not calculate the coverage through an adsorption isotherm. Although, reversible tuning of the $\boldsymbol{\lambda}_{LSPR}$ of metal nanostructures through applied electrochemical potential has been reported in the literature, to the best of our knowledge, for the first time this work demonstrates reversible modulation of the $\boldsymbol{\lambda}_{LSPR}$ of metal nanostructures in solid-state by controlling the electronic properties of organic ligands. Depending on the chemical nature of para-substitution, we hypothesize that the sequential ligand exchange with X-Ph-SH reestablishes HOMOs' and LUMOs' that allow electron or hole wave functions delocalization from Au TNPs to passivating ligands. Our ϕ calculations also support this hypothesis. The reversibility of tuning $\boldsymbol{\lambda}_{LSPR}$ also suggests that no charge transfer has taken place

between TNPs and X-Ph-S- because under such condition, Au TNPs would accumulate excess changes (electron or holes). Excess charge would potentially destroy TNPs, and thus the λ_{LSPR} position and FWHM should not be fully reversible for many cycles, as observed under our experimental conditions.

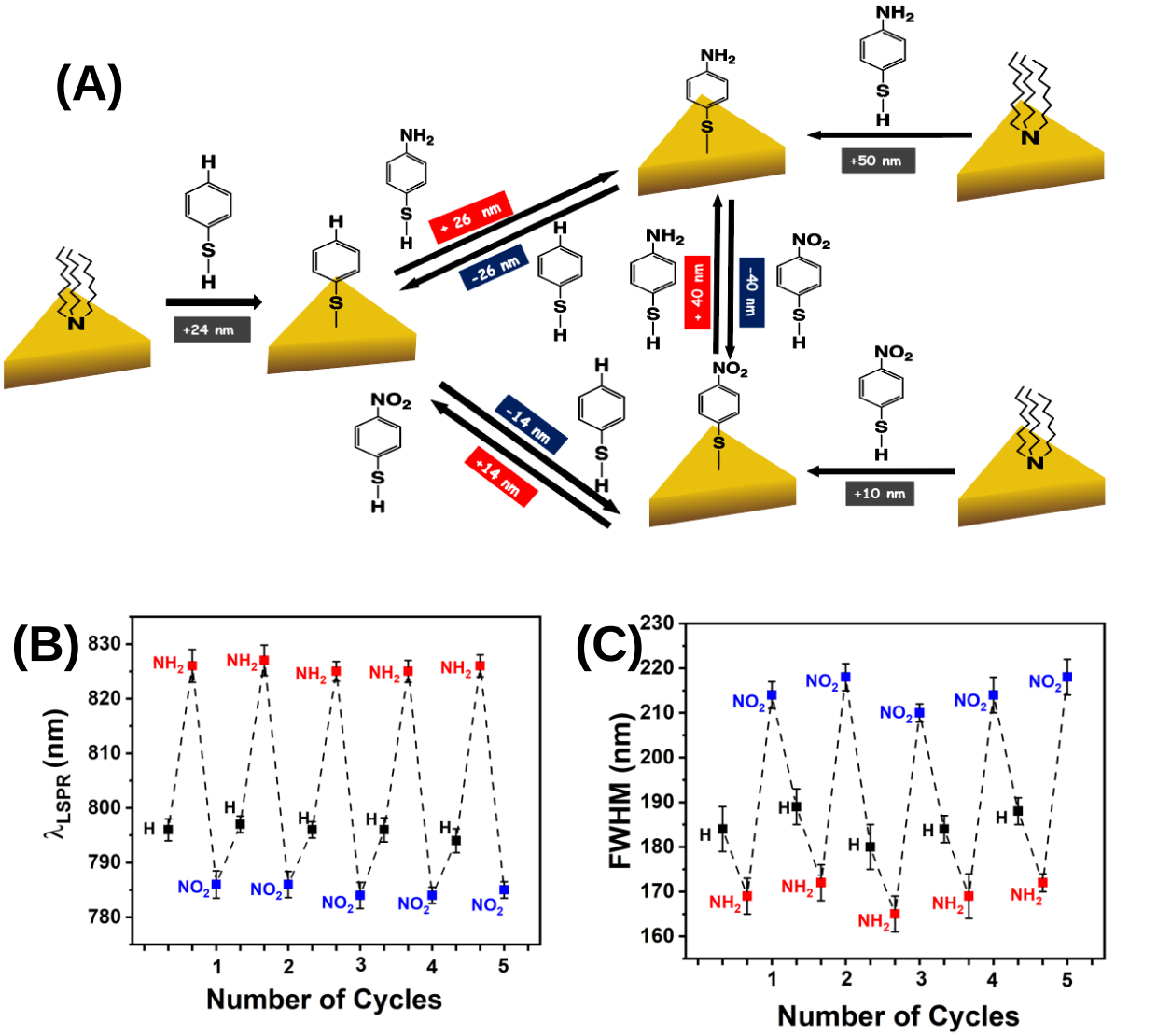

Figure 2.4. Ligand-controlled reversible modulation of LSPR properties of Au TNPs. (A) Schematic representation showing reversible ligand exchange reactions with various X-Ph-S- ligands. (B) Position of the λ_{LSPR} after passivating the surface of TNPs with H-Ph-S- (black squares, λ_{LSPR} = ~796 nm) and then H-Ph-S- was exchanged with NH_2-Ph-S- (red squares, λ_{LSPR} = ~828 nm), which was replaced by NO_2-Ph-S- (blue squares, λ_{LSPR} = ~782 nm). Representative UV-visible extinction spectra are provided in the supporting Information. Reversible tuning of λ_{LSPR} position is carried out for five successive cycles. (C) An average FWHM value of the dipole peak of Au TNPs during the sequential ligand exchange with three different-type of X-Ph-S- ligands.

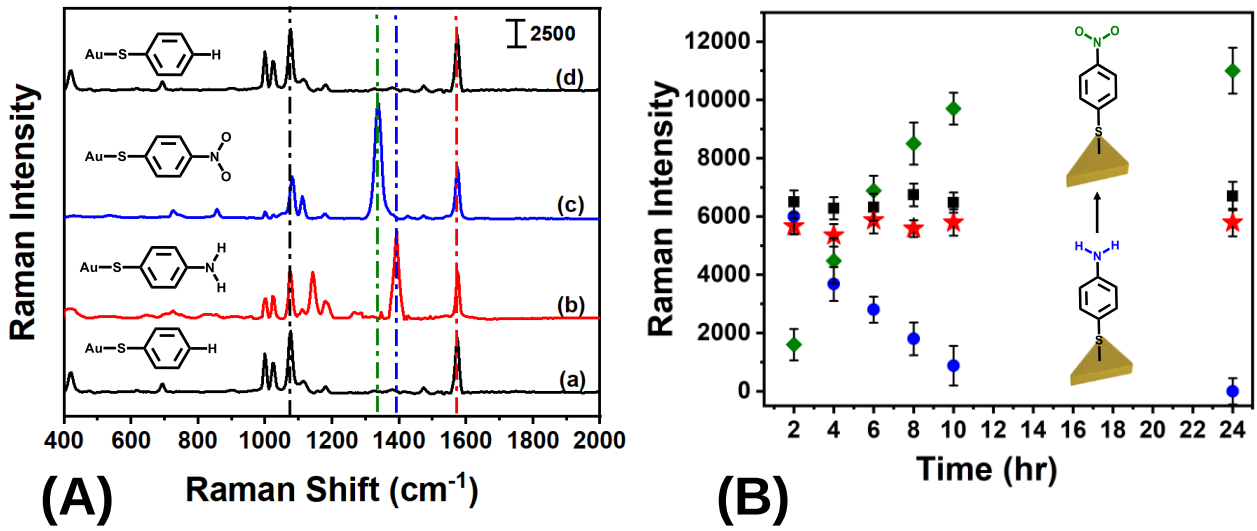

Figure 2.5. SERS-based Monitoring of Sequential Exchange Reactions of Au TNPs with X-Ph-S-Ligands. (A) SERS spectrum of H-Ph-S-passivated Au TNPs (a), after exchanging H-Ph-S- with NH_2-Ph-S- (b), which is again replaced by NO_2-Ph-S- (c), and then H-Ph-S-passivated Au TNPs were prepared by exchanging NO_2-Ph-S- with H-Ph-S-. Black, red, green, and blue dash lines represent C-S stretch at 1083 cm^{-1}, aromatic C=C stretch at 1573 cm^{-1}, N-O stretch at 1340 cm^{-},[1] and N-H stretch at 1390 cm^{-1}. (B) Time dependent SERS intensity of different stretches during 24 hr ligand exchange reactions at room temperature: C-S (black squares), aromatic C=C- (red stars), N-H (blue spheres), and N-O (green diamonds) stretches.

Finally, another possibility for the $\Delta\lambda_{LSPR}$ modulation of Au TNPs upon X-Ph-S- ligands passivation is the variable degree of ligand attachment in which higher is the number of bound ligands, larger is the $\Delta\lambda_{LSPR}$ value. One could argue that the ligand density (number of ligand/nm^2) on a TNP varies in the following order, NO_2-Ph-S- > H-Ph-S- > NH_2-Ph-S- that provides the highest and the lowest $\Delta\lambda_{LSPR}$ for NH_2-Ph-S- and NO_2-Ph-S-, respectively. To quantify the number of ligands attached to the TNP surface, we conducted ^{1}H NMR analysis using ferrocene as an internal standard (see **Figure 2.6A-C**) for three different thiophenolate-passivated Au TNPs, X-Ph-S- (X = -NH_2, -H, and –NO_2). Supporting Information provides detailed experimental procedure and quantification methods. Our results show nearly an identical surface coverage for all three X-Ph-S- (3.1-3.4 ligand/nm^2). This value is well consistent with the thiolated ligand grafting density on metal nanostructures. Taken together, unique structural characteristics of the Au TNP allow reversible modulation of the exciton wave functions and $\Delta\lambda_{LSPR}$ in which the energy level alignment between Au and ligands profoundly influences the magnitude of the N_e values.

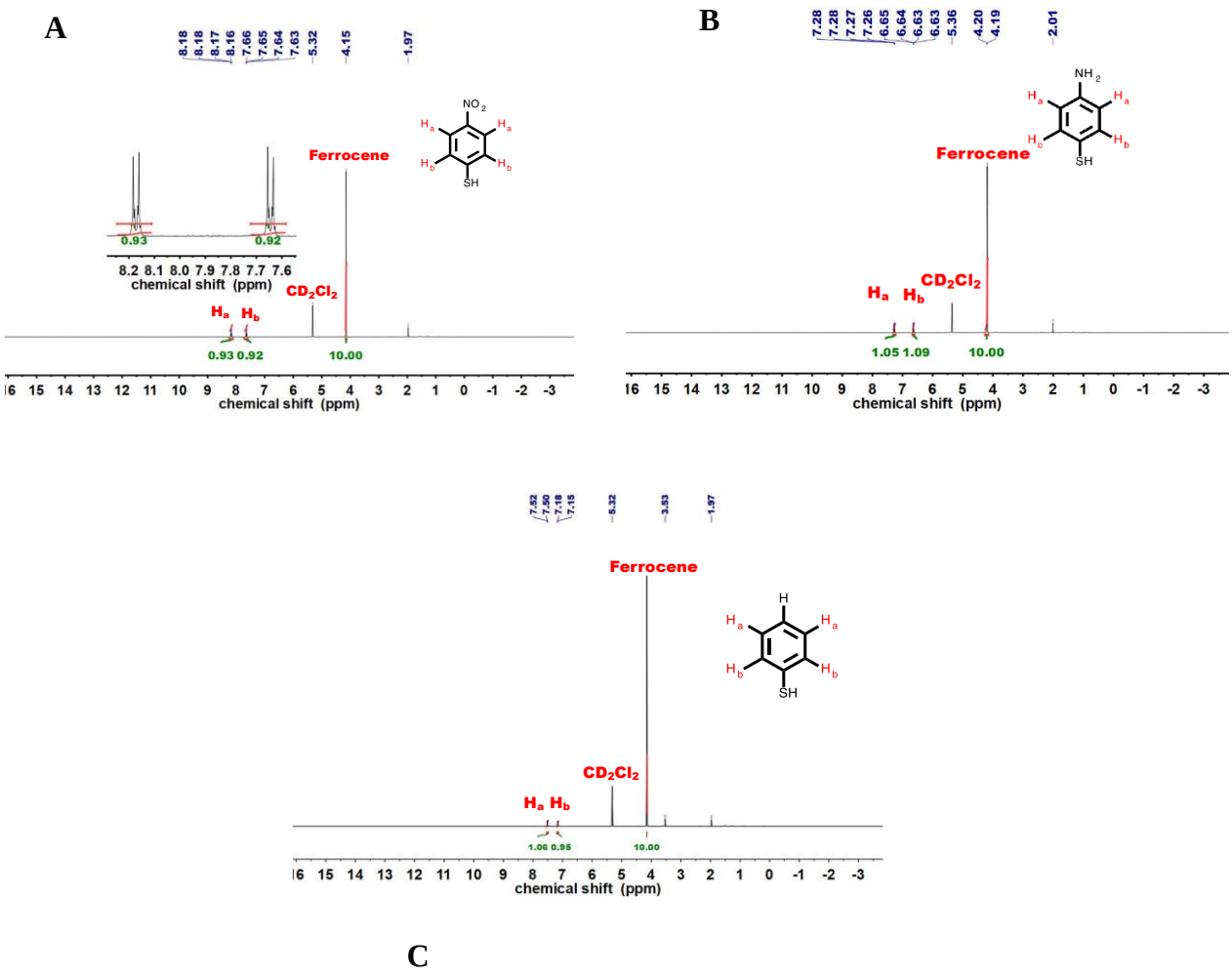

Figure 2.6. [1]H NMR spectrum of A) NO2-Ph-S- after detaching from Au TNPs using ligand exchange reactions. The inset shows the aromatic proton region B) NH2-Ph-S- after detaching from Au TNPs using ligand exchange reactions. C) of H-Ph-S- after detaching from Au TNPs using ligand exchange reactions.

In Summary, this work capitalizes on the previously unexplored nanostructure surface ligand system, which demonstrates reversible tuning (up to five cycles) of the plasmoelectric effect of metallic nanostructures. Our in-depth spectroscopic characterizations show that an ~12% of LSPR active N_e of Au TNPs can be modulated through passivating their surface with X-Ph-S- ligands with electron withdrawing and donating functional groups. The trends in observed LSPR shifts and spectra linewidth of TNPs upon functionalization with different X-Ph-S- ligands [electron donating group (-NH_2) provides an ~26 nm LSPR red-shift while electron withdrawing group (-NO_2) provides an ~14 nm blue-shift with respect to –H] are opposite to the Drude model.

We have developed orbital interaction diagrams in the solid-state to explain the LSPR properties of TNPs under our experimental conditions. We hypothesize that the energy level alignment between continuum of states of the Au TNP and HOMO/LUMO of X-Ph-S- produces hybrid MOs that participate in excitons wave function delocalization, which in return reversibly alters the LSPR properties (plasmoelectric effects). Therefore, we would expect that the degree of excitons wave function delocalization will vary if the strength of electron withdrawing or donating ability of the functional groups further increases. As a proof-of-concept, we investigated the plasmoelectric effect of Au TNPs by passivating their surface with a very strong electron donating group, 4-(dimethylamino) thiophenol (4-DMAT) and a very strong electron withdrawing group, 3,5-Bis(trifluoromethyl)benzenethiol (3,5-TFMBT). We observe a +36 nm $\boldsymbol{\lambda}_{\mathrm{LSPR}}$ red-shift and a -36 nm $\boldsymbol{\lambda}_{\mathrm{LSPR}}$ blue-shift for 4-DMAT and 3,5-TFMBT, respectively, in comparison to H-Ph-S-passivated TNPs (data not shown). We believe that these $\boldsymbol{\lambda}_{\mathrm{LSPR}}$ shifts and magnitude of the plasmoelectric effect resulting from excitons wave function delocalization are strongly controlled by electronic interactions between TNPs and surface passivating ligands. Nevertheless, the unique LSPR behavior of ligand-passivated Au TNPs could be due to their sharp tips and edges. The higher density of free electrons of TNPs potentially reduce effective energy barrier and facilitate the delocalization of exciton wave functions that together result in an unprecedentedly large change in their work functions. This is the first example in which LSPR, and UPS spectroscopy techniques have been used to monitor the plasmoelectric effect of metallic nanostructure. Taken together, controlling charge delocalization at the metal nanostructure-organic ligand (hybrid nanoconjugate) interface should lead to discovery of unique hybrid nanoplasmonic materials in which LSPR properties of metallic nanostructures can be tuned through programmable manipulation of charge injection/withdraw by surface ligand shells. The hybrid conjugates are capable of providing chemical versatility of organic ligands and shape dependency of LSPR properties of metal nanostructures that are expected to expedite the fabrication of hybrid nanoplasmonic devices and preparation of efficient photocatalysts.[11-15, 40]

2.5 References

1. Zhao, J.; Pinchuk, A. O.; McMahon, J. M.; Li, S.; Ausman, L. K.; Atkinson, A. L.; Schatz, G. C., Methods for Describing the Electromagnetic Properties of Silver and Gold Nanoparticles. *Accounts of Chemical Research* **2008,** *41* (12), 1710-1720.

2. Mie, G., Contributions to the Optics of Turbid Media, Especially Colloidal Metal Solutions. *Annalen der Physik (Weinheim, Germany)* **1908,** *25*, 377-445.
3. Halas, N. J.; Lal, S.; Chang, W.-S.; Link, S.; Nordlander, P., Plasmons in Strongly Coupled Metallic Nanostructures. *Chem. Rev.* **2011,** *111* (6), 3913-3961.
4. Mayer, K. M.; Hafner, J. H., Localized Surface Plasmon Resonance Sensors. *Chem. Rev.* **2011,** *111* (6), 3828-3857.
5. Dionne, J. A., Nanoplasmonics: Plasmons rock in metal bands. *Nat. Mater.* **2013,** *12* (5), 380-381.
6. Mulvaney, P., Surface Plasmon Spectroscopy of Nanosized Metal Particles. *Langmuir* **1996,** *12* (3), 788-800.
7. Warren, S. C.; Walker, D. A.; Grzybowski, B. A., Plasmoelectronics: Coupling Plasmonic Excitation with Electron Flow. *Langmuir* **2012,** *28* (24), 9093-9102.
8. Sheldon, M. T.; van de Groep, J.; Brown, A. M.; Polman, A.; Atwater, H. A., Plasmoelectric potentials in metal nanostructures. *Science (Washington, DC, United States)* **2014,** *346* (6211), 828-831.
9. Hoener, B. S.; Zhang, H.; Heiderscheit, T. S.; Kirchner, S. R.; De Silva Indrasekara, A. S.; Baiyasi, R.; Cai, Y.; Nordlander, P.; Link, S.; Landes, C. F.; Chang, W.-S., Spectral Response of Plasmonic Gold Nanoparticles to Capacitive Charging: Morphology Effects. *Journal of Physical Chemistry Letters* **2017,** *8* (12), 2681-2688.
10. Navarrete, J.; Siefe, C.; Alcantar, S.; Belt, M.; Stucky, G. D.; Moskovits, M., Merely Measuring the UV-Visible Spectrum of Gold Nanoparticles Can Change Their Charge State. *Nano Letters* **2018,** *18* (2), 669-674.
11. Ueno, K.; Oshikiri, T.; Sun, Q.; Shi, X.; Misawa, H., Solid-State Plasmonic Solar Cells. *Chem. Rev.* **2018,** *118* (6), 2955-2993.
12. Atwater, H. A.; Polman, A., Plasmonics for improved photovoltaic devices. *Nat. Mater.* **2010,** *9* (3), 205-213.
13. Pastoriza-Santos, I.; Kinnear, C.; Pérez-Juste, J.; Mulvaney, P.; Liz-Marzán, L. M., Plasmonic polymer nanocomposites. *Nat. Rev. Mater.* **2018,** *3* (10), 375-391.
14. Linic, S.; Christopher, P.; Ingram, D. B., Plasmonic-metal nanostructures for efficient conversion of solar to chemical energy. *Nat. Mater.* **2011,** *10* (12), 911-921.

15. Zhou, L.; Swearer, D. F.; Zhang, C.; Robatjazi, H.; Zhao, H.; Henderson, L.; Dong, L.; Christopher, P.; Carter, E. A.; Nordlander, P.; Halas, N. J., Quantifying hot carrier and thermal contributions in plasmonic photocatalysis. *Science* **2018,** *362* (6410), 69-72.
16. Wu, K.; Chen, J.; McBride, J. R.; Lian, T., Efficient hot-electron transfer by a plasmon-induced interfacial charge-transfer transition. *Science* **2015,** *349* (6248), 632.
17. Stetsenko, M. O.; Rudenko, S. P.; Maksimenko, L. S.; Serdega, B. K.; Pluchery, O.; Snegir, S. V., Optical Properties of Gold Nanoparticle Assemblies on a Glass Surface. *Nanoscale Research Letters* **2017,** *12* (1), 1-10.
18. Joshi, G. K.; Deitz-McElyea, S.; Liyanage, T.; Lawrence, K.; Mali, S.; Sardar, R.; Korc, M., Label-Free Nanoplasmonic-Based Short Noncoding RNA Sensing at Attomolar Concentrations Allows for Quantitative and Highly Specific Assay of MicroRNA-10b in Biological Fluids and Circulating Exosomes. *ACS Nano* **2015,** *9*, 11075-11089.
19. Joshi, G. K.; McClory, P. J.; Dolai, S.; Sardar, R., Improved localized surface plasmon resonance biosensing sensitivity based on chemically-synthesized gold nanoprisms as plasmonic transducers. *J. Mater. Chem.* **2012,** *22* (3), 923-931.
20. Joshi, G. K.; Blodgett, K. N.; Muhoberac, B. B.; Johnson, M. A.; Smith, K. A.; Sardar, R., Ultrasensitive Photoreversible Molecular Sensors of Azobenzene-Functionalized Plasmonic Nanoantennas. *Nano Letters* **2014,** *14* (2), 532-540.
21. Lee, S. Y.; Tsalu, P. V.; Kim, G. W.; Seo, M. J.; Hong, J. W.; Ha, J. W., Tuning chemical interface damping: Interfacial electronic effects of adsorbate molecules and sharp tips of single gold bipyramids. *Nano Letters* **2019,** *19* (4), 2568-2574.
22. Liyanage, T.; Masterson, A. N.; Oyem, H. H.; Kaimakliotis, H.; Nguyen, H.; Sardar, R., Plasmoelectronic-Based Ultrasensitive Assay of Tumor Suppressor microRNAs Directly in Patient Plasma: Design of Highly Specific Early Cancer Diagnostic Technology. *Anal. Chem.* **2019,** *91* (3), 1894-1903.
23. Joshi, G. K.; Deitz-McElyea, S.; Johnson, M.; Mali, S.; Korc, M.; Sardar, R., Highly Specific Plasmonic Biosensors for Ultrasensitive MicroRNA Detection in Plasma from Pancreatic Cancer Patients. *Nano Letters* **2014,** *14* (12), 6955-6963.
24. Yu, S.; Wilson, A. J.; Heo, J.; Jain, P. K., Plasmonic Control of Multi-Electron Transfer and C–C Coupling in Visible-Light-Driven CO2 Reduction on Au Nanoparticles. *Nano Letters* **2018,** *18* (4), 2189-2194.

25. Hoffmann, R., A chemical and theoretical way to look at bonding on surfaces. *Reviews of Modern Physics* **1988,** *60* (3), 601-28.
26. Govorov, A. O.; Zhang, H.; Demir, H. V.; Gun'ko, Y. K., Photogeneration of hot plasmonic electrons with metal nanocrystals: Quantum description and potential applications. *Nano Today* **2014,** *9* (1), 85-101.
27. Zhu, M.; Aikens, C. M.; Hollander, F. J.; Schatz, G. C.; Jin, R., Correlating the Crystal Structure of A Thiol-Protected Au25 Cluster and Optical Properties. *J. Am. Chem. Soc.* **2008,** *130* (18), 5883-5885.
28. Sardar, R.; Funston, A. M.; Mulvaney, P.; Murray, R. W., Gold Nanoparticles: Past, Present, and Future‚Ä†. *Langmuir* **2009,** *25* (24), 13840-13851.
29. Jadzinsky, P. D.; Calero, G.; Ackerson, C. J.; Bushnell, D. A.; Kornberg, R. D., Structure of a Thiol Monolayer-Protected Gold Nanoparticle at 1.1 Å Resolution. *Science* **2007,** *318* (5849), 430-433.
30. Teunis, M. B.; Nagaraju, M.; Dutta, P.; Pu, J.; Muhoberac, B. B.; Sardar, R.; Agarwal, M., Elucidating the role of surface passivating ligand structural parameters in hole wave function delocalization in semiconductor cluster molecules. *Nanoscale* **2017,** *9* (37), 14127-14138.
31. Foerster, B.; Joplin, A.; Kaefer, K.; Celiksoy, S.; Link, S.; Sönnichsen, C., Chemical Interface Damping Depends on Electrons Reaching the Surface. *ACS Nano* **2017,** *11* (3), 2886-2893.
32. Brown, P. R.; Kim, D.; Lunt, R. R.; Zhao, N.; Bawendi, M. G.; Grossman, J. C.; Bulović, V., Energy Level Modification in Lead Sulfide Quantum Dot Thin Films through Ligand Exchange. *ACS Nano* **2014,** *8* (6), 5863-5872.
33. Alloway, D. M.; Graham, A. L.; Yang, X.; Mudalige, A.; Colorado, R.; Wysocki, V. H.; Pemberton, J. E.; Lee, T. R.; Wysocki, R. J.; Armstrong, N. R., Tuning the Effective Work Function of Gold and Silver Using ω-Functionalized Alkanethiols: Varying Surface Composition through Dilution and Choice of Terminal Groups. *Journal of Physical Chemistry C* **2009,** *113* (47), 20328-20334.

34. Kroupa, D. M.; Voros, M.; Brawand, N. P.; McNichols, B. W.; Miller, E. M.; Gu, J.; Nozik, A. J.; Sellinger, A.; Galli, G.; Beard, M. C., Tuning colloidal quantum dot band edge positions through solution-phase surface chemistry modification. *Nature Communications* **2017,** *8*, 15257.
35. Guo, R.; Murray, R. W., Substituent Effects on Redox Potentials and Optical Gap Energies of Molecule-like Au38(SPhX)24 Nanoparticles. *J. Am. Chem. Soc.* **2005,** *127* (34), 12140-12143.
36. Scarabelli, L.; Coronado-Puchau, M.; Giner-Casares, J. J.; Langer, J.; Liz-Marzán, L. M., Monodisperse Gold Nanotriangles: Size Control, Large-Scale Self-Assembly, and Performance in Surface-Enhanced Raman Scattering. *ACS Nano* **2014,** *8* (6), 5833-5842.
37. Liyanage, T.; Rael, A.; Shaffer, S.; Zaidi, S.; Goodpaster, J. V.; Sardar, R., Fabrication of a self-assembled and flexible SERS nanosensor for explosive detection at parts-per-quadrillion levels from fingerprints. *Analyst* **2018,** *143* (9), 2012-2022.
38. Joshi, G. K.; White, S. L.; Johnson, M. A.; Sardar, R.; Jain, P. K., Ultrashort, Angstrom-Scale Decay of Surface-Enhanced Raman Scattering at Hot Spots. *Journal of Physical Chemistry C* **2016,** *120* (43), 24973-24981.
39. Kim, J.; Song, X.; Ji, F.; Luo, B.; Ice, N. F.; Liu, Q.; Zhang, Q.; Chen, Q., Polymorphic Assembly from Beveled Gold Triangular Nanoprisms. *Nano Letters* **2017,** *17* (5), 3270-3275.
40. Knight, M. W.; Sobhani, H.; Nordlander, P.; Halas, N. J., Photodetection with Active Optical Antennas. *Science* **2011,** *332* (6030), 702-704.

CHAPTER 3. FABRICATION OF SELF-ASSEMBLED AND FLEXIBLE SERS NANOSENSORS FOR EXPLOSIVE DETECTION IN FINGERPRINTS AT PARTS-PER-QUADRILLION LEVELS

This article has been reprinted with permission. Liyanage, T.; Rael, A.; Shaffer, S.; Zaidi, S.; Goodpaster John, V.; Sardar, R., Fabrication of a self-assembled and flexible SERS nanosensor for explosive detection at parts-per-quadrillion levels from fingerprints. The Analyst 2018, 143 (9), 2012-2022. DOI:10.1039/C8AN00008E

3.1 Synopsis

Apart from high sensitivity and selectivity of surface-enhanced Raman scattering (SERS)-based trace explosive detection, efficient sampling of explosive residue from real world surfaces is very important for homeland security applications. Herein, we demonstrate an entirely new SERS nanosensors fabrication approach. The SERS nanosensors were prepared by self-assembling chemically synthesized gold triangular nanoprisms (Au TNPs), which display strong electromagnetic field enhancements at the sharp tips and edges, onto a pressure-sensitive flexible adhesive film. Our SERS nanosensors provide excellent SERS activity (enhancement factor = ~6.0 x 10^6) and limit of detection (as low as 56 parts-per-quadrillions) with high selectivity by chemometric analyses among three commonly used explosives (TNT, RDX, and PETN). Furthermore, the SERS nanosensors present outstanding reproducibility (<4.0% relative standard deviation) and unprecedentedly high stability with shelf life of at least 5 months. Finally, TNT and RDX were analyzed and quantified by transferring solid explosive residues from fingerprints left on solid surfaces to the SERS nanosensors. Taken together, the demonstrated sensitivity, selectivity, and reliability of the measurements together with the excellent shelf life of our SERS nanosensors obviate the need for complicated sample processing steps required for other analytical techniques, and thus these nanosensors will find tremendous potential not only in the field of measurement science but also for homeland security applications to combat acts of terror and military threats.

3.2 Introduction

Today, terrorism has become a high-tech game of cat and mouse, making it imperative to detect trace amounts of explosives that can be identified to prevent terrorist attacks[1, 2]. Therefore, devising

a detection method that can be performed on-the-spot, which is automated and highly sensitive, accurate, reliable, and reproducible, is more important now than at any time. Most of the current existing methods for explosive detection have been involving with liquid-liquid extraction[3-6] or swabbing[7-9] methods. However, the efficiency of sample collecting is one of the biggest challenges due to the law vapor pressure of explosives.

In our reported technique, we used self-assembled chemically synthesized gold triangular nanoprisms (Au TNPs) onto the adhesive flexible support which has provided convenient sampling efficiency for surface-enhanced Raman scattering/spectroscopy (SERS) based label free explosive detection. We have been able to detect three different explosives (TNT, RDX, and PETN) using developed nanosensor with the parts-per-quadrillion (ppq) levels sensitivity. Additionally, our detection has shown the 100% classification accuracy which determined using the chemometric analyses. Further our developed nanosensor has shown unprecedented stability over 5 moths even under normal laboratory condition and we believe it's due to the unreactive nature of adhesive films. This high stability of the developed sensor has provided the opportunity to advance as an effective SERS substrate.

SERS is a potent technique in analytical chemistry which open up a new window for the trace-level detection[7-9]. Raman spectroscopy provides molecular fingerprints due to unique vibrations of the target analyte[10]. However, Raman signals are weak and therefore using them for ultra-level detection is challenging. The Raman signal can be amplified when a metalic nanostructure come closer to the molecule and that process is identified as SERS[11]. Additionally, SERS also helps avoid strong fluorescence background noise[11, 12]. There are two main mechanism involve in the SERS, named as electromagnetic (EM) filed enhancement and chemical enhancement (CE)[10]. However, EM occurs due to localized surface plasmon resonance (LSPR) properties of the nanostructure Here, as explained chapter 1 EM field enhancement occur due to the collective oscillation of conduction electrons, which resulted as their resonance frequency matches that of the incident photons[13-15]. and EM provides the main contribution for the SERS enhancement mechanism over CM. Moreover, EM mainly depends on two aspects: noble-metal structures and orientation on to the surface[16]. As discussed in chapter 1 the LSPR property of metalic nanostructure is mainly control the EM field enhancement and the size, shape and the distance of the metalic nanostcurures is directly influence for the EM field enhancement due to the "hot spots" creates around the nanostructure. Enhancement factor (EF) is mainly involve determining the

SERS efficiency[16-19]. EF can be calculated by using **Equation 3.1**[20]. Accordingly, here we compare the Raman signal amplification by considering the Raman and SERS signal for the (I_{SERS}, I_{RAMAN}) concentration. N_{BULK} and N_{SERS} represents the number of molecules in Raman and SERS respectively, the less sensitive substrates show the SERS peaks around the range of ~10-10^3 and typical range for the SERS substrates lies in the range of ~10^5-10^6 range. When nanostructures consist with large number of hotspots that creates very prominent EM field enhancement which is resulted as a highly efficient SERS substrate.

$$EF = \left(\frac{I_{SERS}}{I_{BULK}}\right)\left(\frac{N_{BULK}}{N_{SERS}}\right) \quad \textbf{(3.1)}$$

Overall SERS draws the attention of a trace-level detection of explosives, due to their ability to miniaturize in a microsystem and their ability to perform an automated analysis over other available techniques, such as mass spectrometry[21], electrochemistry[22], and fluorescence-based sensors[23-27].

Au spherical particles/ Au nanorods were most frequently used SERS substrates for the explosive detection platforms. However, for this reported work we have been utilized the chemically-synthesized Au TNPs for the explosive detection SERS platform, mainly due to the very strong EM-field enhancement at their sharp tips[28-34]. Furthermore. Ag nanostructures reported as the highest SERS sensitive substrate which used in very efficient explosive detection[35, 36]. However, due to the less stability of Ag nanostructures it subjected to easy decomposition process which caused the false positive and negative response of the senor. On the other hand, Au is very stable even in very harsh conditions and it has shown very negligible photobleaching/photodecomposition process when expose to the laser light[37, 38]. Additionally, due to the high efficiency of Au and nitrogen atom, which is commonly available element in almost explosives, Au is an ideal material for SERS applications[39-41]. Interestingly, in this reported work we have experimentally shown the SERS EF of an ~6.0 x 10^6 for our Au TNP-based flexible SERS nanosensors.

On the other hand, the efficiency of collecting samples still needs to be addressed, as most of the explosives have very low vapor pressure and it is important to have the ability to collect very small samples efficiently[42, 43]. Lately, people have utilized flexible, soft substrates to overcome this issue. For instance, the literature has demonstrated that a paper-based SERS swab[20,

[44], based on AU nanorods decorated filter papers as SERS substrate has allowed conformal contact with real-world samples. However, this method still fails to address the required sampling efficiency and it is involved with organic solvents. Adhesive tape has been utilized in various research applications and has recently been used as a support for the SERS substrate[45, 46]. Accordingly, various research applications have successfully exploited the flexible nature and sticky features of adhesive tape for efficient and effective pesticide extraction, hence, SERS-based detection. However, this reported method has involved the drop-cast technique for nanoparticle decoration onto the substrate, which leads to having nanoparticles aggregation onto the support. Therefore, the reproducibility of data is doubtful. To conquer the current challenges, we have utilized novel approach of assembling Au TNPs onto a flexible adhesive as illustrated in **Figure 3.1**, Accordingly, a programmable "stamping" technique was executing to prepare label-free SERS "nanosensors". Due to high sampling efficiency the newly develop substrate creates direct contact in-between target analyte and the Au TNPs. As a result, we were able to achieve highest sensitivity for TNT, RDX, and PETN which has shown as ~900, 50, and 50 ppq sensitivity respectively.

This developed ultra-sensitive SERS substrate has shown at least 10^3-fold better than other previously reported SERS-based explosive detection methods and 10^6-fold more sensitive than commonly available explosive detection techniques such as gas chromatography-mass spectrometry (GC-MS).

As a proof concept, the developed sensor used to detect explosives in fingerprint samples which provides the simulate real-world applications for homeland security applications. Taken together, our highly sensitive selective and highly reproducible, flexible SERS substrate will have a great effect on efficient and accurate explosive detection applications and hence will enhance the quality of human life by reducing the public safety threats.

3.3 Materials and Method

3.3.1 Chemicals

Chloro(triethylphosphine) gold (I) (Et_3PAuCl, 97%), poly(methylhydrosiloxane) (PMHS, M_n = 1700-3300), trioctylamine (TOA, 98%), ACS grade acetonitrile (CH_3CN, 99.9%), methanol (99.8%), (3-aminopropyl)-triethoxysilane, APTES, 94%) were purchased from Sigma-Aldrich, and ethanol (alcohol 190 proof) was from Decon laboratories. Glass coverslips (Cat. No. 12548C)

were purchased from Fisher Scientific. RBS35 Detergent was obtained from Thermo Scientific and used as received. A Thermo Scientific Barnstead Nanopure system was utilized to achieve water Purity at 18.2 MΩ-cm and the same nanopure water was used for all cleaning process. Separate explosive solutions of pentaerythritol tetranitrate (PETN), cyclotrimethylenetrinitramine (RDX) 2,4,6 trinitrotoluene (TNT), 2,4-dinitrotoluene (DNT), and trinitrobenzene (TNB) were purchased from RETSEK Chromatography Products and Solutions. Scotch magic-tape (Cat. No. 810) was purchased from 3M corporation.

3.3.2 SERS Measurements

SERS analysis was performed using a Foster + Freman Foram 785 HP Raman system with a 785 nm diode laser excitation source with 20 mW of power and 5-µm spot size. The SERS data were acquired for nanosensors with 10 scans (1 x 20 mW, 9 x 80 mW) from 400-2000 cm^{-1}, 16 sec acquisition time and with a 5-µM laser spot diameter. Automatic baseline correction was performed in OMNIC software before acquired spectra were plotted.

3.3.3 Spectroscopy and Microscopy Characterization

A Varian Cary 50 Scan UV-visible spectrophotometer was used to collect absorption and extinction spectra in the range of 300 - 1100 nm. Absorption spectra of Au TNP solutions were obtained by diluting 0.3 mL of reaction solution to a final volume of 2.0 mL with acetonitrile in a 1 cm quartz cuvette. Acetonitrile was used as a background in each run before collecting the absorbance spectra. Background subtracted (using 3M adhesive tape) extinction spectra of our SERS nanosensors were measured in air (pH 7.4) at room temperature. Scanning electron (SEM) and Transmission electron (TEM) microscopy techniques were used to determine the average edge-length of gold nanoprisms used in our SERS nanosensor fabrication.

3.3.4 Silanization of Glass Coverslips

Glass coverslips were functionalized based the same procedure on chapter 2.3.3

3.3.5 Synthesis of Gold Triangular Nanoprisms (Au TNPs)

Gold triangular nanoprisms (Au TNPs) were synthesized according same method on Chapter 2.3.4.

3.3.6 Preparation of SERS Nanosensors and Explosive Detection

The preparation of our flexible and adhesive SERS nanosensor is described in **Figure 3.1**. Au TNPs with ~42 nm edge lengths were synthesized according to our literature procedure[28-32]. Au TNPs in acetonitrile were immobilized onto a APTES-functionalized glass substrate through incubation to form a self-assembled layer of TNPs (A), which avoided unwanted Au TNP aggregation. The Au TNP-bound coverslips were washed thoroughly with acetone to remove loosely adsorbed organic compounds (PMHS and TOA) and dried under nitrogen flow. 3M adhesive tape was placed on the Au TNP-containing glass substrate, pressed gently with the thumb, and removed at a 90^0 angle (B). This procedure resulted in successful transfer of the self-assembled Au TNPs from the glass to a flexible adhesive substrate by stamping, producing the nanosensor (C). We selected the 3M adhesive tape for SERS nanosensor fabrication because has a less "sticky" nature that should extract a solid residue from the contaminated surface, whereas "stickier" adhesive would be expected to destroy the sample. The explosive detection and quantification were performed via two different methods. Firstly, each explosive solution in methanol was separately drop-casted on the SERS nanosensor, followed by slow evaporation of solvent at room temperature (D). Secondly, our adhesive nanosensor was directly placed onto glass coverslips containing explosive molecules as thumb impressions and these were directly transferred onto the surface of Au TNPs (E). In both cases, the explosives molecules were physorbed onto the Au TNPs surface through Ag-N interactions (F). SERS spectra were collected using a bench-top Raman spectrometer (G). The EFs and limit of detections (LODs) were determined using literature procedures, which are described in the Supporting Information.

Simulation of Extinction Spectrum and Electromagnetic Field Calculations. Discreet Dipole Approximation (DDA) (DDASCAT+ tool5, DDSCAT 7.36) was used as previously described to calculate the extinction spectra (600-1000 nm, circularly polarized simulating unpolarized) and electromagnetic field (785 nm, linear polarized) for an Au TNP (8 nm thickness, 42 nm edge length. The dielectric constant was from Johnson and Christy8) with an ambient medium

representative of the ligand environment (TOA, n = 1.4485). Enhancement Factor Calculations. We followed the literature procedure9 to determine the EF of our Au TNP-containing flexible adhesive SERS substrate at the 1380 cm-1 Raman peak (C-N stretch), using Eq. 1. With a 5 μM diameter laser spot and a TNT molecule footprint of 0.25 nm^2, N_{Bulk} was determined to be 7.9 x 107. From the SEM analysis, we estimated that ~4% of the 3M tape surface was covered with ~42 nm edge length Au TNPs. Considering Au TNPs are equilateral triangles and a monolayer of TNT molecules was present on the surface of Au TNPs, N_{SERS} was calculated to be 2.9 x 105.

3.3.7 Limit of Detection (LOD) Calculations

We used a sophisticated mathematical equation (Eq.2) for limit of detection (LOD) calculations. For LOD determination a 1.0 millimolar (mM) stock solution of explosive in methanol was prepared and then various concentrations up to 100
femtomolar (fM) with 10-fold concentration changes were obtained through serial dilutions.

$$LOD_B = \bar{Y}_b + t_\alpha^{n-1} s_b^{n-1} \sqrt{\frac{1+1}{n}} \quad \textbf{(2)}$$

$$\bar{Y}_b = Average\ blank\ signal\ value$$

$$t_\alpha^{n-1} = critical\ value\ of\ the\ distribtion$$

$$s_b^{n-1} = standered\ devaition$$

$$\sqrt{\frac{1+1}{n}} = Replacement\ of\ the\ true\ mean\ by\ \bar{Y}_b, n = 3\ number\ of\ blank\ spectrum$$

3.3.8 Chemometric Analysis

The SERS spectra were automatically baseline corrected by the Foster and Freeman FORAM FireWire instrument software at the time of collection. Some incomplete baseline correction of nM and μM concentrations of TNT and PETN occurred and the correction was completed in Origin. The baseline corrected spectra were subsequently normalized using the square root of the sum of squares or 2-norm11. Multivariate calibration curves from 100 fM to 100 μM were obtained with Partial Least Squares (PLS) using the baseline corrected spectra and the log of the

concentration using in JMP 13 with the NIPALS method and Leave-One-Out validation. Principal Components Analysis (PCA) on the sample covariance matrix and Discriminant Analysis (DA) on the PCs were conducted using the normalized spectra and JMP 13. PCA used the Row-Wise method. DA for single concentrations used the linear method with 3 PCs for the quadripartite analysis (PETN, RDX, TNT, blank; n=24). and 2 PCs for tripartite analysis (TNT, TNB, DNB; n=18). DA for the full concentration ranged from 100 fM to 100 μM using the Quadratic method (4 PCs for pairwise of either RDX or TNT with PETN, n=120; 8 PCs for pairwise of RDX and TNT, n=120; and 8 PCs for tripartite, n=180).

3.4 Results and Discussion

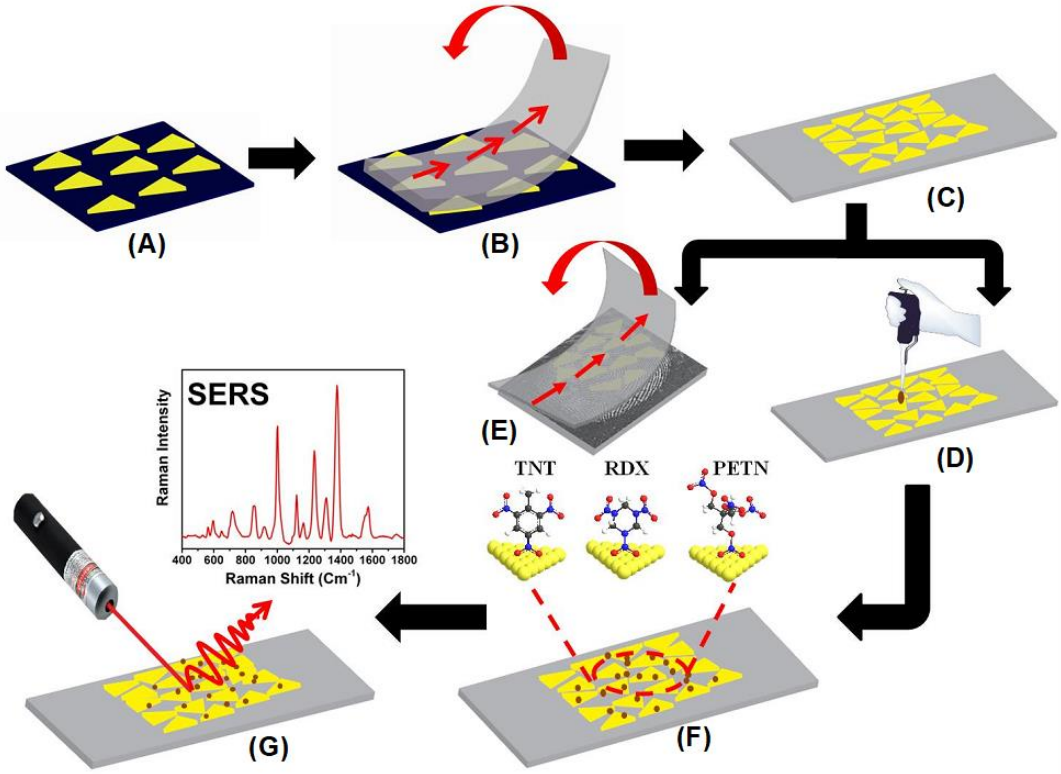

Figure 3.1. Design of Au TNP-based SERS nanosensor for detection of trace explosives. (A) a self-assembled layer of Au TNPs onto an APTES functionalized glass coverslip were prepared. (B) Au TNPs were transferred to a flexible adhesive substrate by the stamping technique, which produced a SERS nanosensor (C). Explosive molecules either drop-casted from a solution (D) or transferred from a thumb impression (E) directly onto the SERS nano-sensor (F). (G) SERS spectra were collected using benchtop Raman spectrometer at a 785 nm diode laser excitation. The fabrication approach of SERS nanosensor is a schematic representation; none of the figures present an exact number and/or density of Au TNPs in each step. The image is not to scale.

3.4.1 Microscopy and Spectroscopy Characterizations of SERS Nanosensors and Their Explosive Detection Ability

To construct the self-assembled SERS nanosensors, we selected the NH_2-surface terminal group to bind to Au TNP because it forms relative weak electrostatic interactions with metal nanostructures[47] that can be broken by applying moderately strong mechanical force such as found with lifting the adhesive tape substrate followed as described in the Experimental Section. We characterized our SERS nanosensor by scanning electron microscopy (SEM) as shown in **Figure 3.2A and B**. The images show randomly distributed and oriented Au TNPs on the adhesive substrate. Such disorder creates a unique SERS substrate because of *"accidental"* formation of a large number of hot spots where TNPs come into close contact with each other. Moreover, through discrete dipole approximation (DDA) calculations, we calculated the local field intensity enhancement at 785 nm excitation for an Au TNP (see **Figure 3.2C)**. Clearly, a strong and localized EM-field enhancement was observed at their sharp tips, which is an ideal LSPR property for SERS-based trace analyte detection and quantification. Furthermore, it is important to recognize that the LSPR peak position of metal nanostructures and the wavelength of the incident light source (i.e., the laser) control the hot spot intensity. An ideal nanostructure for SERS application should be one whose LSPR peak is longer than but close to the wavelength of the laser source. In this context, for trace explosive detection, laser excitation with low energy photons (e.g., 785 nm) is a prerequisite to avoid sample decomposition. According to our DDA calculations, the LSPR dipole peak of ~42 nm Au TNPs was at 781 nm (**Figure 3.2D**, black curve). The LSPR dipole peak of our Au TNPs attached onto flexible adhesive films appeared at ~820 nm (**Figure 3.2D,** red curve). This ~40 nm red-shift in dipole peak position of TNPs compared to DDA calculations could be due to near-field plasmonic coupling between randomly distributed and oriented Au TNPs, as shown in **Figure 3.2B**. Furthermore, LSPR dipole peak of Au TNPs at ~820 nm makes them ideal SERS substrates for low energy laser excitation as compared to Ag nanoparticles, which display an LSPR peak <600 nm and have been previously studied for SERS applications[48-50].

Because TNT is a very commonly used military grade high explosive and it also serves as a reference of explosive power, we used it as a model system to investigate the detection, identification, and quantification capabilities of our SERS nanosensor. **Figure 3.2E** shows Raman spectra detailing parts of the nanosensor and the responses that were collected as following: (a)

bare transparent 3M adhesive film, (b) 6.0 microliter (µL) of a 1.0 millimolar (mM) TNT solution in methanol drop-casted on adhesive film, (c) only the SERS nanosensor, and (d) 6.0 µL of a 1.0 mM TNT solution drop-casted on the SERS nanosensor.

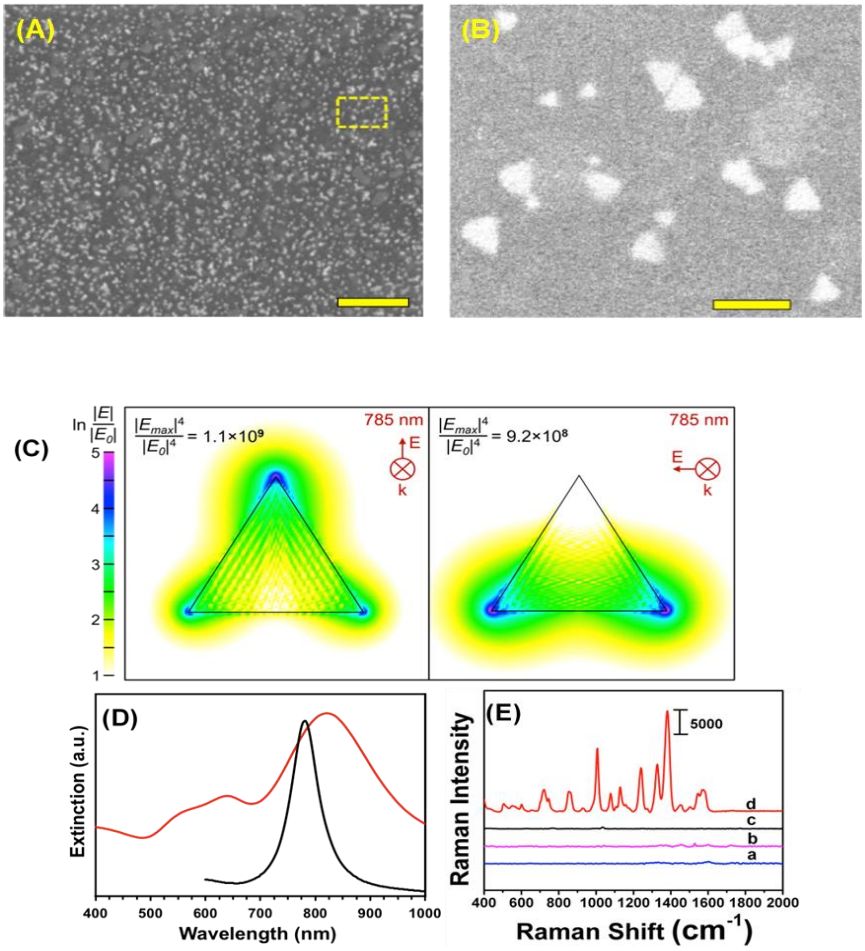

Figure 3.2. Spectroscopic and theoretical characterization of developed sensor. (A) Low magnification SEM image of our SERS nanosensor (1.0 µm scale bar). (B) High magnification SEM image of the expanded region of the nanosensor shown in dotted box in (A). Scale bar is 100 nm. (C) DDA simulated EM-field for a TOA-coated Au TNP (42 nm edge length, 8 nm thick); TNP is denoted by the triangle overlay. The EM-field is presented in the surface plane of the TNP in both primary modes and resulted from excitation with 785 nm linear polarized light as used with the SERS measurements reported. (D) Experimental LSPR spectra of Au TNPs self-assembled onto 3M adhesive tape (red curve) and their DDA-simulated spectrum (black curve). (E) Comparison of Raman signals under different experimental conditions: bare transparent 3M adhesive tape (a), total 6.0 µL of 1.0 mM TNT solution drop-casted on 3M tape (b), bare SERS nanosensor (c), total 6.0 µL of methanol drop-casted on SERS nanosensor (d), and total 6.0 µL of 1.0 mM TNT solution in methanol drop-casted on SERS nanosensor (e). Scale bar represents counts per second.

The nanosensor demonstrates significant enhancement in characteristic Raman peak intensities of TNT at 1380 (C-N stretch), 1240 (benzene ring), 1130 (CH_3 deformation), 1010 (symmetry aromatic stretch), and 860 cm^{-1} (NO_2 scissoring) as compared with TNT on just 3M adhesive film. **Figure 3. 3. (A-E)** providing additional SERS spectra utilized for EF calculation. Our experimentally observed Raman peaks were slightly shifted as compared to normal Raman vibrational modes of bulk TNT, which could be due to changes in orientation of TNT molecules upon adsorption onto (111) planes of Au TNP during slow solvent evaporation. Finally, we experimentally calculated the EF of our nanosensor to determine the SERS performance and it found to be ~6 x 10^6. For additional information concerning experimental EF calculation, please see the materials and methods section and **Figure. 3.3**. To the best of our knowledge, this is the highest value reported in the literature for Au nanostructure-based, flexible SERS nanosensors. However, we are not certain of the reason for the nearly three orders of magnitude difference between the experimentally determined and DDA-calculated SERS EF of our nanosensor. Perhaps, one possible reason for this deviation could be an overestimation of the number of TNT molecules ($N_{SERS,}$ 2.9 x 10^5) that were present on the surface of Au TNPs. Furthermore, the highest SERS enhancement value from the DDA calculations was obtained at the tips of TNP in contrast to the experimental value, which can have TNT molecules adsorbed onto the entire Au TNP surface.

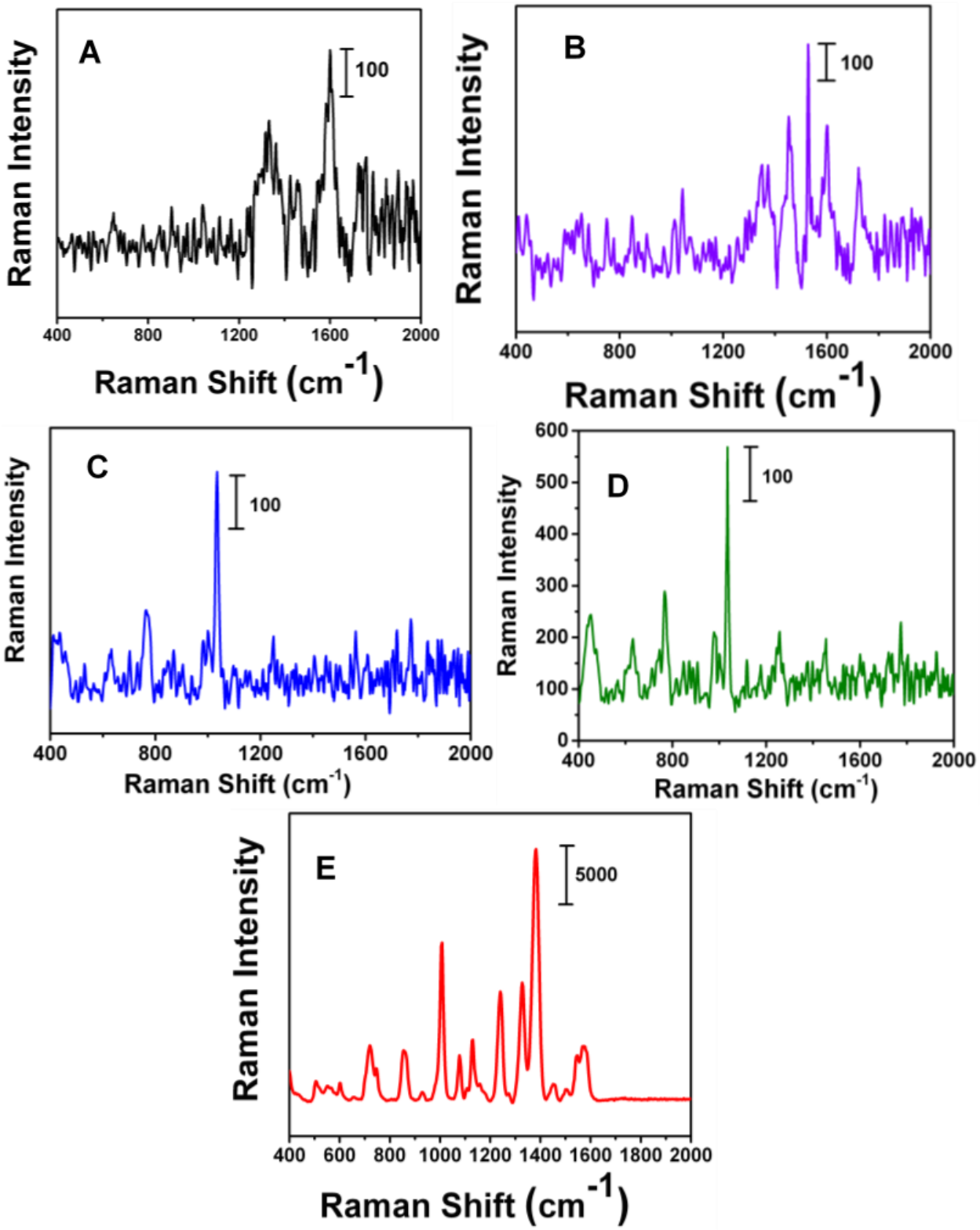

Figure 3.3. **Spectroscopy analysis of various components in the SERS nanosensor**: (A) Raman spectrum of 3M adhesive tape, (B) Raman spectrum of 3M adhesive tape containing 6 µL of 1.0 mM TNT solution, (C) SERS spectrum of our nanosensor, (D) 6 µL methanol drop-casted on SERS nanosensor, and (E) 6.0 µL of a 1.0 mM TNT solution drop-casted on SERS nanosensor.

3.4.2 Selectivity of SERS Nanosensors.

An analytical technique with extremely high selectivity is of paramount importance for homeland security applications because most items of evidence are either impure or may contain many interferents. In most trace analytes detection, defining selectivity at a very low concentration provides an added advantage for label-free analytical techniques in comparison to traditional methods such as GC-MS and electrochemistry that require fairly large number of samples. In this context, TNT samples are often contaminated with trinitrobenzene (TNB) and dinitrotoluene (DNT). To investigate the selectivity, a 6.0µL, 100 fM solution of either TNB or DNT was drop-casted onto SERS nanosensors and the Raman spectra were acquired. **Figure 3.4A** illustrates a comparison of SERS spectra of TNB, DNT, and TNT. Though the frequency and intensity of vibrational bands are visibly different in each spectrum, we performed principle component (PCA) and discriminant (DA) analyses for specificity testing and precise differentiation between these compounds. As shown in **Figure 3.4B**, the variation between these three nitrobenzene derivatives in SERS spectra was well described by PC 1 (70.1% of total variance) and PC 2 (24.5% of total variance). The first two PCs (cumulatively 94.6% of total variance) readily separated the compounds. DA analysis using PCs 1 and 2 resulted in 100% classification accuracy, with all spectra being predicted with a probability of 1. Taken together, our label-free SERS characterization demonstrates excellent classification capacity.

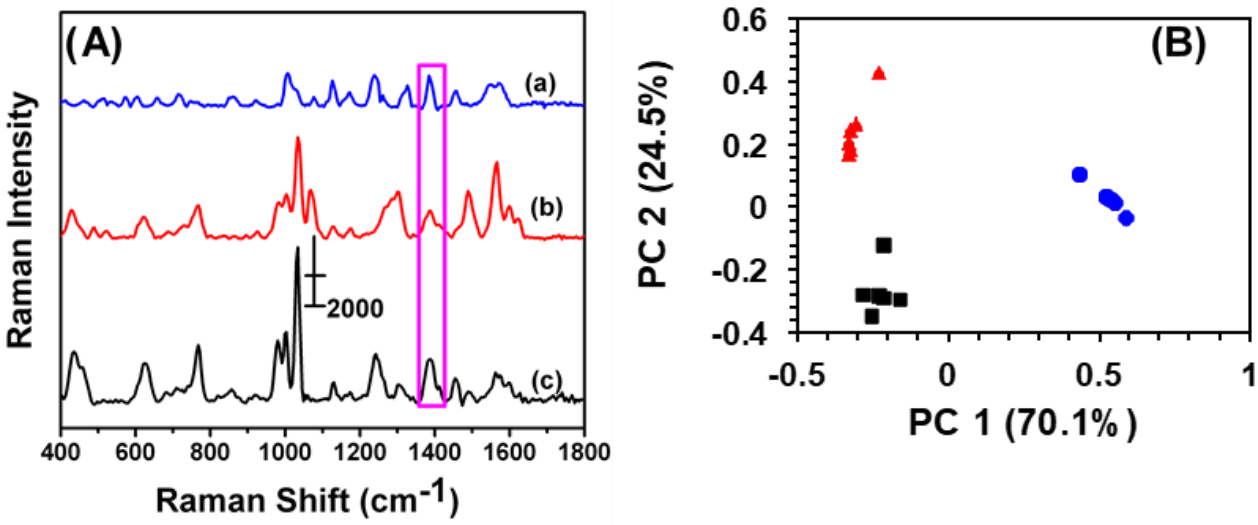

Figure 3.4. (A) Representative SERS spectra acquired using the nanosensor from 100 fM of: (a) TNT, (b) TNB, and (c) DNT at 1380 cm^{-1} (purple box). (B) Plot of PCA scores for SERS at 100 fM concentration of TNT (blue spheres), TNB (red triangles), and DNT (black square). DA classified 100% of spectra correctly. Here n= 18, DA prediction 100%.

3.4.3 Reproducibility of SERS Nanosensors

For any type of a label-free sensing approach, reproducibility in SERS nanosensors fabrication and long shelf life are prerequisites for accurate analytical measurement and for bringing the technology forward for real world applications. We have adopted two different reproducibility tests for our SERS nanosensor for trace explosive detection: (1) Analyze multiple spots in the same nanosensor (i.e., spot-to-spot variation) and (2) measure the SERS characteristics of multiple nanosensors (i.e., batch-to-batch variation). In the first reproducibility test, SERS spectra from nine randomly selected spots of a single nanosensor were collected using TNT as a standard explosive at 1.0 µM concentration. A negligible variation of SERS intensity was observed with the relative standard deviation (RSD) determined to be 2.7% (**Figure 3.5A).** This value is better than other flexible SERS nanosensors constructed with adhesive tape[51]and with other substrates[20, 52-55]including those used for explosive detection. In the second reproducibility test, four SERS nanosensors were prepared from four different batches of Au TNPs and SERS spectra were collected from four randomly selected spots on each nanosensor. As illustrated in (**Figure 3.5B).** stability/shelf life of our SERS nanosensors under normal laboratory storage conditions but protected from prolong light exposure. In this case, we also formulated two different approaches: Firstly, a 6.0 µL 1.0 µM of TNT solution was drop-casted onto six randomly selected spot of a nanosensor and the SERS spectrum were collected each day for an entire month. **Figure 3.5C** shows SERS peak intensity at 1380 cm^{-1} as a function of day where a small difference in intensity was observed with 3.1% RSD. Secondly, we prepared twenty SERS nanosensors from five different batches of Au TNPs at once, and SERS spectra were collected weakly using one nanosensor. Importantly, only 3.5% RSD (**Figure 3.5D**) was observed over the course of five months. We believe that such extraordinary characteristics of our SERS nanosensors arise from the programmable fabrication approach we adopted along with the high stability of Au TNPs under normal laboratory storage conditions. Taken together, our results demonstrate the outstanding reproducibility and shelf life of SERS nanosensors that will be crucial for future technological development. Furthermore, the long shelf life is very encouraging, specifically for the analysis of explosive residue in field blast samples when the nanosensor-containing explosive residue will be stored and analyzed days later from the sample collection location.

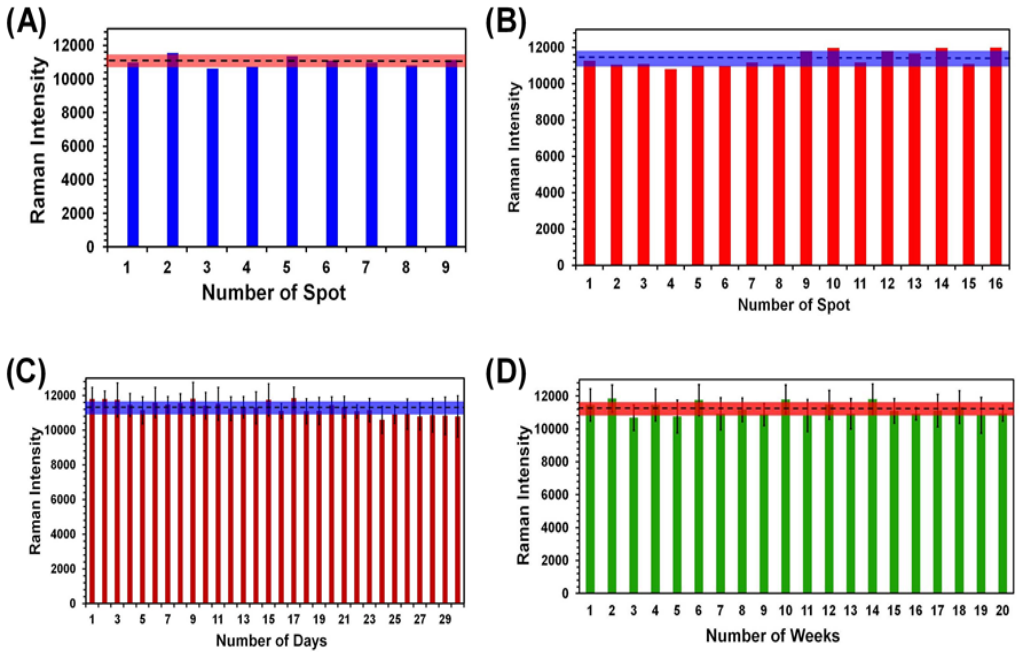

Figure 3.5. Histograms of SERS intensity of TNT at 1380 cm^{-1} collected from: (A) 9 randomly selected spots on a particular nanosensor; (B) four randomly selected areas of four different nanosensors (1-4, 5-8, 9-12, and 13-16), which were prepared from four different batches of Au TNPs; (C) one SERS nanosensor over an entire month; (D) 20 individual nanosensors over the course of 5 months. The error bars in (C) and (D) represent measurements from six spots each.

3.4.4 Detection, Quantification, and Classification of TNT, RDX and PETN Using SERS Nanosensors

With proven selectivity and reproducibility, we now investigate the feasibility of use of our SERS nanosensors for quantitative detection of TNT as a standard explosive. We prepared a TNT solution in methanol over the range of 1.0 mM to 100 fM through serial dilution. A 6.0 µL solution of a particular concentration was drop-casted on three different spots and two different nanosensors. **Figure 3.6A** shows the SERS spectra for different TNT concentrations where the low standard deviation of the Raman peak intensity supports exceptional reproducibility in our fabrication. Furthermore, a wide linear range spanning eight orders of magnitude (**Figure 3.6B)**, 10^{5} to 10^{-2} nM) between the TNT concentration and the Raman peak intensity was observed. The LOD was determined using a more sophisticated equation and found to be ~0.9 parts-per-trillions (ppt) (see Supporting Information for detail LOD calculation). Importantly, we were able to quantify TNT at 100 fM concentration with signal-to-noise ratio of 5.9. The sensitivity of our

SERS nanosensor is at least two orders of magnitude better than another Au nanostructure-based SERS nanosensors (see Table S2). We believe this excellent sensitivity is because of the strong EM field enhancement of Au TNPs at their sharp tips and edges. Furthermore, our detection technique provides multiple advantages over conventional and well-established analytical methods such as GC-MS, ion-mobility MS, electrochemistry, and fluorometry that require large sample amounts, expensive sample processing, a specific laboratory environment, and labeling.

RDX and PETN are also commonly used in acts of terror but only six and two SERS-based detection reports, respectively, are available. Furthermore, the literature methods not only suffer from poor sensitivity, but because the use of Klarite substrate, the advantages of flexibility and adhesive properties are diminished versus our SERS nanosensor. Therefore, there is an unmet need to develop an ultrasensitive nanosensor that is capable of detecting and quantifying these explosives along with an efficient sampling process, which better would expand potential applications of SERS nanosensor. With this aim we were able to quantitatively measure RDX and PETN utilizing SERS nanosensors with LODs of 56 and 56 ppq, respectively. **Figure 3.6C-F** show Raman spectra and calibration plots for RDX and PETN. Strikingly, RDX and PETN display an unprecedentedly large linear range spanning ten (10^5 to 10^{-4} nM) and nine (10^4 to 10^{-4} nM) orders of magnitude between the concentration and the Raman peak intensity. To rationalize an ~15-fold better sensitivity for either RDX or PETN in comparison to TNT we proposed a simple adsorption model of these explosive onto (111) facets of Au TNP (**Figure 3.6G-I**). TNT is a planar and rigid molecule, and thus the adsorption onto Au TNP surface requires TNT to be flat. Under this circumstance, number of TNT molecule per nm^2 surface area is expected to be low if one would envision multiple flat Au-N interactions. In contrast, RDX and PETN molecules are capable of forming multiple Au-N interactions without occupying a large surface area because of the high degree of flexibility in their molecular structure, which could result in more molecules effectively adsorb onto the TNP surface. Nevertheless, the sensitivity (3.1 femtogram) we achieved for either RDX or PETN is at least three-orders of magnitude better than current literature reports

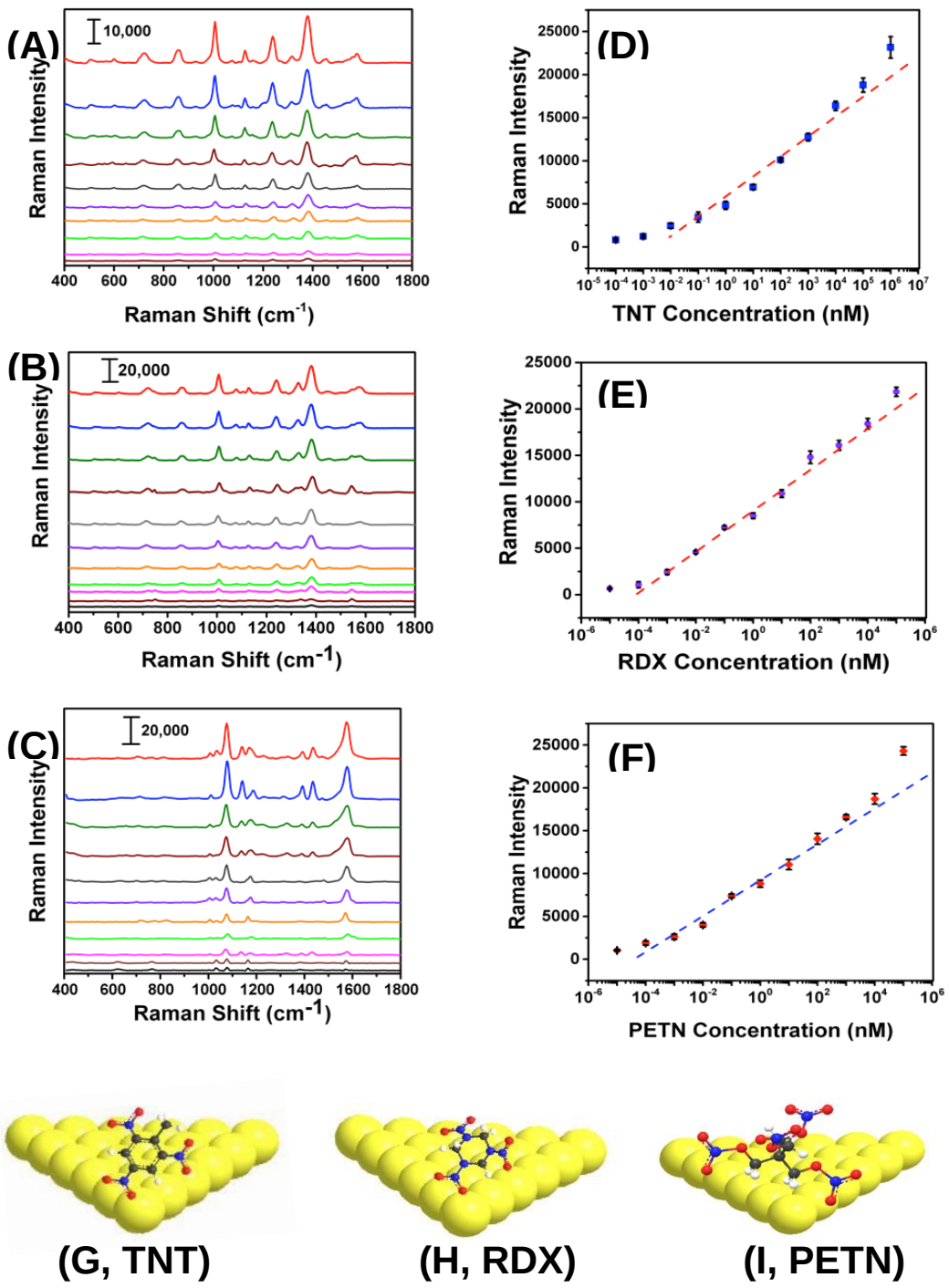

Figure 3.6. SERS spectra of (A) TNT from 1.0 mM to 100 fM, (B) RDX from 1.0 mM to 10 fM, and (C) PETN from 100 μM to 10 fM concentration range on flexible and adhesive SERS nanosensors. The plot of SERS intensity as function of (D) TNT and (E) RDX (at 1380 cm-1), and (F) PETN (at 1570 cm-1) versus explosive concentration on logarithm scale. The dashed lines represent the linear concentration ranges. Average SERS intensity was determined from 6 measurements. (G-I) Schematic illustration of physorption of the three different explosive molecules onto the Au TNP surface. The images are not to scale.

Next, we performed chemometric analysis to develop univariate calibration plots for TNT, RDX, and PETN for Raman peaks at 1380, 1380, and 1570 cm^{-1}, respectively. PCA loadings exhibited a very high magnitude at these positions in agreement with the high intensity, concentration dependence, and absence in the blank of these peaks. Multivariate calibration in the 100 fM to 100 μM concentration range with partial least square (PLS) corroborated the univariate calibration curves, but PLS did not provide improvement under these conditions (PLS calculation not shown). At the reported limit of quantification of 100 fM, PCA and DA were highly effective in separating the blank, PETN, RDX, and TNT, as shown in **Figure 3.7A**. The variation described by PC 1 (58.2% of total) distinguished TNT and RDX from the blank and PC 2 (27.9% of total) differentiated PETN from the Blank. DA using the 3 PCs yielded a 100% prediction accuracy. This is representative of our sensor ability to discern the blank from the analytes in the investigated range of 100 fM to 100 □M using PCA and DA.

Classification of RDX, TNT, and PETN using the reported sensor was highly effective, resulting in greater than 98% classification accuracy from DA (8 PCs, n=180) of the normalized SERS spectra of RDX, TNT, and PETN across the entire concentration range tested, i.e., 100 fM to 100 μM (**Figure 7B**). Due to the similarity of TNT and RDX SERS spectra in the 400 cm^{-1} to 2000 cm^{-1} range, the PCs that most strongly differentiate TNT and RDX yield very small amounts of variation, PC 5 (3.3%) and PC 8 (1.4%). The dominance of PCs 5 and 8 in the differentiation of TNT and RDX and in the structure of Canonical 2 is evident in the scoring coefficients. PC 5 and 8 also provided the most obvious visual division of TNT and RDX in three-dimensional PCA plots of the normalized spectra from 100 fM to 100 μM (not shown), which is a rational based for the role they play in structuring canonical 2. PC 1 (61.9 % of total variance) is the primary contributor to Canonical 1 and provides the differentiation of PETN from RDX and TNT. Three 1.0 nM RDX spectra were misclassified as TNT by DA of the normalized spectra from 100 fM to 100 μM. This misclassification is visually attributable to the abnormally high intensity of the 1075, 1130, and 1325 cm^{-1} peaks, which were not present in the blank, making the misclassified spectra characteristic of higher concentrations of TNT. The 1130 and 1325 cm^{-1} regions have intense loadings in PCs 5 (both) and 8 (1325 cm^{-1}) corroborating the observations concerning the role of these peaks in misclassification due to the importance of PCs 5 and 8 for the differentiation of RDX and TNT. Colocation of a PETN peak at 1075 cm^{-1} obscured the effect of this peak on misclassification in the PC Loadings. This misclassification did not occur in pairwise DA of

PETN/RDX, PETN/TNT, and RDX/TNT (n = 120) from 100 fM to 100 µM. Pairwise DA resulted in 100% classification accuracy for all spectra and the previously misclassified spectra were predicted with a probability of one. Taken together, detection, quantification, and classification of three explosives by our experimental measurement using Au TNP-based SERS nanosensors and our statistical investigation using chemometric will open new opportunities for trace explosive detection.

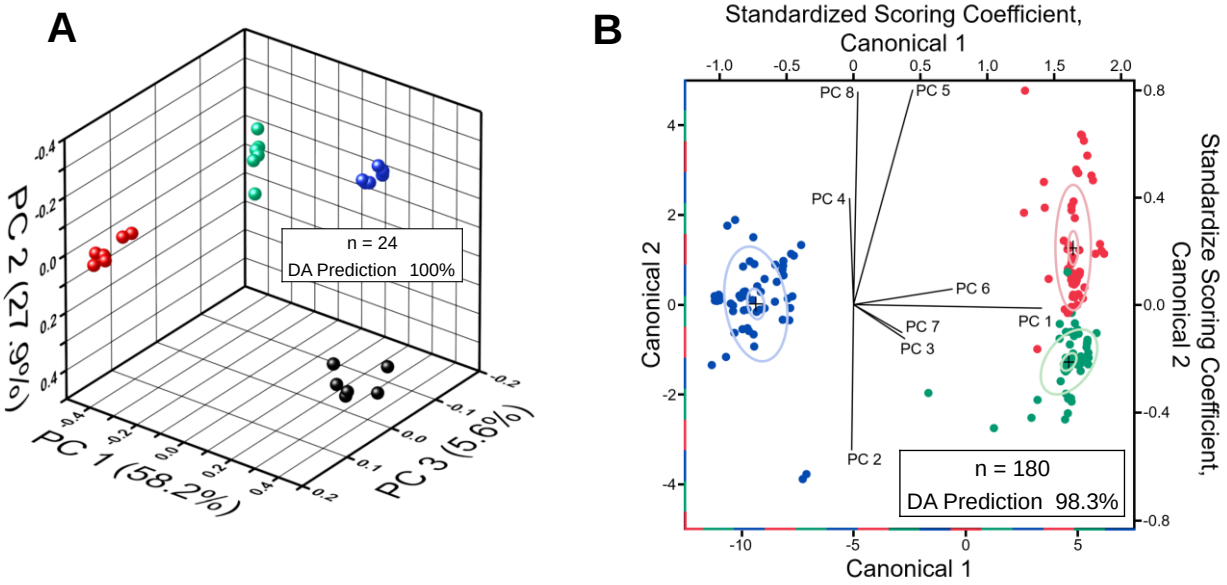

Figure 3.7. (A) PCA scores plotted at the 100 fM LOQ for SERS of RDX (red), TNT (green), PETN (blue), and blank (black) using the SERS nanosensor. Inset, DA classified 100% of spectra correctly, all with a probity of 1, using PCs 1-3 (91.7% of total variance). **(B)** DA canonical biplot (left and bottom axis) for SERS from 100 fM to 100 µM showing differentiation of RDX (red), TNT (green), and PETN (blue). DA coefficient loadings ray plot (top and left axis) for PCs 1-8 used in DA. Inset, DA classified 98.3% of spectra correctly, using PCs 1-8 (93.6% of total variance).

3.4.5 Direct Sampling of TNT and PETN on Fingerprints Using SERS Nanosensors

We expected that one of the unique aspects of our flexible and adhesive SERS nanosensor would be efficient sampling from real-world surfaces by placing the nanosensor on top of the trace residue without the need of any solvent wetting and swabbing steps. To test our assumption, here we demonstrated direct sampling of T3.NT from fingerprints that were prepared by thumb pressing TNT powder onto glass slides. **Figure 8A** illustrates Raman spectra of TNT after transferring the solid residue from glass and that the symmetric $–NO_2$ Raman vibrational stretch of TNT is clearly

visible even from the 10th slide. Clearly, trace amount of solid was transferred from coverslip to nanosensor unequivocally proving a very effective sample collection strategy with our SERS-based sensing approach. It is important to mention that the lack of linearity in the Raman signal versus glass coverslip number (**Figure 3.8B**) originates because the nature of transferring solid residue from one coverslip to another through pressing is not identical. Finally, as shown in **Figure 3.8C and D**, we also analyzed PETN from fingerprint samples because no such study is currently available for this explosive with results showing nearly similar characteristic of trace detection as TNT. Taken together, the demonstrated sample collection efficiency and trace detection of solid explosive residue is a step forward for successful application of our flexible and adhesive SERS nanosensors in both homeland and military applications.

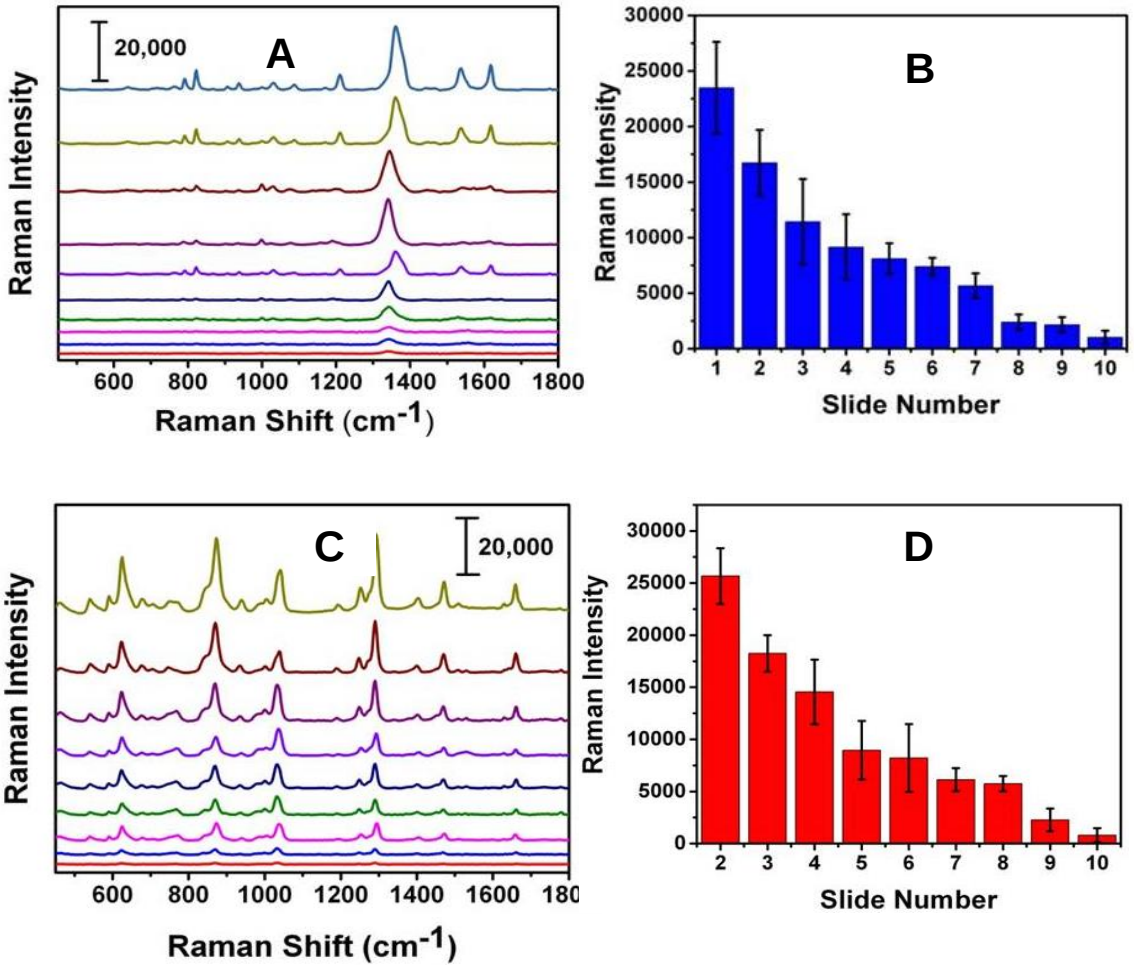

Figure 3.8. SERS nanosensor spectra of (A) TNT and (C) PETN collected by transferring fingerprint explosive residue from glass to SERS nanosensors. The top and bottom spectra are number 1 and 10 glass slides in which explosives powder was transferred from 1 to 2 to higher number slides through subsequent thumb pressing. The plot of SERS intensity (B) TNT (1380 cm-1) and (D) PETN (1290 cm-1) as function of slide number.

3.5 Summary

In summary, we have developed an ultrasensitive SERS nanosensors for trace explosive detection by self-assembling Au TNPs onto a commercially available, flexible and adhesive substrate through a programmable stamping method. This level of versatility has not been previously demonstrated in nanosensor-based explosive detection. By utilizing SERS nanosensors, we quantitatively detected TNT, RDX, and PETN from standard solutions with LODs as low as of 56 ppq, which is the highest sensitivity ever reported in the literature for trace explosive detection. We hypothesize that such outstanding sensitivity arises from the strong EM field enhancement of TNPs at their sharp tips and edges. Importantly, our demonstrated selectivity through experimental SERS characterizations and statistical calculations provides unique ability of our nanosensors to distinguish various types of explosives. Notably, the SERS nanosensors showed unprecedentedly high stability and shelf life with the RSD values of Raman signal of <4.0%. Furthermore, the direct sampling efficiency of our nanosensors on fingerprints from glass will obviate the need of the swabbing technique, which requires a wet surface for extraction of solid explosive residue and is currently very commonly used at the airports for screening purposes. We believe our flexible and adhesive SERS nanosensor will have the ability to collect trace amounts of sample from field blast residue and thus greatly improve explosive detection and instant analysis in homeland security applications when coupled with portable Raman spectrometers. Additionally, use of commercially available inexpensive adhesive substrate could potentially allow large scale, low-cost production of SERS nanosensors. Finally, our SERS nanosensors for trace explosive detection can successfully be used for other chemical detection such as pesticides reside on fruits and vegetables, forensic drug analysis, and biological sensing (e.g. DNA and microRNAs), thus opening new avenues in measurement science.

3.6 References

1. Guo, L.; Yang, Z.; Dou, X., Artificial Olfactory System for Trace Identification of Explosive Vapors Realized by Optoelectronic Schottky Sensing. *Advanced Materials (Weinheim, Germany)* **2017,** *29* (5), n/a.

2. Lopresto, V.; Langella, A.; Papa, I., Interaction of Water with Carbon Fiber Reinforced Polymer Laminates under Dynamic Loading Conditions. *Journal of Materials Engineering and Performance* **2019,** *28* (6), 3220-3227.
3. DeTata, D. A.; Collins, P. A.; McKinley, A. J., A comparison of solvent extract cleanup procedures in the analysis of organic explosives. *Journal of Forensic Sciences* **2013,** *58* (2), 500-507.
4. Gamble, S. C.; Campos, L. C.; Morgan, R. M., Detection of trace peroxide explosives in environmental samples using solid phase extraction and liquid chromatography mass spectrometry. *Environmental Forensics* **2017,** *18* (1), 50-61.
5. Gledhill, M.; Beck, A. J.; Stamer, B.; Schlosser, C.; Achterberg, E. P., Quantification of munition compounds in the marine environment by solid phase extraction - ultra high performance liquid chromatography with detection by electrospray ionisation - mass spectrometry. *Talanta* **2019,** *200*, 366-372.
6. Zarei, A. R.; Nedaei, M.; Ghorbanian, S. A., Ferrofluid of magnetic clay and menthol based deep eutectic solvent: Application in directly suspended droplet microextraction for enrichment of some emerging contaminant explosives in water and soil samples. *Journal of Chromatography A* **2018,** *1553*, 32-42.
7. Holubowitch, N.; Beaudoin, S. P.; Medina, G.; Wray, J., Electropolymerization of molecularly imprinted polypyrrole for sensing explosive compounds. *Abstracts of Papers, 257th ACS National Meeting & Exposition, Orlando, FL, United States, Mar. 31-Apr. 4, 2019* **2019**, ANYL-0309.
8. Liu, J.; Si, T.; Zhang, Z., Mussel-inspired immobilization of silver nanoparticles toward sponge for rapid swabbing extraction and SERS detection of trace inorganic explosives. *Talanta* **2019,** *204*, 189-197.
9. Shi, Y.-e.; Wang, W.; Zhan, J., A positively charged silver nanowire membrane for rapid on-site swabbing extraction and detection of trace inorganic explosives using a portable Raman spectrometer. *Nano Research* **2016,** *9* (8), 2487-2497.
10. Sharma, B.; Frontiera, R. R.; Henry, A.-I.; Ringe, E.; Van Duyne, R. P., SERS: Materials, applications, and the future. *Materials Today (Oxford, United Kingdom)* **2012,** *15* (1-2), 16-25.

11. Jain, P. K.; Huang, X.; El-Sayed, I. H.; El-Sayed, M. A., Noble Metals on the Nanoscale: Optical and Photothermal Properties and Some Applications in Imaging, Sensing, Biology, and Medicine. *Accounts of Chemical Research* **2008,** *41* (12), 1578-1586.
12. Cadusch, P. J.; Hlaing, M. M.; Wade, S. A.; McArthur, S. L.; Stoddart, P. R., Improved methods for fluorescence background subtraction from Raman spectra. *Journal of Raman Spectroscopy* **2013,** *44* (11), 1587-1595.
13. Moronshing, M.; Bhaskar, S.; Mondal, S.; Ramamurthy, S. S.; Subramaniam, C., Surface-enhanced Raman scattering platform operating over wide pH range with minimal chemical enhancement effects: Test case of tyrosine. *Journal of Raman Spectroscopy* **2019,** *50* (6), 826-836.
14. Qi, Y.; Xing, T.-y.; Zhao, J.; Weng, G.-j.; Li, J.-j.; Zhu, J.; Zhao, J.-w., Tuning the surface enhanced Raman scattering performance of anisotropic Au core-Ag shell hetero-nanostructure: The effect of core geometry. *Journal of Alloys and Compounds* **2019,** *776*, 934-947.
15. Wei, W.; Du, Y.; Zhang, L.; Yang, Y.; Gao, Y., Improving SERS hot spots for on-site pesticide detection by combining silver nanoparticles with nanowires. *Journal of Materials Chemistry C: Materials for Optical and Electronic Devices* **2018,** *6* (32), 8793-8803.
16. Schluecker, S., Surface-Enhanced Raman Spectroscopy: Concepts and Chemical Applications. *Angewandte Chemie, International Edition* **2014,** *53* (19), 4756-4795.
17. dos Santos, D. P.; Temperini, M. L. A.; Brolo, A. G., Intensity Fluctuations in Single-Molecule Surface-Enhanced Raman Scattering. *Accounts of Chemical Research* **2019,** *52* (2), 456-464.
18. Kneipp, J.; Li, X.; Sherwood, M.; Panne, U.; Kneipp, H.; Stockman Mark, I.; Kneipp, K., Gold nanolenses generated by laser ablation-efficient enhancing structure for surface enhanced Raman scattering analytics and sensing. *Analytical chemistry* **2008,** *80* (11), 4247-51.
19. Sanchez-Iglesias, A.; Aldeanueva-Potel, P.; Ni, W.; Perez-Juste, J.; Pastoriza-Santos, I.; Alvarez-Puebla, R. A.; Mbenkum, B. N.; Liz-Marzan, L. M., Chemical seeded growth of Ag nanoparticle arrays and their application as reproducible SERS substrates. *Nano Today* **2010,** *5* (1), 21-27.

20. Lee, C. H.; Tian, L.; Singamaneni, S., Paper-based SERS swab for rapid trace detection on real-world surfaces. *ACS Applied Materials & Interfaces* **2010,** *2* (12), 3429-3435.
21. Zhang, W.; Tang, Y.; Shi, A.; Bao, L.; Shen, Y.; Shen, R.; Ye, Y., Recent Developments in Spectroscopic Techniques for the Detection of Explosives. *Materials (Basel, Switzerland)* **2018,** *11* (8).
22. Alizadeh, N.; Ghoorchian, A., Hybrid Optoelectrochemical Sensor for Superselective Detection of 2,4,6-Trinitrotoluene Based on Electrochemical Reduced Meisenheimer Complex. *Analytical Chemistry (Washington, DC, United States)* **2018,** *90* (17), 10360-10368.
23. Dey, S.; Purkait, R.; Pal, K.; Jana, K.; Sinha, C., Aggregation-Induced Emission-Active Hydrazide-Based Probe: Selective Sensing of Al3+, HF2-, and Nitro Explosives. *ACS Omega* **2019,** *4* (5), 8451-8464.
24. Fan, S.; Lai, J.; Burn, P. L.; Shaw, P. E., Solid-State Fluorescence-based Sensing of TATP via Hydrogen Peroxide Detection. *ACS Sensors* **2019,** *4* (1), 134-142.
25. Li, W.; Wang, D.; Han, D.; Sun, R.; Zhang, J.; Feng, S., New polyhedral oligomeric silsesquioxanes-based fluorescent ionic liquids: synthesis, self-assembly and application in sensors for detecting nitroaromatic explosives. *Polymers (Basel, Switzerland)* **2018,** *10* (8), 917/1-917/13.
26. Liu, T.; Fang, Y., Film-based fluorescent gas sensors. *Yingyong Huaxue* **2018,** *35* (9), 1133-1137.
27. Zhang, X.; Hu, J.; Wang, B.; Li, Z.; Xu, S.; chen, Y.; Ma, X., A chiral zinc(II) metal-organic framework as high selective luminescent sensor for detecting trace nitro explosives picric acid and Fe3+ ion. *Journal of Solid State Chemistry* **2019,** *269*, 459-464.
28. Joshi, G. K.; Blodgett, K. N.; Muhoberac, B. B.; Johnson, M. A.; Smith, K. A.; Sardar, R., Ultrasensitive Photoreversible Molecular Sensors of Azobenzene-Functionalized Plasmonic Nanoantennas. *Nano Letters* **2014,** *14* (2), 532-540.
29. Joshi, G. K.; Deitz-McElyea, S.; Liyanage, T.; Lawrence, K.; Mali, S.; Sardar, R.; Korc, M., Label-free nanoplasmonic-based short noncoding RNA sensing at attomolar concentrations allows for quantitative and highly specific assay of MicroRNA-10b in biological fluids and circulating exosomes. *ACS Nano* **2015,** *9* (11), 11075-11089.

30. Joshi, G. K.; McClory, P. J.; Muhoberac, B. B.; Kumbhar, A.; Smith, K. A.; Sardar, R., Designing Efficient Localized Surface Plasmon Resonance-Based Sensing Platforms: Optimization of Sensor Response by Controlling the Edge Length of Gold Nanoprisms. *Journal of Physical Chemistry C* **2012,** *116* (39), 20990-21000.
31. Joshi, G. K.; Smith, K. A.; Johnson, M. A.; Sardar, R., Temperature-Controlled Reversible Localized Surface Plasmon Resonance Response of Polymer-Functionalized Gold Nanoprisms in the Solid State. *Journal of Physical Chemistry C* **2013,** *117* (49), 26228-26237.
32. Joshi, G. K.; White, S. L.; Johnson, M. A.; Sardar, R.; Jain, P. K., Ultrashort, Angstrom-Scale Decay of Surface-Enhanced Raman Scattering at Hot Spots. *Journal of Physical Chemistry C* **2016,** *120* (43), 24973-24981.
33. Liyanage, T.; Masterson, A. N.; Oyem, H. H.; Kaimakliotis, H.; Nguyen, H.; Sardar, R., Plasmoelectronic-Based Ultrasensitive Assay of Tumor Suppressor microRNAs Directly in Patient Plasma: Design of Highly Specific Early Cancer Diagnostic Technology. *Analytical Chemistry (Washington, DC, United States)* **2019,** *91* (3), 1894-1903.
34. Liyanage, T.; Sangha, A.; Sardar, R., Achieving biosensing at attomolar concentrations of cardiac troponin T in human biofluids by developing a label-free nanoplasmonic analytical assay. *The Analyst* **2017,** *142* (13), 2442-2450.
35. Chen, K.; Zhang, X.; Zhang, Y.; Lei, D. Y.; Li, H.; Williams, T.; MacFarlane, D. R., Highly Ordered Ag/Cu Hybrid Nanostructure Arrays for Ultrasensitive Surface-Enhanced Raman Spectroscopy. *Advanced Materials Interfaces* **2016,** *3* (13), n/a.
36. Ou, Y.; Wang, L.-Y.; Zhu, L.-W.; Wan, L.-S.; Xu, Z.-K., In-Situ Immobilization of Silver Nanoparticles on Self-Assembled Honeycomb-Patterned Films Enables Surface-Enhanced Raman Scattering (SERS) Substrates. *Journal of Physical Chemistry C* **2014,** *118* (21), 11478-11484.
37. Demeritte, T.; Kanchanapally, R.; Fan, Z.; Singh, A. K.; Senapati, D.; Dubey, M.; Zakar, E.; Ray, P. C., Highly efficient SERS substrate for direct detection of explosive TNT using popcorn-shaped gold nanoparticle-functionalized SWCNT hybrid. *Analyst (Cambridge, United Kingdom)* **2012,** *137* (21), 5041-5045.

38. Guo, Z.; Hwang, J.; Zhao, B.; Chung, J. H.; Cho, S. G.; Baek, S.-J.; Choo, J., Ultrasensitive trace analysis for 2,4,6-trinitrotoluene using nano-dumbbell surface-enhanced Raman scattering hot spots. *Analyst (Cambridge, United Kingdom)* **2014,** *139* (4), 807-812.
39. Lan, X.; Chen, Z.; Lu, X.; Dai, G.; Ni, W.; Wang, Q., DNA-Directed Gold Nanodimers with Tailored Ensemble Surface-Enhanced Raman Scattering Properties. *ACS Applied Materials & Interfaces* **2013,** *5* (21), 10423-10427.
40. Liz-Marzan, L. M., New composite nanomaterials for SERS detection. *Pacifichem 2010, International Chemical Congress of Pacific Basin Societies, Honolulu, HI, United States, December 15-20, 2010* **2010**, PTC-1158.
41. Xiang, Q.; Li, Z.; Zheng, M.; Liu, Q.; Chen, Y.; Yang, L.; Jiang, T.; Duan, H., Sensitive SERS detection at the single-particle level based on nanometer-separated mushroom-shaped plasmonic dimers. *Nanotechnology* **2018,** *29* (10), 105301/1-105301/7.
42. Cai, L.; Dong, J.; Wang, Y.; Chen, X., A review of developments and applications of thin-film microextraction coupled to surface-enhanced Raman scattering. *Electrophoresis* **2019,** *40* (16-17), 2041-2049.
43. Eryilmaz, M.; Acar Soykut, E.; Cetin, D.; Boyaci, I. H.; Suludere, Z.; Tamer, U., SERS-based rapid assay for sensitive detection of Group A Streptococcus by evaluation of the swab sampling technique. *Analyst (Cambridge, United Kingdom)* **2019,** *144* (11), 3573-3580.
44. Kwon, G.; Kim, J.; Kim, D.; Ko, Y.; Yamauchi, Y.; You, J., Nanoporous cellulose paper-based SERS platform for multiplex detection of hazardous pesticides. *Cellulose (Dordrecht, Netherlands)* **2019,** *26* (8), 4935-4944.
45. Huang, X.; Zhu, Y.; Zhang, X.; Bao, Z.; Lei, D. Y.; Yu, W.; Dai, J.; Wang, Y., Clam-inspired nanoparticle immobilization method using adhesive tape as microchip substrate. *Sensors and Actuators, B: Chemical* **2016,** *222*, 106-111.
46. Suresh, V.; Yap, F. L., Flexible, transparent and robust SERS tapes through a two-step block copolymer self-assembly process. *RSC Advances* **2015,** *5* (76), 61671-61677.
47. Sardar, R.; Park, J.-W.; Shumaker-Parry, J. S., Polymer-induced synthesis of stable gold and silver nanoparticles and subsequent ligand exchange in water. *Langmuir* **2007,** *23* (23), 11883-11889.
48. Stiles, P. L.; Dieringer, J. A.; Shah, N. C.; Van Duyne, R. P., Surface-enhanced Raman spectroscopy. *Annual Review of Analytical Chemistry* **2008,** *1*, 601-626.

49. Mayer, K. M.; Hafner, J. H., Localized surface plasmon resonance sensors. *Chemical Reviews (Washington, DC, United States)* **2011,** *111* (6), 3828-3857.
50. Stewart, M. E.; Anderton, C. R.; Thompson, L. B.; Maria, J.; Gray, S. K.; Rogers, J. A.; Nuzzo, R. G., Nanostructured plasmonic sensors. *Chemical Reviews (Washington, DC, United States)* **2008,** *108* (2), 494-521.
51. Chen, J.; Huang, Y.; Kannan, P.; Zhang, L.; Lin, Z.; Zhang, J.; Chen, T.; Guo, L., Flexible and Adhesive Surface Enhance Raman Scattering Active Tape for Rapid Detection of Pesticide Residues in Fruits and Vegetables. *Analytical Chemistry (Washington, DC, United States)* **2016,** *88* (4), 2149-2155.
52. Chen, N.; Ding, P.; Shi, Y.; Jin, T.; Su, Y.; Wang, H.; He, Y., Portable and Reliable Surface-Enhanced Raman Scattering Silicon Chip for Signal-On Detection of Trace Trinitrotoluene Explosive in Real Systems. *Analytical Chemistry (Washington, DC, United States)* **2017,** *89* (9), 5072-5078.
53. Han, Z.; Liu, H.; Meng, J.; Yang, L.; Liu, J.; Liu, J., Portable Kit for Identification and Detection of Drugs in Human Urine Using Surface-Enhanced Raman Spectroscopy. *Analytical Chemistry (Washington, DC, United States)* **2015,** *87* (18), 9500-9506.
54. Wang, P.; Wu, L.; Lu, Z.; Li, Q.; Yin, W.; Ding, F.; Han, H., Gecko-Inspired Nanotentacle Surface-Enhanced Raman Spectroscopy Substrate for Sampling and Reliable Detection of Pesticide Residues in Fruits and Vegetables. *Analytical Chemistry (Washington, DC, United States)* **2017,** *89* (4), 2424-2431.
55. Gong, Z.; Du, H.; Cheng, F.; Wang, C.; Wang, C.; Fan, M., Fabrication of SERS Swab for Direct Detection of Trace Explosives in Fingerprints. *ACS Applied Materials & Interfaces* **2014,** *6* (24), 21931-21937.

CHAPTER 4 PROGRAMMABLE ASSEMBLY OF PLASMONIC GOLD TRIANGULAR NANOPRISMS BASED ON THE SUBSTRATE PROPERTY FOR HIGHLY SENSITIVE SERS BASED EMERGENCY ROOM PATIENT PLASMA ASSAY.

4.1 Synopsis

Today, the use of illicit drugs has been a long-standing problem in American society[1-4]. It is very crucial to have an efficient and accurate diagnosis method for drug toxicology screening in the emergency room. It is an unmet requirement to develop widely applicable, nondestructive, highly sensitive, less costly, quantitative, analytical techniques for an efficient diagnose of illicit drug at the emergency room patient samples. Herein we have reported effective surface-enhanced Raman scattering (SERS) substrate using gold triangular nanoprisms (Au TNPs) for highly sensitive, selective assaying technique of drug screening directly in-patient plasma. This self-assembly of Au TNPs achieved by using simple droplet evaporation method based on the surface properties (hydrophilicity and hydrophobicity) of the substrate. Accordingly, we have achieved programmable highly dense homogeneous 2D, 2D/3D or 3D supper lattice array by assembling polyethylene glycol (PEG_{60}-SH) functionalized Au TNPs on to the (3-aminopropyl)-triethoxysilane, (APTES), n-octyl-triethoxysilane (OTES) or phenyl-triethoxysilane (PTES) functionalized substrates respectively. Further, this efficient substrate was used for assaying three different types of analytes, including **Opiates**- Fentanyl, **Coca Alkaloids**- Cocaine and **Cannabinoids**- JWH-O18 and achieved the 130, 32.3 and 118.9 ppq sensitivity respectfully. Finally, the developed substrate was executed for the ultrasensitive SERS based detection of fentanyl and cocaine in parts per trillion (ppt) level by directly using only 10% diluted, 6 µL emergency room patient plasma samples without further purification. Also, we have further confirmed the high selectivity of the assay for the targeted analytes by detecting different patient samples which do not contain the target analytes. Taken together, the demonstrated sensitivity, selectivity, and reliability of the measurements as well as with the excellent reproductivity of our SERS based assay, obviate the need for complicated sample processing steps and easy to execute even with basic knowledge. We believe this newly designed sensor will be highly beneficial in efficient the battle of "war against drugs,".

4.2 Introduction

Today the United States faces expanding difficulties in public health and national security because of the critical increment in the production, carrying and maltreatment of controlled substances[1-4]. The center for disease control and prevention (CDC) has reported 64,000 mortalities from drug overdoses in year 2016 was reported. Further they have expected increases in opioid overdoses of 30% in 45 states of the Unites States and 70% in the Midwest alone[5-13]. Further along with fatalities drugs are implicated in other criminal justice issues such as assaults, probations and parole violations and driver impairment[14]. Therefore, herein this report we address the unmet requirement of the development of widely applicable, nondestructive, highly sensitive, less costly, quantitative, analytical techniques which are able to detect and quantify drugs directly in few microliters of human plasma.

Usually in the Emergency Department where the diagnosis and treatment in an acute setting take place, it is often important to know if the patient's clinical condition can be explained by effects of drugs-of-abuse (DOA) or therapeutic medications[15]. Here toxicology screening is carried out using different methods including immunoassays[16-20] and chromatography-based[21-24] assays to detect DOA and therapeutic drugs in various biological samples such as plasma. However, these analytes mostly take place in central facilities and the process is quite time consuming and expensive, depending on laboratory techniques. Also, most cases require trained personnel for the analysis[15]. Further toxicological analysis of unknown drug is extremely challenging because of the interference of the biological matrix and lack of available antibodies[25]. Among excessively use opiates fentanyl analogous[26-29] and synthetic cannabinoids such as JWH-018[30-31] is extremely challenging to detect in ultra-trace levels. According to the Controlled Substance Act, fentanyl has been progressively used as an adulterant in illicit substances, such as coca alkaloids cocaine[32]. Also, they are extremely powerful where 10 ppb level in blood is considered to be fatal[32]. Altogether, lack of efficient, highly sensitive, highly accurate, technique for emergency room drug detection implicated in the sharp expansion of drug related deaths in all around the world.

The Scientific Working Group for Forensic Toxicology has reported (SWGTOX), the development of sensing application for forensic toxicological applications should be enriched with the prerequisite of sensors including sensitivity, selectivity, specificity and reproducibility. Herein we proposed Raman instrument-based analysis technique to achieve the above-mentioned criteria. Raman spectroscopy observes the vibrational frequency mode which provides characteristic

spectrum of molecular fingerprint. This unique spectrum can be utilized to develop a highly selective detection and quantification method. However, Raman effect itself is fairly weak[33-35] which avoids usage in forensic toxicology applications which require the detection of parts per billion (ppb) or even smaller analytes. In order to amplify the Raman signal, target analyte needs to be in contact with a metallic nanoparticle (NPs) which results in surface enhanced Raman scattering/Spectroscopy (SERS)[36]. Here NPs is considered as a SERS substrate and localized surface plasmon property (LSPR) of the NPS causes the signal amplifications when the resonance frequency of collective oscillations of conductive electrons of the metallic nanoparticles matches with the incident photons[37]. The LSPR property of the metallic nanoparticles create strong electromagnetic field enhancement ("hot spots") around the nanoparticles[38-41]. If we can increase the number of hotspots on by bringing NPs closer in 3D packing, it will provide the potential to enormously enhance the normal Raman signature.

Self-Assembly of nanoparticles into 2D or 3D array is the best way to attain such supper substrate to achieve high enhancement of Raman signature[42-45]. In this study we have utilized the Gold triangular nanoprisms (Au TNPs) as anisotropic structure for suitable self-assembled superstructures due to their possibility of tailoring strong EM field enhancement at sharp edges and tips based on the local density and Au TNPs orientation on to the substrate which further enhance the collective plasmonic properties[46-56]. The biggest challenge of assembly of plasmonic nanoparticles is to achieve more uniform 2D or 3D superlattice array in millimeter scales where they can be easily adopted for SERS based applications. Droplet evaporation is the most commonly executed self-assembly process due to their wide applicability and the cost effectiveness[57-62]. However, obtaining the uniform distribution by pinning and depinning of the contact line, also so-called coffee ring effect, is normally implemented to pattern the solute on surfaces[63-67]. Previous literature has reported different approaches to overcome one or the other obstacle. However, here we mainly focus on all the factors that control the self-assembly process such as particle–particle interaction, particle–suspension interaction, and droplet–substrate interaction to achieve homogenous programmable self-assembly of Au TNPs[63].

Herein we have executed simple effective droplet evaporation based self-assembly by controlling the surface properties of Au TNPs and by regulating the hydrophilicity and hydrophobicity of the substrate. Finally, we have achieved programmable highly dense homogeneous 2D, 2D/3D or 3D supper lattice array by assembling polyethylene glycol (PEG_{60}-

SH) functionalized Au TNPs on to the APTES, ODTS or PMTS functionalized substrate. Further we utilized the developed substrate as SERS substrate for the trace level detection of **Opiates**- Fentanyl, **Coca Alkaloids**- Cocaine and **Cannabinoids**- JWH-O18 as analytes and achieved the 130, 32.3 and 118.9 ppq sensitivity respectfully. Finally, the developed substrate was executed for the ultrasensitive SERS based detection of fentanyl and cocaine in parts per trillion level by directly using only 6 µL emergency room patient plasma samples without further purification. Also, we have proved the high selectivity of the assay for the targeted analytes by detecting different patient samples which do not contain the target analytes.

4.3 Material and Methods

4.3.1 Methods

Chemicals. Chloro(triethylphosphine) gold (I) (Et_3PAuCl, 97%), poly(methylhydrosiloxane) (PMHS, M_n = 1700-3300), triethylamine (TEA, 98%), ACS grade acetonitrile (CH_3CN, 99.9%), methanol (99.8%), (3-aminopropyl)-triethoxysilane, APTES, 94%), were purchased from Sigma-Aldrich, and Phenyl-triethoxysilane (PTES) and n-octyl-triethoxysilane 98% (OTES) were purchased from Gelest Inc. Ethanol (alcohol 190 proof) was purchased from Decon laboratories. Glass coverslips (Cat. No. 12548C) were purchased from Fisher Scientific and silicon wafer were purchased from UniversityWafer. RBS35 Detergent was obtained from Thermo Scientific and used as received. A fisher Scientific Barnstead Nanopure system was utilized to achieve water Purity at 18.2 MΩ-cm and the same Nanopure water was used for all cleaning processes. Separate drug solution of Fentanyl, Cocaine D3 and JWH-018 were purchased from fisher scientific.

4.3.2 SERS Measurements

For this study we used the exact same instrumentation utilized in chapter 3.

4.3.3 Spectroscopy and Microscopy Characterization

Absorption spectra were collected using Varian Cary 50 Scan UV-visible spectrophotometer in the range of 300- 1100 nm. Absorption spectra of TEA capped Au TNP solutions were obtained by diluting 0.3 mL of reaction solution to a final volume of 2.0 mL with acetonitrile in a 1 cm

quartz cuvette. Acetonitrile was used as a background in each run before collecting the absorbance spectra. The UV- visible spectra of solid state self-assembled coverslips of TEA capped Au TNPs and after ligand exchange with PEG_{60}-SH were obtained in air and for that plain silanized coverslip in air was used as a background. The UV- visible spectra of PEG60-SH functionalized Au TNP, after liftoff was obtained in ethanol medium and ethanol was used as background in each run before collecting the absorbance spectra. Scanning electron (SEM) and Transmission electron (TEM) microscopy techniques were used to determine the average edge-length of gold nanoprisms used in our SERS nanosensor fabrication.

4.3.4 Synthesis of Gold Triangular Nanoprisms (Au TNPs)

Au TNPs were synthesized according to our published method with minor modifications where we utilized a different stabilizing agent than the previously reported method in chapter 2.3.3.[46-56]. Briefly, $Et_3PAu(I)Cl$ (0.010 g) was dissolved in 20 mL of purged acetonitrile and stirred for 5 min at room temperature followed by addition of 0.019 mL of TEA and then the reaction mixture was gradually increased in temperature , to reach 40 ℃, Once at 40 ℃ 0.3 mL of PMHS were added. Then the Au TNP formation was allowed to proceed at this temperature. During this time the color of the solution changed from colorless to pink, purple blue and then to a deep purple color. The reaction mixture was monitored through UV-visible absorption spectroscopy to follow the dipole peak position (λ_{LSPR}) of Au TNPs. The reaction mixture was removed from heat once the dipole peak reached 800 nm in acetonitrile, which represented average edge-lengths of 42 nm. The edge-lengths were confirmed by SEM analyses.

4.3.5 Silanization of Glass Coverslips

For the salinization process we followed the same procedure published in chapter 2.3.2.

4.3.6 Silanization of Silicon Wafer

Silicon wafer was first cut into 25mm*25mm squares and incubated in a solution containing 7:3 concentrated sulfuric acid (H2SO4) and hydrogen peroxide (H2O2) for 30 minutes. The coverslips were then thoroughly rinsed with nanopure water and further incubated in a solution containing 5:1:1 nanopure water, ammonium hydroxide (NH4OH) and hydrogen peroxide (H2O2)

and sonicated in that solution for an hour. Then the coverslips were thoroughly rinsed with copious amount of nanopure water and placed in a vacuum oven at 60 ℃ overnight. Next the cleaned coverslips were immersed in a 15% APTES/PTES/OTES solution in ethanol for 30 min, and then sonicated for 15 min followed by five time rinsing with ethanol. Finally, these APTES/PTES/OTES functionalized coverslips were dried in a vacuum oven at 120 ^{0}C for 3 h.

4.3.7 Preparation of SERS Nanosensors and Drug Detection

The preparation of SERS nanosensor is described in **Figure 4.1**. Au TNPs with ~42 nm edge lengths were synthesized as explained in section 4.3.6. Then APTES-functionalized glass coverslips were incubated four an hour in freshly synthesized Au TNPs in order to self-assemble a layer of Au TNPs on the glass coverslips. The Au TNP-bound coverslips were washed thoroughly with acetonitrile to remove loosely adsorbed organic compounds (PMHS and TEA) and dried under nitrogen flow. After drying, 3M adhesive tape was placed on the Au TNP-containing glass substrate, pressed gently with the thumb, and removed at a 90^0 angle to remove the truncated structures and the aggregated AuTNPs. Once there is a nice assembly of Au TNPs on the substrates, the coverslips were incubated in 1 mM PEG_{60}-SH solution for overnight. The obtained LSPR peak (before and after functionalization) were utilized to ensure the functionalization. After that, the functionalized Au TNPS containing coverslips were placed in a glass container with 2 mL of ethanol to cover the coverslips and sonicated for 3-5 minutes. During the sonication, the PEG_{60}SH functionalized Au TNPs were easily lifted off into solution due to the Au-TNPs were self-assembled to APTES functionalized coverslips via Au-NH2 weak bond. We added functionalized Au TNPS containing coverslips into the same solution until desired LSPR intensity of the solution obtained. Finally, collected PEG_{60}SH functionalized Au TNPs containing ethanol solution was subjected to the ultracentrifugation (10 minutes at 13,000 rpm) to precipitated out the functionalized Au TNPs. The solution was decanted and the functionalized Au TNPs were then re dissolved in fresh ethanol (1 mL) solution and same procedure was carried out 4-5 times to make sure that excess PEG_{60}-SH is removed. After the final wash, all the ethanol was evaporated and the separated PEG60-SH functionalized Au TNPs were dissolved in 100 µL of nanopure water and sonicated for 5 minutes to avoid aggregation.25 µL of the solution was drop casted on each substrate and was covered with a plastic lid overnight to make the sensor via slow evaporation method.

Once the substrate was prepared, the drug (Fentanyl, Cocaine and JWH-018) concentration series was prepared in 10% human plasma in RNA's free water. 6 µL of sample solution was drop casted on to the developed sensor (2 µl X 3) and was left to dry overnight. Then SERS spectrum of each concentration were obtained.

For the patient sample analysis, same procedure was carried out. Accordingly, 6 µL of patient sample were diluted to make 10% plasma solution and the sample were introduced to the developed sensor via drop cast technique.

4.3.8 Analytical Enhancement Factor Calculations

We followed the literature procedure to determine the analytical EF of the nanosensor which was prepared on an OTES substrate.

According to the literature, the analytical enhancement factor (AEF) of a 3D self-assembly of Au TNPs can be estimated using the **Equation 1**. Here we utilize the ratio between the SERS intensity for the selected concentration of the analyte (fentanyl) (I_{SERS}) and the corresponding Raman intensity (I_{RS}) under same identical experimental conditions.

$$AEF = \frac{I_{SERS}}{I_{RS}} \frac{C_{RS}}{C_{SERS}} \quad (4.1)$$

C_{SERS} and C_{RS} are the concentrations of the analyte (Fentanyl) in the SERS and Raman experiments, respectively. Here, we selected for I_{SERS} the obtained intensity of 1334cm^{-1} peak, 6209 at 10^{-10} M concentration for I_{RS}, intensity of 97 at 10^{-3} M concentration. Accordingly, we have estimated 6.4 x 10^{8} AEF for the developed 3D assembly of Au TNPs on the OTES substrate.

4.4 Results and Discussion

In this chapter we report a simple droplet evaporation technique for the thermodynamically driven self-assembly process for Au TNPs by controlling the substrate property to obtain the highly sensitive 2D and 3D array for SERS Based Emergency room patient plasma assay.

Here in Au TNPs were used as the building blocks for the self-assembly process and synthesized using previously reported well establish method of our lab in which triethyl amine (TEA) was used as a capping agent. Detail synthesis procedure has been explained in the experimental section. After the synthesis, Au TNPs were transferred on to the solid substrate using APTES functionalized glass coverslips. However, TEA a C 2 hydrophobic straight-chain tertiary

amine does not facilitate the self-assembly process due to the nonexistence of attractive forces. Therefore, as shown in (**Figure 4.1A**) we subjected solid state ligand exchange of TEA capped AuTNPs with Poly (ethylene glycol) thiol (PEG_{60} -SH) average M_n 2,165 via overnight incubation in a 1 mM concentration. PEG_{60} -SH gradually replaced the TEA due to high affinity of Au-S bond. During this process we have investigated the effect of Poly (ethylene glycol) thiol chain length and the concentration (data is not reported) and optimized that 1 mM concentration PEG_{60} -SH has provided most efficient effective ligand exchange.

After the ligand exchange the properties of the solid-state substrate was determined by using Surface Enhanced Raman Spectroscopy as shown in **Figure 4.11Ba**.TEA capped Au TNPs has very distinguished peak around 1035 cm^{-1} and that peak has completely disappeared after PEG_{60}-SH functionalization which proves the 100% ligand exchange after overnight incubation. Also, SERS stretching of C-O-C was appeared at 1100 cm^{-1} which further confirms the successful ligand exchange reaction. Further we have used localized surface plasmon references (LSPR) peak changes upon ligand exchange to confirm the ligand exchange and accordingly LSPR peak has shown apparent 80 nm redshift and additionally FWHM of the peak has been increased upon PEG_{60} SH binding **Figure 4.1Bc**. That further provides evidence of successful ligand exchange process.

In order to achieve effective self-assembly process via selective evaporation, the PEG_{60}-SH functionalized Au TNPs needed to be transferred from solid state to solution phase. For this we have executed the simple lift off technique via gentle sonication over few minutes. TEA capped Au TNPs were originally transferred on to the APTES factionalized glass coverslips by forming Au -N bond. It is well known that SH terminated silane forms a strong covalent bond via Au-S bond and that NH_2 terminated alkanes are described to have a weak covalent interaction.[68-69] Further such interaction can be destroyed using small mechanical power. Due to that, during mild sonication, Au TNPs detached from the glass substrate and leave to the solution phase. As explained in experimental section here we have covered the 25 mm* 25 mm PEG_{60}-SH functionalized glass coverslips using 2 mL of reagent alcohol. Each coverslip has been sonicated 3-5 minutes and the sonicator temperature has been controlled under 20 ^{0}C to avoid the heat generation during the sonication. After the lift off process the 2 mL of PEG_{60}-SH functionalized Au TNPs were centrifuged at 13,000 rpm for 10 min to remove the loosely bound PEG_{60}-SH. The same procedure was repeated 5-6 times to make sure no unbounded PEG_{60}-SH existed. Before the

final wash UV spectrum of solution was measured and we always maintained the final concentration as 3 X 10^9. After the final wash, supernatant was carefully decanted, and solid substrate were carefully dried using N_2 gas. Succeeding careful removal of ethanol, 25 µL of nano-pure water was added to the tube and sonicated for few minutes to get the homogeneous solution. In order to study the deposition and evaporative directed self-assembly process we have utilized colloidal suspensions of PEG_{60} SH functionalized Au TNPs and three different types of functionalized silica substrates. **Figure 1B** summarizes the entire evaporation process and the substrate effect of the obtained self-assembly.

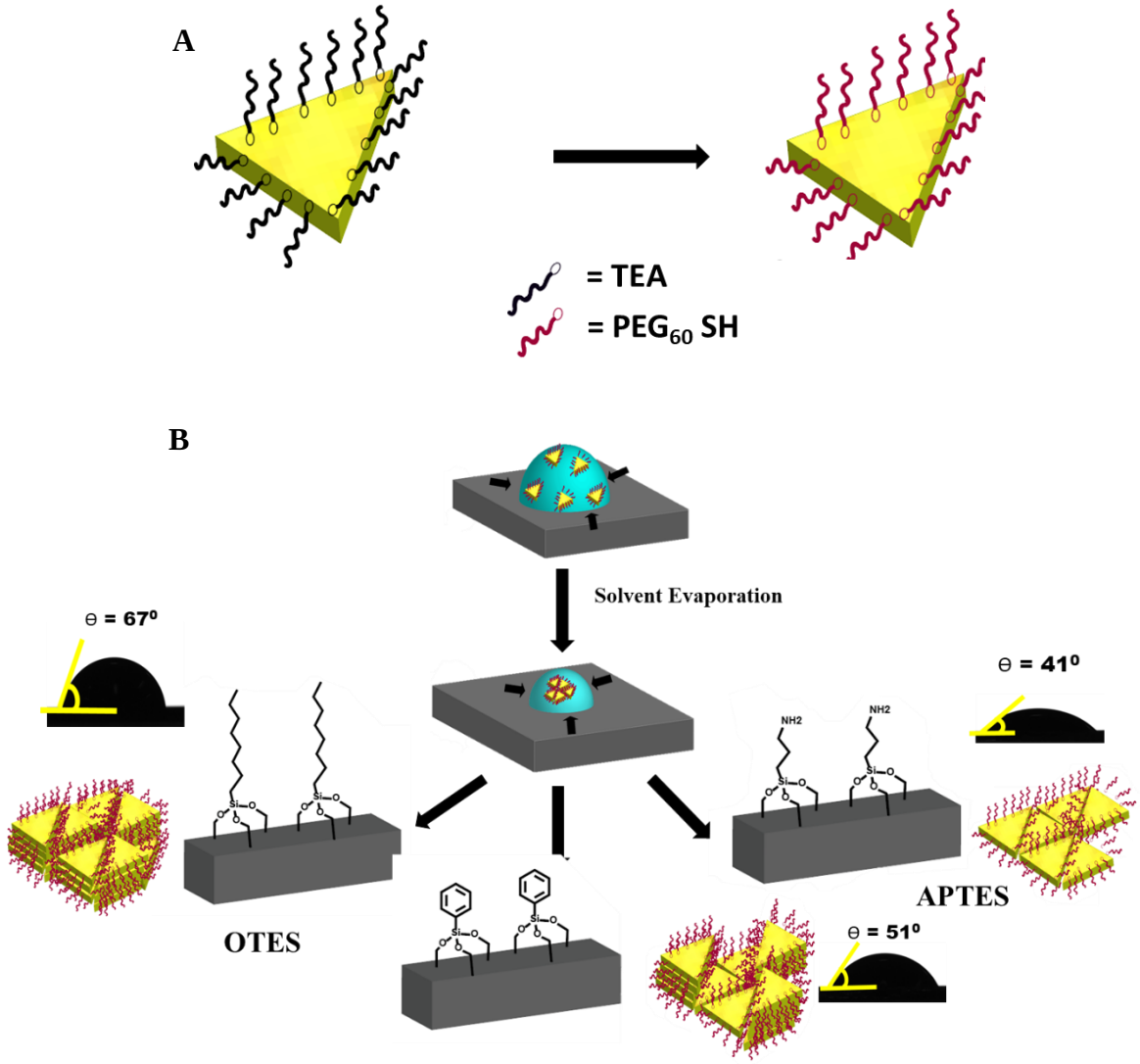

Figure 4. 1.A SERS sensor preparation via evaporative self-assembly process. A) Shows the schematic representation of ligand exchange of triethyl amine (TEA) capped Au TNPs with 1 mM Polyethylene glycol Mw (2160) (PEG60-SH), Figure 4.1B schematically show the droplet evaporation in order form a self-assembly on to the substrate, Further 1B-a) summarizes the formation of more uniform 3D self-assembly on to the OTES functionalized Si wafer and 1B-b) represents the formation mixture of 2D/3D self- assembly on to the PTES functionalized substrate and finally 1B-c) shows the formation of uniform 2D self-assembly on to the APTES functionalized Si wafer. Next to each substrate the nature of the obtained assembly has shown as a schematic representation. Additionally, it has shown how the contact angle of the obtained self-assembly varied upon functionalization.

Recent literature has reported many evaporations based self-assembly processes for different shapes of nanostructures. The working hypothesis of conventional droplet evaporation method is mainly controlled by kinetically formed capillary forces and convective liquid flow. In this case nanoparticles in the droplets move until they settle on to the substrate. Three main droplet evaporation modes are known. The constant contact radius (CCR) mode, in here the contact line is pinned on the solid substrate and the droplet evaporates with constant area and fading the contact angle. The second method is constant contact angle (CCA) mode where the contact line keeps on disappearing towards the center of the droplet and during the process the contact angle remains unchanged. Last of all, the mixed mode which usually occurs at the end of evaporation process. During evaporative self-assembly process it is possible to encounter serious obstacles during the process such as, pinning and depinning of the contact line can be occurred also so-called coffee ring effect, which is normally implemented to pattern of solute on surfaces. Recent scientists found that coffee ring effect can be suppressed by regulating the shape, stickiness, type, charge and the concertation of the particles. latest research has reported that by regulating the surface property of nanoparticles it can be completely reverse the coffee ring effect.

It is important to consider the leading factors which determine the transition from CCR to CCA mode during the evaporation in order to fully avoid the pinning dipping effect and the coffee ring effect in order to obtaining the effective self-assembly process. Literature has supported that CCR mode is prominent on a smooth hydrophilic surface and the CCA mode is prominent on a smooth hydrophobic surface.

Therefore, here in our study it is reported for the first time the effective large scale programmable homogenous self-assembly of Au TNPs by controlling the particle- particle interaction particle- suspension interaction, and droplet- substrate interaction.

As explained above we have obtained the efficient particle-particle interaction via PEG_{60}-SH functionalized Au TNPs. PEG_{60}-SH generates steric stabilization of the Au TNPs and PEG_{60}-SH functionalized Au TNPS are hydrophilic in nature due to the O bonds in the PEG_{60}-SH chain. Further this high molecular wait PEG_{60}-SH chain induces an additional stabilization via the short-range repulsive hydration forces. Besides that, this steric stabilization provides more adequate substrate for biological applications[70-73]. Since we are using PEG_{60} SH functionalized Au TNPs as colloidal suspension in water, we further introduce the steric stabilization of PEG_{60} SH functionalized Au TNPs.

Finally, in order to achieve the droplet substrate effect, we have used three different types of substrates, including n-octyltriethoxysilane (OTES) functionalized Si wafer, phenyltrimethoxysilane functionalized Si Wafer, (PTMS) and (3-Aminopropyl) triethoxysilane (APTES) functionalized Si wafer. Here, OTES functionalized Si Wafer acts as a super hydrophobic substrate due to the thick hydrophobic layer created by the long hydrocarbon chain and PTMS functionalized Si Wafer is considered to have a medium hydrophobic layer due the considerably shorter aromatic ring. The APTES functionalized Au TNPs is considered as the hydrophilic chain owing to terminal amine group. The detail explanation of substrate preparation is given in the experimental section.

As shown in the (**Figure 4.1C-a)** the PEG_{60}-SH capped Au TNPs creates a large contact angle with the ODTES functionalized Si-wafer due to the hydrophobicity nature and with less hydrophobic PTMS functionalized substrate they had a comparatively smaller contact angle (**Figure 4.1C-b)**. When it comes to the hydrophilic APTES functionalized substrate, the contact angle was so small (**Figure 4.1C-c)**.

Finally, the droplets were covered with a plastic lid and allowed to slowly evaporate on a substrate at humidity of $60\% \pm 5\%$ at room temperature.

Further, as shown in **Figure 4.1C-a-c** we have measured the contact angle of the droplet using ramé-hart Contact Angle Goniometer and confirmed that contact angle increases with increasing hydrophobicity. Based on the contact angle variation here we have successfully obtained three different types of assembly structure. During the evaporation process of PEG_{60} SH functionalized Au TNPs on APTES functionalized hydrophilic surface, we have obtained the 2D assembly and on the less hydrophobic (PTMS) substrate it was given the mixture of 2D and 3D assembly where more hydrophobic substrate (OTES) provided uniform ordered close 3D stacking on to the substrate.

The mechanism of formation of three different types of Au TNPs were proposed according to the previously reported literature. Accordingly**,** APTES functionalized Si wafer substrate where the angle is closer to the contact line and is pinned on the solid substrate and the droplets evaporates with constant area and fading the contact angle which resulted in 2D assembly. When substrate is more hydrophobic, OTES functionalized Au TNPs, the CCA mode is more prominent and the contact line keeps disappearing towards the center of the droplet and during the process the contact

angle remains unchanged. Therefore, the PEG_{60} functionalized Au TNPs started forming 3D uniform stacking. In this as we are tailoring the all three interactions, particle- particle interaction, particle- suspension interaction, and droplet- substrate interaction, it provided the more uniform plasmonic 3D super lattice array. However, on the moderate hydrophobic PTMS substrate both CCR and CCS modes are existing, therefore it ended with a mixture of 2D and 3D assembly. Obtained 2D and or 3D assembly is shown in the **Figure 4.2-(A-F)**.

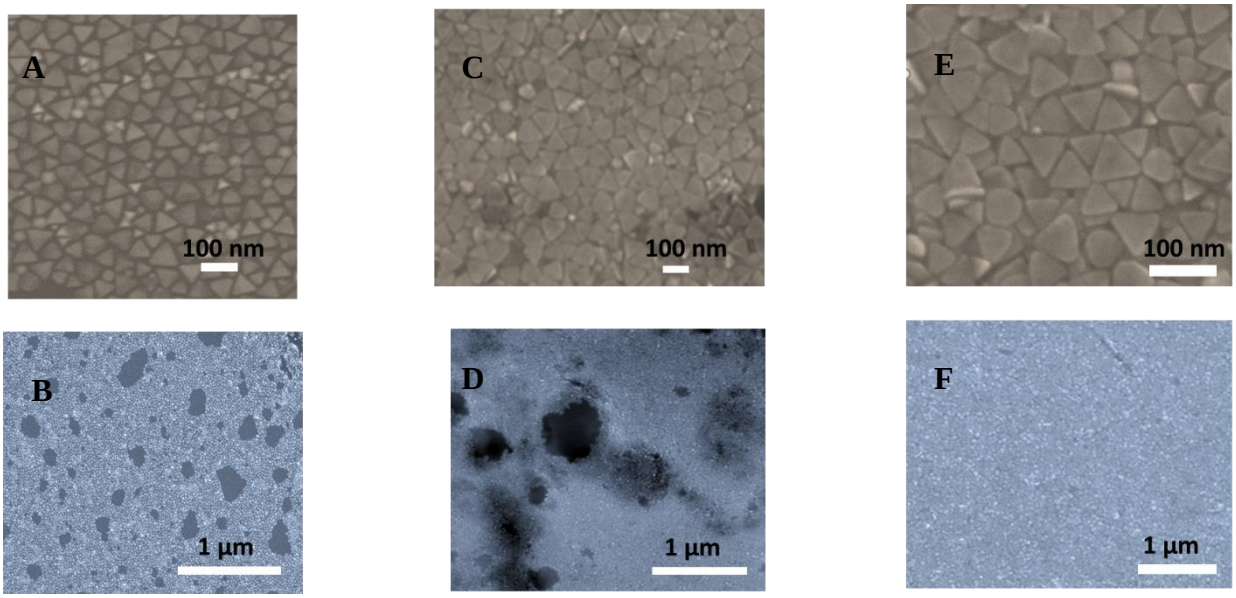

Figure 4. 2. The SEM images of the obtained self-assembly. Accordingly, 2D self-assembly obtained on APTES substrates has shown in **A, B** and obtained mixture of 2D/3D self-assembly obtained on PTES substrates has shown in **C, D.** Finally, 3D assembly on to the OTES substrate has shown in **E, F.** The respect scale bar represents inside the image.

4.4.1 Developed Substrate for SERS Based Drug Analysis

After successful optimization of the evaporative self-assembly of PEG_{60} capped Au TNPs the super plasmonic properties of the developed substrate was determined based on the vibration spectra obtained from the SERS. For this study we mainly focused on developing noninvasive highly sensitive SERS based analysis for simulated toxicology samples. For that we have selected the analyte based on their occurrence as forensic exhibits. Accordingly, we utilize Opiates- Fentanyl, Coca Alkaloids- Cocaine and Cannabinoids- JWH-O18 as analytes. Therefore, after preparation the 2D, 2D/3D and 3D assembly we drop casted 6 µL of 100 nM- 100 pM dilution series of the analyte in 10% of human plasma and let the sample be deposited on the developed substrate. Then the Raman spectra were acquired.

4.4.2 Detection, Quantification, and Classification of Fentanyl, Cocaine and JWH-018 Using SERS

We have studied the use of our SERS nanosensors for quantitative detection of Fentanyl as a standard drug. As explained earlier we prepared a fentanyl solution in 10% plasma over the range of 1.0 mM to 1pM through serial dilution. A 6.0 µL solution of each concentration was drop-casted on six different nanosensors of each substrate. **Figure 4.3A** shows the SERS spectra for different Fentanyl concentrations on OTES functionalized substrate where the low standard deviation of the SERS peak intensity proves the exceptional reproducibility in our 3D assembly. Furthermore, a wide linear range spanning 10 orders of magnitude (**Figure 4.3D-black squares**, 10^{6} to 10^{-3} nM) between the fentanyl concentration and the SERS peak intensity was observed. The LOD was determined using a more sophisticated equation and found to be 130 parts-per-quadrillion (ppq) (see the experimental section for detailed LOD calculation). Importantly, we were able to quantify fentanyl at 1 pM concentration with signal-to-noise ratio of 3.3. The sensitivity of our 3D assembled SERS nanosensor is at least several order magnitudes better than other Au nanostructure-based SERS nanosensors for opiates detection. We believe this excellent sensitivity is because of the strong EM field enhancement of Au TNPs at their sharp tips and the large number of hot spots created upon 3D self-assembly on to the OTES substrate. Additionally, **Figure 4.3B** shows the fentanyl concentrations (1 mM to 100 pM) on PMTS functionalized substrate and using **Figure 4.3D-circles** of Raman intensity vs the Fentanyl concentration plot, we calculated LOD of the PTES functionalized substrate as 2.4 ppt. It also showed a wide linear range spanning five orders of magnitude (10^{3} to 10^{-2} nM) between the fentanyl concentration and the SERS peak intensity on PMTS functionalized substrate. We have observed comparatively large deviation of the standard deviation on this substrate, and we believe it's due to the less homogeneity of the SERS substrates. This observation further proved our proposed mechanism of self-assembly on to PTES substrate where we have obtained mixture of 2D and 3D self-assembly. Furthermore, **Figure 4.3C** shows the fentanyl concentrations (1 mM to 100 pM) on APTES functionalized substrate and we have obtained an LOD of 22 ppt using **Figure 4.3 blue triangle** of Raman intensity vs the Fentanyl concertation plot**.** As we expected when the self-assembly changes from 2D to 3D, a drastic change of sensitivity occurs. Our developed self-assembly based detection technique stipulates numerous rewards over conventional analytical methods which included GC-MS, ion-mobility MS, and electrochemistry. Those well-established techniques required large amount

sample volumes and required particular laboratory environment and it may include expensive sample processing and labeling for the final analysis.

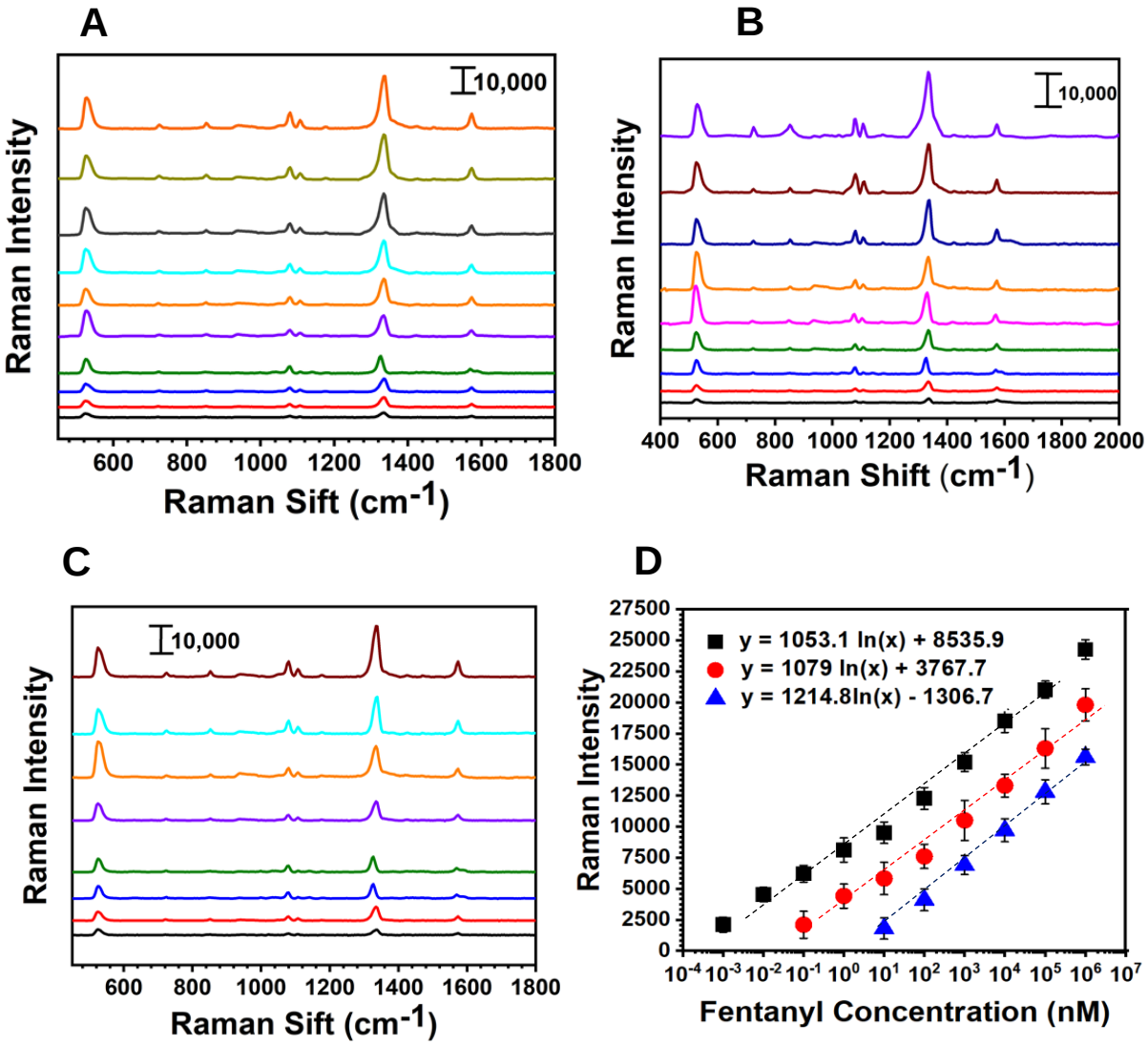

Figure 4. 3. SERS spectra of Fentanyl on to the three different functional groups containing SERS substrate. (A) Fentanyl from 1.0 mM to 1 PM on OTES functionalized Si Wafer (B) Fentanyl from 1.0 mM to 10 PM on PTES functionalized Si Wafer and (C) Fentanyl from 1.0 mM to 1 PM on APTES functionalized Si Wafer. (D) The plot of SERS intensity as function of Fentanyl C-N stretching at 1334 cm^{-1}versus Fentanyl concentration on logarithm scale shows in black squares, red circles and blue triangles on OTES, PMTS and APTES functionalized substrate respectively. The dashed lines represent the linear concentration ranges. Average SERS intensity was determined from 6 measurements.

After optimization of the highest SERS sensitivity of the OTES functionalized Si Wafer substrate we used Coca Alkaloids- Cocaine and Cannabinoids- JWH-O18 as analytes for further

detection. Synthetic cannabinoids such as JWH-018 are commonly used as a psychoactive substance and is associated in large with vivo toxicological effects in public health due to the less knowledge. Therefore, this compound is hugely associated with emergency room visits and mortalities[74]. Also, Cocaine is a highly addictive coca alkaloids stimulant and it is the most commonly abused drug in the United States. Many people are attracted to cocaine for the quick, euphoric high the drug provides. Literature has reported that the use of cocaine and cannabis either individually or in combination resulted in significantly higher mortality risk compared with other ED patients.[75] Therefore we have selected these two compounds because there is an unmet need to develop an ultrasensitive nanosensor that is capable of detecting and quantifying these drugs along with an efficient sampling process, which better would expand the potential applications of SERS nanosensor.

With this aim we were able to quantitatively measure cocaine and JWH-018 utilizing SERS nanosensors with LODs of 32.3 and 118.9 ppq, respectively. **Figure 4.4A-D** show SERS spectra and calibration plots for cocaine and JWH-018. Here we utilized the aromatic ring (C=C) stretch at 1586 cm^{-1} for calibration peak[76] for cocaine and naphthalene CH stretching at 1393 cm^{-1} for JWH-018.[74] Amazingly, Cocaine and JWH-018 also display an unprecedentedly large linear range spanning nine (10^5 to 10^{-3} nM) orders of magnitude between the concentration and the Raman peak intensity. This observation rationalizes the uniform 3D self-assembly of our developed sensors. However, among these compounds' cocaine has shown the highest sensitivity with a ~4-fold increase compared to fentanyl and JWH-01. Here we proposed a simple adsorption model of these drugs onto (111) facets of Au TNP (**Figure 4.4E-G**). Among these analytes, cocaine has the highest number of SP3 C compared to the more planar and rigid molecules of fentanyl and JWH-018, and thus the adsorption onto Au TNP surface requires fentanyl and JWH-018 to be flat. Under this circumstance, number analyte molecule per nm^2 surface area is expected to be low. In contrast, cocaine molecules can form multiple Au-N and Au-O interactions without occupying a large surface area because of the high degree of flexibility in their molecular structure due to the more SP3 nature, which could result in more molecules effectively adsorbed onto the TNP surface.

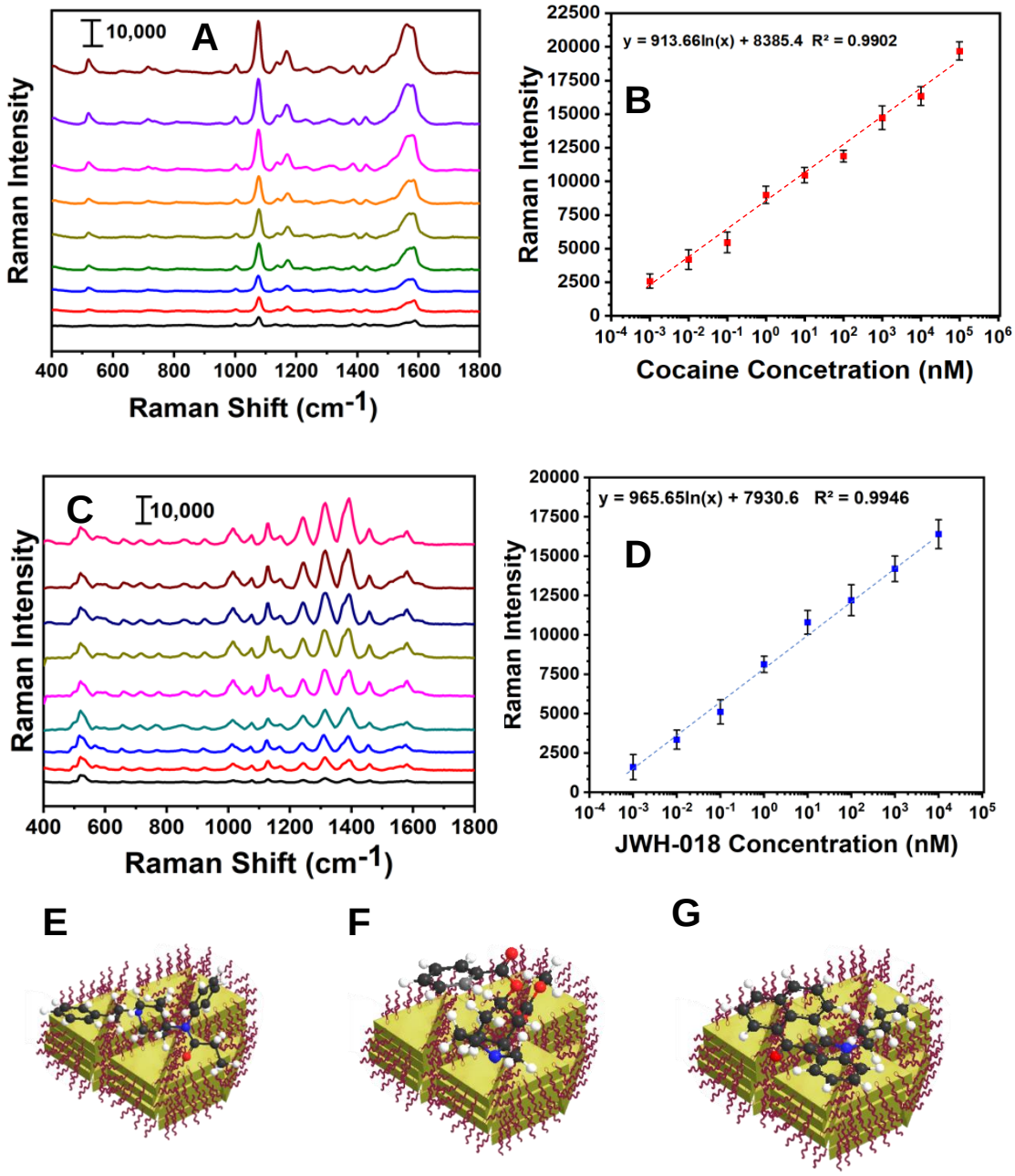

Figure 4. 4. SERS spectra and LOD plots for drugs on to the OTES SERS substrate. (A) Cocaine from 100 µM to 1 PM and (B) JWH-018 from 100 µM to 1 PM on OTES functionalized Si Wafer and. The plot of SERS intensity as function of Cocaine C=C stretching at 1586 cm-1 versus cocaine concentration on logarithm scale shows in (C), and (D) intensity of JWH-018 naphthalene CH stretching at 1393 cm-1 versus JWH-018 concentration on logarithm scale shows in on OTES functionalized nanosensors. The dashed lines represent the linear concentration ranges. Average SERS intensity was determined from 6 measurements. (E-G) Schematic illustration of adsorption of the three different drug molecules fentanyl, Cocaine and JWH-018 respectively onto the PEG60-SH functionalized Au TNP self-assembly on to the OTES Si wafer surface. The images are not to scale.

4.4.3 Direct Quantification of Cocaine and Fentanyl on Human Plasma of Emergency Room Patient Sample Using Developed 3D Self-Assembled SERS Nanosensors

The initial assessment and treatment of suspected drug poisoning of patients who attends an emergency room rapidly decide to buy the physicians based on the therapeutic measures and disposal. But the efficiency of this process mainly depends on the clinical status and the resources available at the hospital. The special challenge for emergency physicians for rapid accurate certain diagnosis for efficient treatment procedure. Moreover, at the emergency room has a specific procedure for drug screening and it required a separate unit to perform the analysis. These procedures can determine of over 900 drugs and their metabolites, but the analysis may take over of 20 to 60 minutes. However, the effectiveness of the screening process has been questioned[77]. Therefore, the aim of this study is to mainly focus on developing cost effective highly sensitive simple SERS based drug screening technique for emergency room patient samples for rapid and high accurate assessment of drugs and hence decrease drug overdose death rates. For this purpose, we have assayed seven patient sample plasma obtained from an emergency room using our developed highly sensitive SERS based 3D assembled nanosensors. **Figure 4.5A** shows the SERS spectra obtained from seven different patient samples. Here we have drop casted 6 µL of 10% diluted patient sample on to the 3D self-assembled $PEG_{60}SH$ capped AU-TNPs containing nanosensors. After obtaining the spectra we have evaluated it using developed calibration curves using the intensity of the peak of interest. For cocaine we used we utilized the aromatic ring (C=C) stretch at 1586 cm^{-1} and for fentanyl we used C-N stretching at 1334 cm^{-1}.

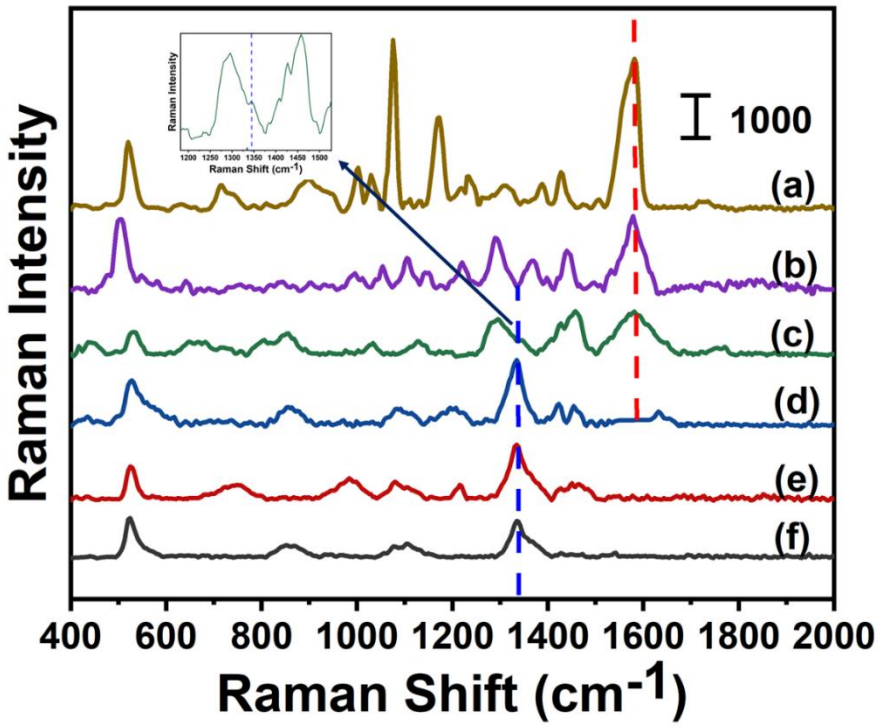

Figure 4. 5. SERS spectra of 6 UL of patient sample diluted 10% in Rnase free water a) patient 46 (b) patient 52 (C) patient 5 (D) patient 44 (E) patient 55 (F) patient 43 onto the PEG60-SH functionalized Au TNP self-assembly on to the OTES Si wafer surface. The blue dashed lines represent the peaks appears with respect to the C-N stretching at 1334 cm-1 of Fentanyl and red line represent the C=C stretching at 1586 cm-1 of cocaine. Average SERS intensity was determined from 6 measurements.

As summarized in **Table 4.1** we have quantified the concentration of a drug using developed calibration curve.

Table 4.1. Summarize the assayed analyte concentration in emergency room patient plasma. Column 1 shows the patient description and column 2 provide detail explanation of GCMS identified analyte composition. Column 3 summarizes the calculated concentration based on developed fentanyl and cocaine calibration of nanosensor on to the OTES Si wafer surface. Last column was given the semiquantitative concentrations obtained using GC-MS.

Sample Number	**Type of Analyte**	**Concentration of Cocaine 10% diluted 6 mL sample (pg/mL)**	**Concentration of Cocaine 10% diluted 6 mL sample (pg/mL)**
(a)	Cocaine	1.47	
(b)	Cocaine	0.23	
(c)	Fentanyl or acryl fentanyl, cocaine, furanyl fentanyl	0.11	0.13
(d)	AB-PINACA, Furanyl Fentanyl, Methamphetamine		0.40
(e)	Acrylfentanyl or Fentanyl, Codeine		0.36
(f)	Acryl fentanyl or fentanyl, furanyl fentanyl		0.22

Additionally, we were curious to see the SERS spectra of patient samples that do not contain the interested cocaine or fentanyl analytes. As shown in **Figure 4.6B** obtained SERS spectra clearly shows an absence of our interested aromatic ring (C=C) stretch at 1586 cm^{-1} of cocaine and C-N stretching at 1334 cm^{-1} for fentanyl. This confirms the high selectivity of the developed nanosensor for more accurate screening process**.**

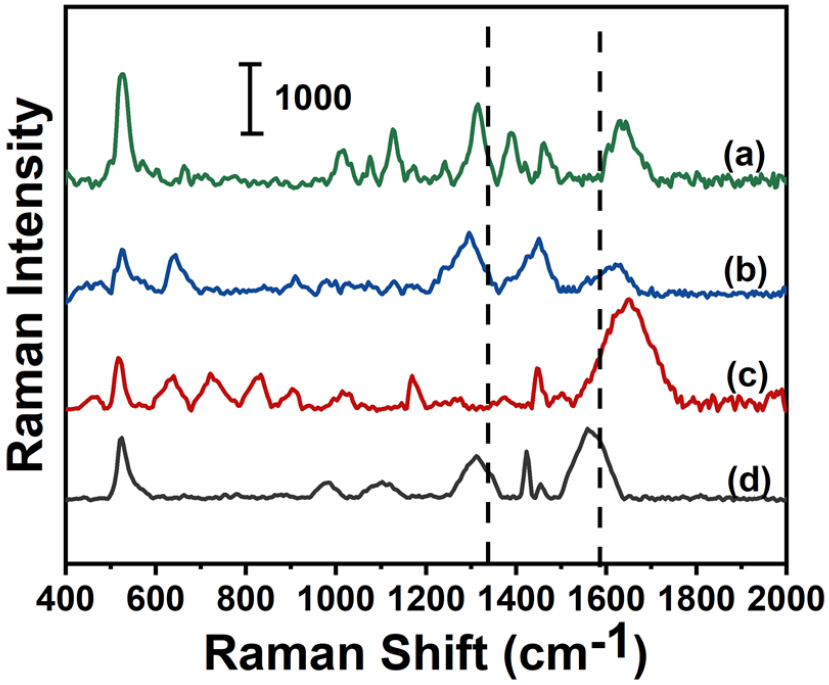

Figure 4. 6. SERS spectra of 6 μL of patient sample diluted 10% in Rnase free water for selectivity test a) patient 11 (b) patient 2 (C) patient 17 (D) patient 45 (E) patient 55 (F) patient 43 onto the PEG60-SH functionalized Au TNP self-assembly on to the OTES Si wafer surface. The black dashed lines represent the absence of peaks appears with respect to the C-N stretching at 1334 cm-1 of Fentanyl and the C=C stretching at 1586 cm-1 of cocaine.

4.5 Summary

In summary, we have developed a highly sensitive and selective SERS nano- sensor for trace level drug detection by successful 3D self-assembling Au TNPs onto a substrate using simple molecular tailored droplet evaporation technique. Here, we mainly utilized the surface property (hydrophilicity and hydrophobicity) of the substrate Accordingly, we were able to achieve 2D, 2D/3D and 3D self-assembly of PEG60-SH capped Au TNPS on to the APTES, ODTES, PMTES functionalized substrates respectively. By utilizing our SERS 3D nanosensors, we quantitatively detected Opiates- Fentanyl, Coca Alkaloids- Cocaine and Cannabinoids- JWH-O18 and achieved the 130, 32.3 and 118.9 ppq sensitivity respectfully. This level of sensitivity has not been previously demonstrated in nanosensor- based drug detection. We assumed that such outstanding sensitivity evolves from the strong EM field enhancement of TNPs at their sharp tips and edges

during the 3D assembly and based on the we have calculated our EM field enhancement as 6.4 x 10^8.

This is one of highest EM field enhancement that could occur on Au based SERS substrates. Furthermore, the developed substrate was successfully utilized direct analysis fentanyl and cocaine of the emergency room patient plasma, using our developed ultrasensitive SERS based nanosensor. Accordingly, we only use 10% diluted, 6 µL emergency room patient plasma samples without further purification and we were able to quantify in ppt concentrations. Also, we have further confirmed the high selectivity of the assay for the targeted analytes by detecting different patient samples which do not contain the target analytes. All our data were validated using standard paper spray mass spectrometry-based evaluation. Altogether, our newly design sensor showing promising application for an efficient diagnosis of drugs during toxicology screening at emergency room applications and we believe this sensor will be highly beneficial for in the challenges that the united states in public health and national security because of the illicit drugs.

4.6 References

1. Dombrowski, K.; Crawford, D.; Khan, B.; Tyler, K., Current Rural Drug Use in the US Midwest. *Journal of drug abuse* **2016,** *2* (3).
2. Harrison, L. D., Trends in illicit drug use in the United States: conflicting results from national surveys. *The International journal of the addictions* **1992,** *27* (7), 817-47.
3. Novak Scott, P.; Kral Alex, H., Comparing injection and non-injection routes of administration for heroin, methamphetamine, and cocaine users in the United States. *Journal of addictive diseases* **2011,** *30* (3), 248-57.
4. Schulden Jeffrey, D.; Thomas Yonette, F.; Compton Wilson, M., Substance abuse in the United States: findings from recent epidemiologic studies. *Current psychiatry reports* **2009,** *11* (5), 353-9.
5. Harduar Morano, L.; Steege Andrea, L.; Luckhaupt Sara, E., Occupational Patterns in Unintentional and Undetermined Drug-Involved and Opioid-Involved Overdose Deaths - United States, 2007-2012. *MMWR. Morbidity and mortality weekly report* **2018,** *67* (33), 925-930.

6. Kariisa, M.; Scholl, L.; Wilson, N.; Seth, P.; Hoots, B., Drug Overdose Deaths Involving Cocaine and Psychostimulants with Abuse Potential - United States, 2003-2017. *MMWR. Morbidity and mortality weekly report* **2019,** *68* (17), 388-395.
7. Knutson, D. E.; Li, G.; Prevot, T.; Arnold, L.; Chiou, L.-C.; Ernst, M.; Mihovilovic, M.; Savic, M.; Sieghart, W.; Sibille, E.; Cook, J. M., Combatting the opioid and benzodiazepine epidemic by the synthesis of novel safer drugs designed to be functionally selective for α5- or α6-containing GABAA receptors. *Abstracts of Papers, 258th ACS National Meeting & Exposition, San Diego, CA, United States, August 25-29, 2019* **2019**, MEDI-0157.
8. Mack, K. A.; Jones, C. M.; Ballesteros, M. F., Illicit Drug Use, Illicit Drug Use Disorders, and Drug Overdose Deaths in Metropolitan and Nonmetropolitan Areas-United States. *American Journal of Transplantation* **2017,** *17* (12), 3241-3252.
9. Mack Karin, A.; Ballesteros Michael, F.; Jones Christopher, M., Illicit Drug Use, Illicit Drug Use Disorders, and Drug Overdose Deaths in Metropolitan and Nonmetropolitan Areas-United States. *American journal of transplantation : official journal of the American Society of Transplantation and the American Society of Transplant Surgeons* **2017,** *17* (12), 3241-3252.
10. Mack Karin, A.; Ballesteros Michael, F.; Jones Christopher, M., Illicit Drug Use, Illicit Drug Use Disorders, and Drug Overdose Deaths in Metropolitan and Nonmetropolitan Areas - United States. *Morbidity and mortality weekly report. Surveillance summaries (Washington, D.C. : 2002)* **2017,** *66* (19), 1-12.
11. O'Donnell Julie, K.; Halpin, J.; Mattson Christine, L.; Goldberger Bruce, A.; Gladden, R. M., Deaths Involving Fentanyl, Fentanyl Analogs, and U-47700 - 10 States, July-December 2016. *MMWR. Morbidity and mortality weekly report* **2017,** *66* (43), 1197-1202.
12. Scholl, L.; Seth, P.; Kariisa, M.; Wilson, N.; Baldwin, G., Drug and Opioid-Involved Overdose Deaths - United States, 2013-2017. *MMWR. Morbidity and mortality weekly report* **2018,** *67* (5152), 1419-1427.
13. VanHouten Jacob, P.; Rudd Rose, A.; Ballesteros Michael, F.; Mack Karin, A., Drug Overdose Deaths Among Women Aged 30-64 Years - United States, 1999-2017. *MMWR. Morbidity and mortality weekly report* **2019,** *68* (1), 1-5.
14. National Highway Traffic Safety Administration (NHTSA) and the National, I. o. A. A. a. A. N., A Guide to Sentencing DWI Offenders. **2005**.

15. Lager, P. S.; Attema-de Jonge, M. E.; Gorzeman, M. P.; Kerkvliet, L. E.; Franssen, E. J. F., Clinical value of drugs of abuse point of care testing in an emergency department setting. *Toxicology reports* **2018,** *5*, 12-17.
16. Ashraf, Z.; Rahmati, E.; Bender, J. M.; Nanda, N.; She, R. C., GDH and toxin immunoassay for the diagnosis of Clostridioides (Clostridium) difficile infection is not a 'one size fit all' screening test. *Diagnostic Microbiology and Infectious Disease* **2019,** *94* (2), 109-112.
17. Dziadosz, M.; Teske, J.; Henning, K.; Klintschar, M.; Nordmeier, F., LC-MS/MS screening strategy for cannabinoids, opiates, amphetamines, cocaine, benzodiazepines and methadone in human serum, urine and post-mortem blood as an effective alternative to immunoassay based methods applied in forensic toxicology for preliminary examination. *Forensic Chemistry* **2018,** *7*, 33-37.
18. McKenna, J.; Jett, R.; Shanks, K.; Manicke, N. E., Toxicological drug screening using paper spray high-resolution tandem mass spectrometry (HR-MS/MS). *Journal of Analytical Toxicology* **2018,** *42* (5), 300-310.
19. Schackmuth, M.; Kerrigan, S., Immunoassay-based detection of fentanyl analogs in forensic toxicology. *Forensic Toxicology* **2019,** *37* (1), 231-237.
20. Zhong, J.; Hu, X.; Zhang, X.; Liu, Y.; Xu, C.; Zhang, C.; Lin, M.; Liu, X., Broad specificity immunoassay for detection of Bacillus thuringiensis Cry toxins through engineering of a single chain variable fragment with mutagenesis and screening. *International Journal of Biological Macromolecules* **2018,** *107* (Part_A), 920-928.
21. Ciasca, B.; Pascale, M.; Altieri, V. G.; Longobardi, F.; Suman, M.; Catellani, D.; Lattanzio, V. M. T., In-house validation and small-scale collaborative study to evaluate analytical performances of multimycotoxin screening methods based on liquid chromatography-high-resolution mass spectrometry: Case study on Fusarium toxins in wheat. *Journal of Mass Spectrometry* **2018,** *53* (9), 743-752.
22. Glicksberg, L.; Bryand, K.; Kerrigan, S., Identification and quantification of synthetic cathinones in blood and urine using liquid chromatography-quadrupole/time of flight (LC-Q/TOF) mass spectrometry. *Journal of Chromatography B: Analytical Technologies in the Biomedical and Life Sciences* **2016,** *1035*, 91-103.

23. Revel'skii, I. A.; Chivarzin, M. E.; Revel'skii, A. I.; Buryak, A. K., Analysis of total concentration of halogen- and sulfur-containing organic compounds at trace level in water and foods. *Journal of Analytical Chemistry* **2019,** *74* (2), 176-181.
24. Shi, W.; Guo, J.; Yu, H. Effect-oriented target/non-target androgen disruptor identification method [Machine Translation]. 2016-10252354 105891365, 20160421., 2016.
25. Song, S.; Yang, L.; Trepicchio, W. L.; Wyant, T., Understanding the supersensitive anti-drug antibody assay: unexpected high anti-drug antibody incidence and its clinical relevance. *Journal of Immunology Research* **2016**, 3072586/1-3072586/8.
26. Krinsky Clarissa, S.; Lathrop Sarah, L.; Crossey, M.; Baker, G.; Zumwalt, R., A toxicology-based review of fentanyl-related deaths in New Mexico (1986-2007). *The American journal of forensic medicine and pathology* **2011,** *32* (4), 347-51.
27. Lee, J.; Krotulski, A. J.; Fogarty, M. F.; Papsun, D. M.; Logan, B. K., Chromatographic separation of the isobaric compounds cyclopropylfentanyl, crotonylfentanyl, methacrylfentanyl, and para-methylacrylfentanyl for specific confirmation by LC-MS/MS. *Journal of Chromatography B: Analytical Technologies in the Biomedical and Life Sciences* **2019,** *1118-1119*, 164-170.
28. Lee, J.; Krotulski Alex, J.; Fogarty Melissa, F.; Papsun Donna, M.; Logan Barry, K., Chromatographic separation of the isobaric compounds cyclopropylfentanyl, crotonylfentanyl, methacrylfentanyl, and para-methylacrylfentanyl for specific confirmation by LC-MS/MS. *Journal of chromatography. B, Analytical technologies in the biomedical and life sciences* **2019,** *1118-1119*, 164-170.
29. Palmer, R. B., Fentanyl in postmortem forensic toxicology. *Clinical Toxicology* **2010,** *48* (8), 771-784.
30. Chimalakonda, K. C.; Bratton, S. M.; Le, V.-H.; Yiew, K. H.; Dineva, A.; Moran, C. L.; James, L. P.; Moran, J. H.; Radominska-Pandya, A., Conjugation of synthetic cannabinoids JWH-018 and JWH-073, metabolites by human UDP-glucuronosyltransferases. *Drug Metabolism and Disposition* **2011,** *39* (10), 1967-1976.
31. Hutter, M.; Moosmann, B.; Kneisel, S.; Auwaerter, V., Characteristics of the designer drug and synthetic cannabinoid receptor agonist AM-2201 regarding its chemistry and metabolism. *Journal of Mass Spectrometry* **2013,** *48* (7), 885-894.
32. adminstration, U. D. o. j. d. e., 2018 National drug threat assesment. **2018**.

33. Al Mamun, A.; Yu, F.; Stoddart, P. R., Double clad fiber improves the performance of a single-ended optical fiber sensor. *Journal of Lightwave Technology* **2018,** *36* (18), 3999-4005.
34. Huefner, A.; Kuan, W.-L.; Muller, K. H.; Skepper, J. N.; Barker, R. A.; Mahajan, S., Characterization and Visualization of Vesicles in the Endo-Lysosomal Pathway with Surface-Enhanced Raman Spectroscopy and Chemometrics. *ACS Nano* **2016,** *10* (1), 307-316.
35. Tratt, D. M.; Whiteman, D. N.; Demoz, B. B.; Farley, R. W.; Wessel, J. E., Active Raman sounding of the earth's water vapor field. *Spectrochimica Acta, Part A: Molecular and Biomolecular Spectroscopy* **2005,** *61A* (10), 2335-2341.
36. Schluecker, S., Surface-Enhanced Raman Spectroscopy: Concepts and Chemical Applications. *Angewandte Chemie, International Edition* **2014,** *53* (19), 4756-4795.
37. Sharma, B.; Frontiera, R. R.; Henry, A.-I.; Ringe, E.; Van Duyne, R. P., SERS: Materials, applications, and the future. *Materials Today (Oxford, United Kingdom)* **2012,** *15* (1-2), 16-25.
38. Al-Shammari, R. M.; Al-attar, N.; Manzo, M.; Gallo, K.; Rodriguez, B. J.; Rice, J. H., Single-Molecule Nonresonant Wide-Field Surface-Enhanced Raman Scattering from Ferroelectrically Defined Au Nanoparticle Microarrays. *ACS Omega* **2018,** *3* (3), 3165-3172.
39. Jia, Q.; Geng, Z.-Q.; Liu, Y.; Wang, W.; Han, C.-Q.; Yang, G.-H.; Li, H.; Qu, L.-L., Highly reproducible solid-phase extraction membrane for removal and surface-enhanced Raman scattering detection of antibiotics. *Journal of Materials Science* **2018,** *53* (21), 14989-14997.
40. Piorek, B. D.; Lee, S. J.; Moskovits, M.; Meinhart, C. D., Free-Surface Microfluidics/Surface-Enhanced Raman Spectroscopy for Real-Time Trace Vapor Detection of Explosives. *Analytical Chemistry (Washington, DC, United States)* **2012,** *84* (22), 9700-9705.
41. Piorek Brian, D.; Lee Seung, J.; Moskovits, M.; Meinhart Carl, D., Free-surface microfluidics/surface-enhanced Raman spectroscopy for real-time trace vapor detection of explosives. *Analytical chemistry* **2012,** *84* (22), 9700-5.
42. Kim, I.-H.; Kim, J. H.; Choi, J.-Y.; Shin, C. H.; Kim, J.-H.; Bae, G.-T.; Shin, K. S., Tuning the interparticle distances in self-assembled gold nanoparticle films with their plasmonic responses. *Chemical Physics Letters* **2019,** *715*, 91-99.

43. Li, H.; Gu, Y.; Guo, H.; Wang, X.; Liu, Y.; Xu, W.; Xu, S., Tunable Plasmons in Shallow Silver Nanowell Arrays for Directional Surface-Enhanced Raman Scattering. *Journal of Physical Chemistry C* **2012,** *116* (44), 23608-23615.
44. Meng, J.; Tang, X.; Zhou, B.; Xie, Q.; Yang, L., Designing of ordered two-dimensional gold nanoparticles film for cocaine detection in human urine using surface-enhanced Raman spectroscopy. *Talanta* **2017,** *164*, 693-699.
45. Seo, S.; Chang, T.-W.; Liu, G. L., 3D Plasmon Coupling Assisted Sers on Nanoparticle-Nanocup Array Hybrids. *Scientific Reports* **2018,** *8* (1), 1-11.
46. Joshi Gayatri, K.; Liyanage, T.; Lawrence, K.; Mali, S.; Sardar, R.; Deitz-McElyea, S.; Korc, M.; Sardar, R., Label-Free Nanoplasmonic-Based Short Noncoding RNA Sensing at Attomolar Concentrations Allows for Quantitative and Highly Specific Assay of MicroRNA-10b in Biological Fluids and Circulating Exosomes. *ACS Nano* **2015,** *9* (11), 11075-89.
47. Joshi, G. K.; Blodgett, K. N.; Muhoberac, B. B.; Johnson, M. A.; Smith, K. A.; Sardar, R., Ultrasensitive Photoreversible Molecular Sensors of Azobenzene-Functionalized Plasmonic Nanoantennas. *Nano Letters* **2014,** *14* (2), 532-540.
48. Joshi, G. K.; Deitz-McElyea, S.; Johnson, M.; Mali, S.; Korc, M.; Sardar, R., Highly Specific Plasmonic Biosensors for Ultrasensitive MicroRNA Detection in Plasma from Pancreatic Cancer Patients. *Nano Letters* **2014,** *14* (12), 6955-6963.
49. Joshi, G. K.; Deitz-McElyea, S.; Liyanage, T.; Lawrence, K.; Mali, S.; Sardar, R.; Korc, M., Label-free nanoplasmonic-based short noncoding RNA sensing at attomolar concentrations allows for quantitative and highly specific assay of MicroRNA-10b in biological fluids and circulating exosomes. *ACS Nano* **2015,** *9* (11), 11075-11089.
50. Joshi, G. K.; McClory, P. J.; Muhoberac, B. B.; Kumbhar, A.; Smith, K. A.; Sardar, R., Designing Efficient Localized Surface Plasmon Resonance-Based Sensing Platforms: Optimization of Sensor Response by Controlling the Edge Length of Gold Nanoprisms. *Journal of Physical Chemistry C* **2012,** *116* (39), 20990-21000.
51. Joshi, G. K.; Smith, K. A.; Johnson, M. A.; Sardar, R., Temperature-Controlled Reversible Localized Surface Plasmon Resonance Response of Polymer-Functionalized Gold Nanoprisms in the Solid State. *Journal of Physical Chemistry C* **2013,** *117* (49), 26228-26237.

52. Joshi, G. K.; White, S. L.; Johnson, M. A.; Sardar, R.; Jain, P. K., Ultrashort, Angstrom-Scale Decay of Surface-Enhanced Raman Scattering at Hot Spots. *Journal of Physical Chemistry C* **2016,** *120* (43), 24973-24981.
53. Liyanage, T.; Masterson, A. N.; Oyem, H. H.; Kaimakliotis, H.; Nguyen, H.; Sardar, R., Plasmoelectronic-Based Ultrasensitive Assay of Tumor Suppressor microRNAs Directly in Patient Plasma: Design of Highly Specific Early Cancer Diagnostic Technology. *Analytical Chemistry (Washington, DC, United States)* **2019,** *91* (3), 1894-1903.
54. Liyanage, T.; Rael, A.; Shaffer, S.; Zaidi, S.; Goodpaster John, V.; Sardar, R., Fabrication of a self-assembled and flexible SERS nanosensor for explosive detection at parts-per-quadrillion levels from fingerprints. *The Analyst* **2018,** *143* (9), 2012-2022.
55. Liyanage, T.; Rael, A.; Shaffer, S.; Zaidi, S.; Goodpaster, J. V.; Sardar, R., Fabrication of a self-assembled and flexible SERS nanosensor for explosive detection at parts-per-quadrillion levels from fingerprints. *Analyst (Cambridge, United Kingdom)* **2018,** *143* (9), 2012-2022.
56. Liyanage, T.; Sangha, A.; Sardar, R., Achieving biosensing at attomolar concentrations of cardiac troponin T in human biofluids by developing a label-free nanoplasmonic analytical assay. *Analyst (Cambridge, United Kingdom)* **2017,** *142* (13), 2442-2450.
57. Chen, X.; Wen, J.; Zhou, J.; Zheng, Z.; An, D.; Wang, H.; Xie, W.; Zhan, R.; Xu, N.; Chen, J.; She, J.; Chen, H.; Deng, S., Superhydrophobic SERS substrates based on silicon hierarchical nanostructures. *Journal of Optics (Bristol, United Kingdom)* **2018,** *20* (2), 024012/1-024012/9.
58. Liu, X.; Zhao, L.; Shen, H.; Xu, H.; Lu, L., Ordered gold nanoparticle arrays as surface-enhanced Raman spectroscopy substrates for label-free detection of nitroexplosives. *Talanta* **2011,** *83* (3), 1023-1029.
59. Yang, S.; Dai, X.; Stogin Birgitt, B.; Wong, T.-S., Ultrasensitive surface-enhanced Raman scattering detection in common fluids. *Proceedings of the National Academy of Sciences of the United States of America* **2016,** *113* (2), 268-73.
60. Zhang, D.; Hao, R.; Fang, J.; You, H.; Yuan, L.; Li, T., Hydrophobic Slippery Surface-Based Surface-Enhanced Raman Spectroscopy Platform for Ultrasensitive Detection in Food Safety Applications. *Analytical chemistry* **2019,** *91* (7), 4687-4695.

61. Zhang, D.; You, H.; Yuan, L.; Hao, R.; Li, T.; Fang, J., Hydrophobic Slippery Surface-Based Surface-Enhanced Raman Spectroscopy Platform for Ultrasensitive Detection in Food Safety Applications. *Analytical Chemistry (Washington, DC, United States)* **2019,** *91* (7), 4687-4695.
62. Zhang, H.; Zhou, F.; Liu, M.; Liu, D.; Men, D.; Cai, W.; Duan, G.; Li, Y., Spherical Nanoparticle Arrays with Tunable Nanogaps and Their Hydrophobicity Enhanced Rapid SERS Detection by Localized Concentration of Droplet Evaporation. *Advanced Materials Interfaces* **2015,** *2* (9), 1500031/1-1500031/9.
63. Li, P.; Li, Y.; Tang, S.; Yu, X.-F.; Xiao, Q.; Zhao, Y.; Wang, H.; Li, P.; Chu Paul, K.; Zhou, Z.-K.; Xiao, S.; Wu, Z., Evaporative Self-Assembly of Gold Nanorods into Macroscopic 3D Plasmonic Superlattice Arrays. *Advanced materials (Deerfield Beach, Fla.)* **2016,** *28* (13), 2511-7.
64. Shaikeea, A.; Basu, S.; Hatte, S.; Bansal, L., Insights into Vapor-Mediated Interactions in a Nanocolloidal Droplet System: Evaporation Dynamics and Affects on Self-Assembly Topologies on Macro- to Microscales. *Langmuir* **2016,** *32* (40), 10334-10343.
65. Jia, Y.; Chen, C.; Jia, D.; Li, S.; Ji, S.; Ye, C., Silver Nanowire Transparent Conductive Films with High Uniformity Fabricated via a Dynamic Heating Method. *ACS applied materials & interfaces* **2016,** *8* (15), 9865-71.
66. Kim, C.; Nogi, M.; Suganuma, K.; Saitou, Y.; Shirakami, J., Absorption layers of ink vehicles for inkjet-printed lines with low electrical resistance. *RSC Advances* **2012,** *2* (22), 8447-8451.
67. Liu, C.-F.; Lin, Y.; Lai, W.-Y.; Huang, W., Improved performance of inkjet-printed Ag source/drain electrodes for organic thin-film transistors by overcoming the coffee ring effects. *AIP Advances* **2017,** *7* (11), 115008/1-115008/7.
68. Akkerman, H. B.; Blom, P. W. M.; de Leeuw, D. M.; de Boer, B., Towards molecular electronics with large-area molecular junctions. *Nature (London, United Kingdom)* **2006,** *441* (7089), 69-72.
69. Podstawka, E.; Ozaki, Y.; Proniewicz Leonard, M., Part III: Surface-enhanced Raman scattering of amino acids and their homodipeptide monolayers deposited onto colloidal gold surface. *Applied spectroscopy* **2005,** *59* (12), 1516-26.

70. Gref, R.; Luck, M.; Quellec, P.; Marchand, M.; Dellacherie, E.; Harnisch, S.; Blunk, T.; Muller, R. H., 'Stealth' corona-core nanoparticles surface modified by polyethylene glycol (PEG): influences of the corona (PEG chain length and surface density) and of the core composition on phagocytic uptake and plasma protein adsorption. *Colloids and Surfaces, B: Biointerfaces* **2000,** *18* (3,4), 301-313.
71. Morla-Folch, J.; Guerrini, L.; Pazos-Perez, N.; Arenal, R.; Alvarez-Puebla, R. A., Synthesis and Optical Properties of Homogeneous Nanoshurikens. *ACS Photonics* **2014,** *1* (11), 1237-1244.
72. Moore, T. L.; Rodriguez-Lorenzo, L.; Hirsch, V.; Balog, S.; Urban, D.; Jud, C.; Rothen-Rutishauser, B.; Lattuada, M.; Petri-Fink, A., Nanoparticle colloidal stability in cell culture media and impact on cellular interactions. *Chemical Society Reviews* **2015,** *44* (17), 6287-6305.
73. Guerrini, L.; Alvarez-Puebla Ramon, A.; Pazos-Perez, N.; Alvarez-Puebla Ramon, A., Surface Modifications of Nanoparticles for Stability in Biological Fluids. *Materials (Basel, Switzerland)* **2018,** *11* (7).
74. Deriu, C.; Conticello, I.; Mebel, A. M.; McCord, B., Micro solid phase extraction surface-enhanced Raman spectroscopy (μ-SPE/SERS) screening test for the detection of the synthetic cannabinoid JWH-018 in oral fluid. *Analytical Chemistry (Washington, DC, United States)* **2019**, Ahead of Print.
75. Gilmore, D.; Zorland, J.; Akin, J.; Emshoff James, G.; Kuperminc Gabriel, P.; Johnson, J. A., Mortality risk in a sample of emergency department patients who use cocaine with alcohol and/or cannabis. *Substance abuse* **2018,** *39* (3), 266-270.
76. Yang, L.; Liu, H.; Wang, J.; Zhou, F.; Tian, Z.; Liu, J., Metastable state nanoparticle-enhanced Raman spectroscopy for highly sensitive detection. *Chemical Communications (Cambridge, United Kingdom)* **2011,** *47* (12), 3583-3585.
77. Fabbri, A.; Marchesini, G.; Morselli-Labate, A. M.; Ruggeri, S.; Fallani, M.; Melandri, R.; Bua, V.; Pasquale, A.; Vandelli, A., Comprehensive drug screening in decision making of patients attending the emergency department for suspected drug overdose. *Emergency medicine journal : EMJ* **2003,** *20* (1), 25-8.

CHAPTER 5 ACHIEVING BIOSENSING AT ATTOMOLAR CONCENTRATIONS OF CARDIAC TROPONIN T IN HUMAN BIOFLUIDS BY DEVELOPING A LABEL-FREE NANOPLASMONIC ANALYTICAL ASSAY

This article has been reprinted with permission. Liyanage, T.; Sangha, A.; Sardar, R., Achieving biosensing at attomolar concentrations of cardiac troponin T in human biofluids by developing a label-free nanoplasmonic analytical assay. The Analyst 2017, 142 (13), 2442-2450 DOI:10.1039/C7AN00430C.

5.1 Synopsis

Noble metal nanoparticles display localized surface plasmon resonance (LSPR) properties. By utilizing such unique optical properties of nanoparticles (Nps) various label-free sensors were developed to detect proteins, DNAs, and microRNAs. However, a precise knowledge demonstrating how to effectively immobilize bio-recognition molecules. ("receptor") on the surface of the nanoparticles to enhance the sensitivity is still elusive. To fill this gap, we have investigated the effects of structural parameters of receptor molecules for detection of Cardiac Troponin T (cTnT). We have selected cTnT as a model system for detection and quantification because this protein regulates actin and tropomyosin during muscle contraction and is present in cardiomyocytes. During myocardial infarction (MCI), myocytes disintegrate, releasing free cTnT into the bloodstream, which causes a short-term increase in concentration of cTnT. Through selectively controlling the spacing between receptor and nanoprism, and the number of receptors per nanoprism we are able to quantify cTnT in human serum and plasma as low as 0.5 pg/L. We believe our ultrasensitive detection of cTnT would result early diagnostic for heat attack.

5.2 Introduction

The field of label free detection of biomolecules (protein, DNA, RNA) using on Localized surface plasmon resonance (LSPR) of metalic nanostructures has been advanced over the past the decades[1-11]. The LSPR of the nobel metals generates due to the collective oscillation of the conduction electrons upon light irradiation and as we discussed in chapter 1 the size, shape and the local dielectric environment is mainly controlling the LSPR frequencies[4, 5, 9, 12]. Here in this report we have been developed LSPR based bio sensor which can be characterized using LSPR

extinction spectral changes upon changes of the dielectric environment[8, 13-15], to assay utilized cardiac Troponin-T (cTnT) which is a highly studied biomarker in the cardiovascular diseases. This study has reported limit of detection (LOD) as low as 507 fg/L (10^4 folds better sensitivity than commercialized technology) and the capability of detecting cTnT in complex biological fluids[16, 17].

The quantification of surface bound proteins using LSPR technique has been reported in the literature, which is started from Chilkoti[18] and Van Duyne[5] group for the chip-based sensors and Arnold and coworkers[19] and Stenberg et al.[20] has also utilized the LSPR for protein assay. Here they mainly utilized the nanoparticles inducing refractive index (RI) change in the LSPR properties which can be monitored via the variation in the peak intensity or as a shift in the LSPR peak position ($\Delta\lambda_{LSPR}$)[4, 5].

The sensing mechanism of the LSPR based sensors are mainly controlled from several parameters including shape, size, sensing volume, decay length which is directly control the electromagnetic (EM) field enhancement[6, 8, 21] and hence the sensitivity of the developed sensors. Additionally, number of receptor molecules on to the nanostructure also plays a critical role on the final sensitivity[4, 6, 22]. Accordingly, it is important to consider the linker length, the position of analyte-receptor complex and the density of the receptor on to the nanostructure. Therefore, systematic understanding of effect these surface ligand structural parameters together for highly sensitive LSPR based sensing application is much more important.

In this article, we have studied the effect of sensing volume by mainly considering the structural parameters of receptor molecules for Au TNPs for sensing application by considering cTnT as the model analyte. The fabrication of the chip- based sensor was carried out as depicted in **Figure 5.1** and with our findings we have shown that the decay length of the Au TNPs which is controlled by the number of methylene units of the alkylthios of the self-assembled monolayer (SAM) plays a critical role to achieve the highest sensitivity for cTnT detection even in different types of undiluted biological fluids without losing the high specificity. Further we investigated the effect of the receptor concentration which was the (anti-cTnT) for cTnT bindings to obtain the highest sensitivity without disturbing the selectivity of the developed sensors.

Altogether, we have developed the sensor based on three different structural parameters that controls the sensing volume. Accordingly. (i) an ~42 nm edge-length Au TNP, (ii) 1.7 nm distance between Au TNP and anti-cTnT, and (iii) an 8:2 ratio of receptor-to-spacer ration utilized

and under the optimized condition we were successfully able to detect cTnT with the highest sensitivity LODs of 7.2, 14.5, 21.9 aM in phosphate buffer saline (PBS), human plasma, and human se-rum, respectively. Additionally, experimentally validate the reproducibility of the developed sensor by accounting batch to batch variation and found high reproducibility of our sensor responses.

cTnT is an ideal biomarker which has been consider for symptom free early diagnosis of heart attack (>10 ng/L level is considered to be high risk for Myocardial Infarction) and the developed simple, cost-effective, and ultrasensitive assay in real human biofluids will be capable of highly efficient assay of cTnT, hence prevent heart attack by early diagnosis[23, 24].

5.3 Materials and Methods

5.3.1 Materials

Chloro(triethylphosphine) gold (I) (Et3PAuCl, 97%), poly(methylhydrosiloxane) (PMHS, Mn = 1700-3300), trioctylamine (TOA, 98%), ACS grade acetonitrile (CH3CN, 99.9%), methanol (99.8%), N-hydroxysulfosuccinimide solution (NHS), 1-ethyl-3-(3-dimethylamino) pro-pyl carbodiimide (EDC), human plasma, human serum, and all alkylthiols were purchased from Sigma-Aldrich and were used without further purification. Human urine was purchased from (UTAK Laboratories). Human cTnT and sheep anti-cTnT were obtained from Protein-Specialists and Fisher Scientific, respectively. 3-Mercaptopropyl)-triethoxysilane (MPTES, 94%) was pur-chased from Alfa Aesar. All organic solvents, reagents for PBS buffer (pH = 7.4) preparation, RBS35 detergent, and the glass coverslips (Cat. No. 12548C) were purchased from Thermo Fisher Scien-tific. Nanopure water was used for PBS buffer preparation and for all cleaning purposes.

5.3.2 Spectroscopy and Microscopy Characterization

A Varian Cary 50 Scan UV-visible spectrophotometer was used to collect absorption and extinction spectra in the range of 300- 1100 nm. Absorption spectra of gold nanoprism solutions were obtained by diluting 0.3 mL of reaction solution to a final volume of 2.0 mL with acetonitrile in a 1 cm quartz cuvette. Acetonitrile was used as a background in each run before collecting the absorbance spectra. Background subtracted (using silanized glass coverslips) extinction spectra of our LSPR cTnT biosensors were measured in PBS buffer (pH 7.4) at room temperature. Before

each measurement, the sensors were incubated in buffer solution for 10 min to equilibrate and then extinction spectra were collected. Scanning Electron Microscopy (SEM) was used to determine the average edge-length of gold nanoprisms used in our biosensor fabrication.

5.3.3 Silanization of Glass Coverslips

Glass coverslips were functionalized based on previously reported procedure at chapter 2.3.3.

5.3.4 Synthesis of Gold Nanoprisms

We synthesized gold triangular nanoprisms (Au TNPs) according to same procedure reported in chapter 2.3.4.

5.3.5 LOD and KD Calculations

The LODs were determined according to the literature as follows: (1) Measure the ΔλLSPR for the blank sample (anti-cTnT functionalized Au TNPs attached onto glass coverslips). (2) Determine the Z (mean + 3σ) value, where σ is the standard deviation.5 (3) Convert Z value into relative concentration using a calibration curve. We determined the effective dissociation constant (KD) using the highest ΔλLSPR value and then best fit the data to a Langmuir isotherm.

5.3.6 Preparation of Chip-Based Format Biosensors and Quantification of cTnT in Biofluids

To understand the effects of nanoscale structural parameters on sensor performance, coverslips containing Au TNPs were incubated in an ethanolic solution of thiols to prepare self-assembled monolayers (SAMs) as follows: (a) For sensing volume optimization, 16-mercaptohexadecanoic acid (MHDA) and 1-dodecanethiol (DDT) each of 1.0 mM concentration were used. (b) For decay length optimization in addition to the MHDA/DDT SAM, two ad-additional SAMs were prepared using 6-mercaptohexanoic acid (MHNA) and 1-hexanethiol (HT), or 11-mercaptoundecanoic acid (MUDA) and 1-nonanethiol (NT) each using 1.0 mM concentration. (c) For optimization of cTnT binding sites, we used MUDA/NT SAMs of varying mole ratios. After the SAM preparation, coverslips were washed with plenty of ethanol and then extinction spectra were collected. Next, SAM-modified Au TNPs were incubated in a PBS buffer solution containing EDC/NHS (0.2 M

each) for 2h to activate the carboxylic group. The coverslips were then placed in-to a solution containing 10.0 μg/L of sheep-anti-TnT, incubated overnight at room temperature, then washed with a copious amount of PBS buffer, and stored in buffer for further use. This produced our chip-based format LSPR biosensors. The biosensors were then used to determine the LODs in PBS buffer and various biological fluids (pure human plasma and serum, and 50% human urine) by incubating for 8-12 h in different concentrations of cTnT, which were prepared through serial dilution. An ~2.5 mL of cTnT solution is required to incubate 5 LSPR cTnT biosensors.

5.4.1 Optimization of Sensing Volume of Chip-Based LSPR cTnT Biosensor

We selected Au TNPs to fabricate our LSPR biosensors for their unique structural and optical properties as delineated below:

(i) In order use the LSPR biosensors as analytical tools it is important to perform measurements under normal atmosphere and in actual biofluids. Non-noble metal nanoparticles such as copper and aluminum are susceptible to corrosion under these conditions.[14] Although silver nanoparticles display very high LSPR sensitivity, they undergo fast photooxidation in air under physiological conditions, and thus optical measurements are generally performed under more inert conditions.

(ii) TNPs demonstrate strong EM-field enhancement at their sharp tips and edges[16, 30, 31]and are thus capable of providing higher sensitivity than spherical gold nanoparticles or nanorods.6 Although nanostars could provide better sensitivity41 due to the presence of multiple arms with sharp tips in their structure, controlling the overall size and arm length is extremely difficult. Therefore, large batch-to-batch variations in their structure could result in large deviations in analytical measurements. A few other geometries of Au such as nanorice, nanorings, and nanoshells provide high LSPR sensitivity but, they display λLSPR >900 nm.[8] This spectral region is not ideal for biosensing applications in part because of high background absorption and scattering from endogenous chromophores in biofluids (e.g., plasma, serum, urine). In this context, the spectral region between 700-900 nm is the most suitable for LSPR-based biosensing and we can utilize this by controlling the edge-length of the Au TNPs.[25]

(iii) TNPs display larger sensing volume than spherical/disk-shaped nanoparticles. Furthermore, this volume can be controlled by varying their edge-lengths while maintaining their

thickness, and longer edge-length TNPs provide larger LSPR sensing volume (Vs).[5] The Vs is defined as the fixed volume surrounding a TNP that contains 95% of its sensitivity.[32]

We first chemically synthesized 34, 42, and 47 nm average edge-length Au TNPs that displayed LSPR dipole extinction peak (λLSPR) at 750, 800, and 820 nm, respectively using our published procedure.[14, 15]**Figure 5.2A-C** show representative SEM images of three different edge-length Au TNPs bound onto glass coverslips. Based on our published work, these Au TNPs are found to be nearly same (± 1.5 nm) thickness.[15, 26, 27, 29, 33]A representative atomic force microscopy image is shown in **Figure. 5.2D**. We investigated three nanoscale structural parameters to maximize the biosensor response, and further evaluated the sensor performance in quantifying cTnT in complex biofluids. **Figure 5.2E** illustrates the stepwise λ_{LSPR} shifts of 42 nm edge-length Au TNPs at different functionalization steps. Firstly, incubation of glass coverslip containing Au TNPs in mixed MHDA/DDT solution (1:1 ratio) (**see Figure 5.1B**) provided an ~27 nm redshift. The direction of the LSPR shift is in agreement with an increase in local R.I. (n = 1.5) of Au TNPs due to formation of the SAM. We selected DDT as part of the SAM because it would not only act as a spacer and reduce steric hindrance between proteins, but it would also avoid nonspecific adsorption of unwanted biomolecules onto the surface of TNPs. Secondly, the SAM-modified Au TNPs were then reacted with 0.2 M EDC/NHS solution to active the acid group of MHDA followed by incubation in anti-cTnT overnight (**Figure 5.1C**), which resulted in an additional 12 nm red-shift of the λ_{LSPR} (see **Figure 5.2E** and insert red double headed arrow). Attachment of anti-cTnT produced our chip-based format LSPR cTnT biosensor. We selected chemical attachment of anti-cTnT to Au TNPs through an amide bond to enhance stability and increase reproducibility by lowering loss of protein during various incubation steps. Thirdly, incubation of the biosensors in cTnT solution (**Figure 5.1D**) should provide an addition-al red-shift in λ_{LSPR} (**Figure 5.1E**) as a consequence of the change in the local R.I. that occurred from cTnT binding to anti-cTnT-cTnT. As shown in Fig. 2E (insert black double headed arrow), this hypothesis is in agreement with an ~7 nm red shift of λLSPR upon incubation of biosensors in 10 nM (350,000 ng/L) cTnT solution in PBS buffer. Finally, concentration-dependent λLSPR shifts ($\Delta\lambda_{LSPR}$) of the biosensors before and after cTnT incubation were calculated from the center of the LSPR peak, which was used to determine LODs (**Figure. 5.1E**). We also determined the stepwise λ_{LSPR} shifts of the other two edge-length Au TNPs (**Figure. 5.2F**). We indeed observed that the largest edge-length Au TNPs displayed the highest shift as a consequence of their highest sensing volume.

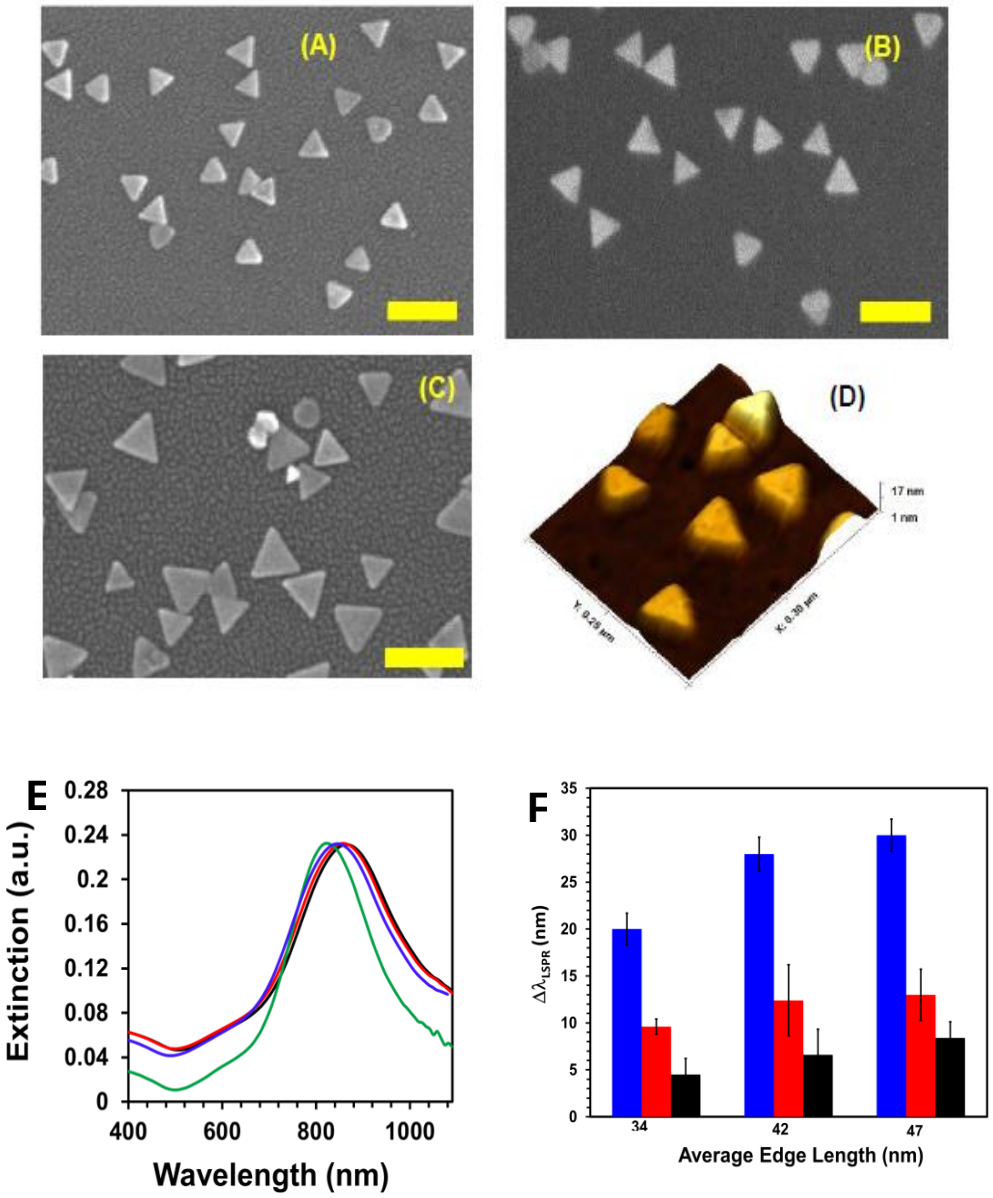

Figure 5.1. Microscopy and spectroscopy characterization of chip based LSPR cTnT biosensors. Scanning electron microscopy (SEM) image of 34 nm (A), 42 nm (B), and 47 nm (C) edge-length Au TNPs. The scale bars are 100 nm. (D) Atomic force microscopy image of 42 nm edge-length Au TNPs. (E) UV-visible extinction spectra of 42 nm edge-length Au TNPs attached onto silanized glass substrate (green, λLSPR = 825 nm) and after MHDA/DDT SAM formation (blue, λLSPR = 852 nm), after attachment of anti-cTnT through EDC/NHC coupling (red, λLSPR = 864 nm), and after incubation in 10 nM cTnT solution (black, λLSPR = 871 nm). All extinction spectra were collected in PBS buffer in order to avoid the effects of bulk refractive index (R.I.) caused by surrounding media.(F) Average ΔλLSPR values for three different edge-lengths Au TNPs after

MHDA/DDT SAM formation (blue bars), anti-cTnT attachment (red bars), and incubation in 10 nM cTnT solution (black bars).

Table 5.1. Calibration curve and the limit of detection (LOD) for chip based LSPR cTnT sensors constructed with various edge lengths of Au TNPs. The LSPR dipole peak position ($\boldsymbol{\lambda}_{LSPR}$) of Au TNPs in acetonitrile. S.D. represents standard deviation. At least 500 Au TNPs to determine the average $\boldsymbol{\Delta\lambda}_{LSPR}$.

Edge Length (S.D)	Equation	R^2 Value	Z value	LOD (ng/L)	LOD (pM)
34 (2.6)	y = 0.3909ln(x) - 0.389	0.99	2.3	974	27.8
42 (3.5)	y = 0.5993ln(x) - 0.888	0.98	1.7	75.4	2.2
47 (4.9)	y = 0.5025ln(x) + 1.628	0.98	1.6	0.9	0.026

Table 5.1 summarize the LODs of our LSPR cTnT biosensors fabricated with 34, 42, and 47 nm edge-length Au TNPs, which were determined to be 974, 75.4, and 0.9 ng/L, respectively. A de-tail procedure for LOD calculation is provided in the Experimental Section. Our LOD values for cTnT (protein) detection are in agreement with the literature report in which gold nanoparticles with the largest diameter displayed the highest LSPR sensing ability for detection of streptavidine (protein) in PBS buffer.[18] Importantly, the concentration-dependent λ_{LSPR} shifts are found to be linear at lower cTnT concentration (**Figure. 5.3**). The linear detection ranges of cTnT for 47, 42, and 34 nm edge-length Au TNPs were 3.5-35000, 350-35000, and 350-35000 ng/L, respectively. Our finding of a 3-4 order of magnitude linear range for cTnT detection corroborates literature report on LSPR-based detection of protein (antibody).[33] Furthermore, the error bars are smaller at lower concentration, indicating better quantifying ability of our biosensors at lower

concentration range. These experimental values are critical in terms of detecting low abundance biomolecules, which has been found challenging using LSPR biosensors.[34] Nevertheless, the lowest LOD of 0.9 ng/L (26 fM) is ~13 fold better than the commercial instrument, which is commonly used to quantify cTnT levels in patients with cardiovascular diseases.[35] It is important to mention that we did not con-sider the effect of potential plasmonic coupling between the adjacent Au TNPs that could enhance the overall sensitivity.

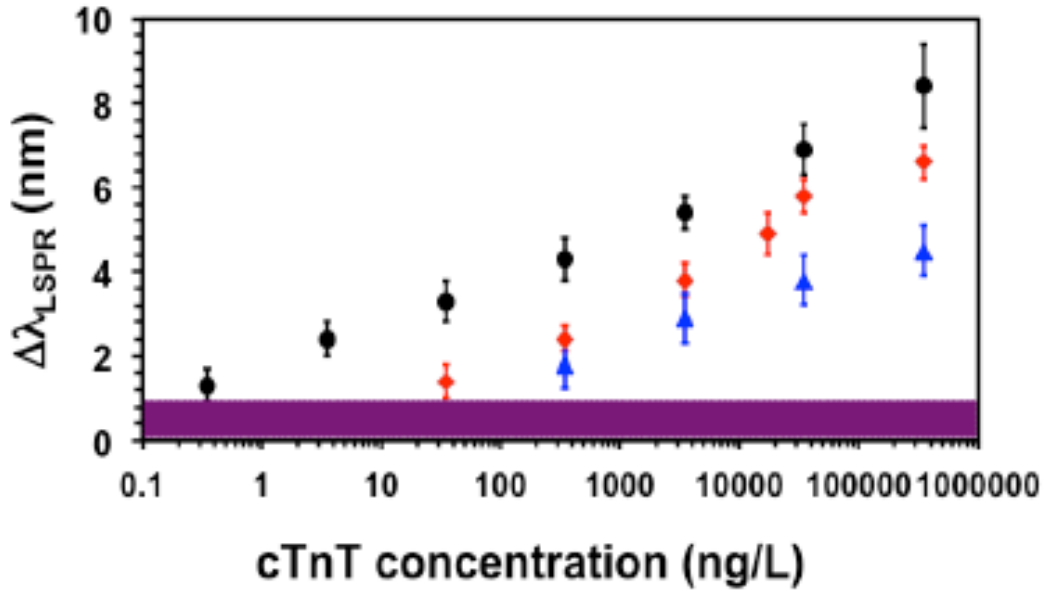

Figure 5.2. Determination of sensing efficiency of LSPR cTnT biosensors. Plot of average ΔλLSPR of biosensors that were fabricated with three different edge length Au TNPs as a function of cTnT concentration (in logarithm) in PBS buffer: black dots (47 nm edge-length), red diamonds (42 nm edge-length), and blue triangles (34 nm edge-length). The purple bar represents three times the standard deviation (σ) of the blank (mixed anti-cTnT/DDT functionalized Au TNPs attached onto a glass coverslip). The concentration was plotted in log scale to examine the non-specific adsorption of proteins at the lower concentration range, as is routinely used to characterize the sensitivity of the LSPR biosensors.[18, 36]

Our LSPR cTnT biosensors with the best sensitivity were prepared with 47 nm edge-length Au TNPs and displayed an LOD of 26 fM in PBS buffer. This is in agreement with the literature that the largest nanostructures display the highest sensitivity because of their largest sensing volume. However, the various required surface functionalization in the process of sensors fabrication for this edge-length Au TNPs resulted a λLSPR peak in the near-infrared region at ~910 nm. Here the water absorption peak can potentially interfere with the λLSPR maximum of Au TNPs and cause misleading LOD values. To avoid potential challenges in precise quantification of cTnT in complex biological fluids using our biosensors, we decided to use 42 nm edge length Au TNPs (LOD = 2.2 pM) for further investigation of the effects of decay length.

5.4. Results and Discussion

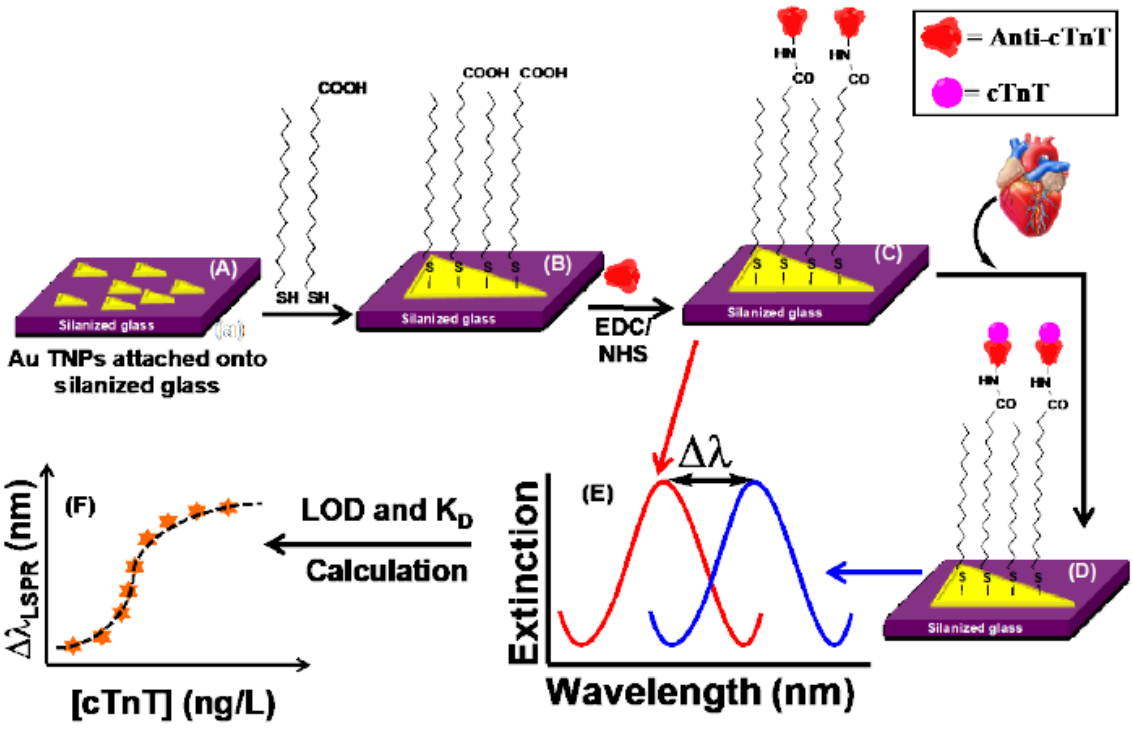

Figure 5.3. Design of a chip-based format LSPR cTnT biosensor. (A) Au TNPs attached onto silanized glass, (B) after being functionalized with a 1:1 mole ratio of 1-dodecanethiol and 16-mercaptohexadecanoic acid, (C) further functionalization with anti-cTnT through EDC/NHS amide coupling to complete the nanosensor, (D) detection of cTnT upon binding to anti-cTnT on sensor surface, (E) representation of nanosensor ab-sorption maxima (λLSPR) peak shift before and after binding of cTnT, and (F) relationship between ΔλLSPR and cTnT concentration to calculate the LOD and KD. For simplicity, only one Au TNP is shown in the functionalization steps. The image is not to scale.

5.4.2 Standardization of Surface Chemistry and Decay Length of LSPR cTnT Biosensors

The **Equation-1** below reported by Campbell and coworkers to quantify the overall response of surface plasmon resonance sensors[37] is commonly used to characterize the sensitivity of LSPR biosensors:[5, 37]

$$\Delta\lambda_{LSPR} = m\Delta n e^{-2r/L}\left(1 - e^{-2r/L}\right) \quad \textbf{(1)}$$

Here Δn is the change in refractive index caused by the analyte adsorption, m is the refractive index sensitivity, r is the distance between the nanostructure surface and analyte, and L is the EM-field decay length. This equation shows that $\Delta\lambda_{LSPR}$ decreases exponentially as r increases because

of the exponential decrease of the EM-field. According to our previous experimental determination, the EM-field decay length of 34, 42, and 47 nm edge-length Au TNPs are 22, 24, and 26 nm, respectively.[25] Therefore, we hypothesize that the sensitivity of our LSPR-based cTnT biosensor will increase as distance between the Au TNP and anti-cTnT receptor decreases, which can be achieved by shorting the chain length of the alkylthiols used in the SAM. To validate our hypothesis, as described before, we selected MUDA/NT and MHNA/HT SAMs to fabricate our biosensors. We followed the same fabrication strategy as described for the MHDA/DDT SAM.

Figure. 5.4 shows the concentration dependent λLSPR shifts for our cTnT biosensors that were prepared with three different spacer length 3 fM (**see Table 5.2**). We purposefully selected a lower concentration range for LOD determination for the sensor constructed with MHNA/HT SAM in comparison to the sensors fabricated with MUDA/NT and MHDA/DDT SAMs to evaluate the limitation of the LSPR biosensors. In general, in the case of miniaturize LSPR biosensors, quantifying low concentrations of analyte is extremely challenging. Even though the cTnT sensor constructed with MHNA/HT SAMs. As expected, the sensor prepared with MHNA/HT SAM provided the shortest distance between the nanostructure and analyte and produced the lowest LOD of SAM provided the best sensitivity, there are still several drawbacks associated with this sensor:

(i) Firstly, there was a large variation between performance with different sensors as observed with the large error bars in $\Delta\lambda_{LSPR}$. This could have resulted from nonspecific adsorption of analyte as a consequence of defects in the MHNA/HT SAMs, which contained alkylthiols with 6 methylene units. It is known that for formation of a perfectly packed SAM of alkylthiols on a gold surface (i.e., without the presence of defects or pinholes), a minimum of 9 methylene units is required.[38]

(ii) Secondly, non-linearity was observed in the concentration range of 3.5 -350 ng/L (Fig. 4, red squares). This concentration range is critical because a patient with cTnT concentration >10 ng/L can be identified potential risk for MCI.[24, 38]

(iii) Thirdly, a shorter distance between the nanostructure and receptor will induce long-range attractive forces originating from the underlying solid substrate, which results in error in the anal-ysis. Thus, a relative larger distance is required to reduce such forces.

(iv) Finally, for potential application it is extremely important to examine the selectivity of our LSPR cTnT biosensors. Therefore, we performed two important control experiments on our sensors prepared with MHNA/HT and MUDA/NT SAMs. In the first experiment, MHNA/HT and

MUDA/NT SAM-modified Au TNPs attached onto silanized glass substrates were incubated overnight in 35 ng/L cTnT in PBS buffer, rinsed thoroughly, and then exhibited $\Delta_{\lambda LSPR}$ values of 2.7 and 0.4 nm, respectively. Therefore, the actual sensor (**Figure. 5.1**) design involving MHNA/HT SAM has the possibility of providing false positive responses. In contrast, the negligible shift observed for MUDA/NT SAM is within the instrument noise level. In the second control experiment, we selected cTnT sensors, which were prepared with both the above-mentioned SAMs and then incubated in 35 ng/L tropomyosin, a protein that is present in the heart muscle and is also released during a heart attack. Clearly for practical application, it is very important to study the selectivity of our chip format LSPR cTnT biosensor. Fig. S5 illustrates UV-visible extinction spectra of our sensors constructed with two different SAMs before and after tropomyosin incubation. The sensor constructed with MUDA/NT SAM displayed no noticeable λLSPR shift, whereas an ~4 nm $\Delta\lambda_{LSPR}$ was observed with the sensor constructed with MHNA/HT SAM, indicating a non-specific response of the sensor in the latter case. We should mention that this 4 nm shift corresponds to a concentration of 2.4 ng/L which is within the concentration range of patients with the risk of a heart attack. Based on our experimental data and literature reports, our LSPR biosensor constructed with MUDA/NT SAMs is more capable of avoiding false positive responses in terms of nonspecific adsorption of an important unwanted analyte on the sensors surface. Thus, we selected MUDA/NT SAM for chip-based fabrication of our LSPR cTnT biosensor as part of our further investigation.

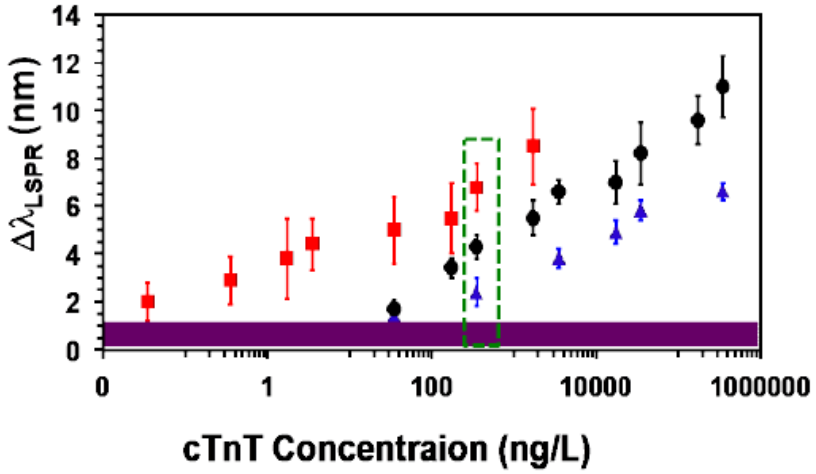

Figure 5.4. Determination of efficient decay length of LSPR cTnT biosensors. Plot of average ΔλLSPR of the LSPR biosensors, which were fabricated with three different types of SAMs: blue triangles (MHDA/DDT), black dots (MUDA/NT), and red squares (MHNA/HT) versus the logarithm of cTnT concentration. The purple bar represents three times the standard deviation (σ) of the blank (mixed anti-cTnT/DDT functionalized Au TNPs attached onto a glass coverslip). Green dotted box shows ΔλLSPR for three different SAM-modified sensors at 350 ng/L cTnT concentration in PBS buffer. The linear detection ranges of cTnT for MHDA/DDT, MUDA/NT, and MHNA/HT SAMs were 350-35000, 35-17500, and 0.035-3.5 ng/L, respectively.

Table 5.2. LOD derived for chip-based LSPR cTnT sensors constructed with three different type of SAMs while keeping the edge-length of Au TNPs constant.

Edge Length	Decay Length	Equation	R^2 Value	Z value	LOD (pM)
42	MHDA/DDT	y = 0.598ln(x) - 0.888	0.98	1.7	2.2
42	MUDA/NT	y = 0.937ln(x) - 1.472	0.98	1.2	0.5
42	MHNA/HT	y = 0.548ln(x) + 3.529	0.94	2.2	0.003

5.4.3 Enhancement of cTnT Binding onto LSPR cTnT Biosensors

In addition to the sensing volume and decay length of metal nanostructures, the number of receptor sites present on the LSPR biosensor directly influences the λLSPR shift, as reported by Chilkoti and coworkers for Au nanorods as described by **Equation 2**.[32]

Here S_0 is bulk R.I. sensitivity, ΔRI is the difference in R.I. between the analyte and the

$$\Delta\lambda_{LSPR} = \frac{3S_0 e^{-2r/L}}{V_s} \Delta RI.N.V_A \quad \textbf{(5.1)}$$

medium, and N and VA are the number of molecules bound to the sensor and volume of the analyte molecule, respectively.

Using Eq. 2 we hypothesize that by increasing the number of cTnT binding sites while not causing steric and/or electrostatic repulsion between anti-cTnT molecules and thus decreasing non-specific analytes adsorption, we will be able to increase the sensitivity of our LSPR cTnT sensor. To validate our hypothesis, we selected 42 nm edge-length Au TNPs and MUDA/NT SAMs to keep sensing volume and decay length, respectively, to their optimum values and best selectivity for chip-based cTnT biosensor fabrication as described above. Then N was varied by changing the ratio of MUDA:NT (Equation 2). We expect that an increase of MUDA concentration on the Au TNP surface would increase the number of receptor anti-cTnT sites on the sensor and thus more cTnT would bind, resulting in larger λLSPR shifts. Fig. S6 shows the LSPR shift of our sensor before and after incubation in 1750 ng/L cTnT in PBS buffer. Table S5 summarizes the average ΔλLSPR value for four different ratios. The highest ΔλLSPR we observed of 11.5 nm for 8:2 MUDA/NT is in agreement with our hypothesis and **Equation 2**. We did not investigate the sensor responses for 100% MUDA SAM be-cause the presence of a spacer in SAMs is extremely important in reducing repulsion between the receptor sites and avoiding the non-specific adsorption of analytes in LSPR biosensors, as report-ed in the literature.[3, 32, 34]Therefore, we determined that the best nanoscale structural parameters for chip-based fabrication of our LSPR cTnT biosensor are: (i) an ~42 nm edge-length Au TNP - optimization of sensing volume, (ii) 1.7 nm distance between Au TNP and anti-cTnT - standardization of decay length (MUDA/NT SAMs), and (iii) an 8:2 ratio of receptor-to-spacer – enhancement of cTnT binding (MUDA:NT SAMs). Based on these optimized parameters, we determined the LOD of cTnT in PBS buffer and found it to be 7.2 aM (**Figure. 5.5A**). To the best of our knowledge, this is the best sensitivity for cTnT detection reported in the literature.[16] More importantly, our LOD is nearly 50 times better

than recently reported for label-free detection of cTnT using a diode-based electrochemical technique, which requires a complex fabrication strategy.[16] As shown in **Figure. 5.5B**, we calculated the KD value by fitting the data to a Langmuir isotherm and found it to be 4.23 x 10^{-7} M in PBS buffer. This result suggests that the target protein cTnT has relative strong affinity toward its antibody. Under our experimental conditions where the LOD reaches to few tens of aM, the cTnT can easily detach from the sensors surface because of their relatively high KD value. This could be a potential reason from the deviation of linearity at such very low concentration. Surprisingly, even though the KD value is relatively high for cTnT, the ultrasensitive nature of our LSPR biosensor, which was constructed with appropriate optimization of structural parameters, allowed us to assay concentration as low as 3.5 x 10^{-4} ng/L with a LOD of 251 x 10^{-6} ng/L in PBS buffer.

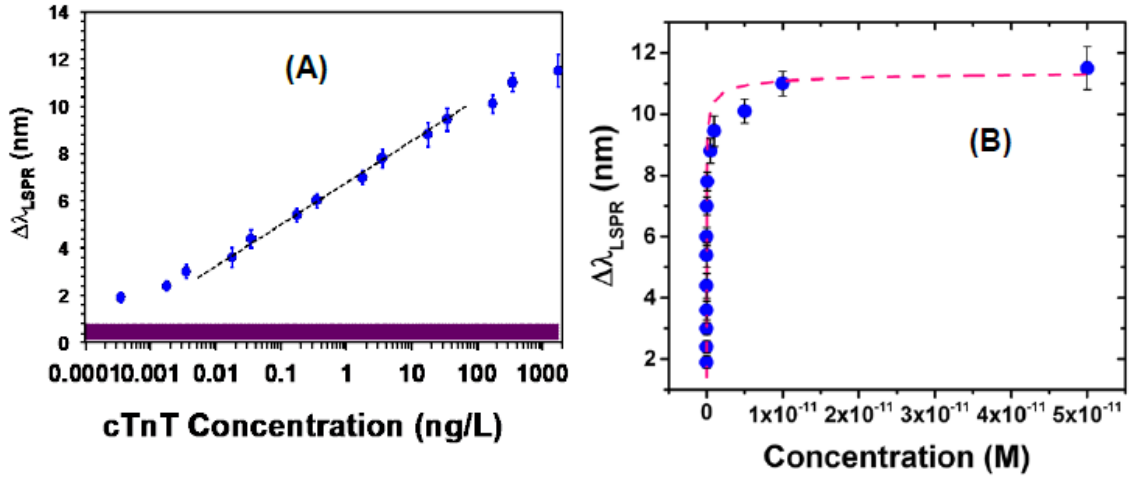

Figure 5.5. Determination of Sensing Efficiency of LSPR cTnT biosensors. (A) Plot of average ΔλLSPR of the LSPR biosensors that were fabricated with 42 nm edge length Au TNPs functionalized with 8:2 mole ratio of MUDA:NT SAMs versus the logarithm of cTnT concentration. The dotted black line shows the linear con-centration range that is within the level identified for patients at high risk for heart attack.29,34 The purple bar represents three times the standard deviation (σ) of the blank (mixed anti-cTnT/NT-functionalized Au TNPs attached onto a glass coverslip). (B) Binding of cTnT to LSPR biosensor in PBS buffer. The data were fitted to a Langmuir isotherm (dotted line) to determine the KD value.

5.4.4 Potential Applicability of Chip-Based LSPR cTnT Biosensor for Point-of-Care Diagnostics.

Over the last 10 years there has been a growing interest in LSPR-based assays as label-free, low cost medical diagnostic tools. To meet the needs not only of point-of-care diagnostics but also potential laboratory applications, it is important that the LSPR biosensors be able to assay analytes in complex biofluids, such as plasma, serum, urine, etc. With the aim of potential biomedical applications, we examined the working capability of our chip based LSPR cTnT biosensor in undiluted human plasma and serum, and 50% human urine. We prepared a cTnT stock solution using these biological fluids and then lowered the cTnT concentrations through a series of dilutions with the respective biological fluids. The sensor was fabricated using our optimized parameters as de-scribed for PBS buffer. **Figure. 5.6A** illustrates concentration-dependent average ΔλLSPR value of our cTnT biosensors in the three different fluids. The LODs in plasma and serum were determined to be ~14 and 22 aM, respectively, whereas the LOD value is slightly higher (1.9 fM) in urine (see **Table 5.3**).

Considering that tens of thousands of proteins are present in these complex human biofluids, our results, specifically the sensitivity and selectivity of the cTnT assay in human plasma and serum, is outstanding. Strikingly, the LOD we determined in undiluted plasma (~14 aM) is more than 103 times better than that the LOD reported for cTnT detection of ~300 fM using a microfluidic diode-based device monitoring current-voltage response in undiluted human serum.19 Furthermore, our sensor in plasma displays 4×10^3 times better LOD than the electrochemically determined cTnT concentration involving a ZnO nanostructure. Importantly, to the best of our knowledge, our label-free LSPR-based cTnT assay displayed the lowest LOD in the literature. This highlights the unique advantage of designing and utilizing LSPR biosensors to assay disease biomarkers with an unprecedentedly low LOD. Surprisingly, we observed a high value of LOD and large variation of ΔλLSPR values in urine. One would expect better sensitivity of the LSPR biosensors in urine in comparison to either plasma and/or serum because of a relatively lower concentration of proteins, thus reducing nonspecific binding onto the sensor surface. We believe that the high urea concentration in urine screens the interaction between anti-cTnT and cTnT, resulting in low sensitivity. The calculated high KD value of cTnT in urine of 1.1×10^{-5} M (see **Figure. 5.6B**) shows nearly 100-fold less affinity to-ward its antibody in comparison to the other two human biofluids.

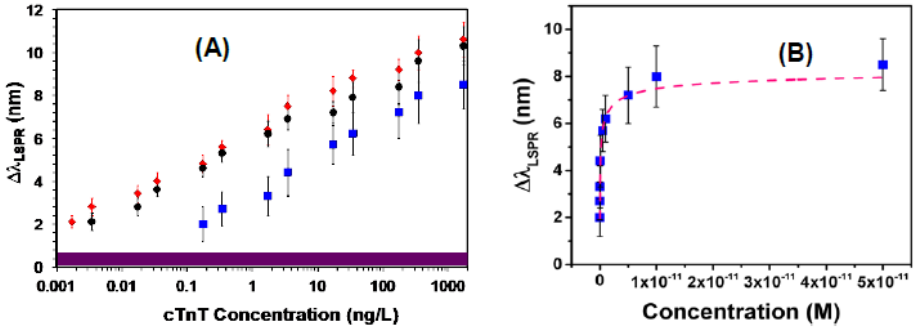

Figure 5.6. Assaying cTnT in human biofluids. (A) Plot of average ΔλLSPR of the chip-based format cTnT biosensors in undiluted plasma (red diamonds), serum (black dots), and 50% urine (blue squares) versus the logarithm of cTnT concentration. Urine samples were diluted with PBS buffer. (B) Binding of cTnT to biosensor in 50% urine. The data were fitted to a Langmuir isotherm (dot ted line) to determine the KD value of 1.1 x 10-5 M. The linear detection ranges of cTnT for plasma, serum, and urine were 0.0175-35, 0.0035-3.5, and 3.5-350 ng/L, respectively.

Table 5.3. LOD of chip based LSPR cTnT sensors fabricated using three different type of SAMs while keeping the edge-length of Au TNPs constant.

Physiological medium	Equation	R^2 Value	Z value (nm)	LOD (ng/L)	LOD
Buffer	y = 0.671ln(x) + 6.761	R^2 = 0.99	1.2	261	7.2
Buffer	y = 0.591ln(x) + 6.888	R^2 = 0.98	1.4	190	5.8
Plasma	y = 0.615ln(x) + 6.224	R^2 = 0.98	1.5	507	14.5
Plasma	y = 0.587ln(x) + 5.973	R^2 = 0.97	1.5	460	13.1
Serum	y = 0.624ln(x) + 5.676	R^2 = 0.98	1.2	766	21.9
Urine	y = 0.707ln(x) + 3.506	R^2 = 0.98	1.6	67360	1900

5.5 Summary

In conclusion, our systematic study unravels the effects of various nanoscale parameters, which modulate the overall sensitivity of our chip-based format LSPR biosensor. This plasmonic nanosensor uses LSPR shifts to quantitate an important disease biomarker without complicated fabrication strategies. Our sensor displayed LOD as low as ~250 x 10^{-6} ng/L in untreated human plasma, and also showed feasibility of working in other human biofluids (serum and urine) in a

concentration range much lower than that of the commercial ECLIA instrument from Roche Diagnostic.18 Importantly, development of our LSPR-based assay provides several guiding principles in the fabrication of optical-based biosensors: Firstly, longer edge length (larger sensing volume) Au TNPs display the highest sensitivity for cTnT detection, however their near infra-red LSPR peak position could potentially be interfered with by overlapping with the absorption peaks of water and other biomolecules. Thus, metal nanostructures with LSPR peaks in the near infrared region should be avoided for sensor fabrication. Secondly, appropriate selection of SAM length, which connects receptor and nanostructure and positions the anti-cTnT at the appropriate EM-field de-cay length is also critical to reducing non-specific adsorption of biomolecules on the surface of sensor while maintain the highest sensitivity. Additionally, increasing the number of receptor molecules on the surface of Au TNPs while reducing the steric and/or electrostatic repulsion between analytes is critical to achieving highest sensitivity. Taken together, we have determined that the following structural parameters are the best combination for assaying cTnT: (i) an ~42 nm edge-length Au TNP, (ii) 1.7 nm distance between Au TNP and anti-cTnT using MUDA/NT SAMs, and (iii) an 8:2 ratio of receptor-to-spacer. We believe that our work on control manipulation of surface functionalization and immobilization of bio-recognition molecules will provide an experimental benchmark for the fabrication of chip-based format, ultrasensitive nanoplasmonic biosensors. Finally, we have demonstrated excellent reproducibility (batch-to-batch variation) of our sensor fabrication technique, and thus it has the potential for chip-based technology development for practical applications for early diagnosis of heart attack.[16, 23, 24]Though, our biosensors demonstrate exceptional LOD for cTnT detection but this sensor may not be able to quantitatively determine cTnT concentration from a single cell extracts.

5.6 References

1. Haes, A. J.; Hall, W. P.; Chang, L.; Klein, W. L.; Van Duyne, R. P., A localized surface plasmon resonance biosensor: First steps toward an assay for Alzheimer's disease. *Nano Letters* **2004,** *4* (6), 1029-1034.
2. Haes, A. J.; Chang, L.; Klein, W. L.; Van Duyne, R. P., Detection of a Biomarker for Alzheimer's Disease from Synthetic and Clinical Samples Using a Nanoscale Optical Biosensor. *Journal of the American Chemical Society* **2005,** *127* (7), 2264-2271.

3. Haes, A. J.; Zou, S.; Zhao, J.; Schatz, G. C.; Van Duyne, R. P., Localized Surface Plasmon Resonance Spectroscopy near Molecular Resonances. *Journal of the American Chemical Society* **2006,** *128* (33), 10905-10914.
4. Willets, K. A.; Van Duyne, R. P., Localized surface plasmon resonance spectroscopy and sensing. *Annual Review of Physical Chemistry* **2007,** *58*, 267-297.
5. Anker, J. N.; Hall, W. P.; Lyandres, O.; Shah, N. C.; Zhao, J.; Van Duyne, R. P., Biosensing with plasmonic nanosensors. *Nature Materials* **2008,** *7* (6), 442-453.
6. Stewart, M. E.; Anderton, C. R.; Thompson, L. B.; Maria, J.; Gray, S. K.; Rogers, J. A.; Nuzzo, R. G., Nanostructured plasmonic sensors. *Chemical Reviews (Washington, DC, United States)* **2008,** *108* (2), 494-521.
7. Halas, N. J.; Lal, S.; Chang, W.-S.; Link, S.; Nordlander, P., Plasmons in Strongly Coupled Metallic Nanostructures. *Chemical Reviews (Washington, DC, United States)* **2011,** *111* (6), 3913-3961.
8. Mayer, K. M.; Hafner, J. H., Localized surface plasmon resonance sensors. *Chemical Reviews (Washington, DC, United States)* **2011,** *111* (6), 3828-3857.
9. Saha, K.; Agasti, S. S.; Kim, C.; Li, X.; Rotello, V. M., Gold nanoparticles in chemical and biological sensing. *Chemical Reviews (Washington, DC, United States)* **2012,** *112* (5), 2739-2779.
10. Ahijado-Guzman, R.; Prasad, J.; Rosman, C.; Henkel, A.; Tome, L.; Schneider, D.; Rivas, G.; Soennichsen, C., Plasmonic Nanosensors for Simultaneous Quantification of Multiple Protein-Protein Binding Affinities. *Nano Letters* **2014,** *14* (10), 5528-5532.
11. Guerreiro, J. R. L.; Frederiksen, M.; Bochenkov, V. E.; De Freitas, V.; Ferreira Sales, M. G.; Sutherland, D. S., Multifunctional Biosensor Based on Localized Surface Plasmon Resonance for Monitoring Small Molecule-Protein Interaction. *ACS Nano* **2014,** *8* (8), 7958-7967.
12. Jain, P. K.; Huang, X.; El-Sayed, I. H.; El-Sayed, M. A., Noble Metals on the Nanoscale: Optical and Photothermal Properties and Some Applications in Imaging, Sensing, Biology, and Medicine. *Accounts of Chemical Research* **2008,** *41* (12), 1578-1586.
13. Mock, J. J.; Smith, D. R.; Schultz, S., Local Refractive Index Dependence of Plasmon Resonance Spectra from Individual Nanoparticles. *Nano Letters* **2003,** *3* (4), 485-491.

14. Joshi, G. K.; Deitz-McElyea, S.; Liyanage, T.; Lawrence, K.; Mali, S.; Sardar, R.; Korc, M., Label-free nanoplasmonic-based short noncoding RNA sensing at attomolar concentrations allows for quantitative and highly specific assay of MicroRNA-10b in biological fluids and circulating exosomes. *ACS Nano* **2015,** *9* (11), 11075-11089.
15. Joshi, G. K.; Deitz-McElyea, S.; Johnson, M.; Mali, S.; Korc, M.; Sardar, R., Highly Specific Plasmonic Biosensors for Ultrasensitive MicroRNA Detection in Plasma from Pancreatic Cancer Patients. *Nano Letters* **2014,** *14* (12), 6955-6963.
16. Liu, Y.; Yobas, L., Label-Free Specific Detection of Femtomolar Cardiac Troponin Using an Integrated Nanoslit Array Fluidic Diode. *Nano Letters* **2014,** *14* (12), 6983-6990.
17. Shanmugam, N. R.; Muthukumar, S.; Prasad, S., Ultrasensitive and low-volume point-of-care diagnostics on flexible strips - a study with cardiac troponin biomarkers. *Scientific Reports* **2016,** *6*, 33423.
18. Nath, N.; Chilkoti, A., Label-Free Biosensing by Surface Plasmon Resonance of Nanoparticles on Glass: Optimization of Nanoparticle Size. *Analytical Chemistry* **2004,** *76* (18), 5370-5378.
19. Vollmer, F.; Braun, D.; Libchaber, A.; Khoshsima, M.; Teraoka, I.; Arnold, S., Protein detection by optical shift of a resonant microcavity. *Applied Physics Letters* **2002,** *80* (21), 4057-4059.
20. Stenberg, E.; Persson, B.; Roos, H.; Urbaniczky, C., Quantitative determination of surface concentration of protein with surface plasmon resonance using radiolabeled proteins. *Journal of Colloid and Interface Science* **1991,** *143* (2), 513-26.
21. El-Sayed, M. A., Some Interesting Properties of Metals Confined in Time and Nanometer Space of Different Shapes. *Accounts of Chemical Research* **2001,** *34* (4), 257-264.
22. Kedem, O.; Vaskevich, A.; Rubinstein, I., Critical Issues in Localized Plasmon Sensing. *Journal of Physical Chemistry C* **2014,** *118* (16), 8227-8244.
23. Wang Thomas, J., Significance of circulating troponins in heart failure: if these walls could talk. *Circulation* **2007,** *116* (11), 1217-20.
24. Omland, T.; de Lemos, J. A.; Sabatine, M. S.; Christophi, C. A.; Murguia Rice, M.; Jablonski, K. A.; Tjora, S.; Domanski, M. J.; Gersh, B. J.; Rouleau, J. L.; Pfeffer, M. A.; Braunwald, E., A sensitive cardiac troponin T assay in stable coronary artery disease. *New England Journal of Medicine* **2009,** *361* (26), 2538-2547.

25. Joshi, G. K.; McClory, P. J.; Muhoberac, B. B.; Kumbhar, A.; Smith, K. A.; Sardar, R., Designing Efficient Localized Surface Plasmon Resonance-Based Sensing Platforms: Optimization of Sensor Response by Controlling the Edge Length of Gold Nanoprisms. *Journal of Physical Chemistry C* **2012,** *116* (39), 20990-21000.
26. Joshi, G. K.; Smith, K. A.; Johnson, M. A.; Sardar, R., Temperature-Controlled Reversible Localized Surface Plasmon Resonance Response of Polymer-Functionalized Gold Nanoprisms in the Solid State. *Journal of Physical Chemistry C* **2013,** *117* (49), 26228-26237.
27. Joshi, G. K.; Blodgett, K. N.; Muhoberac, B. B.; Johnson, M. A.; Smith, K. A.; Sardar, R., Ultrasensitive Photoreversible Molecular Sensors of Azobenzene-Functionalized Plasmonic Nanoantennas. *Nano Letters* **2014,** *14* (2), 532-540.
28. Joshi, G. K.; Johnson, M. A.; Sardar, R., Novel pH-responsive nanoplasmonic sensor: controlling polymer structural change to modulate localized surface plasmon resonance response. *RSC Advances* **2014,** *4* (30), 15807-15815.
29. Joshi, G. K.; White, S. L.; Johnson, M. A.; Sardar, R.; Jain, P. K., Ultrashort, Angstrom-Scale Decay of Surface-Enhanced Raman Scattering at Hot Spots. *Journal of Physical Chemistry C* **2016,** *120* (43), 24973-24981.
30. Hao, E.; Schatz, G. C., Electromagnetic fields around silver nanoparticles and dimers. *Journal of Chemical Physics* **2004,** *120* (1), 357-366.
31. Chien, M.-H.; Nien, L.-W.; Chao, B.-K.; Li, J.-H.; Hsueh, C.-H., Effects of the rotation angle on surface plasmon coupling of nanoprisms. *Nanoscale* **2016,** *8* (6), 3660-3670.
32. Nusz, G. J.; Curry, A. C.; Marinakos, S. M.; Wax, A.; Chilkoti, A., Rational Selection of Gold Nanorod Geometry for Label-Free Plasmonic Biosensors. *ACS Nano* **2009,** *3* (4), 795-806.
33. Endo, T.; Kerman, K.; Nagatani, N.; Hiepa, H. M.; Kim, D.-K.; Yonezawa, Y.; Nakano, K.; Tamiya, E., Multiple Label-Free Detection of Antigen-Antibody Reaction Using Localized Surface Plasmon Resonance-Based Core-Shell Structured Nanoparticle Layer Nanochip. *Analytical Chemistry* **2006,** *78* (18), 6465-6475.
34. Feuz, L.; Jonsson, M. P.; Hoeoek, F., Material-Selective Surface Chemistry for Nanoplasmonic Sensors: Optimizing Sensitivity and Controlling Binding to Local Hot Spots. *Nano Letters* **2012,** *12* (2), 873-879.

35. Katus, H. A., Development of the cardiac troponin T immunoassay. *Clinical Chemistry (Washington, DC, United States)* **2008,** *54* (9), 1576-1577.
36. Marinakos, S. M.; Chen, S.; Chilkoti, A., Plasmonic Detection of a Model Analyte in Serum by a Gold Nanorod Sensor. *Analytical Chemistry (Washington, DC, United States)* **2007,** *79* (14), 5278-5283.
37. Jung, L. S.; Campbell, C. T.; Chinowsky, T. M.; Mar, M. N.; Yee, S. S., Quantitative Interpretation of the Response of Surface Plasmon Resonance Sensors to Adsorbed Films. *Langmuir* **1998,** *14* (19), 5636-5648.
38. Love, J. C.; Estroff, L. A.; Kriebel, J. K.; Nuzzo, R. G.; Whitesides, G. M., Self-Assembled Monolayers of Thiolates on Metals as a Form of Nanotechnology. *Chemical Reviews (Washington, DC, United States)* **2005,** *105* (4), 1103-1169.

CHAPTER 6. PLASMOELECTRONIC-BASED ULTRASENSITIVE ASSAY OF TUMOR SUPPRESSOR MICRORNAS DIRECTLY IN-PATIENT PLASMA: DESIGN OF HIGHLY ACCURATE EARLY CANCER DIAGNOSTIC TECHNOLOGY AND FURTHER MITIGATING FALSE POSITIVE AND NEGATIVE RESPONSES

This article has been reprinted with permission. Liyanage, T.; Masterson, A. N.; Oyem, H. H.; Kaimakliotis, H.; Nguyen, H.; Sardar, R., Plasmoelectronic-Based Ultrasensitive Assay of Tumor Suppressor microRNAs Directly in-Patient Plasma: Design of Highly Specific Early Cancer Diagnostic Technology. Analytical Chemistry (Washington, DC, United States) 2019, 91 (3), 1894-1903, DOI: 10.1021/acs.analchem.8b03768

6.1 Synopsis

microRNAs are small noncoding RNAs that are implicated in enhancing metastasis in breast, pancreatic, liver, and bladder cancers (BCs). State-of-the art PCR-based microRNA quantification requires biological fluid treatment, RNA extraction, labeling, amplification, and large samples, in addition to having measurement bias and variability, which together restrict its use. To overcome these challenges, we reported an ultrasensitive, nanoparticle-based, multiplexing sensor utilizing localized surface plasmon resonance (LSPR) gold triangular nanoprisms (Au TNPs) for accurate microRNA assay and here in we have reported new transduction mechanism involving delocalization of photoexcited conduction electrons wave function of Au TNP in the presence of -ssDNA/microRNA duplexes. Due to this unique finding, the electronic dimension and LSPR properties of the Au TNPs has been increase which resulted in highly sensitive microRNA assay for as low as 140 zeptomolar concentrations for our nanoplasmonic sensors. With this novel sensing platform, we were able to assay four different microRNAs (microRNA-10b, -182, -143, and -145) from bladder cancer patient plasma (50 μL/sample) and here for the first time, we utilized optical label free biosensor to quantify the tumor suppressor microRNAs which provides more accurate diagnosis results as confirmed with the statistical analysis. However false positive (When the test result indicates the positive for the diseases when actually the patient is negative for the disease/condition) and false negative (the test result that inform a person negative disease condition when the person actually positive for the disease/condition) are main challenges for more accurate diagnosis of such sensitive technique therefore further we have modified our developed sensors to eliminate false positive and false negative results by utilizing UV-Vis and fluorescence techniques

for simultaneous quantification of microRNA. This newly proposed design was mainly based on the DNA/RNA hybridization kinetics.

6.2 Introduction

Here for the first time, we have unraveled the electron wave function delocalization mechanism of the gold triangular nanoprisms (Au TNPs) hence reached unprecedented sensitivity for localized surface plasmon resonance (LSPR) properties of nanoplasmonic sensors for the efficient biomolecular recognition. With this fundamentally novel transduction mechanism, we have demonstrated that tumor suppressor microRNAs are ideal biomarkers compare to the oncogenic biomarkers for early diagnosis of bladder cancer. For this study we have been compared the microRNA levels (oncogenic and tumor suppressor) in the unmodified bladder cancer (BC) patient plasma of different stage of cancer (metastatic and nonmetastatic) vs normal control (NC).

Small single stranded noncoding RNA which may contains (18-25 nucleotides) called microRNA and that holds the promise of many discoveries and understanding of critical biological phenomena and pathologies[1-4]. These microRNAs play a significant role as oncogenic, or tumor suppressor, in various types of cancers including BCs. During the cancer progression stage, oncogenic microRNA levels increase, and level of tumor suppressor microRNA decreases compared to the healthy individuals. Many studies have proven that early detection of microRNAs could prevent metastasis of cancer and increase the chances of patient survival[5, 6]. Among different biological fluids microRNA containing in plasma found to be more stable as plasma environment supports them to be survive even in harsh conditions[7]. Therefore, microRNAs in plasma can be consider as an ideal biomarker for early cancer diagnosis[1-3, 8].

BC is the 6th most common cancer in the United States and among men[9], BC is the fourth most common cancer and men are in four times more risk of diagnosis of BC compare to women[10]. Muscle invasive BC is the more advanced stage of bladder cancer and this occurs when the cancer has grown up to the inner wall of the bladder (T2 and beyond). Also, BCs shows high recurrence rate, as an example for the patient with T2 stage who undergoes cystectomy has 20-30% chance of the cancer to returned for T3 stage that could be around 40%[11-14]. Higher the stage the recurrence rate is high and also when lymph nodes are involving the recurrence rate reach to the highest[15-23]. Unfortunately, it is hard to predict the nodal disease by using conventional BC diagnosis procedure[24]. Therefore, it is an urgent requirement to build up highly accurate assay which has the

capability of noninvasive assaying (detect and quantifying) of BC microRNA in blood circulation. Such type of liquid biopsy will be highly advantage for early diagnosis of BC will be the "holy grail" of urologic oncology.

Literature has been reported various techniques which help to diagnosed cancer using oncogenic microRNA (oncogenic microRNA levels increase upon the cancer growing) in human biological samples[25-28] however, to the best of my knowledge there is no report available which utilized tumor suppressor microRNA using label free optical based assay. Tumor suppressor microRNAs are down regulated microRNA upon cancer progression, and it is required to have ultra-sensitive technology in order to quantify the tumor suppressor microRNA assay. Here in this report we have utilized the unique "plasmoelectronic" properties of solid state nanoplasmonic sensor to quantify four different microRNAs including (oncogenic microRNAs, microRNA-10b and -182; tumor suppressor microRNAs, microRNA-143 and -145) at zeptomolar (zM) concentrations. Interestingly this assay carried out using direct plasma and the volume utilized was as low as 50 μL. This newly designed method has drawn the attention as it does not requirement treatment of the biological fluids and RNA extraction and amplification steps which is essential for the current available real-time PCR and microarray-based microRNA quantification methods. Altogether, we have programmably controlled the structural parameters of Au TNPs in order to influence the LPSR property to achieve the unprecedented sensitivity and selectivity. According to our findings, the concertation of microRNAs in MT-NMT vs MT-NC varies nearly 4- and 3-order of magnitude difference and specially for tumor suppressor (microRNA-143 and -145) shows the p values of <0.0001. But for the oncogenic (microRNA-10b and -182) it shows only a 10- fold difference in concentrations.

The next important phenomena that need to consider with such highly sensitive assay is to mitigate the false positive and false negative responses in order to increase the overall accuracy of the developed assay[29, 30]. The national institute of health (NIH) has reported the three main parameters which can be identified as cause of false positive and negative responses[31].

1. Biomarker is not strong enough to distinguish the healthy individual vs diseased conditions.
2. Depend on one biomarker to distinguish the condition
3. Depend on only one technique in order to diagnose the condition.

   However, we have rule out the effect of the first two parameter for the false positive and negative response for the developed sensor. In order to address the third parameter, we

have remodified the sensing plat form where the response can be diagnosed using LSPR and confocal microscopy images.

Here in this work we have been utilized the DNA/RNA hybridization kinetic to design the sensing plat form. According to the literature it is possible to design a less favorable hybridization of DNA/RNA duplex for the easy kick off with the more favorable complimentary strands (DNA/RNA) by engineering the thermodynamic parameters of the nucleic acid sequences. Molecular bacon could take as an example for such application, where they complement is fringed by extra bases and the hairpin structure. Upon hybridization of the target analyte with the bacon, hairpin structure gets disturbed. Similarly, Peng Yin et al. reported a theoretical framework to calculate the nucleic acid hybridization specificity based on the thermodynamic parameters which has the capability of deriving the single nucleotide changes and applicable in wide range of the temperature. Accordingly, they have been developed the 'toehold exchange' probes and further experimentally discriminate the single range single-base changes[31-33].

To understand the hybridization kinetics of a reaction where correct target (x) probe replacing the protector (P) from complimentary probe (X) is shown in the **Equation 1.** Here XP is the protector- complimentary hybridized complex and after the replacement target will form a target- complimentary complex XC.

$$X + PC \rightleftharpoons XC + P \tag{6.1}$$

The standard free energy ΔG^0 of the reaction kinetic can be calculated using **Equation 2**

$$\Delta G^0_{Reaction} = \Delta G^0_{XC} + \Delta G^0_P - \Delta G^0_X - \Delta G^0_{PC} \tag{6.2}$$

Here, in this reported work we simply utilized this phenomenon in order design a promoter which carried a fluorophore that can loosely bound to the sensor plat form. Once the target analyte bound to the complimentary based on the favorable Gibbs free energy the promoter will be replaced and hence fluorescence intensity will be dropdown. The varies of the fluorescence intensity could be measured using confocal microscopy which provided simultaneous assay with LSPR for more accurate diagnosis. The detailed sensor design is shown in **Figure 6.1**.

6.3 Materials and Methods

6.3.1 Materials

Chloro(triethylphosphine) gold(I) (Et3PAuCl, 97%) was purchased from Ge l e s t Inc. Poly -(methylhydrosiloxane) (PMHS, Mn = 1700−3300), trioctylamine (TOA, 98%), and ACS grade acetonitrile (CH3CN, 99.9%) and methanol (99.8%) were purchased from Sigma-Aldrich. Thiol modified 5′-SH-(CH_2)n-ssDNAs and micro- RNAs were purchased from Integrated DNA Technologies (IDT). (3-Mercaptopropyl)-triethoxysilane (MPTES, 94%) was purchased from Alfa Aesar. Ethanol (alcohol 200 proof) was purchased from Decon Laboratories. Thiolated polyethylene glycols were purchased from purePEG. All of the chemicals were used without any further purifications. Rnase free sterile water was obtained from Baxter Healthcare Corporation. The glass coverslips were purchased from Fisher Scientific. RBS 35 detergent was obtained from Thermo Scientific and used as received. Bladder cancer patient plasma samples were obtained from the Indiana University medical school and used as received. All water was purified using a Thermo Scientific Barnstead Nanopure system. Thiol modified -ssDNAs, microRNAs, and patient samples were stored at −80 °C. PBS buffer (pH = 7.2) was prepared using RNase-free sterile water.

6.3.2 Nucleic Acid Sequences

Table 6.1. DNA (oligomer) sequences used for this study.

Name	**Sequence**	**Modification**
-ssDNA-10b	5’ CACAAATTCGGTTCTACAGGGTA 3’	5’ Thiol-$(CH_2)_6$
-ssDNA-182	5’ TGTGAGTTCTACCATTGCCAAA 3’	5’ Thiol-$(CH_2)_6$
-ssDNA-145	5’ AGGGATTCCTGGGAAAACTGGAC 3’	5’ Thiol-$(CH_2)_6$
-ssDNA-10b	5’ CACAAATTCGGTTCTACAGGGTA 3’	3’ Thiol-$(CH_2)_3$
-ssDNA-182	5’ TGTGAGTTCTACCATTGCCAAA 3’	3’ Thiol-$(CH_2)_3$
-ssDNA-145	5’ AGGGATTCCTGGGAAAACTGGAC 3’	3’ Thiol-$(CH_2)_3$
-ssDNA-143	5’CCTCGTCACGACGTAGAGACCA3’	3’ Thiol-$(CH_2)_3$
-ssDNA-10b	5’ CACAAATTCGGTTCTACAGGGTA 3’	5’Thiol C_6/iSp$(CH_2)_3$

Table 6.2. microRNA sequences used for this study.

Name	Sequence	Modification
microRNA-10b	5’ UACCCUGUAGAACCGAAUUUGUG 3’	N/A
microRNA-182	5’ UUUGGCAAUGGUAGAACUCACA 3’	N/A
microRNA-145	5’ GUCCAGUUUUCCCAGGAAUCCCU 3'	N/A
microRNA-143	5’GGUGCAGUGCUGCAUCUCUGGU3’	N/A
microRNA-p: 18th mismatch in 10b sequences	5’ UACCCGGUAGAACCGAAUUUGUG 3’	N/A
microRNA-10a: 12th mismatch in10b sequences	5’ UACCCUGUAGAUCCGAAUUUGUG 3’	N/A
MicroRNA-q: 4th mismatch in 10b sequences	5’ UACCCUGUAGAACCGAAUUCGUG 3’	N/A
microRNA-r: first 3 nucleotides missing in 10b sequences	5’ UACCCUGUAGAACCGAAUUU 3’	N/A
microRNA-s: 18th mismatch in 182 sequences	5’ UUUGACAAUGGUAGAACUCACA 3’	N/A
microRNA-t: 12th mismatch in 182 sequences	5’ UUUGGCAAUGAUAGAACUCACA 3’	N/A
microRNA-v: 4th mismatch in 182 sequences	5’ UUUGGCAAUGGUAGAACUAACA 3’	N/A
microRNA-w: first 3 nucleotides missing in 182 sequences	5’ UUUGGCAAUGGUAGAACUC 3’	N/A

6.3.3 Spectroscopy and Microscopy Characterizations

Here we used the same techniques reported in chapter 5.

6.3.4 Silanization of Glass Coverslips

The glass coverslips were functionalized according to our previously reported method at chapter 5.2.3.

6.3.5 Synthesis of Au TNPs

Gold triangular nanoprisms (Au TNPs) were chemically synthesized according to the same procedure reported in chapter 5.2.4.

6.3.6 Preparation of Nanoplasmonic Sensors for microRNA Assay

As developed by our laboratory, we performed a tape-cleaning procedure on the glass coverslip-attached Au TNPs to remove non-prismatic nanostructures[34-37]. Briefly, tape cleaning was performed by placing the adhesive scotch tape (3M corporation) onto the Au TNP-attached coverslips, gently pressed down with a finger, and then slowly removed at a 90° angle. The Au TNP-attached coverslips were then cut into four pieces using a diamond cutter. Au TNPs containing supporting substrates were then incubated into HS-C_n-ssDNA-X: $PEG_{n'}$-SH (1 μM each) PBS buffer solution for overnight. Next, the HS-C_n-ssDNA-X: $PEG_{n'}$-SH functionalized Au TNPs were rinsed with PBS buffer to remove loosely bound reactants that serve as nanoplasmonic sensors, which were further used for microRNA assay.

6.3.7 Development of microRNA Calibration Plots

The mixed -S–$(CH_2)_n$-ssDNA (n = 3, 6, and 9) and -S-PEG functionalized Au TNPs (nanoplasmonic sensors) were incubated in different concentrations (range 1.0 nM to 10.0 zM) of microRNA solution in PBS buffer for overnight. MicroRNA-bound nanoplasmonic sensors were washed with PBS buffer to remove any nonspecifically adsorbed species, and then the LSPR extinction spectra were collected and λ_{LSPR} was determined. During the spectral collection the refractive index of the bulk medium kept constant by measuring all spectrum in PBS buffer.

6.3.8 Quantification of microRNA for Bladder Cancer Patient Samples

Nanoplasmonic sensors were incubated in a solution containing 50 uL of a bladder cancer patient sample (MT/ NMT/ Normal control samples) diluted into 3 mL PBS buffer for 12 h. Then the sensors were thoroughly washed with PBS buffer to remove any nonspecifically adsorbed biomolecules. Finally, the LSPR extinction spectra were recorded to determine λ_{LSPR}.

6.3.9 Fluorescence Quantification of microRNA for Different Single Base Pair Mismatches

An approximate concentration of microRNAs (fully complementary and having a single base-pair) attached onto the nanoplasmonic sensor were quantified by fluorescence spectroscopy using the procedure reported in the literature. First, we prepared our nanoplasmonic sensors ($HS–(CH_2)_6$-ssDNA-10b and PEG_6-SH) as described above and then hybridized with target microRNAs. Here we used 1.0 nM solution of 5' FAM fluorophore functionalized microRNA for the complementary (microRNA-10b), single base-pair mismatch (microRNA-p, microRNA-10a, and microRNA-q), and three starting nucleotides missing (microRNA-r). After the 12 h hybridization nanoplasmonic sensors with microRNAs, they were thoroughly rinsed with PBS buffer, and then incubated in aqueous 20 mM of mercaptoethanol solution for overnight for ligand exchange reaction. The exchanged solution was collected and centrifuged at 10,000 rpm for 40 minutes. Then the solution part was carefully removed and the solid was collected that was further dissolved in 1.5 mL of PBS buffer. Finally, photoluminescence spectra were collected.

6.3.10 Data Processing and statistical analysis

The λ_{LSPR} was obtained by using maxima of the UV- visible extinction spectra, and then $\Delta\lambda_{LSPR}$ was derived by taking the difference between LSPR peak of nanoplasmonic sensors before and after hybridization with target microRNA. Calibration curves were obtained by plotting $\Delta\lambda_{LSPR}$ vs. microRNA concentration. Finally, the LOD was determined by using z value (**mean+ 3σ**), which was obtained from six $\Delta\lambda_{LSPR}$ measurements of the sensors incubated in buffer solution without microRNAs. Concentration of target microRNAs in patient and normal control samples were determined from the calibration curves developed in human plasma. We used six $\Delta\lambda_{LSPR}$ values

and corresponding concentrations, and then average concentration was calculated. Each patient sample was independently analyzed twice (two weeks apart).

6.4 Results and Discussion

In principle, the working hypothesis of any nanoplasmonic sensors is heavily dependent on detecting changes in local dielectric environment.**16,18−21** MicroRNAs with a single nucleotide difference in their sequence would expect to display nearly identical refractive indices, and thus the change in local dielectric environment of Au TNPs and LSPR response upon formation of the -ssDNA/microRNA duplex should be nearly identical. Recently, we demonstrated that our nanoplasmonic sensors are capable of differentiating between microRNAs with single nucleotide specificity in the picomolar (pM) to femtomolar (fM) concentration range. A fully complementary. microRNA-10b and a single base-pair mismatch at the 12^{th} position (microRNA-10a) provided limit of detections (LODs) of 32 aM and 0.15 pM, respectively[36]. We rationalized that the nearly 10^4-fold difference in sensitivity observed is a consequence of delocalization of surface plasmon excitation of Au TNP into the -ssDNA/microRNA duplex that alters the electronic dimension of the TNPs through delocalization of excitonic wave functions, resulting in a variation of the LSPR properties. Furthermore, the single nucleotide specificity of our nanoplasmonic sensors is based on the excitonic wave functions delocalization mechanism, which provides variable magnitude of LSPR response for different microRNAs. This selectivity is different than the traditional biological assay in which the stronger the interaction (a fully complementary -ssDNA/microRNA duplex should display a stronger binding interaction than the -ssDNA/microRNA duplex containing nucleotide mismatches) between the receptor and analyte, the higher the signal is, and thus, the selectivity is better. In this article, for the first time, we examine the surface plasmon excitation delocalization mechanism by varying base-pair mismatch between -ssDNA and microRNA and controlling the distance between the surface of TNP and -ssDNA. Taken together, this unique electronic phenomenon, which has not been demonstrated before with respect to the characterization of LSPR-based transduction mechanisms, has allowed us to assay microRNA at ultralow concentrations directly in unmodified BC patient plasma.

6.4.1 Controlling Surface Plasmon Excitation Delocalization by Varying Base-Pair Mismatch

Delocalization of surface plasmon excitation (conduction electrons) of metallic nanoparticles is a steady-state electronic phenomenon in which wave functions of conduction electrons are expected to leave the metallic construct and expand into the surrounding environment, including into ligand moieties. When this occurs, the electron density around the nanoparticle reduces, resulting in the LSPR peak redshifts[38]. **Figure 6.1A** shows the construction of our solid-state nanoplasmonic sensor using chemically synthesized, ∼42 nm edge-length and ∼8 nm width, Au TNPs (**Figure 6.1B**) attached onto a silanized glass substrate. Light irradiation onto TNP induces the collective oscillation of conduction electrons and creates the LSPR properties. The electron wave functions are then allowed to delocalize through a highly π-stacked -ssDNA/microRNA duplex. Our hypothesis is that both the extent of delocalization and the LSPR sensitivity will decrease upon presence of base-pair mismatches in the -ssDNA/microRNA duplex, where the largest reduction in LSPR sensitivity is expected to be observed when the mismatches are closest to the surface of the TNP. To investigate the effects of base-pair mismatch on wave function delocalization and the LSPR sensitivity of nanoplasmonic sensors, in the current work we select -ssDNA-10b as a model oligomer for the microRNA-10b recognition molecule. Sequences for other microRNAs are shown in **Figure 6.1C** and the experimental section Tables (**Tables 6.1 and 6.2**).

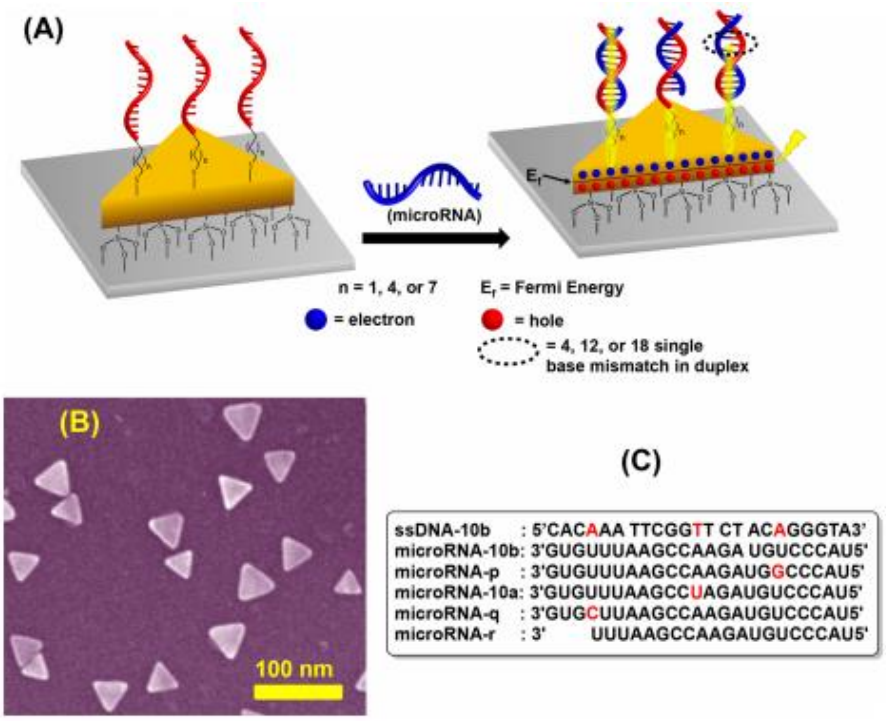

Figure 6.1. Structural parameters of nanoplasmonic sensors modulating the plasmoelectronic effects at the Au TNP and -S-ssDNA/microRNA interface. (A) Schematic representation of characterizing the delocalization of conduction electron wave functions of TNPs into a -ssDNA/ microRNA duplex. (A, left panel) Au TNPs are chemically attached onto a silanized glass substrate, and then their surfaces are functionalized with mixed HS-PEG: $HS(CH_2)n$-ssDNA-X to prepare LSPR-based nanoplasmonic sensors. (A, right panel) Incubation of sensors in microRNA solution results in the formation of a -ssDNA/microRNA duplex. Photoexcitation of TNP results in generation of localized surface plasmon. Wave function of conduction electrons (surface plasmon excitation) delocalizes into the -ssDNA/microRNA duplex (yellow shading) that is manipulated through single base-pair mismatch in the duplex and spacing (varying alkyl chain length, $-(CH_2)n-$, n = 3, 6, and 9) between the TNP surface and 5′-end of -ssDNA-10b ("linker"). For simplicity, wave function delocalization along the TNP edges and -S-PEG_n (n = 4 and 6) spacer are not showing. The image is not to scale. (B) Scanning electron microscopy image of ~42 nm edge-length and ~8 nm height Au TNPs attached onto silanized glass substrate used for nanoplasmonic sensors fabrication. (C) Depiction of -ssDNA-10b and microRNA molecules used in the studies to investigate conduction electrons wave function delocalization. The red letters represent the position of the single base-pair mismatch in the duplex structure.

We measured the LSPR response ($\Delta\lambda_{LSPR}$) of $-S(CH_2)_6$- ssDNA-10b-functionalized Au TNPs (nanoplasmonic sensor) after attachment of microRNAs as a function of concentration (1.0 nM to 100.0 aM) and location of single base-pair mismatch in PBS buffer (wet nanoplasmonic sensors). The detailed experimental procedure for the fabrication of nanoplasmonic sensors is

provided in the Supporting Information. **Figure 6.2A** illustrates $\Delta\lambda_{LSPR}$ values (nm) for different microRNAs. Using our published procedure, we calculated LODs for different microRNAs in buffer, and it is 32 aM for microRNA-10b, while microRNAs with 18 (microRNA-p), 12 (microRNA-10a), and 4 (microRNA-q) base-pairs mismatched display LODs of 5.2 fM, 0.15 pM, and 0.4 nM, respectively (see **Tables 6.3**). These results support our above-mentioned hypothesis that the LSPR sensitivity of our nanoplasmonic sensor decreases as the mismatch is closer to the surface of the TNPs, because when there is a mismatch, the wave function of conduction electrons of TNPs are not able to delocalize throughout the duplex -ssDNA/microRNA structure. Thus, with mismatch, the width of plasmon excitation does not increase (consider an Au TNP to be a plasmonic slab), as well the aspect ratio (edge-length: thickness) of TNPs remains constant[39]. This plasmoelectronic phenomenon is discussed in more detail below. Most strikingly, microRNA-r, in which the first three nucleotides are completely missing from the 3′-end but are fully complementary to -ssDNA-10b for the remaining 20 nucleotides, does not display any observable $\Delta\lambda_{LSPR}$ values. The same nanoplasmonic sensor was then treated with RnaseH enzyme to regenerate the sensor [35, 36]and incubated in 1.0 nM solution of microRNA-10b. We observe ∼10 nm $\Delta\lambda_{LSPR}$ shifts, suggesting appropriate sensitivity and selectivity of the sensors (**Figure 6.2B**). If the underlying physical property, of greatest significance was the change in local dielectric environment of nanoprisms, we would expect a large influence on the LSPR properties when microRNA-r formed its duplex with the LSPR-sensor (-ssDNA-10b) and would expect it to induce a large λLSPR red-shift. The attachment of microRNA-r to the sensor was confirmed by a fluorescence study described below. The experimental data are remarkable and suggest that our sensing mechanism is most likely controlled by the delocalization of conduction electrons wave function and an increase in the slab height rather than the influence of dielectric change, which is the traditionally accepted theory of LSPR-based detection and quantification (assay) of biomolecules. Taken together, the specific physicochemical property of the microRNA enabling delocalization of conduction electron wave functions through the coupled ssDNA/microRNA duplex leading to the zM sensitivity is reported.

A single base-pair match in the short -ssDNA/microRNA duplex should not influence their binding constant significantly[40]. Furthermore, long incubation time of our sensors in the microRNA solution should allow all of the microRNAs to be attached on the sensors regardless of their nucleic acid sequence. One could, however, argue that the observed $\Delta\lambda_{LSPR}$ values for

different mismatches are due to the variable number of microRNAs that are attached onto the nanoplasmonic sensor, and thus, the change in local dielectric environment varies between them. We overruled such an argument by quantifying sensor-bound microRNAs using fluorescence spectroscopy. MicroRNAs were labeled at the 5′-end with FAM. Nanoplasmonic sensors were prepared with $-S(CH2)_6$- ssDNA-10b, incubated in 1.0 nM FAM-labeled microRNA solution, and allowed to hybridize overnight, and then each sensor was washed to remove loosely bound microRNAs. Finally, the $-S(CH2)_6$-ssDNA-10b/microRNA duplex was released in solution through a ligand exchange reaction[41]. **Figure 2C** shows PL spectra for each microRNA listed in Figure 1C, in which the characteristic PL peak of FAM, ~525 nm, is observed. Noticeably, PL peak intensity for different microRNA is within the experimental error. This result is significant because it suggests that the number of microRNA attached to the sensors is identical irrespective dielectric environment of TNPs in the presence of different microRNAs is presumably similar and should provide similar $\Delta\lambda_{LSPR}$ values, as opposed to our experimental data (see **Figure 6.2A**). On the basis of the LSPR and PL data for different microRNAs, we alternatively suggest that the unprecedentedly high sensitivity of our nanoplasmonic sensors for detection of microRNAs arises from the increase of the confinement box size of Au TNPs through wave function delocalization that substantially affects their aspect ratios (edge-length: thickness of a TNP) and LSPR properties, and thus, provides a new plasmoelectronic phenomenon that has not been demonstrated before with respect to the characterization of LSPR-based transduction mechanisms for assaying short nucleotides.

Table 6.3. Calculated LOD values for -S-(CH2)6-ssDNA-10b functionalized nanoplasmonic sensors for various microRNAs in PBS buffer.

Alkyl Chain	**microRNA Type**	**Mismatch Position**	**Equation from Calibration Curve**	**R^2 value**	**Z value (nm)**	**LOD (aM)**
$-(CH_2)_6$	10b	Fully complimentary	y = 0.5105ln(x)+10.599	0.96	1.80	32.6
$-(CH_2)_6$	p	18^{th}	y = 0.4132ln(x) + 6.5286	0.99	1.5	5.2E3
$-(CH_2)_6$	10a	12^{th}	y = 0.3605ln(x) + 5.17	0.96	2.0	1.5E5
$-(CH_2)_6$	q	4^{th}	y = 0.2389ln(x) + 2.2167	0.94	2.0	4.0E8
$-(CH_2)_6$	r	First-3 nucleotide removed	-	-	-	-

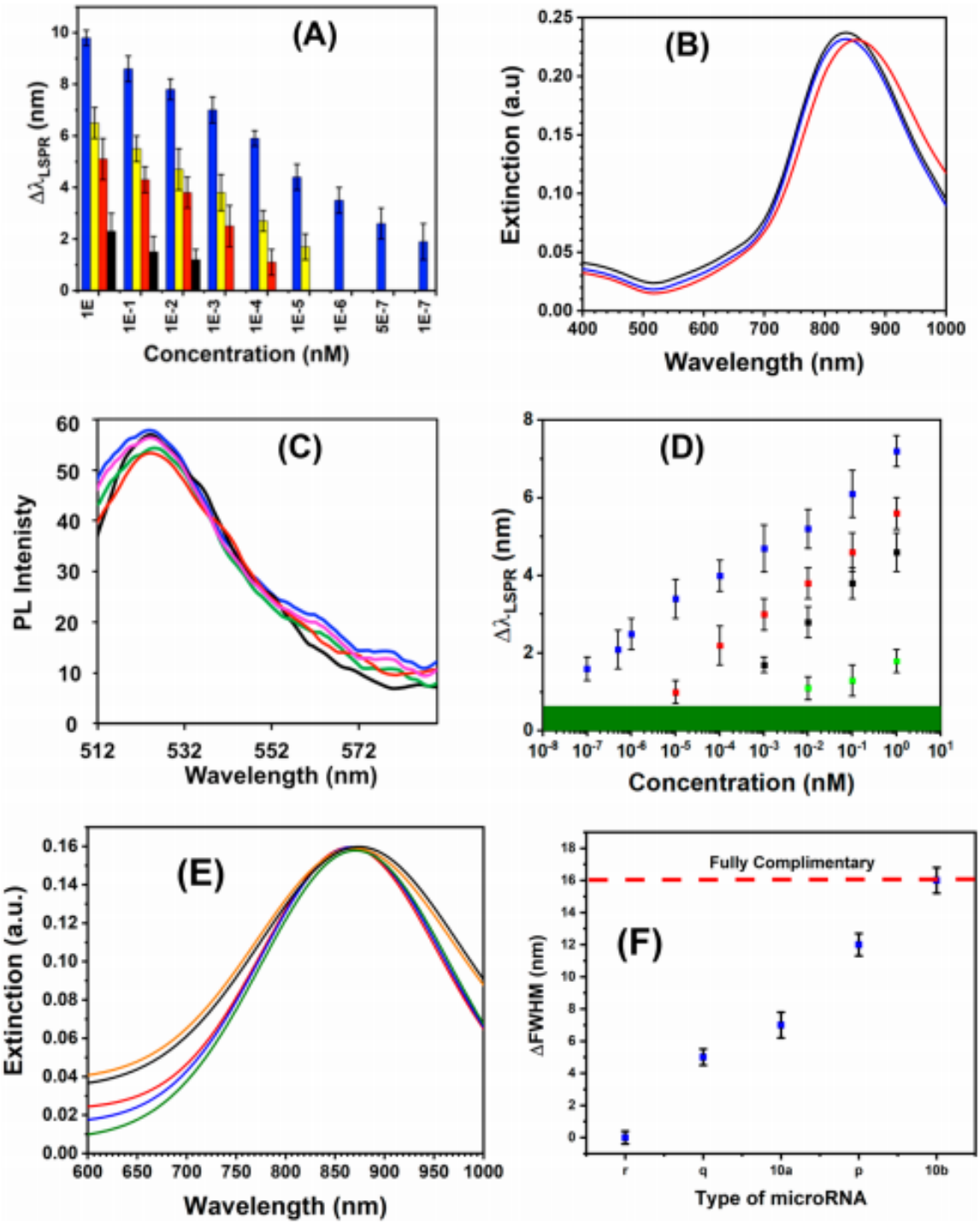
(A)
$\Delta\lambda_{LSPR}$ (nm)
Concentration (nM)
1E
1E-1
1E-2
1E-3
1E-4
1E-5
1E-6
5E-7
1E-7
(B)
Extinction (a.u)
Wavelength (nm)
(C)
PL Intenisty
Wavelength (nm)
(D)
$\Delta\lambda_{LSPR}$ (nm)
Concentration (nM)
(E)
Extinction (a.u.)
Wavelength (nm)
(F)
Fully Complimentary
ΔFWHM (nm)
r
q
10a
p
10b
Type of microRNA

Figure 6.2. Spectroscopy characterization of surface plasmon excitation delocalization by manipulating the structural parameters of microRNAs. (A) Comparison of microRNA-10b (blue bars), microRNA-p (yellow bars), microRNA-10a (red bars), and microRNA-q (black bars) concentration dependent LSPR response in PBS buffer. For microRNA-r, no detectable LSPR shift was observed. The sensors were constructed with mixed HSPEG:HS(CH2)6-ssDNA-10b. (B) UV−visible extinction spectrum of nanoplasmonic sensors prepared with mixed HS-PEG:HS(CH2)6-ssDNA-10b (black curve), after incubation with 1.0 nM microRNA-r (blue curve), treatment with 15 units of RNase H for 2 h, and then incubation in 1.0 nM microRNA-10b solution (red curve). All the spectra were collected in PBS buffer. (C) PL spectra of different microRNAs, microRNA-10b (red curve), microRNA-p (green curve), microRNA-10a (purple curve), microRNA-q (blue curve), and microRNA-r (black curve). For this study, 5′- FAM-tagged microRNAs were used. PL spectra were collected at a 496 nm excitation wavelength. (D) Average $\Delta\lambda_{LSPR}$ value of nanoplasmonic sensors after incubation in different microRNAs of varying concentrations, microRNA-182 (blue squares), microRNA-s (red squares), microRNA-t (black squares), and microRNA-v (green squares). The sensors were constructed with mixed HS-PEG: $HS(CH2)_6$-ssDNA-182. The standard deviation of the blank (6 measurements) was 0.25 nm, and the green bar represents three times this value. Concentrations were plotted on the axis in log scale in order to investigate nonspecific adsorption at a lower concentration range. (E) UV−visible extinction spectrum of nanoplasmonic sensors for different microRNAs at 1.0 nM concentration, microRNA-10b (black curve), microRNA-p (yellow curve), microRNA-10a (green curve), and microRNA-q (blue curve). Red curve represents the LSPR spectrum of nanoplasmonic sensors. (F) Measured relative change in fullwidth at half-maximum after and before microRNA (Δ_{fwhm}) attachment from panel E for different microRNAs.

In fact, our above-mentioned experimental data provide a guideline for the surface plasmon excitation delocalization-based sensing mechanism. (i) A fully complementary nucleotide sequence is required for extended delocalization of conduction electron wave functions throughout the entire -ssDNA/microRNA duplex, and (ii) this transduction mechanism is not controlled by the specific identity of nucleotide in the -ssDNA/microRNA duplex. To investigate this further, we turned to microRNA-182, which contains an entirely different nucleotide sequence than microRNA-10b There are 22 nucleotides in microRNA-182 as opposed to 23 in microRNA-10b, thus a slightly higher delocalization is expected in the latter case. Second, microRNA-182, an oncogenic microRNA that promotes the MT process of bladder cancer, can be used as a biomarker for early detection of BC. We prepared our nanoplasmonic sensor by attaching $-S(CH2)_6$-ssDNA-182 on Au TNPs and then incubated it in 1.0 nM microRNA-182 solution. We observe LSPR red-shifts in the UV−visible absorption spectrum with an $\Delta\lambda_{LSPR}$ value of 7.2 nm. As shown in **Figure 6.2D**, the LOD for fully complementary microRNA-182 is 82 aM, which is nearly 2.5-fold lower than that of microRNA-10b. We believe this is related to the overall length of the -ssDNA/microRNA duplex, which influences the extent of delocalization. Finally, nanoplasmonic sensors containing $-S(CH2)_6$-ssDNA-182 were treated with single base-pair mismatch microRNA-s, -t, and -v, and the ΔλLSPR values and LODs (**see Figure 6.3**) are in good agreement with the hypothesis of the wave functions delocalization process. Taken together, our experimental results show that the transduction mechanism does not depend on the chemical identity of nucleotide in the -ssDNA/microRNA duplex.

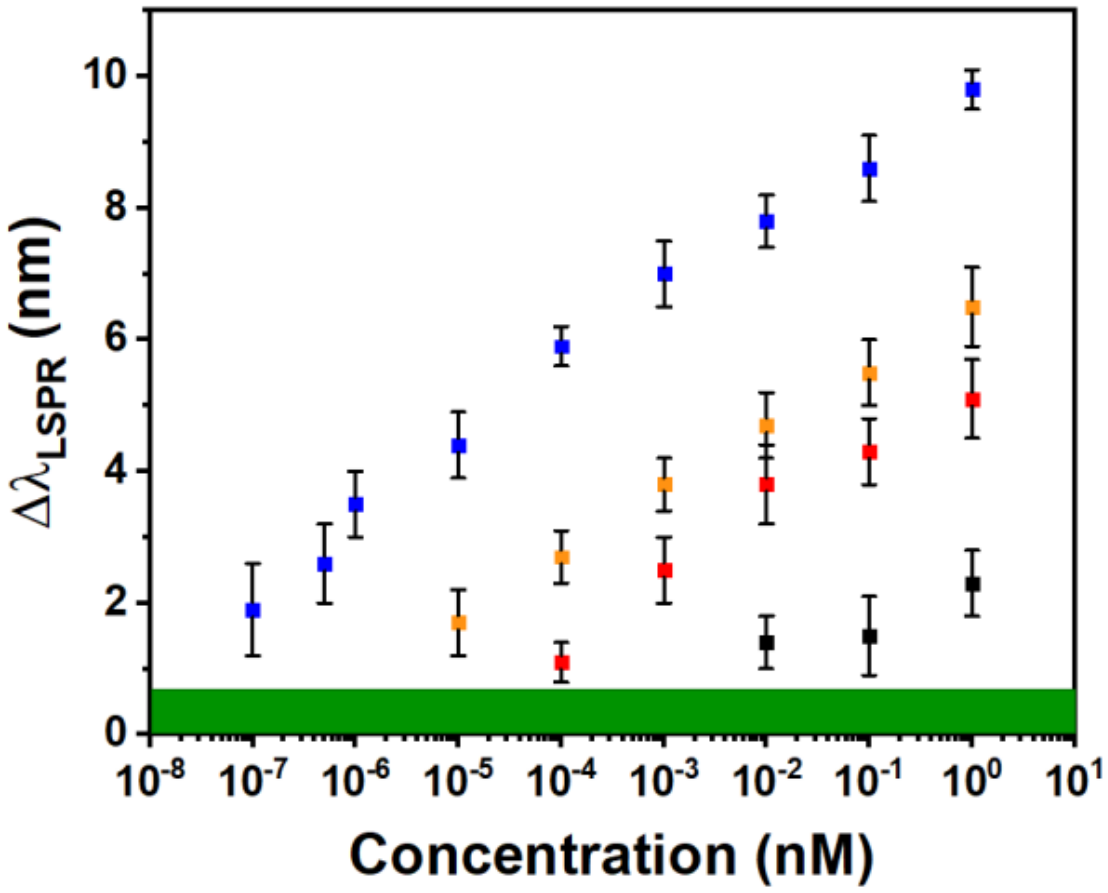

Figure 6.3. Average ΔλLSPR value of nanoplasmonic sensors after incubation in different microRNAs of varying concentrations: microRNA-10b (blue bars), microRNA-p (yellow bars), microRNA-10a (red bars), and microRNA-q (black bars). The sensors were constructed with mixed -S-PEG6: -S(CH2)6-ssDNA-10b. The standard deviation of the blank (6 measurements) was 0.25 nm and the green bar representing three times that value. Concentrations were plotted on the axis in log scale in order to investigate non-specific adsorption at a lower concentration range.

Most importantly, the proposed plasmoelectronic phenomenon has allowed us to quantify short noncoding RNAs with a single nucleotide specificity. In literature, both experimental and theoretical data have shown that the line-width (full-width at half maxima, fwhm) of LSPR peak of metal nanoparticles increases as the physical dimension (aspect ratio) of a nanoparticle increases[42-46]. In this context, it might be argued that upon conduction electron wave function delocalization, both height (thickness) and width (edge-length) of the plasmonic slab (e.g., Au TNP) would increase. One would also expect that the thiolated -ssDNAs preferentially attach along

the high-index facets, i.e., three sides, edges, and sharp tips of a TNP, as compared to the planner top surface. Therefore, TNPs grow more along the edges than the height and thus, increase their overall aspect ratio. Together, the plasmoelectronic effect causes a difference in fwhm (Δfwhm: after − before microRNA attachment) depending on the extent of delocalization and increase in aspect ratio that are controlled by the location of the base-pair mismatch in the -ssDNA/microRNA duplex (**see Figure 6.1A**) that elucidate the delocalization mechanism. Figures 2E and S4 illustrate the LSPR extinction spectra of -S(CH2)6-ssDNA-10bfunctionalized nanoplasmonic sensors in the presence of different microRNAs with a single base-pair mismatch. Indeed, an increase in Δfwhm of the LSPR dipole peak of Au TNP is observed from the 4th to 12th to 18th position mismatches in the -ssDNA-10b/microRNA duplex (**see Figure 6.2F**). The largest Δfwhm of 16 nm is observed for the fully complementary -ssDNA-10b/microRNA-10b duplex. Although our PL analysis unequivocally supports the attachment of microRNA-r to nanoplasmonic sensors, no noticeable differences in Δfwhm are observed. Therefore, the higher the delocalization, the greater the confinement box size, and consequently the larger the Δfwhm value.

6.4.2 Role of Linker between Au TNP and -ssDNA on Conduction Electron Wave Function Delocalization

To improve the delocalization of conduction electron wave functions of Au TNPs into the -ssDNA/microRNA duplex, it is necessary to reduce the insulating barrier between the TNP and the duplex. For the study described above, we used a $-(CH2)_6$ linker to attach -ssDNA-10b (182) onto TNPs and to prepare nanoplasmonic sensors. The presence of the linker is absolutely necessary to create homogeneous packing of -ssDNAs onto the surface of the TNPs and avoid their coiling[26, 28]. We believe that the shorter alkyl chain length creates a thinner insulating barrier and increases the conduction electron wave function delocalization into the -ssDNA/microRNA duplex, which results in a larger shift in ΔλLSPR and higher sensitivity. To test this, we varied the linker chain length from $-(CH_2)_3$ to $-(CH_2)_9$, see **Figure 6.1A**. We used -ssDNA-10b as a model receptor for microRNA-10b quantification in PBS buffer, while keeping other parameters in the nanoplasmonic sensor fabrication identical. **Figure 6.4A** illustrates the average $\Delta\lambda_{LSPR}$ values for three different linkers as a function of microRNA-10b concentration. The LODs for $-(CH_2)_3$ and $-(CH_2)_9$ are 137 zM and 0.81 pM, respectively (see Tables S5 and S6 and Figure S5). We also attached a $-(CH_2)_{16}$ linker, but no noticeable $\Delta\lambda_{LSPR}$ is observed (data not shown). Strikingly, the

sensitivity of our nanoplasmonic sensors constructed with $-S(CH_2)_3$-ssDNA-10b is nearly 240-fold higher than that of $-S(CH_2)_6$-ssDNA-10b. Only recently, nanoplasmonic sensors consisting of Au−Ag core−shell nanocubes and tetrahedral structured DNA were used for microRNA quantification at an aM concentration range using a single nanoparticle scattering measurement[10]. Nevertheless, we conclude that unprecedentedly high sensitivity of our nanoplasmonic sensors constructed with $-(CH_2)_3$-ssDNA-10b arises due to improved delocalization of conduction electrons wave function of Au TNPS into the -ssDNA/microRNA duplex by reducing the insulating barrier between the TNP and duplex. Finally, we observe the highest (21 nm) and lowest (10 nm) Δfwhm values for the $-(CH_2)_3$ and $-(CH_2)_9$ linkers, respectively (**Figures 4B**). This trend also supports our surface plasmon excitation delocalization mechanism. We should mention, that at a 500 zM detection limit, ~ 3000 microRNAs would present in 10 mL of solution. A typical size of our nanoplasmonic sensors is 25 × 5 mm2 (1.25 × 1014 nm2), and we calculated that ~12% of the substrate was covered with TNPs (ca. 2.0 × 1010 TNP). In this context, the probability of microRNA attachment to each TNP is exceedingly low. The area of a sensor exposed to Xenon flash lamp light of the UV−visible spectrophotometer was determined to be 1.96 × 1013 nm^2. Therefore, nearly an entire nanoplasmonic sensor resides within the path of the light beam that allows quantification of ~3000 microRNAs in order to obtain a limit of detection of 500 zM.

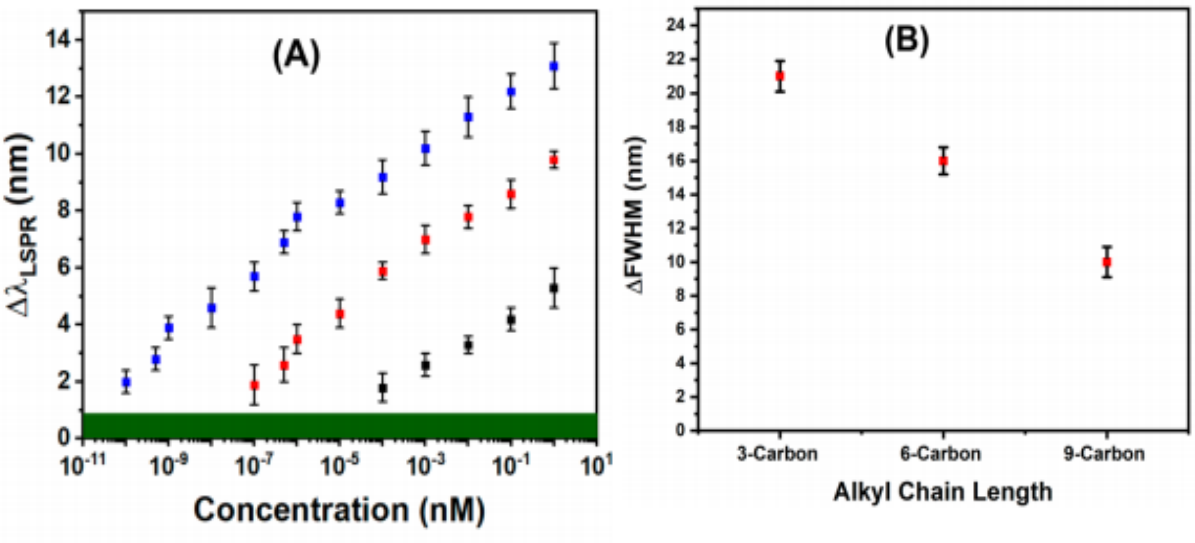

Figure 6.4. Characterization of the linker's role on conduction electron wave function delocalization. (A) Average $\Delta\lambda_{LSPR}$ value of nanoplasmonic sensors, which were prepared with three different spacers, $-(CH_2)_3-$ (blue squares), $-(CH_2)_6-$ (red squares), and $-(CH_2)_9-$ (black squares) as a function of microRNA-10b concentration. Each spacer was connected with -ssDNA-10b as a recognition molecule for microRNA-10b. The standard deviation of the blank (6 measurements) was 0.32 nm, and the green bar represents three times this value. Concentrations were plotted on the axis in log scale in order to investigate nonspecific adsorption at a lower concentration range. (B) Measured Δfwhm for different alkyl chain length for 1.0 nM microRNA-10b concentrations.

6.4.3 Mechanistic Understanding of Surface Plasmon Excitation Delocalization-Driven Plasmoelectronic Phenomenon

The plasmonic slab model proposed by Govorov et al.[39] suggests that a large number of highly excited electrons can be generated for a slab of 8 nm (the height of our Au TNPs) when Fermi gas is perturbed upon light excitation. These excited electrons can be used for various catalytic transformations where electrons are transferred from plasmonic nanoparticles to their surroundings, and holes are neutralized by using scavengers. In contrast, photoexcited electrons have the ability to delocalize their wave functions into the immediate surrounding, such as to a ligand environment. Therefore, the confinement box size (also aspect ratio of TNPs) increases that results in red shifting of the LSPR peak. We refer to this plasmoelectronic effect as surface plasmon excitation delocalization. Most important, this plasmoelectronic effect should be reversible by disrupting the delocalization process. Recently, we[47, 48] and others[49] have demonstrated reversible electron wave function delocalization of CdSe quantum dots and

manipulated their optoelectronic properties. This delocalization mechanism, which should be applicable to plasmonic nanoparticles under light excitation, however, has not been explored in metal nanoparticles yet. On the basis of the experimental data, we propose **Figure 6.5** as the possible mechanism for light-induced plasmoelectronic phenomenon of -ssDNA-functionalized Au TNPs. Here, highly π- stacked -ssDNA/microRNA duplexes facilitate electron wave function delocalization, which results in an increase in dimension of the plasmonic slab. In this context, as the delocalization improves, the aspect ratio of TNPs becomes higher, which results in more red shifting of the LSPR peak. Therefore, the electronic dimensions, such as edge-length and height, of Au TNP are higher than the physical dimension of 42 and 8 nm of edge-length and height, respectively[37]. Most importantly, electron delocalization through the phosphate backbone of DNA could take place on an attosecond timescale[50], and thus, delocalization is highly feasible under our experimental condition where continuous wave plasmonic excitation is performed during the steady-state extinction measurements. Nevertheless, precise determination of the increase of electronic dimension (plasmonic slab) of our nanoplasmonic sensors requires sophisticated mathematical calculations, beyond our expertise. We should mention that, the electron wave function delocalization mechanism is different than the DNA-mediated charge transport (CT) process, as discussed below. Long distance CT through a duplex DNA backbone has been known for more than two decades[51], where a single base-pair mismatch can disrupt the electron flow and influence the conductivity significantly[52]. Thus, DNA can be considered as a molecular nanowire consisting of multiple highest occupied (HOMO) and lowest unoccupied (LUMO) molecular orbitals, which facilitate the CT process and charge delocalization[53]. Electron donors, such as CdSe quantum dots[54] and Au[55] nanoparticles, can transfer charge to MOs of DNA that transport through DNA nanowires up to several micrometers. However, LSPR (photoexcited conduction electrons) supports the escape of conduction electrons from metallic nanoparticles in the solid-state, influencing their optical properties and causing a permanent electron-based damage of the local dielectric environment of nanoparticles. In other words, if CT processes were the basis for the observed phenomenon, the LSPR properties would not be able to be restored.[55] In contrast, our nanoplasmonic microRNA sensors show excellent regeneration by enzymatic cleaving of the -ssDNA/microRNA duplex and rehybridization of the sensors in microRNA solution for 5 consecutive days.[34-36]Therefore, we believe delocalization of conduction electrons wave function into hybrid MOs (LUMOs′) (**see Figure 6.5, yellow wavy line**) is occurring and not the transfer

of conduction electrons that would permanently change the LSPR properties of Au TNPs, and over time would destroy TNPs because of the building of excess positive charge (hole).We believe that metallic nanostructures should be highly LSPR responsive upon delocalization of exciton wave functions (plasmoelectronic effects) and a minute change in their aspect ratio. Au TNPs display strong LSPR response when small changes occur either in their surrounding medium refractive index or aspect ratios because of their strong electromagnetic (EM) field enhancement, but one would also expect to observe the plasmoelectronic effects for other anisotropically shaped nanostructures, such as nanorods and nanostars, because they also display strong EM-field enhancements. It is therefore imperative to investigate shape and composition (e.g., Ag TNPs)-dependent plasmoelectronic effects of nanostructures and their ability toward ultrasensitive biosensing, a current research focus of our laboratory.

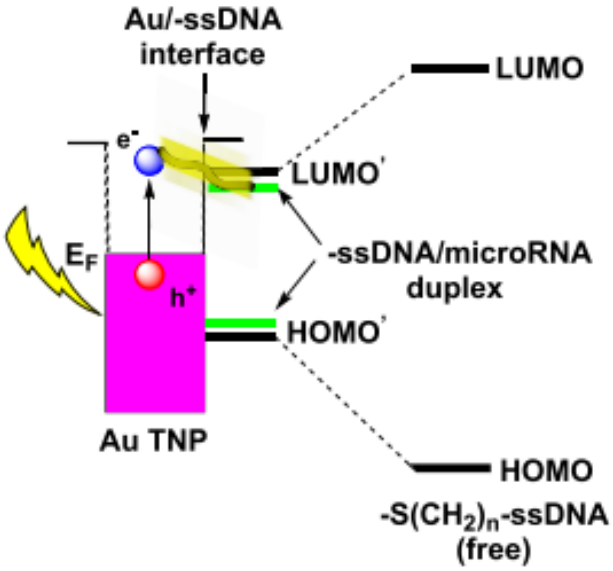

Figure 6.5. Schematic representation of proposed plasmon excitation delocalization at the Au TNP and −S(CH_2) n-ssDNA/microRNA interface. Attachment of −S(CH_2) n-ssDNA onto Au induces hybridization of electronic states and creates hybrid bonding (HOMO′) and antibonding (LUMO′) orbitals. The HOMO′−LUMO′ gap further reduces after formation of the -ssDNA/microRNA duplex.[56] The LUMO′ further facilitates photoexcited conduction electron (blue dot, plasmon excitation) wave function delocalization (yellow wavy line) from Au TNP to the -ssDNA/microRNA moiety. The extended π-stacking in the -ssDNA/microRNA duplex facilitates the wave function delocalization. Delocalization expands the box size ("particle in-a-box model) and increases the aspect ratio of TNP that together red-shifts the LSPR dipole peak. The image is not to scale.

6.4.4 Liquid Biopsy to Identify More Specific Biomarkers for Early Diagnostic of Bladder Cancer

microRNAs are small nonprotein-coding RNAs that have been shown to control cell growth, differentiation, and apoptosis, and thus, variable microRNA expressions are linked to tumorigenesis[57]. Because of their unusually high stability in human biofluids, such as serum and plasma, circulating microRNAs have the unmatched potential to serve as diagnostic markers for cancer for development of a liquid biopsy with unmatched potential to detect cancer faster and much earlier than currently available technology. There are two different types of microRNAs of interest in cancer screening, (i) oncogenic, which promotes tumor development by inhibiting tumor suppressor genes that control either cell differentiation or apoptosis (oncogenic microRNAs are overexpressed in different cancers, including BC), and (ii) tumor suppressors, which prevent tumor development by negatively inhibiting oncogenes that control either cell differentiation or apoptosis. The expression of tumor suppressor microRNAs is decreased in cancer cells[57]. Because tumor suppressor microRNA levels decrease in cancer cells as compared to normal cells, it is extremely difficult to quantify them with a PCR-based assay, which is not very sensitive.

Currently, there is no routine way to selectively detect and quantify (assay) circulating tumor suppressor microRNAs directly in crude human biofluids. Zeptomolar sensitivity of our nanoplasmonic sensors provides a unique advantage to assay both oncogenic and tumor suppressor microRNAs directly in unmodified plasma samples. Here, we present the first label-free assay to compare both oncogenic and tumor suppressor levels between patients with MT (n = 7), NMT (n = 4), and NC (n = 4) from crude plasma. The current FDA-approved urine cytology test shows poor sensitivity for low-grade lesions and significant disparity in specificity for different BC grades; thus, it is a highly unreliable screening test. Biologically, it is reported that microRNA-10b and -182 are upregulated (oncogenic), and microRNA-143 and -145 are downregulated (tumor suppressor) in BC; therefore, they could serve as alternative and more specific biomarkers for early diagnosis of BC.

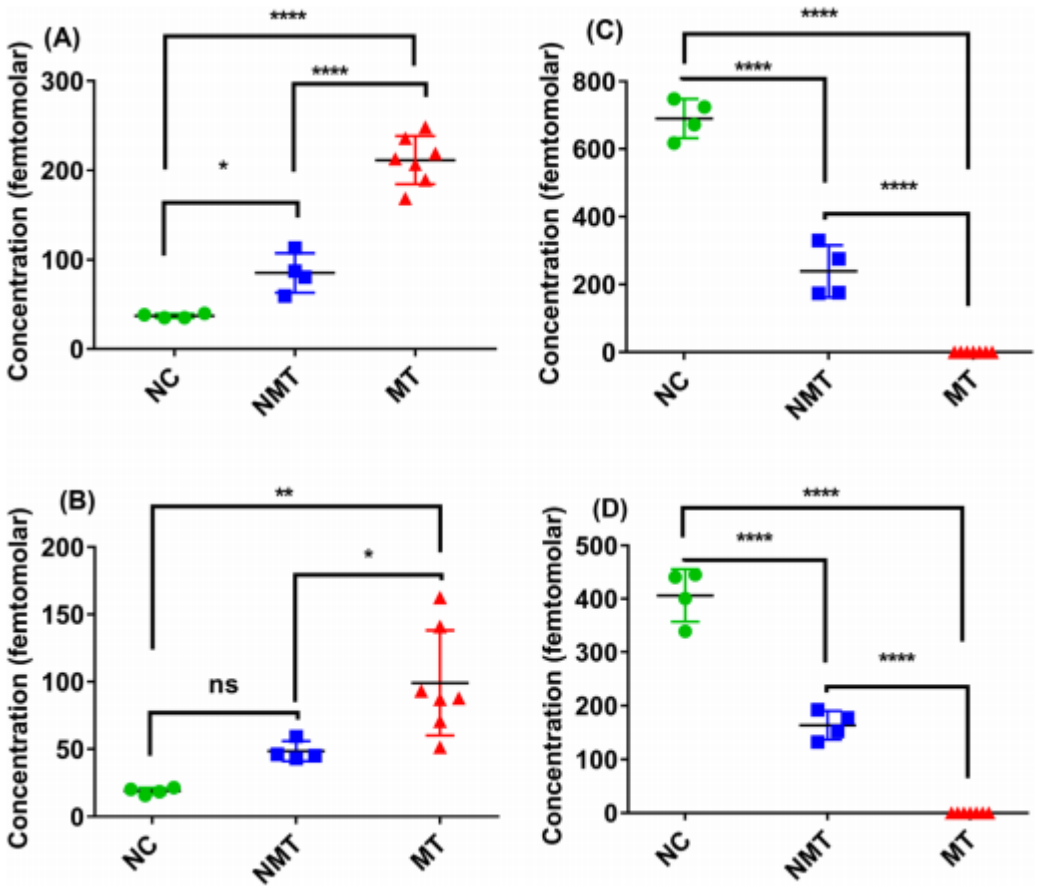

Figure 6.6. Statistical representation of microRNA analysis in BC (MT and NMT) patient plasma and normal control subjects. The concentration of oncogenic microRNAs (microRNA-10b and -182) and tumor suppressor microRNAs (microRNA-143 and -145) are determined in different stages of BC, NMT, and MT, as well as in healthy individuals (NC); n = 4 (NMT), n = 7 (MT), n = 4 (NC), and two experiments for each sample (50 µL/sample) using our nanoplasmonic sensors. (A) microRNA-10b concentration in plasma. (B) Detection of microRNA-182 in plasma. (C) microRNA-143 concentration in plasma. (D) Detection of microRNA-145 in plasma. * $P < 0.05$, **$P < 0.01$, ****$P < 0.0001$, and ns = not significant by one-way ANOVA.

Figure 6.6. A−D shows the concentration of these four microRNAs determined using our nanoplasmonic sensors directly from unmodified patient plasma utilizing the calibration plots developed in human plasma (**Figure 6.7 Table 4**). All seven MT patient samples show high levels of microRNA-10b (**Figure 6.6A**). Moreover, the levels of NC and NMT patient samples are 8- and 2-fold lower, respectively, as compared to MT samples. The results suggest that the microRNA-10b is not the most ideal biomarker for early diagnosis of BC ($p < 0.05$), but it is suitable to differentiate between MT and NMT disease stages ($p < 0.0001$). MicroRNA-182, however, appears to be a less specific biomarker not only for early diagnosis of BC but also in

cancer progression stages (**Figure 6.6B**). Strikingly, microRNA-143 and -145 levels differ by nearly 3- and 4.0 × 103-fold between NC vs NMT, and NMT vs MT BC patient samples, respectively ($p < 0.0001$), see **Figure 6.6C, D**. Moreover, the difference between NC vs MT is >1.0 × 104-fold for tumor suppressor microRNAs, in contrast to the ~6-fold difference observed for oncogenic microRNAs for the same patient samples. To further validate the results, we performed specificity tests of the nanoplasmonic sensors. These tests unequivocally support a high level of specificity toward the target microRNAs without any false positive responses (selectivity). Taken together, microRNAs that our body produces naturally to protect unusual transformation of cellular pathways (tumor suppressor microRNAs) could be more specific biomarkers for early detection of BC and possibly other cancers as well.

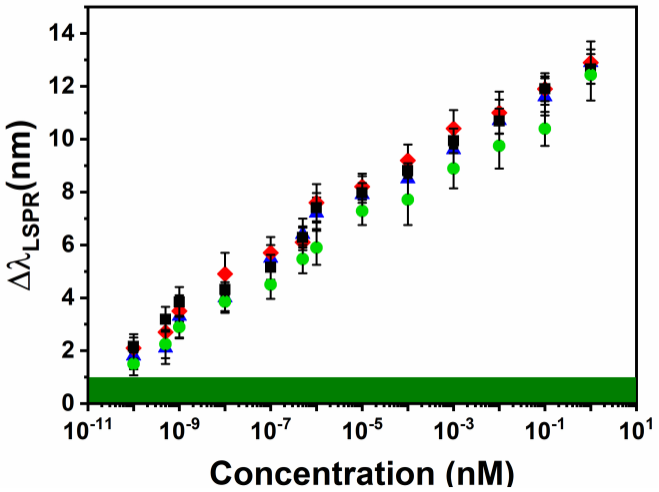

Figure 6.7. Average $\Delta\lambda_{LSPR}$ value of nanoplasmonic sensors for different microRNAs in human plasma: microRNA-10b (blue triangles), microRNA-182 (red diamonds), microRNA145 (black squares) and microRNA-143 (green circles). Each type of nanoplasmonic sensors were constructed with corresponding –ssDNAs as receptor molecules. The standard deviation of the blank (6 measurements) was 0.30 nm and the green bar represents three times that value. Concentrations were plotted on the axis in log scale in order to investigate non-specific adsorption at a lower concentration range.

Table 6.1. Calculated LOD values of LSPR based sensors, which were made using an alkyl chain length spacer, $-(CH_2)_3$, in plasma.

Alkyl Chain	Type of microRNA	Media Condition	Equation from Calibration Curve	R^2 value	Z value (nm)	LOD (zM)
$-(CH_2)_3$	10b	Plasma	y = 0.4714ln(x) + 12.956	0.9905	2.86	499
$-(CH_2)_3$	182	Plasma	y = 0.4706ln(x) + 13.315	0.9889	3.4	707
$-(CH_2)_3$	145	Plasma	y = 0.4844ln(x) + 12.796	0.9912	2.5	587
$-(CH_2)_3$	143	Plasma	y = 0.4182ln(x) + 11.176	0.9931	2.3	605

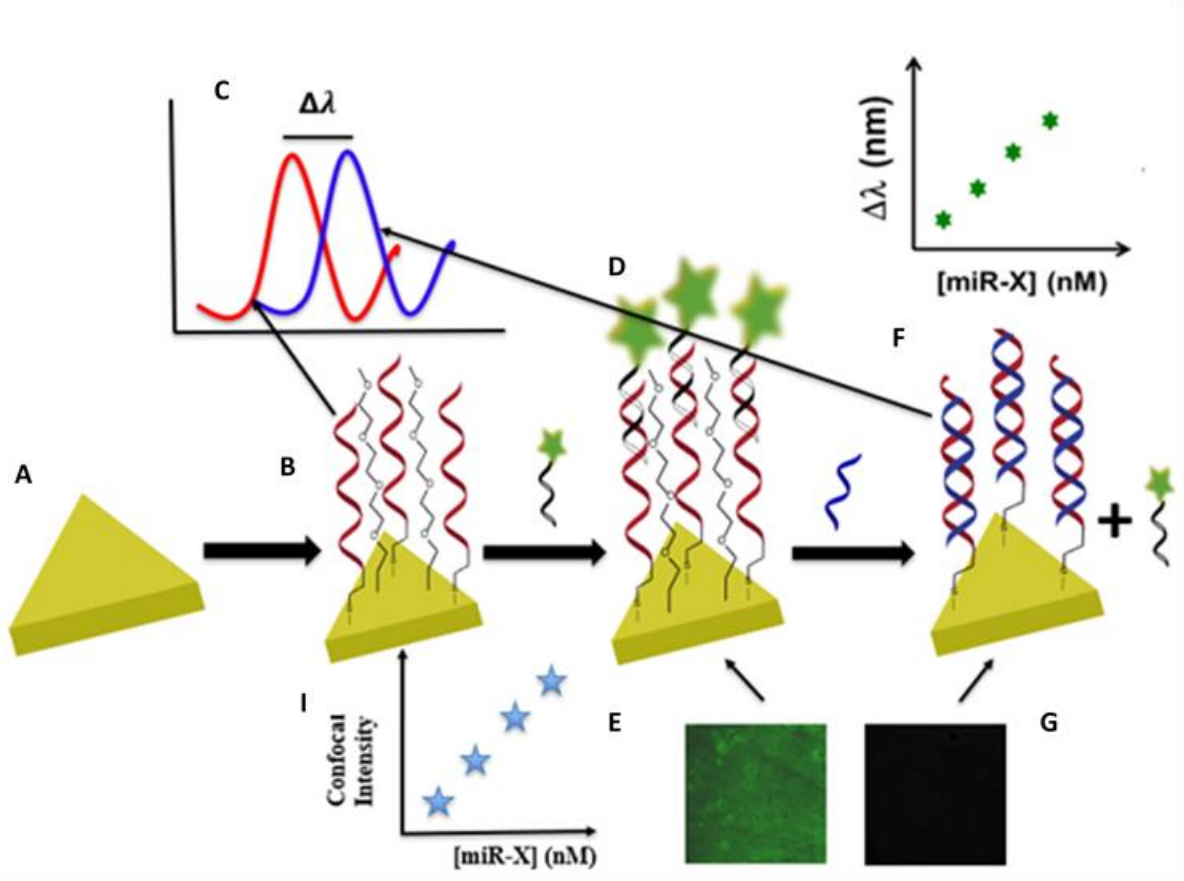

Figure 6.8. Schematic representation of the sensing platform in order mitigate false positive and false negative responses. A) Synthesized Au TNPs are chemically attached onto a silanized glass substrate, and then (B) their surfaces are functionalized with mixed HS-PEG: HS(CH_2)n-ssDNA-X (unique sequence's) to prepare LSPR-based nanoplasmonic sensors. Obtained LSPR shift is shown in red color (C) Incubation of sensors in protector microRNA containing FAM probe attached, solution results in the formation of a -ssDNA/protector duplex (D). Then the sensor was monitored using confocal microscopy and obtained image is shown in (E). After imaging sensor containing ssDNA/protector duplex further incubated in target microRNA containing solution and due to the thermodynamic favorable target microRNA forms ssDNA/TARGET complex (F) and obtained LSPR shift is shown in blue color (C). Same sensor was monitored using confocal microscopy and observed the removal of FAM tag as shown in (G). Finally, two calibration curves were developpes (H) for $\Delta\lambda_{LSPR}$vs microRNA concentration and (I) Confocal fluorescence intensity vs microRNA concentration.

6.4.5 Sensor designing for mitigate the False positive and negative responses

As shown in the **Figure 6.7**, we have modified the previously designed sensor in order to mitigate the false positive and negative responses. Accordingly, chemically synthesized Au TNPs were chemically attached on to the glass coverslips as shown in **Figure 6.7A** and then incubated in a solution containing ssDNA-modified 145 and PEG4-SH (2:1) ratio. Here the sequence

designing was carried out using sequential calculation of $\Delta G^0_{Reaction}$ using ΔG^0_{XC}, ΔG^0_P, ΔG^0_X,ΔG^0_{PC} for every possible sequence select the most favorable sequence according to the **Equation 6.2.** Sample calculation is shown in the **Table 6.4**. Accordingly, gray color high-lighted sequence shows the additional nucleotides to the target ssDNA-145 sequence which is shown in red color based on the target promoter sequence, the calculated $\Delta G^0_{Reaction}$ is given in the last column.

Table 6.2. Calculated $\Delta G^0_{Reaction}$ values for the complimentary, promoter and target complex. The numerical ΔG◦ values (partition function) calculated for each strand and complex by NUPACK [58]

																									ΔG^0_{Reac} kcal/mol.
X	A	A	A	A	G	G	G	A	T	T	C	C	T	G	G	G	A	A	A	A	C	T	G	G	A	C	-20.19
P	T	T	T	T	C	C	C	T	U	U																	
X	G	G	G	A	G	G	G	A	T	T	C	C	T	G	G	G	A	A	A	A	C	T	G	G	A	C	-14.96
P	C	C	C	T	C	C	C	T	U	U																	
X	T	T	T	A	G	G	G	A	T	T	C	C	T	G	G	G	A	A	A	A	C	T	G	G	A	C	-20
P	A	A	A	T	C	C	C	T	U	U																	
X	A	A	A	A	G	G	G	A	T	T	C	C	T	G	G	G	A	A	A	A	C	T	G	G	A	C	-20.19
P	G	G	G	G	C	C	C	T	U	U																	

According to the most favorable $\Delta G^0_{Reaction}$ value we have finally designed the below sequences for the sensor designing **Table 6. 6**.

Table 6.3. Finalized nucleotide sequences based on the most favorable $\Delta G^{0}_{Reaction}$ **calculations.**

Name	Sequences	Modification
-ssDNA-145	5’ AGGGATTCCTGGGAAAACTGGAC 3’	
Modified -ssDNA-145	5’ CCAAAAAGGGATTCCTGGGAAAACTGGAC 3’	3’ Thiol-$(CH_2)_3$
Promoter	3’-GGUUUUUCCCU-5’	3’ FAM
Tareget-microRNA-145	3’UCCCUAAGGACCCUUUUGACCUG5’	

Once Au TNPs functionalized with modified-ss-DNA145 and PEG_4SH the LSPR shift obtained and shown in **Figure 6.8** red color**.** Then the sensor was incubated in a 100 Nm solution containing FAM-attached promoter **(Figure 6.7C) and** the LSPR peak didn’t shift as shown in **Figure 6.8** blue dashed line. This observation is further confirmed our original hypothesis of wave function delocalization via DNA/RNA hybridization. Simultaneously we observed the sensor under confocal microscopic image and observe bright green color fluorescence on the sensor as shown **Figure 6.7E**. Then the developed sensor was incubated in 100 nM target microRNA 145 solution (**Figure 6.7D**) and obtained 18 nm red shift as shown in **Figure 6.8** orange line**.** The same coverslip was subjected to confocal microscopic imaging and we observed all the FAM tagged has removed from the sensor surface as shown in **Figure 6.7F**. This experiment has validated our theoretical calculations and we have designed simultaneous assay of microRNA using LSPR and confocal microcopy which will further help to reduce the false positive and negative responses.

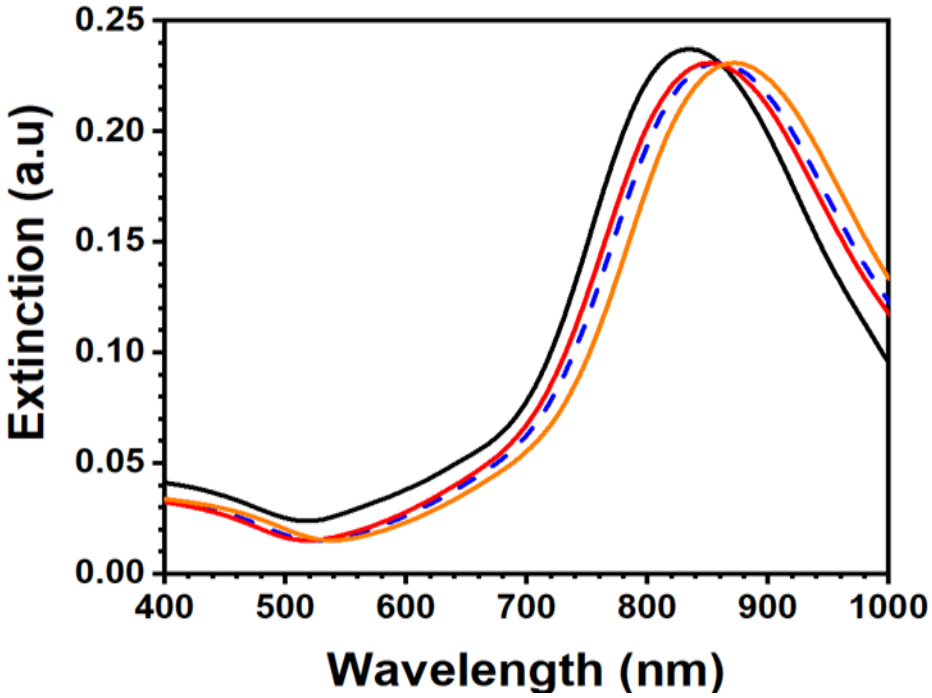

Figure 6.9. UV-visible extinction spectra of Au TNPs before (black curve) and after mixed -SPEG$_4$: modified-S-(CH2)3-ssDNA-145 (nanoplasmonic sensor, red curve) functionalization, and after incubation with 100 nM protector microRNA (blue dashed-curve). Finally, after incubation of target 100 nm microRNA 145 (orange curve). All the spectra were collected in air.

6.5 Summary and Outlook

In summary, we have fabricated a nanoplasmonic sensor, which is capable of assaying microRNAs at ultralow concentration levels from patient plasma. In particular, for the first time we show that tumor suppressor microRNAs are likely to be more specific biomarkers than oncogenic ones for early detection of BC. On the basis of the experimental results, we believe a new transduction mechanism (plasmoelectronic effect), consisting of delocalization of photoexcited conduction electrons wave function of TNP into hybrid LUMOs, is involved for enabling such an unprecedentedly high sensitivity for microRNA detection and quantification. Furthermore, by utilizing Au TNPs as electron donors and their unique LSPR properties as a transduction method, we could experimentally probe the electron wave function delocalization and/or CT properties of short DNA molecules. The process of designing a new class of ultrasensitive nanobioelectronic devices is the current research focus of our laboratory. Taken together, our findings suggest that an ultrasensitive nanoplasmonic sensor, in addition to being a novel liquid biopsy platform for the detection of circulating microRNAs in patient plasma, may

aid in developing early stage, low-volume diagnostic tests for a variety of diseases and analysis for a single cancer cell to better understand tumor heterogeneity.

Further, we have designed and developed the sensor platform for the mitigate false positive and false negative responses by utilizing simultaneous techniques for analysis based on the DNA/RNA hybridization kinetics. As for the first step we have proven that the probe can be designed based on the theoretical calculations and the experimental results further validated the theoretical calculations. However, extensive research needs to be carried out for further optimization and introducing mismatch to the modified ssDNA/Promoter complex may further feasible the leaving process. Also, once optimized the sensor will be utilized for accurately distinguish of different types of cancers.

6.6 References

1. Bartel, D. P., MicroRNAs: Genomics, biogenesis, mechanism, and function. *Cell (Cambridge, MA, United States)* **2004,** *116* (2), 281-297.
2. Esquela-Kerscher, A.; Slack, F. J., Oncomirs-microRNAs with a role in cancer. *Nature Reviews Cancer* **2006,** *6* (4), 259-269.
3. Lockhart, D. J.; Winzeler, E. A., Genomics, gene expression and DNA arrays. *Nature* **2000,** *405* (6788), 827-36.
4. Lu, J.; Getz, G.; Miska, E. A.; Alvarez-Saavedra, E.; Lamb, J.; Peck, D.; Sweet-Cordero, A.; Ebert, B. L.; Mak, R. H.; Ferrando, A. A.; Downing, J. R.; Jacks, T.; Horvitz, H. R.; Golub, T. R., MicroRNA expression profiles classify human cancers. *Nature (London, United Kingdom)* **2005,** *435* (7043), 834-838.
5. Wang, J.; Chen, J.; Sen, S., MicroRNA as Biomarkers and Diagnostics. *Journal of Cellular Physiology* **2016,** *231* (1), 25-30.
6. Petrocca, F.; Lieberman, J., Micromanipulating cancer: microRNA-based therapeutics? *RNA Biology* **2009,** *6* (3), 335-340.
7. Creemers, E. E.; Tijsen, A. J.; Pinto, Y. M., Circulating MicroRNAs: Novel Biomarkers and Extracellular Communicators in Cardiovascular Disease? *Circulation Research* **2012,** *110* (3), 483-495.
8. Lockhart, D. J.; Winzeler, E. A., Genomics, gene expression and DNA arrays. *Nature (London)* **2000,** *405* (6788), 827-836.

9. Polo, A.; Crispo, A.; Giudice, A.; Montella, M.; Cerino, P.; Falzone, L.; Candido, S.; De Petro, G.; Ciliberto, G.; Budillon, A.; Costantini, S., Environment and bladder cancer: molecular analysis by interaction networks. *Oncotarget* **2017,** *8* (39), 65240-65252.
10. Zhang, Y.; Shuai, Z.; Zhou, H.; Luo, Z.; Liu, B.; Zhang, Y.; Zhang, L.; Chen, S.; Chao, J.; Weng, L.; Fan, Q.; Fan, C.; Huang, W.; Wang, L., Single-Molecule Analysis of MicroRNA and Logic Operations Using a Smart Plasmonic Nanobiosensor. *Journal of the American Chemical Society* **2018,** *140* (11), 3988-3993.
11. Alfred Witjes, J.; Lebret, T.; Rouanne, M.; Neuzillet, Y.; Comperat Eva, M.; Cowan Nigel, C.; De Santis, M.; Bruins Harman, M.; van der Heijden Antoine, G.; Hernandez, V.; Espinos Estefania, L.; Dunn, J.; Veskimae, E.; Gakis, G.; Ribal Maria, J., Updated 2016 EAU Guidelines on Muscle-invasive and Metastatic Bladder Cancer. *European urology* **2017,** *71* (3), 462-475.
12. Bokarica, P.; Hrkac, A.; Gilja, I., Re: J. Alfred Witjes, Thierry Lebret, Eva M. Comperat, et al. Updated 2016 EAU Guidelines on Muscle-invasive and Metastatic Bladder Cancer. Eur Urol 2017;71:462-75. *European urology* **2017,** *72* (2), e45.
13. Stenzl, A.; Cowan Nigel, C.; De Santis, M.; Jakse, G.; Kuczyk Marcus, A.; Merseburger Axel, S.; Ribal Maria, J.; Sherif, A.; Witjes, J. A., The updated EAU guidelines on muscle-invasive and metastatic bladder cancer. *European urology* **2009,** *55* (4), 815-25.
14. Witjes, J. A.; Comperat, E.; Cowan Nigel, C.; De Santis, M.; Gakis, G.; Lebret, T.; Ribal Maria, J.; Van der Heijden Antoine, G.; Sherif, A., EAU guidelines on muscle-invasive and metastatic bladder cancer: summary of the 2013 guidelines. *European urology* **2014,** *65* (4), 778-92.
15. Berrahmoune, S.; Bezdetnaya, L.; de Witte, P.; Leroux, A.; Dumas, D.; Guillemin, F.; D'Hallewin, M. A., Prevention of bladder tumor implantion after fluorescence-guided TUR with photodynamic therapy. *Proceedings of SPIE* **2009,** *7380* (Pt. 1, Photodynamic Therapy), 73801V/1-73801V/12.
16. Blasco, E.; Gutierrez-Hoyos, A.; Garrido, C.; Arozena, F., Prognostic markers in transitional carcinoma of the bladder. *Archivos espanoles de urologia* **1991,** *44* (1), 47-52.
17. Branchereau, J.; Larue, S.; Vayleux, B.; Karam, G.; Bouchot, O.; Rigaud, J., Prognostic value of the lymphovascular invasion in high-grade stage pT1 bladder cancer. *Clinical genitourinary cancer* **2013,** *11* (2), 182-8.

18. Carrion-Ballardo, C. J.; Gala-Solana, L.; Portillo-Martin, J. A.; Truan-Cacho, D.; Campos-Juanatey, F.; Azueta-Etxebarria, A., The nested variant of bladder transitional cell carcinoma: Review of 12 cases and review of the literature. *Actas urologicas espanolas* **2015,** *39* (6), 387-91.
19. Cormio, L.; Tolve, I.; Annese, P.; Saracino, A.; Zamparese, R.; Sanguedolce, F.; Bufo, P.; Battaglia, M.; Selvaggi, F. P.; Carrieri, G., Retinoblastoma protein expression predicts response to bacillus Calmette-Guerin immunotherapy in patients with T1G3 bladder cancer. *Urologic Oncology: Seminars and Original Investigations* **2010,** *28* (3), 285-289.
20. Cormio, L.; Tolve, I.; Annese, P.; Saracino, A.; Zamparese, R.; Sanguedolce, F.; Bufo, P.; Battaglia, M.; Selvaggi Francesco, P.; Carrieri, G., Retinoblastoma protein expression predicts response to bacillus Calmette-Guerin immunotherapy in patients with T1G3 bladder cancer. *Urologic oncology* **2010,** *28* (3), 285-9.
21. Glybochko, P. V.; Alyaev Yu, G.; Pshikhachev, A. M.; Sorokin, N. I.; Dymov, A. M., Choosing treatment for patients with bladder cancer combined with prostatic hyperplasia. *Urologiia (Moscow, Russia : 1999)* **2016,** (5), 92-96.
22. Tan, L.-B.; Chen, K.-T.; Guo, H.-R., Clinical and epidemiological features of patients with genitourinary tract tumour in a blackfoot disease endemic area of Taiwan. *BJU international* **2008,** *102* (1), 48-54.
23. Truta, A.; Pop Ioan, V.; Truta, A.; Popon Tudor Adrian, H.; Saraci, G.; Ghervan, L., Health Related Quality of life in bladder cancer. Current approach and future perspectives. *Clujul medical (1957)* **2017,** *90* (3), 262-267.
24. Kouhsar, M.; Azimzadeh Jamalkandi, S.; Moeini, A.; Masoudi-Nejad, A., Detection of novel biomarkers for early detection of Non-Muscle-Invasive Bladder Cancer using Competing Endogenous RNA network analysis. *Scientific Reports* **2019,** *9* (1), 1-15.
25. Cissell, K. A.; Rahimi, Y.; Shrestha, S.; Hunt, E. A.; Deo, S. K., Bioluminescence-Based Detection of MicroRNA, miR21 in Breast Cancer Cells. *Analytical Chemistry (Washington, DC, United States)* **2008,** *80* (7), 2319-2325.
26. Johnson, B. N.; Mutharasan, R., Sample Preparation-Free, Real-Time Detection of microRNA in Human Serum Using Piezoelectric Cantilever Biosensors at Attomole Level. *Analytical Chemistry (Washington, DC, United States)* **2012,** *84* (23), 10426-10436.

27. Zhou, W.-J.; Chen, Y.; Corn, R. M., Ultrasensitive microarray detection of short RNA sequences with enzymatically modified nanoparticles and surface plasmon resonance imaging measurements. *Analytical Chemistry (Washington, DC, United States)* **2011,** *83* (10), 3897-3902.
28. Qavi, A. J.; Kindt, J. T.; Gleeson, M. A.; Bailey, R. C., Anti-DNA:RNA antibodies and silicon photonic microring resonators: Increased sensitivity for multiplexed microRNA detection. *Analytical Chemistry (Washington, DC, United States)* **2011,** *83* (15), 5949-5956.
29. Robinson Bruce, H.; Gelb Michael, H., The Importance of Assay Imprecision near the Screen Cutoff for Newborn Screening of Lysosomal Storage Diseases. *International journal of neonatal screening* **2019,** *5* (2).
30. Henderson, L.; Wolfreys, A.; Fedyk, J.; Bourner, C.; Windebank, S., The ability of the Comet assay to discriminate between genotoxins and cytotoxins. *Mutagenesis* **1998,** *13* (1), 89-94.
31. De Smet, F.; Moreau, Y.; Engelen, K.; Timmerman, D.; Vergote, I.; De Moor, B., Balancing false positives and false negatives for the detection of differential expression in malignancies. *British Journal of Cancer* **2004,** *91* (6), 1160-1165.
32. Tyagi, S.; Bratu, D. P.; Kramer, F. R., Multicolor molecular beacons for allele discrimination. *Nature biotechnology* **1998,** *16* (1), 49-53.
33. Tyagi, S.; Kramer, F. R., Molecular beacons: probes that fluoresce upon hybridization. *Nature Biotechnology* **1996,** *14* (3), 303-8.
34. Joshi, G. K.; Blodgett, K. N.; Muhoberac, B. B.; Johnson, M. A.; Smith, K. A.; Sardar, R., Ultrasensitive Photoreversible Molecular Sensors of Azobenzene-Functionalized Plasmonic Nanoantennas. *Nano Letters* **2014,** *14* (2), 532-540.
35. Joshi, G. K.; Deitz-McElyea, S.; Johnson, M.; Mali, S.; Korc, M.; Sardar, R., Highly Specific Plasmonic Biosensors for Ultrasensitive MicroRNA Detection in Plasma from Pancreatic Cancer Patients. *Nano Letters* **2014,** *14* (12), 6955-6963.
36. Joshi, G. K.; Deitz-McElyea, S.; Liyanage, T.; Lawrence, K.; Mali, S.; Sardar, R.; Korc, M., Label-free nanoplasmonic-based short noncoding RNA sensing at attomolar concentrations allows for quantitative and highly specific assay of MicroRNA-10b in biological fluids and circulating exosomes. *ACS Nano* **2015,** *9* (11), 11075-11089.

37. Joshi, G. K.; Smith, K. A.; Johnson, M. A.; Sardar, R., Temperature-Controlled Reversible Localized Surface Plasmon Resonance Response of Polymer-Functionalized Gold Nanoprisms in the Solid State. *Journal of Physical Chemistry C* **2013,** *117* (49), 26228-26237.
38. Mulvaney, P., Surface Plasmon Spectroscopy of Nanosized Metal Particles. *Langmuir* **1996,** *12* (3), 788-800.
39. Govorov, A. O.; Zhang, H.; Demir, H. V.; Gun'ko, Y. K., Photogeneration of hot plasmonic electrons with metal nanocrystals: Quantum description and potential applications. *Nano Today* **2014,** *9* (1), 85-101.
40. Cisse, I. I.; Kim, H.; Ha, T., A rule of seven in Watson-Crick base-pairing of mismatched sequences. *Nature Structural & Molecular Biology* **2012,** *19* (6), 623-627.
41. Demers, L. M.; Mirkin, C. A.; Mucic, R. C.; Reynolds, R. A., 3rd; Letsinger, R. L.; Elghanian, R.; Viswanadham, G., A fluorescence-based method for determining the surface coverage and hybridization efficiency of thiol-capped oligonucleotides bound to gold thin films and nanoparticles. *Analytical chemistry* **2000,** *72* (22), 5535-41.
42. Willets, K. A.; Van Duyne, R. P., Localized surface plasmon resonance spectroscopy and sensing. *Annual Review of Physical Chemistry* **2007,** *58*, 267-297.
43. Mayer, K. M.; Hafner, J. H., Localized surface plasmon resonance sensors. *Chemical Reviews (Washington, DC, United States)* **2011,** *111* (6), 3828-3857.
44. Nusz, G. J.; Curry, A. C.; Marinakos, S. M.; Wax, A.; Chilkoti, A., Rational Selection of Gold Nanorod Geometry for Label-Free Plasmonic Biosensors. *ACS Nano* **2009,** *3* (4), 795-806.
45. Otte, M. A.; Sepulveda, B.; Ni, W.; Perez Juste, J.; Liz-Marzan, L. M.; Lechuga, L. M., Identification of the Optimal Spectral Region for Plasmonic and Nanoplasmonic Sensing. *ACS Nano* **2010,** *4* (1), 349-357.
46. Mock, J. J.; Smith, D. R.; Schultz, S., Local Refractive Index Dependence of Plasmon Resonance Spectra from Individual Nanoparticles. *Nano Letters* **2003,** *3* (4), 485-491.
47. Lawrence, K. N.; Dutta, P.; Nagaraju, M.; Teunis, M. B.; Muhoberac, B. B.; Sardar, R., Dual Role of Electron-Accepting Metal-Carboxylate Ligands: Reversible Expansion of Exciton Delocalization and Passivation of Nonradiative Trap-States in Molecule-like CdSe Nanocrystals. *Journal of the American Chemical Society* **2016,** *138* (39), 12813-12825.

48. Teunis, M. B.; Nagaraju, M.; Dutta, P.; Pu, J.; Muhoberac, B. B.; Sardar, R.; Agarwal, M., Elucidating the role of surface passivating ligand structural parameters in hole wave function delocalization in semiconductor cluster molecules. *Nanoscale* **2017,** *9* (37), 14127-14138.
49. Jin, S.; Harris, R. D.; Lau, B.; Aruda, K. O.; Amin, V. A.; Weiss, E. A., Enhanced Rate of Radiative Decay in CdSe Quantum Dots upon Adsorption of an Exciton-Delocalizing Ligand. *Nano Letters* **2014,** *14* (9), 5323-5328.
50. Ikeura-Sekiguchi, H.; Sekiguchi, T., Attosecond Electron Delocalization in the Conduction Band through the Phosphate Backbone of Genomic DNA. *Physical Review Letters* **2007,** *99* (22), 228102/1-228102/4.
51. Genereux, J. C.; Barton, J. K., Mechanisms for DNA Charge Transport. *Chemical Reviews (Washington, DC, United States)* **2010,** *110* (3), 1642-1662.
52. Hihath, J.; Xu, B.; Zhang, P.; Tao, N., Study of single-nucleotide polymorphisms by means of electrical conductance measurements. *Proceedings of the National Academy of Sciences of the United States of America* **2005,** *102* (47), 16979-16983.
53. Berlin, Y. A.; Burin, A. L.; Ratner, M. A., DNA as a molecular wire. *Superlattices and Microstructures* **2000,** *28* (4), 241-252.
54. Goodman, S. M.; Singh, V.; Ribot, J. C.; Chatterjee, A.; Nagpal, P., Multiple Energy Exciton Shelves in Quantum-Dot-DNA Nanobioelectronics. *Journal of Physical Chemistry Letters* **2014,** *5* (21), 3909-3913.
55. Wirth, J.; Garwe, F.; Meyer, R.; Csaki, A.; Stranik, O.; Fritzsche, W., Plasmonically enhanced electron escape from gold nanoparticles and their polarization-dependent excitation transfer along DNA nanowires. *Nano letters* **2014,** *14* (7), 3809-16.
56. Rosu, F.; Gabelica, V.; De Pauw, E.; Antoine, R.; Broyer, M.; Dugourd, P., UV Spectroscopy of DNA Duplex and Quadruplex Structures in the Gas Phase. *Journal of Physical Chemistry A* **2012,** *116* (22), 5383-5391.
57. Zhang, B.; Pan, X.; Cobb, G. P.; Anderson, T. A., microRNAs as oncogenes and tumor suppressors. *Developmental Biology (San Diego, CA, United States)* **2007,** *302* (1), 1-12.
58. Zhang, D. Y.; Chen, S. X.; Yin, P., Optimizing the specificity of nucleic acid hybridization. *Nature Chemistry* **2012,** *4* (3), 208-214.

CONCLUSION

Localized plasmon resonance (LSPR) properties of metal NPs that result from the collective oscillation of their conduction electrons upon light irradiation. According to the Drude model when the electron density of the NPs increase (EDG) the LSPR peak of the NPs blue shifting and otherwise (EWG), the LSPR shift will be red shifted. However, we have observed a unique observation for the Au TNPs and accordingly when EDG attached the LSPR peak of Au TNPs was red shifted and when EWG attached the LSPR peak position was blue shifted compare to the neutral molecule. It is well known that the LSPR property is responsive to the concentration, dielectric thickness or refractive index of the attached self-assemble monolayer of ligands onto the nanostructure. With our unique observation of LSPR peak changes of para substituted (EDG/H/ EWG) thiophenol functionalized Au TNPs, we hypothesized that other than the above-mentioned parameters electron wavefunction delocalization from Au TNPs surface to the ligand controls the unique LSPR properties. Our combined LSPR and surface-enhanced Raman Scattering measurements further proved that para substituted conjugated thiols induces delocalization of conduction electrons wave function from nanostructure to ligand monolayer. Furthermore, our density functional theory calculations suggest that the appropriate alignment between the Fermi energy of nanostructure and the highest occupied (HOMO) and lowest unoccupied (LUMO) molecular orbitals energies of ligands are extremely important for efficient charge delocalization that resulted in previously unknown plasmonic properties of hybrid inorganic-organic nanomaterials. We further utilized the UPS spectrum to calculate the work function ϕ changes of the AU TNPs upon functionalization and further validate the hypothesis. We believe this investigation will open new fields of scientific research and promote design of advanced biosensors, plasmon-enhanced photocatalysts, and metamaterials.

We utilized this unique observation of Au TNPs to designed and develop an ultrasensitive highly selective LSPR bio sensor for the microRNA's detection of early cancer diagnosis. Here we believe the electron wavefunction delocalization from Au TNPs surface to DNA/RNA hybridized duplex. microRNAs are small noncoding RNAs that are implicated in enhancing metastasis in breast, pancreatic, liver, and bladder cancers (BCs). With the demonstrated sensitivity and feasibility of our novel methodology, we were able to achieve the zeptomolar concentration for the BC microRNA detection and for the first time we were able to diagnose the

tumor suppressor microRNA in BC patient plasma for highly accurate BC diagnosis. Additionally, we have been advancing our sensing platform to mitigate the false positive and negative responses of the sensing platform using surface enhanced fluorescence technique based on the DNA/RNA hybridization kinetics. This noninvasive, highly sensitive, highly specific, also does not have false positives technique provide strong key to detect cancer at very early stage, hence increase the cancer survival rate.

Surface-enhanced Raman spectroscopy (SERS) is one of the most commonly used techniques for explosive detection. Here we further utilized the unique LSPR property of Au TNPs to develop a SERS based, self-assembled, flexible sensor for explosive detection by utilizing the strong electromagnetic enhancement of Au TNPs. Our sensor is capable of detecting explosives (cyclotrimethylene trinitroamine - RDX, trinitrotoluene-TNT and pentaerythritol tetranitrate-PETN) at parts-perquadrillion, (ppq) levels and has long-term stability and shelf life. Therefore, we believe that this highly sensitive and highly selective SERS based sensor can be utilized for the identification or trace level detection of explosives for investigation of national security concerns. Further we achieved the programable self-assembly of Au TNPs using molecular tailoring to form a 3D supper lattice array based on the substrate effect. Here due to the coupling between nanoparticle plasmon resonances and adsorbate molecular resonances we achieved highest reported sensitivity for potent drug analysis including opioids and synthetic cannabinoids from human plasma obtained from emergency room patient plasma with exquisite sensitivity (parts-per-quadrillion). Altogether we are highly optimistic that our research will not only increase the patient survival rate through early detection of cancer but also help to battle the “war against drugs” that together is expected to enhance the quality of human life.

LIST OF PUBLICATIONS

1. Joshi, G. K.; Deitz-McElyea, S.; **Liyanage, T**.; Lawrence, K.; Mali, S.; Sardar, R.; Korc, M., Label-free nanoplasmonic-based short noncoding RNA sensing at attomolar concentrations allows for quantitative and highly specific assay of MicroRNA-10b in biological fluids and circulating exosomes. *ACS Nano* **2015,** *9* (11), 11075-11089.

2. **Liyanage, T**.; Sangha, A.; Sardar, R., Achieving biosensing at attomolar concentrations of cardiac troponin T in human biofluids by developing a label-free nanoplasmonic analytical assay. *Analyst (Cambridge, United Kingdom)* **2017,** *142* (13), 2442-2450.

3. Teunis, M. B.; **Liyanage, T.**; Dolai, S.; Muhoberac, B. B.; Sardar, R.; Agarwal, M., Unraveling mechanism underlying surface ligand passivation of colloidal semiconductor nanocrystals: Route for preparing advanced hybrid nanomaterials. *Chemistry of Materials* **2017,** *29* (20), 8838-8849.

4. **Liyanage, T**.; Rael, A.; Shaffer, S.; Zaidi, S.; Goodpaster, J. V.; Sardar, R., Fabrication of a self-assembled and flexible SERS nanosensor for explosive detection at parts-per-quadrillion levels from fingerprints. *Analyst (Cambridge, United Kingdom)* **2018,** *143* (9), 2012-2022.

5. **Liyanage, T.**; Masterson Adrianna, N.; Nguyen, H.; Sardar, R.; Oyem Hector, H.; Kaimakliotis, H.; Sardar, R., Plasmoelectronic-Based Ultrasensitive Assay of Tumor Suppressor microRNAs Directly in Patient Plasma: Design of Highly Specific Early Cancer Diagnostic Technology. *Analytical chemistry* **2019,** *91* (3), 1894-1903.

6. Yang, Y.; Lee, J. **T.; Liyanage**, T.; Sardar, R., Flexible Polymer-Assisted Mesoscale Self-Assembly of Colloidal CsPbBr3 Perovskite Nanocrystals into Higher Order Superstructures with Strong Inter-Nanocrystal Electronic Coupling. *Journal of the American Chemical Society* **2019,** *141* (4), 1526-1536.

7. **Liyanage, T.;** Nagaraju M.; Pu Jinghzhi, Sardar, R Investigation of conduction electrons wave function delocalization at the metal nanoparticle–organic ligand interface in solid state, Nano Letters Article, **2019**, ASAP.

8. **Liyanage, T,;** Sardar, R, Programmable Assembly of Plasmonic gold Triangular Nanoprisms Based on the Substrate Property for Highly Sensitive SERS Based Emergency Room Patient Plasma Assay. Manuscript under preparation. Manuscript under preperation.

9. Masterson, A. N.; **Liyanage, T**.; Diess, F,; Kaimakliotis,; H.; Sardar, R., localized-surface plasmon resonance (LSPR)-based, high-throughput assay for early detection of bladder cancer manuscript under preparation.